New insights into the characteristics and dynamics of rhyolite long-lasting volcanic eruptions

Dissertation

zur Erlangung des Grades

“Doktor der Naturwissenchaften”

Im Promotionsfach Geologie/Paleontologie

am Fachberich Chemie, Pharmazie und Geowissenschften

der Johannes Gutenberg-Universität Mainz

Pablo Brian Forte

geb. in Buenos Aires

Mainz, 2018

1. Berichterstatter:

2. Berichterstatter:

Tag der mündlichen Prüfung: 06.05.19

Table of Contents

List of Figures

List of Tables

Preamble

Parts of the contents presented in this thesis have been already published in scientific journals:

Forte, P., Castro, J. M. (2019). H_2O-content and temperature limit the explosive potential of rhyolite magma during Plinian eruptions. *Earth and Planetary Science Letters*, *506*, 157-167.

Forte, P., Domínguez, L., Bonadonna, C., Gregg, C. E., Bran, D., Bird, D., Castro, J. M. (2018). Ash resuspension related to the 2011–2012 Cordón Caulle eruption, Chile, in a rural community of Patagonia, Argentina. *Journal of Volcanology and Geothermal Research*, *350*, 18-32.

Zusammenfassung

Eruptionen rhyolitischer Vulkane innerhalb der letzten Jahre haben, mit beispielsweise monatelanger Ascheproduktion und ihrer weitreichenden Auswirkungen auf die südlichen Hemisphäre, eindrucksvoll die Gefahrenbandbreite unter Beweis gestellt, die von solchen Vulkansystemen ausgehen kann. In 2008 und 2011 brachen in Chile relativ unvermittelt die Vulkane Chaitén und Cordón Caulle aus, beide nach einer fast hundertjährigen Pause größerer Vulkanaktivität. Seither werden große Anstrengungen unternommen, diese lang-anhaltenden rhyolitischen Eruptionen und ihre Produkte näher zu untersuchen. Nichtdestotrotz, verbleiben viele Aspekte der Ausbruchsdynamik und den zugrundeliegenden Mechanismen weiterhin im Dunkeln.

Derartige rhyolitische Eruptionen produzieren einerseits große Mengen vulkanisches Glas—Bimsfragmente und Obsidianglas—welches physikochemische Einblicke in die Eruptionsdynamik ermöglicht, und erlauben andererseits eine genaue zeitliche Einordnung der unterschiedlichen Phasen effusiver und explosiver Aktivität und deren Ablagerungen. In der vorliegenden Studie wurden über 500 rhyolitische Glasfragmente aus Ablagerungen verschiedener Ausbruchsphasen des Chaitén Vulkans in 2008 auf ihren residualen Wassergehalt hin untersucht. Dieser erwies sich über alle Eruptionsprodukte hinweg als sehr variabel mit Konzentrationen zwischen 0.1 bis 3.4 wt.%, wobei sich ein genereller Trend von niedrigen Wassergenalten in effusiven Produkten hin zu hohen Wassergehalten in den explosiven Ablagerungen zeigte. Darüberhinaus ließ sich innerhalb der einzelnen stratigraphischen Horizonte der pyroklastischen Ablagerung ein „Wasserkonzentrations-Fenster“ erkennen, definiert über minimalen und maximalen Wassergehalte der einzelnen Ablagerungshorizonte, welches sich in Breite und Absolutwerte der Wasserkonzentration innerhalb der vertikalen Stratigraphie verändert. Interessanter Weise grenzt dieses Fenster scharf die Wassergehalte der explosiven Produkte von den niedrigeren der effusiven Obsidiangläser ab.

An systematisch ausgewählten Gläsern dieser Ablagerung mit Wassergehalten von 0.13–1.4 wt.% wurden 94 Aufheizexperimente unter Atmosphärendruck und 740–1030°C durchgeführt. In Abhängigkeit des initialen Wassergehaltes zeigten die Proben unterschiedliches Entgasungsverhalten und Deformationszeitskalen des ursprünglich glasigen Materials. Als wichtigste Erkenntnis ergibt sich, dass Gläser mit ausreichend hohem Wassergehalt (≥1.4 wt.%) bei hohen Temperaturen (>874°C) schlagartig fragmentieren. Dies ist der erstmalige Nachweis explosiver Fragmentation durch Vesikulierung einer wässrigen rhyolitischen Schmelze unter experimentellen Bedingungen. Hier wird deutlich, dass initialer Wassergehalt sowie Temperatur maßgeblich das Ausbruchsverhalten beeinflussen. Ein Vergleich mit einem separaten Set an Hochdruckexperimenten in einer Fragmentationsbombe, welche Fragmentation durch rasche Druckentlastung simuliert, legt nahe, dass beide Fragmentationsmechanismen im Laufe der verschiedenen Ausbruchsstadien des Chaitén in 2008 zum Tragen kamen.

Zuletzt werden die Gefahren durch Vulkanasche, die mit solch lang-anhaltenden Eruptionen assoziiert sind, charakterisiert und deren Auswirkungen am Beispiel Patagoniens, Argentinien sondiert. Zusätzlich zu den unmittelbaren Auswirkungen durch primären Tephraregen, zeigte sich, dass weite Gebiete Patagoniens auch stark durch äolisch remobilisierte Asche beeinträchtigt sind. Der kurzzeitige negative Impakt war gravierend, und Umwelt und örtliche Gemeinschaft brauchten 5 Jahre um erkennbare Erholung aufzuweisen. Die Ergebnisse dieser Studie weisen auch auf das Zusammenspiel von Wind, Regen und der Verfügbarkeit von Asche als übergeordnete Kontrollparameter für das Auftreten und die Beständigkeit äolischer Remobilisierung vulkanischer Asche hin.

Abstract

Recent rhyolite eruptions on Earth have demonstrated their capacity to produce a multitude of hazards, including ash formation lasting months and impacting the large reaches of the southern hemisphere. The eruptions of Chaitén volcano in 2008 and Cordón Caulle in 2011, both in Chile, ended a period of almost 100 years without major silicic events. Since then, significant effort has been invested in the characterization of these long-lasting eruptions and their products. However, still many aspects about the dynamics and underlying mechanisms driving rhyolite eruptions remain unravelled.

These rhyolite eruptions provided not only vast amounts of fresh volcanic glass and hence a physicochemical window into the eruption dynamics, but also key temporal aspects of explosive and effusive phases. Here, almost 500 glass shards from the different eruptive phases of 2008 Chaitén eruption were analysed for their H_2O content. Results show that eruptive products preserve a wide range of residual H_2O contents (0.1 to 3.4 wt.%), with an overall trend of H_2O depletion from explosive to effusive. In addition, the presence of "H_2O content windows" within stratigraphic horizons of the pyroclastic sequences, defined by upper and lower H_2O content values, was detected. Interestingly, these windows shift with stratigraphic position and demarcate clear H_2O gaps with respect to effusive obsidians.

Guided by the H_2O distributions observed in the different deposits, 94 heating experiments were carried out at 0.1 MPa, temperatures between 740–1030°C on cylindrical obsidian cores (4X10mm) with water content between 0.13–1.4 wt.%. Results reveal different degassing behaviors and deformation timescales of the glassy material as a function of the initial H_2O content of the sample. The most striking finding is the occurrence of explosive fragmentation at $T > 874°C$ in samples with $H_2O = 1.4$ wt.%. This provides the first observations on explosive fragmentation due to experimental vesiculation of hydrous rhyolite melt and demonstrate that starting H_2O concentration and temperature control eruptive behaviour. A comparison with a separate set of high-P experiments performed in a fragmentation bomb —which simulates fragmentation by rapid decompression— suggest that both fragmentation mechanisms might have operated during different stages of 2008 Chaitén eruption.

Finally, the characteristics and impacts of ash-related hazards associated with these long-lasting events were explored. In addition to the impact of primary tephra fallout, a vast area of the Argentinian Patagonia was also significantly affected by wind-remobilization of ash. Results of this study show the primary importance of wind, rainfall and ash availability in controlling the occurrence and persistence of these events. Regarding the impacts, although in the short-term they were highly negative, the environment and the community start showing signs of recovery after five years.

Chapter 1

Introduction

Rhyolite magmatic systems can generate some of the planet's largest explosive volcanic eruptions, with extensive environmental, atmospheric, and social impacts. Unfortunately, our knowledge of these systems is incomplete and the underlying mechanisms driving rhyolitic eruption styles (ranging from explosive to effusive) are not yet fully understood. Despite significant progress made in experimental volcanology during the last decades (Dingwell, 2010), the typically long-period recurrence intervals of rhyolite volcanism in comparison to intermediate composition and mafic magmatic eruptions has hampered how we interpret observational information in the context of experimental and analytical studies on the eruption deposits.

In fact, 96 years had to pass—since the 1912 Novarupta eruption in Alaska (Hildreth and Fierstein, 2012)—until a new major rhyolitic eruption occurred. In the southern Chilean Andes, and almost without forewarning (Lara, 2009), Chaitén volcano erupted on 1 May 2008. It was the first significant scientifically observed eruption in which rhyolitic magma was produced (Castro and Dingwell, 2009). Three years later, on 4 June 2011, another rhyolitic eruption surprised the world. This time, a silicic fissure eruption of Cordón Caulle, located only 260 km north of Chaitén volcano, injected vast amounts of rhyolitic ash into the atmosphere and produced an extensive lava flow (Castro et al., 2013). These long-lasting events gave the scientific community the opportunity to look at new physical processes that take place during rhyolitic eruptions and showed us that the impact of these events on communities, in particular related to ash fall, can be extensive (e.g., Duhart et al., 2009; Martin et al., 2009; Wilson et al., 2012; Craig et al., 2016a,b; Elissondo et al., 2016). In addition, Chaitén and Cordón Caulle eruptions offered observational frameworks to go back and reinterpret some of the many rhyolite eruptions that occurred in the late Holocene (e.g., Mono craters, Ca; Newberry volcano, Or). Taking the unique opportunity afforded by these recent events, this thesis aims to shed light on the characteristics and dynamics of long-lasting rhyolite eruptions. But to understand the relevance of these eruptions, the first question that should be addressed is: what did we know exactly about rhyolite eruptions before the occurrence of these two volcanic events in the southern Andes?

1.1 Pre-2008 state of knowledge of rhyolite eruptions

Rhyolite magmas (>69 to 73 wt.% SiO_2, for alkalis contents ranging from ~3 to 13 wt.%) represent the SiO_2-rich end member of the magmatic compositions spectrum (Le Bas et al., 1986). More broadly, rhyolite magmas can be placed in a category of silicic magmas that also includes those of dacitic and andesitic compositions. In this context, it is common to refer to rhyolite magmas as highly-silicic. As earlier stated, no rhyolite eruption had been scientifically witnessed before the occurrence of 2008 Chaitén and 2011 Cordón Caulle eruptions. Since the begging of last century until 2008, only three highly-silicic eruptions were recorded in our planet: Novarupta (Alaska, US) in 1912, Cordón Caulle (Chile) in 1960, and Da'Ure (Northern Afar, Ethiopia) in 2005. Despite the 1912 Novarupta eruption being the largest volcanic event of the twentieth century, the only concrete observations of this event came from scattered villages and ship reports (Hildreth and Fierstein, 2012). In ~60 hours that lasted the explosive phase, approximately 28 km^3 of tephra fallout and an ignimbrite deposit of 11±2 km^3 were produced. Pyroclastic products showed compositions ranging from rhyolitic (~78 wt.% SiO_2) to dacitic-andesitic (68–57.9 wt.% SiO_2) (Fierstein and Hildreth, 1992). The initial explosive phase was followed by the extrusion of three lava domes, two dacitic and one rhyolitic. Unfortunately, no accurate constraints exist for the timing of their emplacement. The rhyolitic dome is still preserved and it has become one the iconic pictures of effusive silicic volcanism (Fig. 1.1A). In 1960, the fissure eruption of Cordón Caulle, in the southern Andes, emitted <0.25 km^3 (DRE volume) of rhyolite material (70.3 wt.% SiO_2; Gerlach et al., 1988, Lara et al., 2006). The eruptive cycle lasted for less than 2 months and, unfortunately, only scarce direct observations were made (Lara et al., 2004). Finally, the 2005 rhyolite eruption of Da'Ure was a very short (1 day) and small eruption associated with a rifting event (Wright et al., 2006). Its short duration, together with the inhospitable and remote field area, explains why almost one-hundred years after Novarupta eruption scientists were prevented, one more time, from witnessing a rhyolite eruption. The only evidence of the Da'Ure event is a 500 meters long, 100 meters width and 60 meters deep vent opened at 5 km ENE from the summit of Dabbahu volcano (Fig. 1.1.B). The deposits related to Da'Ure eruption are also scarce: a thin layer of silicic ash (few tens of cm), some bombs at distances up to 20 m from the vent and a small silicic foamed lava body in the central part of the fissure (Ayele et al., 2007). According to Potuzak et al., (2006), these products present glass compositions of 74 wt.% SiO_2 and very low crystal contents (1%).

Due to the lack of direct observations, scientific knowledge about the dynamics of rhyolite eruptions was mainly based on experiments (e.g., Alidibirov and Dingwell, 1996a, Bagdassarov et al., 1996; Stevenson et al., 1997; Navon et al., 1998; Martel et al., 2000 and 2001; Spieler et al., 2004) and forensic volcanology; looking back at the deposits of previous eruptions, piecing evidence together and trying to reconstruct the eruptive dynamics of the volcano (e.g., Eichelberger et al., 1981; Taylor et al., 1983; Eichelberger et al.,1986; Newman et al., 1988; Castro and Mercer, 2004; Rust and Cashman, 2007). All this, together with direct observations of dacite eruptions—which are more frequent in the recent Earth's volcanic history (e.g., Mount Saint Helens (1980, USA), Pinatubo (1991, Philippines), Unzen (1991-1995, Japan)—allowed scientists to identify and characterize the type of volcanic activity and eruptive styles related to silicic eruptions.

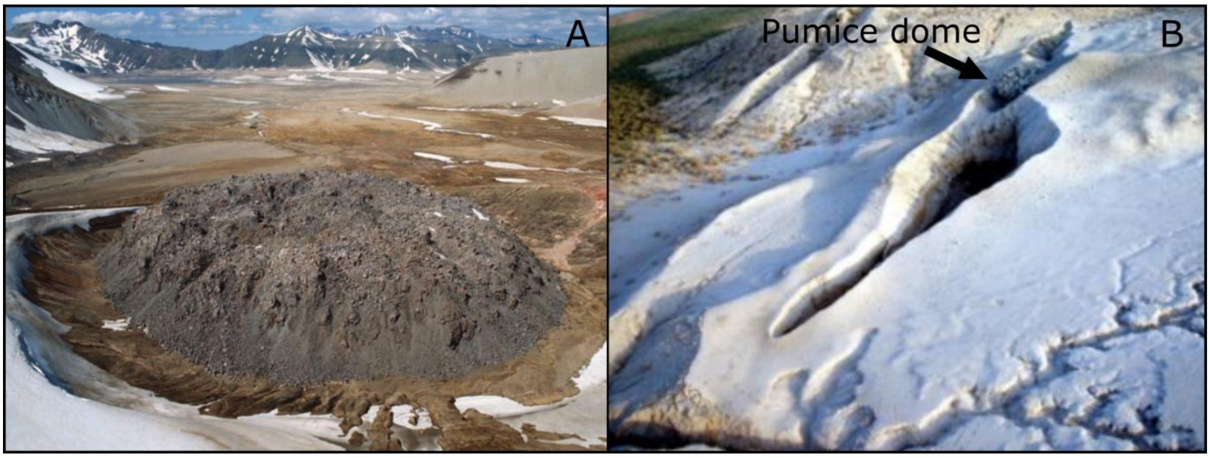

Fig. 1.1. A) 1912 Novarupta rhyolite dome showing a subcircular shape with a diameter of 380 m and an average high of 65 m (Taken from Hildreth and Fierstein (2012)) B). Aerial view of the fissure system where the 2015 Da'Ure eruption occurred. The arrow highlights the location of the 30 m in diameter pumice dome. White ash blanketing the surroundings of the vent can be recognized. Picture taken shortly after the eruption by Asfawossen Asrat and made available online by the Global Volcanism Program (GVP).

Silicic eruptions are often associated with Vulcanian and Subplinian to Plinian eruptive styles, which are among the most explosive volcanic events on Earth and generally involve the generation of large amounts of pyroclastic material (Cioni et al., 2015; Clarke et al., 2015). To generate pyroclasts, the disruption of magma (i.e., mixture of melt ± bubbles ± crystals) into discrete pieces is required. This conversion process of a continuous volume of molten rock into an expanding gas-pyroclast mixture is called fragmentation (Gonnermann, 2015). Understanding the mechanisms underlying magma fragmentation in silicic volcanism has captured the attention of volcanologist since the onset of modern volcanology (e.g., Sparks, 1978), and is also one of the goals of this thesis. For that reason, in section 1.1.2 the main models and existing ideas about how magma fragments are reviewed. But before that, a series of fundamental processes that are necessary for magma to reach fragmentation conditions are described.

1.1.1 Bubble nucleation and growth

Volcanic eruptions are fuelled by magma stored beneath volcanic edifices. In rhyolitic systems, storage areas —named magmatic reservoirs— are generally located between 5 and 10 km depth (Eichelberger, 1995). These depths are equivalent to pressures between 100 and 200 MPa. At these pressures, silicic melts usually contain large amount of dissolved volatiles, being H_2O, by far, the most abundant species (Zhang et al., 2007). With initial values up to 6 wt.% (Bacon et al., 1992; Wallace, 2005), this volatile is one of the main players involved in the evolution of rhyolitic systems and in the occurrence of explosive volcanic eruptions (Eichelberger and Westrich, 1981; Dingwell, 1996; Castro et al., 2005). For that reason, H_2O is a central topic of this thesis. Other volatiles species that can be present in rhyolite magmas are CO_2, SO_2, HF and HCl (Wallace et al., 2015), however, these play little if any role, in driving silicic magma ascent and fragmentation.

The ability of volatiles to remain dissolved in the melt is controlled by the volatile solubility, which depends on pressure, temperature and melt composition (Friedman et al., 1963; Fogel and Rutherford, 1990; Silver et at., 1990; Blank et al., 1993; Dingwell et al., 1997; Tamic et al., 2001; Newman and Lowenstern, 2002; Liu et al., 2005; Ryan et al., 2015). H_2O solubility in rhyolite melts decreases with temperature and increases with pressure. If for any reason, the magma experienced a decrease in pressure (i.e., migration towards surface or removal of overlying rocks), the melt will become supersaturated and volatiles will be exsolved. As a consequence, bubbles will nucleate and growth. Other ways to trigger volatile exsolution include fractional crystallization (e.g., Tait et al., 1989; Taddeucci et al., 2004) and frictional heating (e.g., Lavallée et al., 2015).

Bubbles nucleate at a rate determined by the degree of supersaturation and the activation energy required to overcome the excess energy of the bubble surface. Nucleation can either be homogeneous or heterogeneous (Toramaru, 1989; Mourtara-Bonnefoi and Laporte, 1999; Mangan and Sission, 2000; Gardner and Denis, 2004). First experimental attempts to study nucleation process in rhyolitic melts were performed by Murase and McBirney (1973) and later on by Badgdassarov and Dingwell (1993), which detected the increase in nucleation rates when microlites were present. Hurwitz and Navon (1994) demonstrated that the presence of a crystal-phase reduces the activation energy of the process and consequently, the supersaturation required. According to these authors and later studies by Gardner et al. (1999), $\Delta P \leq 5$–20 MPa are needed to trigger heterogeneous vesiculation; while Mourtara-Bonnefoi and Laporte (1999) found homogeneous nucleation will occur when the pressure drop is > 120–150 MPa (Fig. 1.2A). The fact that homogenous nucleation requires larger supersaturation (larger overpressure), necessarily implies that bubble nucleation will take place at shallower depth. Mangan and Sisson (2000) observed that in this case dissolved water contents in the melt can reach twice its equilibrium value before the onset of vesiculation. Decompression rates also play a role in the nucleation process and in the development of oversaturated melts (Fig.1.2A; Gardner et al., 1999; Mangan and Sisson, 2000)

Once a bubble nucleates, its ability to grow is controlled by a complex interplay of three dynamic processes: diffusion of volatiles into the bubble, viscous deformation of the surrounding melt and decompression rate (Gonnermann and Manga, 2007). Navon et al. (1998) defined three stages during the bubble growth process under constant pressure (Fig. 1.2B): during an initial stage (1), volatile diffusion into the bubble is very efficient and the small bubble grows exponentially. The internal pressure is closed to its initial value and the growth is limited by the viscous resistance of the melt. At stage (2), the growth is parabolic and limited by diffusion. Bubble internal pressure drops and is maintained at slightly above the ambient pressure. Finally, in a multi-bubble situation (3), all excess water is taken by the bubbles, increasing melt viscosity and slowing down the growth rate of the bubble, which asymptotically approaches its final radius. Both, viscous and diffusion regimes that limit bubble growth present characteristic time scales and their ratio is represented by the non-dimensional Peclet number (Lyakhovsky et al., 1996). For the case of continuous decompression of magma, bubble growth is also governed by the decompression rate, and in consequence, a third characteristic time scale has to be considered (Lenksy et al., 2004).

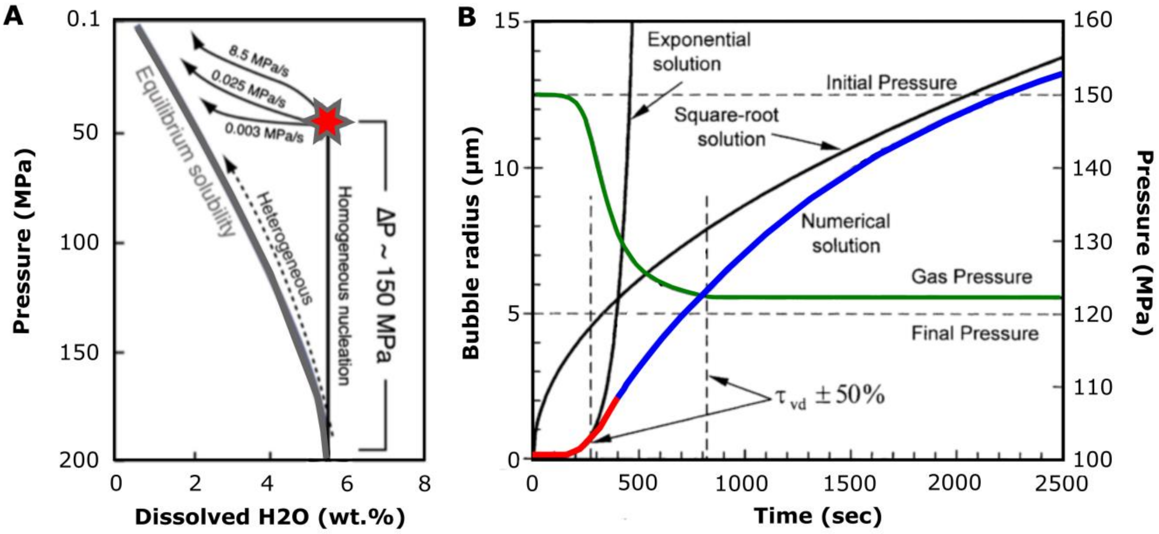

Fig.1.2. A) Degasing paths and changes in dissolved H_2O content for vesiculation controlled by heterogeneous (dash line) and homogeneous (solid lines) bubble nucleation during decompression (Modified from Cashman and Scheu (2015)). For the latest case, nucleation is triggered at overpressure of 120 -150 MPa, regardless of the decompression rate. This variable only affect degassing paths after the onset of nucleation (red star) (Mangan and Sisson, 2000). For the case of heterogeneous nucleation, non-equilibrium degassing only occurs at high decompression rates (i.e., ≥0.25 MPa s^{-1}), in particular during the interval 200 to 140 MPa (Gardner et al., 1999). B) Bubble growth at constant final pressure. Initial growth stage (1) shows exponential behaviour (red line), while during the second stage (2), bubble growth is parabolic (blue line). Green line represents bubble internal pressure evolution. The curves for exponential and square root solutions are also shown (black solid lines). The two vertical lines represent transition time interval ($\tau_{vd} \pm 50\%$) between exponential and square-root (parabolic) solutions. Modified from Navon et al. (1998).

As a consequence of bubble growth, magma vesiculates and increases its volume while it accelerates towards Earth's surface. The study of vesiculation on rhyolite magmas has been approached from theoretical (e.g., Sparks, 1978; Toramaru, 1989; Barclay et al., 1995; Proussevitch and Sahagian, 1996; Lyakhovsky et al., 1996; Navon et al., 1998;

Lensky et al., 2004) as well as from experimental perspectives (e.g., Murase and McBirney, 1973; Bagdassarov and Dingwell, 1993; Bagdassarov et al, 1996; Stevenson et al., 1997; Liu and Zhang, 2000). Many of these studies represent the foundations for the experiments presented in Chapter 3 of this thesis and they are discussed in detail there.

The generation of a gas phase in the magma mixture is of primordial importance to explain explosive behavior of volcanoes, as its high compressibility provides potential for a rapid volume increase during decompression (Sparks, 1978; Gonnermann, 2015). But, is at this point of evolution of the system explosive fragmentation an inevitable process?

1.1.2 The fate of rising magma

The occurrence of explosive fragmentation will depend on the efficiency of the rising magma in releasing its volatiles. Most of the ideas that underlie silicic magmatic degassing models are based on volatiles analysis of obsidian glasses (e.g., Eichelberger and Westrich, 1981; Taylor et al., 1983; Eichelberger et al., 1986; Newman et al., 1988; Dobson et al., 1989; Rust et al., 2004; Rust and Cashman, 2007). These studies, performed mostly on Holocene rhyolite eruptions throughout the Pacific Northwest of the USA (e.g., Newberry volcano, South Sister, Medicine Lake, Mono Craters), showed that H_2O and CO_2 contents and hydrogen isotopic composition of the magma evolves with eruption progress. Degassing models developed from bulk H_2O and hydrogen isotopic data consider close- and open-system volatile exsolution (e.g., Taylor et al., 1983; Newman et al., 1988) as well as multistep combination of these degassing styles (i.e., batch model; Taylor, 1991). In close-system degassing, the exsolved volatiles remain in contact with the melt and the melt composition adjusts to be in equilibrium with the total vapor exsolved. During open-system degassing, exsolved volatiles are immediately removed, preventing equilibrium between exsolved and dissolved volatile in the melt. Taylor et al. (1983) and Eichelberger et al. (1986) were the first to relate explosive-to-effusive transition to these two opposite degassing styles that are controlled by time-varying magma ascent, conduit permeability and deformation modes. This two-stage degassing path, which has historically been assumed to involve a sharp transition between explosive and effusive stages, was adopted as the main eruptive model for silicic eruptions (e.g., Newman et al., 1988; Jaupart and Allegre, 1991; Woods and Koyaguchi et al., 1994; Gonnermann and Manga, 2003). During initial stages, bubbly magma behaves as a chemically close system, allowing the development of bubble overpressure and consequent fragmentation (Fig. 1.3A). With the progression of the eruption, decrease in rates of magma supply and development of permeability in the shallow conduit allows a more efficient outgassing. Consequently, fragmentation is prevented, leading to the extrusion of a degassed lava body (Fig. 1. 3B).

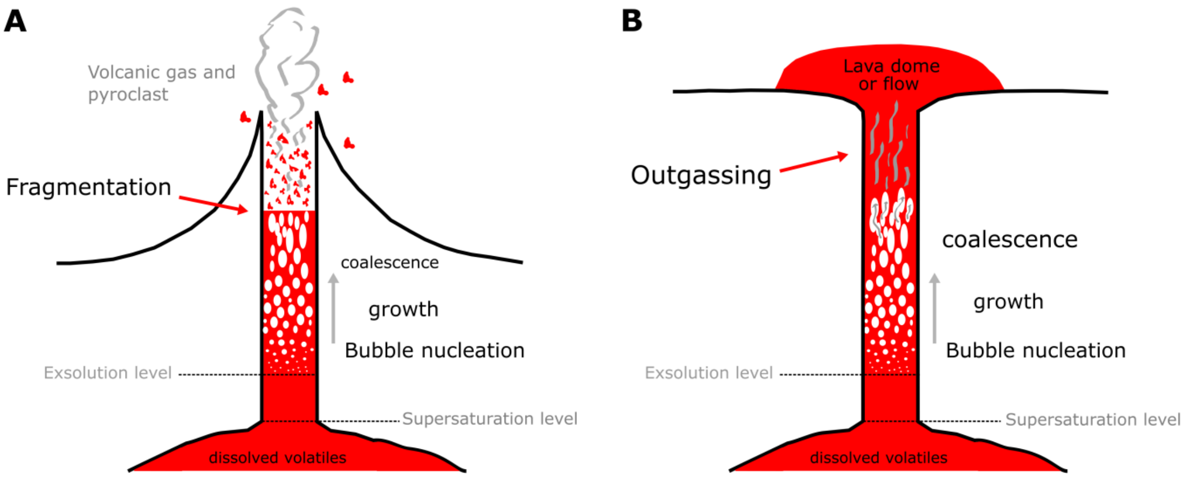

Fig.1.3. Schematic representation of explosive (**A**) and effusive (**B**) stages during the progression of an eruption. Redraft after Gonnermann (2015)

Fragmentation implies the disruption of a coherent volume of magma into a mixture of gas and pyroclasts. For the case of highly-silicic magmas, it can be governed by three different mechanisms: a) brittle fracture, b) external water-magma interaction and c) shear deformation (e.g., Gonnermann, 2015). The first of them, is thought to be the main mechanism involved in the so called, magmatic or "dry" fragmentation; which will be the only one discussed in this thesis. Magmatic fragmentation can be viewed as a bottom-up or top-down driven process (Cashman and Scheu, 2015). In the first of the cases, vesiculation and bubble growth provide the driving force for expansion and fragmentation (Fig. 1.3A), while in the second, fragmentation is accomplished by the failure of suddenly unloaded, already vesicular, magma. This last model better describes explosive events associated with volcanic dome collapse and Vulcanian eruptions, while the first one is more suitable for sustained Plinian and sub-Plinian activity. To date, a number of mechanisms have been proposed for just how brittle failure of magma occurs (e.g., McBirney and Murase, 1970; Sparks, 1978; Alidibirov and Dingwell, 1996a; Dingwell, 1996; Papale, 1999; Zhang, 1999). Fragmentation mechanisms are discussed in Chapter 4, together with the results of experiments performed at variable P-T conditions.

1.2 Witnessing rhyolite eruptions in the southern Andes, Chile.

The occurrence of volcanism in the southern Andes is a consequence of the subduction of the Nazca Plate beneath the South American Plate (Cembrano and Lara, 2009). Along its almost 1500 km length, the Southern Volcanic Zone (SVZ; 33–46°S; Stern, 2004) hosts some of the most active volcanoes in the world (Fig. 1.4A). The SVZ is divided in smaller volcanic arc segments—Northern (NSVZ), Transitional (TSVZ) and Southern (SSVZ) South Volcanic Zone—with distinctive petrological and structural features. A main feature of the TSVZ and SSVZ is the Liquiñe-Ofqui Fault Zone (LOFZ), a 1200 km long intra-arc fault system that accommodates part of the margin-parallel component of the oblique subduction (López-Escobar et al., 1995; Lavenu and Cembrano, 1999). Throughout its extension, LOFZ shows different deformation styles and kinematics, imposing control on the location of many of the volcanic systems in the area (Lavenu and Cembrano, 1999; Stern, 2004; Cembrano and Lara, 2009).

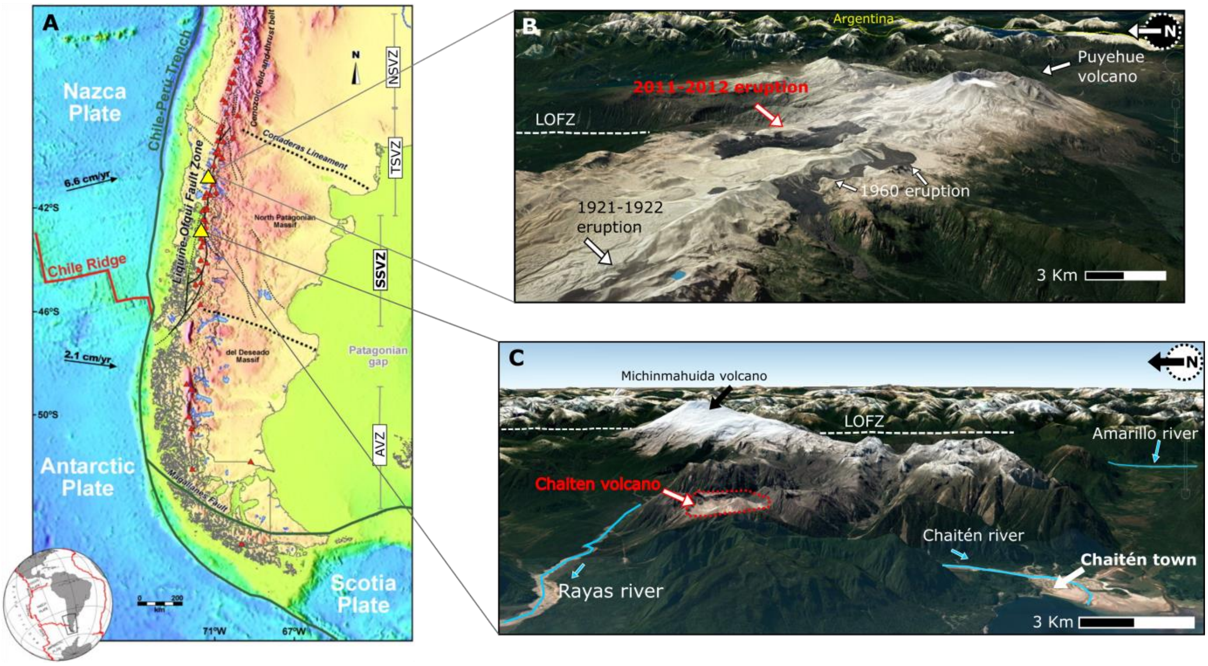

Fig. 1.4 A.) Tectonic setting of the Chilean Andes south of 33°S. Red triangles represent the position of the active volcanic systems at the volcanic front while yellow triangles show the location of Cordón Caulle and Chaitén volcanoes. Modified from Cembrano and Lara (2009). Main features of Cordón Caulle-Puyehue Volcanic Complex (CCPVC) and Chaitén volcano are presented in B and C, respectively. Red dash line in C indicates Chaitén's 3 km wide caldera.

1.2.1 2008–2010 eruption of Chaitén volcano, Chile

Chaitén volcano (42.83°S, 72.65°W) is a relatively small volcanic structure (1120 m.a.s.l) located in the SSVZ, 20 km west of Michinmahuida volcano (2405 m.a.s.l), which is positioned atop the LOFZ (Fig. 1.4C). Michinmahuida is one of the largest volcanic structures in the SSVZ and its deposits evidence a large record of volcanic events, including eruptions in historical times (Amigo et al., 2013). Eruptive products of this volcano show compositions ranging from andesitic to dacitic (López-Escobar et al., 1993; Amigo et al, 2013). Crustal thickness at the latitude of Chaitén is approximately 30–35 km and LOFZ is characterized by transpressive deformation (Cembrano and Lara, 2009). Before its eruption in 2008, Chaitén was considered a dormant volcano. The volcano showed no visual evidences of activity (e.g., gas emissions) and, according to Naranjo and Stern (2004), it last eruption had occurred ~9370 years ago. In consequence, no effort was being invested by the Chilean Geological Service (SERNAGEOMIN) in monitoring its activity. After the 2008 eruption, several studies in the area explored for evidences of previous activity (e.g., Watt et al., 2009; Amigo et al., 2013; Watt et al., 2013; Moreno et al., 2015; Alloway et al., 2017). Watt et al. (2009) were the first to review the stratigraphy proposed for the area by Naranjo and Stern (2004), reassigning to Chaitén eruptive record a 4500 BP event. Amigo et al. (2013) identified two other unknown Holocene moderate-size events: a 6200 -5900 BP rhyolite tephra deposit and another close to the current surface. According to Lara et al. (2013), this last deposit could be correlated to an historical event reported for the 17th century that had been previously associated with activity at Michinmahuida volcano. The authors estimated a bulk tephra volume of 0.5 km^3. Moreno et al. (2015) extended to ten the number of Holocene eruptions of Chaitén by analyzing lake sediment cores from a small closed-basin lake in the vicinity of the volcano (Lago Teo). Alloway et al. (2017) expanded the observational time window, to the end of the Last Glacial Maximum, and identified an additional set of 10 tephra layers, making a total of 20 eruptive events in the last 18000 years. Although with subtle geochemical differences in the major elements, all the products emitted by Chaitén were uniformly rhyolitic (Amigo et al., 2013; Alloway et al., 2017).

As a consequence of the lack of proximal monitoring instruments, very little information exists about the precursory activity that preceded the 2008 eruption. Seismic activity was detected by distant instruments located more than 300 km away only 36 hours before the eruption (Lara, 2009). After this short forewarning, late on the night of 1 May, the eruption started (Castro and Dingwell, 2009). The 2008 Chaitén eruption lasted for almost two years and Pallister et al. (2013) divided it in five phases (Fig. 1.5). An initial (1) ten days-long explosive phase (1–10 May 2008), which showed plinian ash columns that reached altitudes of 19–21 km, the occurrence of directed blasts and pyroclastic density currents (PDCs). Initially, the presence of two vents was reported, which finally merged on 6 May. After this initial purely explosive activity, (2) an extended transitional phase was observed between the 11 and 31 May 2008. Explosive ash emissions and lava effusion occurred simultaneously from the same vent. Finally, phases (3) to (5) represent the purely effusive stages of the eruption, which included both exogenous and endogenous growth of a complex of domes and the extrusion and collapse of aspine. The eruption was over by the end of 2009–beginning of 2010.

The rhyolite nature of this eruption was first reported by Horwell et al. (2008) and confirmed later by many other authors (e.g., Castro and Dingwell 2009, Watt et al., 2009; Alfano et al., 2011; Amigo et al., 2013; Pallister et al.,2013; Moreno et al., 2015; Alloway et al., 2017). Castro et al. (2012a) measured H_2O concentrations in obsidians from all the phases and found values ranging from 0.10 to 1.40 wt%. The Volcanic Explosivity Index (VEI) estimated for the eruption was between 4 and 5 (Carn et al., 2009; Watt et al., 2009).

According to Alfano et al. (2011), the total bulk tephra volume erupted during the whole eruption was ≤1km^3, being ~0.5 km^3 erupted during the first six day of the eruption. The prevailing wind directions in the area caused most of the tephra to deposit in neighboring Argentina (Watt et al., 2009). Regarding the effusive products, Pallister et al. (2013) estimated a total volume of ~0.8 km^3.

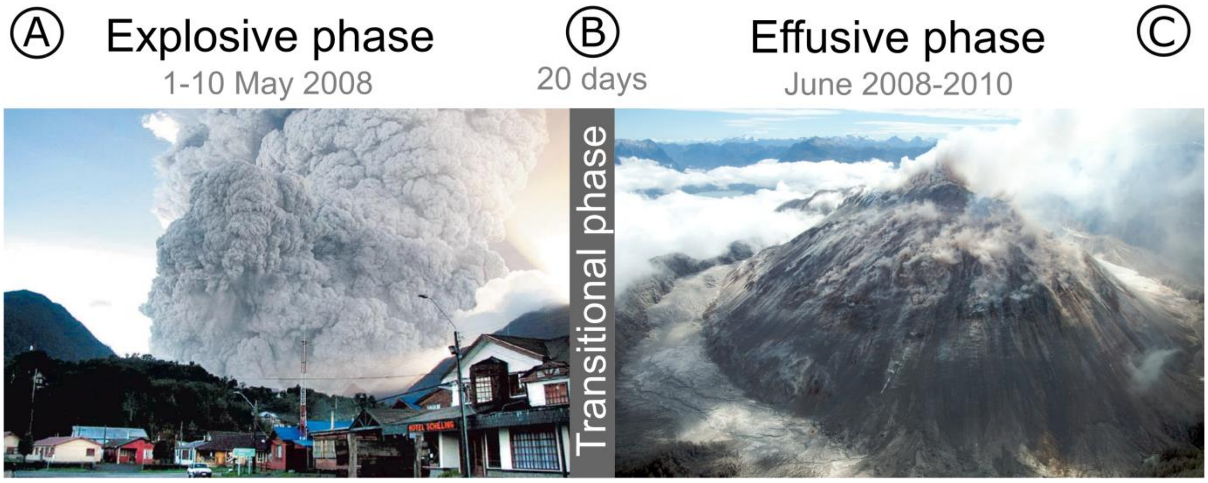

Fig. 1.5 Eruptive phases of 2008–2010 Chaitén volcano eruption. Following Pallister et al. (2013) criterion: A) phase 1= explosive activity, B) phase 2= hybrid activity and C) phases 3 to 5= effusive activity.

1.2.2 2011–2012 eruption of Cordón Caulle, Chile

Cordón Caulle is part of the Cordón Caulle-Puyehue Volcanic Complex (CCPVC), which also comprises Puyehue volcano and erosional remnants of earlier Pleistocene volcanoes (Singer et al., 2008). Located in the TSVZ, 260 km north of Chaitén volcano, the CCPVC forms a 15 km long by 4 km wide NW–SE ridge, built on top of LOFZ. Unlike Chaitén, the eruptive history of CCPVC was well characterized before its last eruption (e.g., Katzui and Katz, 1967; Gerlach et al., 1988; Lara et al., 2004; Lara et al., 2006; Jicha et al., 2007; Singer et al., 2008). This volcanic complex, which encompasses ~140 km^3 of Pleistocene and Holocene volcanic rocks, is unique in the Southern Andes for having erupted a wide range of magma types, from basalts to rhyolites (Gerlach et al., 1988). The most recent activity (pre-2011) of the CCVC took place in the Cordón Caulle fissure system. Last evidence of activity in Puyehue volcano dated from 1.1ka ago, and involves the eruption of andesitic and dacitic lava and scoria from flank vents (Singer et al., 2008). Although the GVP reports ten historical eruptions of Cordón Caulle (from XIIX century to 1990), only two of them can be found in the scientific literature: the ones in 1921–1922 (Stone, 1935; Hantke, 1940) and 1960 (Katsui and Katz, 1967; Lara et al., 2004). While the last one, as already mentioned in section 1.1, was rhyolitic in composition, products of the 1921–1922 eruption were mainly rhyodacitic (Castro et al., 2013). Both events consisted of initial explosive phases followed by the extrusion of lava flows. Extruded lava flows can be easily recognized in satellite images (Fig. 1.4B). Eruptions were short (~2 months) and with small erupted volumes (<0.3 km^3).

On 4 June 2011, after two months of precursory seismic activity, a new eruption of Cordón Caulle occurred (Castro et al., 2013). In contrast to what happened with 2008 Chaitén eruption, the event was well monitored from its onset (Silvia Parejas et al., 2012). The initial phase was characterized by explosive activity (VEI ~4-5) and eruptive columns that reached 10-12 km in height (Bonadonna et al., 2015a). Like in the 2008–2010 Chaitén eruption, lava emission began after 10 days of purely explosive activity, (Lara et al., 2012). Schipper et al. (2013) described the occurrence of gas and ash jets and vulcanian blasts simultaneously with the effusion of the lava flow. Although with lower eruptive columns than during the climatic phase, the emission of tephra continued for several months. In August 2012, SERNAGEOMIN-OVDAS reported the absence of ash emission. By the same time, the lava effusion ceased (Tuffen et al., 2013).

Although the erupted magma was also rhyolite (69.5 to 71 wt.%; Castro et al., 2013), its SiO_2 content was lower than Chaitén, placing it on the compositional boundary with rhyodacitic magma. Residual H_2O contents of the eruptive products were also considerably lower (<0.4 wt.%: Castro et al., 2014). The 2011–2012 Cordón Caulle eruption emitted about 1 km^3 of tephra (Pistolesi et al., 2015) and, again, most of it was deposited to the west, covering vast areas of the Argentinian Patagonia (Wislon et al., 2012; Pistollesi et al., 2015). The impacts of rhyolite tephra fallout, together with the occurrence of associated secondary hazards are discussed in the Chapter 5 of this thesis.

1.3 What have we learned after these eruptions?

Just ten years have elapsed since rhyolite magma reaching the surface was first witnessed. Nevertheless, significant effort has been already invested in the characterization of these eruptions and their products (Castro et al., 2009; Watt et al., 2009; Alfano et al., 2011; Wicks et al., 2011; Alfano et al, 2012; Castro et al. 2012a; Durant et al., 2012; Lowenstern et al., 2012; Castro et al., 2013; Major et al., 2013; Pallister et al., 2013; Schipper et al., 2013; Tuffen et al., 2013; Castro et al., 2014; Jay et al., 2014; Bonadonna et al., 2015a,b; Pistolesi et al., 2015; Schipper et al., 2015; Castro et al., 2016), as well as in the study of the impact they pose for the society (Martin et al., 2009; Pierson et al., 2013; Wilson et al., 2013; Craig et al., 2016a,b; Elissondo et al., 2016). At the same time, these two rhyolite eruptions offered the opportunity to test some of the models and hypothesis developed during the past decades (discussed in section 1.2). They also revealed the occurrence of new physical phenomena and eruptive behaviors previously unknown, in particular related to degassing mechanisms and explosive-effusive transitions. Some existing questions were addressed at the same time new ones have been raised.

The first striking finding was that (hydrous) rhyolite magmas can ascend very rapidly before fragmentation (Castro and Dingwell, 2009). The authors performed petrological experiments and estimated a decompression rate of 40 MPa h^{-1} for 2008 Chaitén rhyolite magma. According to their experiments, the magmatic reservoir was located at P >120 MPa (>5 km depth) and temperatures between 780 and 825°C. Considering this, pre-fragmentation magma average ascent velocity was about 0.5 m s^{-1}. Furthermore, based on the lack of detectable CO_2 and the explosivity of the eruption, they assumed a H_2O-saturated melt (~4 wt.%). By pairing analytical and experimental petrology, Castro et al. (2013) found that the magma involved in the 2011-2012 Cordón Caulle eruption was hotter (870–920°C) and stored at lower pressures (50–100 MPa ≈ 2.5–5 km) than for 2008 Chaitén eruption. At these depths, the magma would contain about 2.6 to 4.5 wt.% dissolved H_2O. These pre-eruptive conditions place Cordón Caulle magma viscosity at the lowest value that can be expected for rhyolite magma under natural conditions.

Remote sensing techniques have also contributed to shed light on rhyolite eruptions dynamics. Based on surface deformation data, Wicks et al. (2009) interpreted that the main magmatic reservoir that fuelled 2008–2010 Chaitén eruption was emplaced 5–9 km below Michinmahuida volcano and that the rapid ascent of rhyolite occurred through dyking. InSAR observations performed by Jay et al. (2014) located 2011–2012 Cordón Caulle magmatic reservoir also at a depth of about 5–9 km. Furthermore, the authors identified three pre-eruptive deformation events and co-eruptive subsidence (from June 2011 to March 2012). With the aid of radar images, Castro et al. (2016) detected an uplift >200 m during the first month of the Cordón Caulle eruption, which was attributed to the syn-eruptive intrusion of a laccolith. Their results showed that explosive rhyolite eruptions may be responsible for shallow magmatic intrusions, and this in turn, raises questions about the hazards related to this phenomenon.

Another striking observation at both Chaitén and Cordón Caulle was that explosive and effusive activity can occur simultaneously. These new evidences compel us to review the existing eruptive models (described in section 1.1.2), which consider a sharp transition (two-stage degassing path) between explosive and effusive phases. How then does magma loses its volatiles and what vent architectures foster simultaneous explosive and effusive activity?

The abundant presence of tuffisite veins in bombs ejected during the explosive phase of Chaitén eruption motivated Castro et al. (2012a) to evaluate the role played by shear-induced fracturing of melt in fostering magma degassing and in controlling the explosive-effusive transition. Tuffisite veins are shear fractures formed by the non-Newtonian response of highly viscous magma to flow-related strain (Tuffen et al., 2003). The authors concluded that, although these pyroclastic and gas pathways may play a key role in transferring gas and pyroclasts to the surface and in linking explosive and effusive eruptive styles, diffusive degassing through tuffisites could not effectively degas magma during 2008 Chaitén eruption. Alternatively, Castro et al. (2014) showed that batched degassing, promoted by variable opening and closing of tuffisite veins, could explain the hydrogen-isotopic evolution of the 2008 Chaitén magma across the explosive-to-effusive transition. Unfortunately, the narrow H_2O content range showed by 2011–2012 Cordón Caulle products prevented the authors from elucidating a significant degassing trend. Schipper et al. (2013) explored the hybrid activity dynamics and, particularly, the vent architecture developed during this last eruption. They suggested the occurrence of a complex shallow vent architecture, with the development of a branching network of permeable degassing structures that extent to depth greater than 1000 m and that allow the long-time open-system degassing regime necessary to promote the effusion of lava. The authors recognized evidence for the interplay of both ductile (i.e., tube-like bubble networks) and brittle processes (i.e., tuffisites veins) of permeability development.

Interestingly, in both eruptions the hybrid (i.e., simultaneous explosive-effusive activity) phase started after ten days of purely explosive activity. In other words, during the first ten days magma degassing was perhaps dominantly closed-system and not efficient enough to prevent explosive fragmentation of the ascending magma. Castro et al. (2013) estimated an ascent rate between 0.3 and 0.6 cm s^{-1} for the first degassed parcel of magma that emerged as lava during 2011–2012 Cordón Caulle eruption. Following their approach, minimum ascent rate values for Chaitén lava were ≥0.6 cm s^{-1}.

Notwithstanding the progress made, the underlying mechanisms driving rhyolitic eruptions are not yet fully understood. There is consensus on the key role of H_2O content in controlling the explosivity of the eruption. However, how melt parcels with variable water contents respond on the local scale to changes in Pressure, Temperature and time (P-T-t) remains unclear, particularly due to the challenges of observing high temperature melt undergoing vesiculation. At the same time, several studies has already shown that residual volatile contents found in rhyolite glasses can shed light on volatile evolution during an eruption. However, up to the ocurrence of 2008 Chaitén and 2011 Cordón Caulle eruptions, an accurate time frame to constrain degassing processes in rhyolite systems was still missing. In the following chapters, effort will be devoted to providing new insights into these open topics.

1.4 Thesis structure

The thesis is comprised of this introduction (Chapter 1) and five additional chapters. In Chapter 2, a detailed description of the H_2O content distribution found in the 2008–2010 Chaitén eruption deposits is presented. To further understand the role played by hydrous volatile species in the dynamics and explosivity of rhyolite systems, a series of high temperature-0.1 MPa experiments were performed at the facilities of the Johannes Gutenberg Universität (JGU) and they along with interpretations and discussion of foaming and explosive behaviour are presented in Chapter 3. Also, adopting an experimental approach, in Chapter 4 different explosive fragmentation mechanisms that could operate during rhyolite eruptions are studied. For that purpose, an additional set of high-pressure experiments were performed at the laboratories of the Ludwig-Maximilians University (LMU). Finally, after characterizing the deposits and exploring dynamics of rhyolite eruptions, Chapter 5 explores the (human and societal) impacts of these long-lasting events. Although the short-term impacts of both Chaitén and Cordón Caulle eruptions have been already studied, in particular the ones related to tephra fallout (e.g., Duhart et al., 2009; Martin et al., 2009; Wilson et al. 2013; Craig et al. 2006a,b; Elissondo et al. 2016), little is known about long-term hazards and impacts of these events. Due to its more recent occurrence and wider affected area, this last research is focus on the 2011–2012 Cordón Caulle eruption. In particular, the phenomenology and impacts of wind-induced ash remobilization are studied. Finally, in Chapter 6 a summary of the entire thesis as well as the implications of the main findings rising from this work are presented.

Regarding the structure of the chapters, it worth to note that each chapter follows the structure of a scientific paper. The reader will find an Introduction, in which the specific topic of that chapter is addressed, Methods, Results, Discussion and Conclusions.

Chapter 2

H_2O evolution in rhyolite systems: the case of the 2008–2010 Chaitén volcano eruption, Chile

2.1 Introduction

H_2O is the most abundant and important volatile component in natural magmas, and it exerts a major influence on the eruptive behaviour of volcanic systems. The presence of dissolved H_2O influences physical and chemical properties of melts as, for example, viscosity (e.g., Shaw, 1972; Hess and Dingwell, 1996; Giordano et al., 2008), chemical diffusivity (e.g., Zhang and Stolper, 1991; Zhang et al., 1991), crystal nucleation and growth (e.g., Fenn, 1977; Davis et al., 1997), liquidus and solidus temperature (e.g., Wasserburg, 1957; Tuttle and Bowen, 1958) and density (e.g., Ochs and Lange, 1999). The existence of H_2O in the Earth can be traced back to the mantle, which is the largest and deepest H_2O reservoir and contains some hundred ppm (~70 to 500) of this volatile component (Wallace et al., 2015). During partial melting, H_2O (and also any other volatile species) behaves as an incompatible element and consequently, migrates and accumulates in shallower reservoirs. At crustal levels, H_2O can reach a variety of concentrations. Basaltic melts in subduction-related reservoirs can contain up to 6 wt.% H_2O (Wallace (2005) and references therein). Lower concentrations can be found in N-MORB (<0.4 wt.%), E-MORB (≤1.5 wt.%), Ocean Island Basalts (0.2–1.5 wt.%) and back-arc basalts (0.1–2.3 wt.%). Silicic reservoirs can also store significant amount of H_2O, with values ranging from 1 to 6 wt.% (e.g., Coombs and Gardner, 2001; Wallace, 2005; Castro and Dingwell, 2009).

This chapter will investigate the H_2O contents in rhyolite systems, but instead of quantifying the abundance of this volatile species at storage conditions (e.g., by phase equilibrium experiments), the focus will be on the characterization of the residual H_2O content preserved in the eruptive products. Taking 2008 Chaitén eruption as a case of study, H_2O content retained in glasses that were produced during the different eruptive phases will be measured. In this way, the study aims to obtain insights about the eruptive dynamics of rhyolite systems. But before proceeding to the methodology section, a brief overview of the main H_2O characteristics as well as a review of existing research on H_2O in rhyolite deposited is presented.

2.1.1 H_2O: main characteristics

H_2O is present in silicate melts as two species: molecular water (H_2O_m) and hydroxyl groups (OH^-). Both species are related via the homogeneous reaction:

$$H_2O_m + O^{2-} \leftrightarrow 2OH^- \quad (2.1)$$

where O^{2-} is an oxygen structurally bound to an anhydrous component of the melt. In the case of fully polymerized melts such as a rhyolite, the O^{2-} is bonded to two tetrahedral cations, constituting what is known as a Bridging Oxygen (BO). According to reaction (2.1), for its progression in any of both possible directions a BO must be created or broken. Due to the fact that BO is the strongest bond in the melt, this reaction will be rate-limited by the exchange frequency of the BO to O^{2-} (Dingwell and Webb, 1990). Furthermore, these authors pointed out that this exchange frequency corresponds to the structural relaxation time of rhyolite melts. Thus, the glass transition curves—which divides liquid and glass field of response of a melt—of hydrous rhyolite should record the glass transition with respect to the reaction (2.1).

Nowadays, the presence of both H_2O species coexisting in melts is a well-established fact (e.g., Silver et al., 1990; Ihinger et al., 1999; Zhang, 1999b; Zhang et al., 2007, Castro et al., 2012a; Dingwell et al., 2016; Mitchell et al. 2018) and its influence on several fundamental processes such as solubility, diffusivity and also on the H isotopic fractionation of H_2O, has been widely demonstrated (e.g., Zhang, 1999b; Zhang and Behrens, 2000; Newman and Lowenstern, 2002). However, before the work of Stolper (1982a,b), it was generally believed that H_2O dissolved in silicate melts dominantly as OH^- (e.g., Hamilton et al., 1964, Burnham,1975), with H_2O_m being present in the melt only perhaps at high pressures or high total dissolved H_2O content (H_2O_t). By using infrared spectroscopy, Stolpers' works proved that any of these two conditions were necessary to stabilize H_2O_m in the melt. Furthermore, Stolper showed that the concentrations of H_2O species in silicate melts are predictable functions of H_2O_t. While OH^- is the dominant species at low H_2O_t, H_2O_m becomes dominant at higher H_2O_t contents. The exact relative OH^-:H_2O_m ratio at which this occurs will depend on the equilibrium constant (K_{eq}) of reaction (2.1), which is defined as:

$$K_{eq} = \frac{[OH]2}{[O][H2Om]} \quad (2.2)$$

where the brackets represent mole fractions. Silver (1988) was the first to identify that the ratio of H_2O species preserved in glasses was quench rate dependent. At higher quench rates, the time spent by the melt at each temperature interval will be shorter and, as a consequence, less interconversion of H_2O species (Eq. 2.1) will take place, leading to higher values of OH^-. Higher quench rates also imply that glass transition will be crossed at a higher temperature (i.e., apparent equilibrium temperature (T_{ae})). Conversely, slower quench rates will result in higher H_2O_m concentrations and a lower T_{ae}. Dingwell and Webb (1990) postulated that this quench-rate dependency implies a temperature-dependence of the species equilibrium in the liquid state. In other words, this means that K_{eq} *(*Eq. 2.2) also is temperature dependent. After that idea was proposed, several studies have demonstrated that K_{eq} increases with temperature (e.g., Ihinger, 1991; Zhang et al., 1991; Nowak and Behrens, 2001), meaning that for a given H_2O_t, equilibrium at higher temperatures leads to higher OH^- contents and vice versa.

The amount of dissolved H_2O preserved in subaerially quenched volcanic glass can be directly measured by spot-based (e.g., Fourier Transform Infrared (FTIR) and Secondary Ion Mass (SIMS) spectroscopy and Raman) and bulk (e.g., Thermogravimetric analysis (TGA) and Karl-Fischer titration (KFT)) analytical techniques. The quantification of H_2O concentration -and the relative abundance of H_2O_m and OH^- species- preserved in the glass, can provide information about its formation (e.g., Dunbar and Kyle, 1992; Rust and Cashman, 2007; Gardner et al., 2017) as well as about melt volatile contents prior fragmentation (e.g., Eichelberger and Westrich, 1981; Bursik et al., 1993) and degassing styles acting during the evolution of an eruption (e.g., Taylor et al., 1983; Newman et al., 1988; Dobson et al., 1989; Taylor et al., 1991). However, volcanic glasses exposed to atmospheric conditions can be altered and therefore may contain secondary—meteoric—H_2O (e.g., Eichelberger and Westrich, 1981; Giachetti and Gonnermann, 2013; Fanara et al., 2015). For that reason, prior to any volcanic interpretation, it is important to know how much of the H_2O retained in the glass has a magmatic origin.

2.1.2 Primary versus secondary H_2O

Once erupted, pyroclastic material is deposited and exposed to atmospheric conditions. If H_2O is available in the environment, it can become absorbed by the glassy pyroclasts, creating a thin H_2O film at their surfaces (Giachetti et al., 2015). During this process, several layers of H_2O molecules are attached to the glass surface. While the first layer is bonded to the glass via Si-O bonds, the subsequent H_2O molecules will do it through hydrogen bonds between them. As rehydration progresses, some of this H_2O can be incorporated to the glass structure by diffusion. Rehydration proceeds from the surface towards the interior of the glass and if sufficient meteoric water is available, it will be a diffusion-limited process. Thus, the degree of rehydration will depend on the time elapsed between sample deposition and collection. The total amount of H_2O gained by rehydration will also depend on the pyroclast specific surface area. A compilation of published matrix-glass H_2O concentrations carried out by Giachetti and Gonnermann (2013) showed a broad positive correlation between porosity and water concentration for a large range of eruptive styles and ages.

A number of methodologies have been developed during last decades to assess whether a glass has incorporated secondary H_2O or not. Some studies have used hydrogen (D/H) and oxygen isotopic signatures to distinguish magmatic from meteoric water (e.g., Taylor et al., 1983; Tuffen et al., 2010; Fanara et al., 2015). Good spatial resolution of Micro-analytical techniques, such as Raman or FTIR, allows for analysis of H_2O concentration gradients from glass surface towards its interior, which are indicative of diffusion profiles (e.g., Watkins et al., 2012; McIntosh et al., 2013). At the same time, based on the idea that secondary H_2O is mainly incorporated as H_2O_m (Denton et al., 2009), FTIR can be also used for the quantification of H_2O species (e.g., Dingwell et al., 2016; Mitchel et al., 2018). Finally, TGA analysis has also shown to be a useful tool to discriminate between primary and secondary H_2O (e.g., Eichelberger and Westrich, 1981; Anovitz et al., 2008; Giachetti and Gonnermann, 2013; Giachetti et al., 2015). This method consists in heating a sample—at a specific rate and to a specific temperature—and recording it loss of weight. The main assumption behind this technique is that secondary H_2O is more weakly bound to the glass chemical structure than magmatic H_2O (Denton et al, 2009; Giachetti et al., 2015). It is important to note that due to the fact that this is a bulk weight loss method, the contribution of other volatile species (e.g., halogens, S, CO_2) has to be ruled out with the aid of a complementary technique. Another weight-loss method used is KFT (e.g., Behrens et al., 1996; Fanara et al., 2015). Although the variety of methods described, none of them can be used to asses quantitatively for post-eruptive rehydration without potential problems. This is mainly because important aspects of glass rehydration at very low temperatures remain unresolved (Giachetti and Gonnermann, 2013).

Other processes that can hinder the interpretation of H_2O degassing signatures preserved in glasses include the interaction of the hot melt/glass with a hydrothermal system (e.g., Tuffen et al., 2010) and bubble resorption (e.g., Yoshimura and Nakamura, 2008; Watkins et al., 2012; McIntosh et al., 2014). Bubble resorption is a solubility dependent process. As a melt experience decompression in its way to the surface, solubility decreases and H_2O is exsolved from the melt into the growing bubbles. However, a subsequent increase in solubility (i.e., increase in P, decrease in T) in the system before quench, can lead to the migration of the volatile back into the melt. Bubble resorption is a process that occurs largely above melt's glass transition (McIntosh et al., 2017).

2.1.3 H_2O contents in rhyolite deposits

During the last decades, a considerable number of works have reported residual H_2O contents in non-vesicular rhyolite volcanic glass (i.e., obsidian). A compilation of many of them is shown in Figure 2.1. Interestingly, while H_2O preserved in glasses associated with explosive activity deposits (i.e., tephra fallout and PDC deposits) ranges from 0.08 to 3.12 wt.%, and a mean of 1.1 wt.%, for effusive products the H_2O range is significantly narrower (0.05 to 0.37 wt.%), with a mean of 0.20 wt.%.

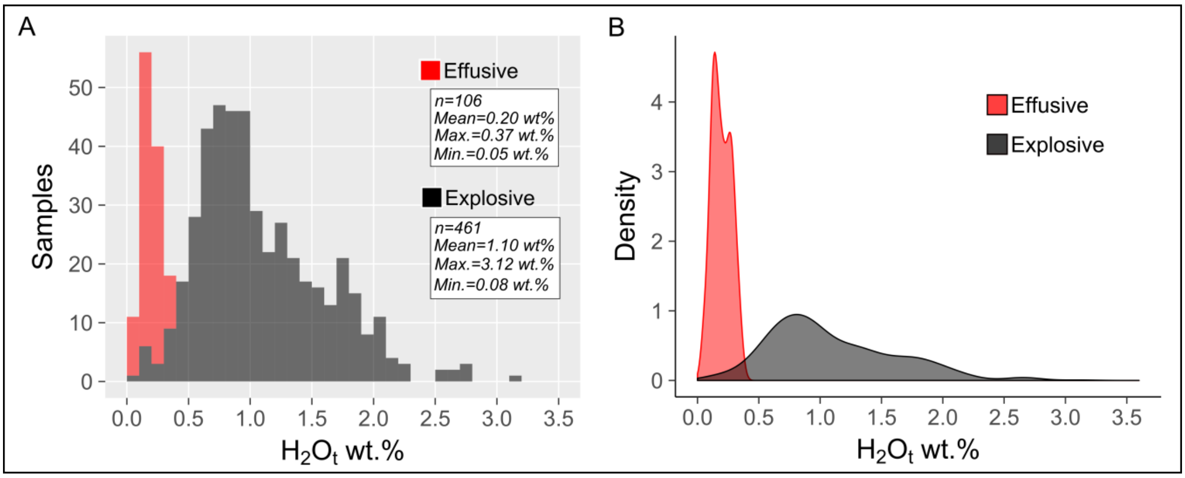

Fig. 2.1 H_2O content distribution of rhyolite obsidian glass for explosive (black) and effusive (red) activity based on available data. Sources: Eichelberger and Westrich, 1981; Taylor et al., 1983; Newman et al., 1988; Bagdassarov and Dingwell, 1993; Bagdassarov et al., 1996; Stevenson et al., 1997; Castro and Mercer, 2004; Tuffen and Castro, 2009; Castro et al., 2012; Barnes et al., 2014; Castro et al., 2014; ; Ryan et al., 2015; Gardner et al., 2017; von Aulock et al., 2017.

Eichelberger and Westrich (1981) were the first to study H_2O content preserved in rhyolite obsidians to constrain its abundance in the deposits and evolution throughout an eruption. The authors performed TGA measurements in glasses from a series of rhyolite volcanic sequences in the Pacific Northwest (USA)—Medicine Lake, Inyo Domes and Crater Lake—deposited up ten thousand years ago. Results showed an abrupt decline in volatile content from explosive (0.3 to 1.3 wt.%) to effusive products (0.05 to 0.2 wt.%). After that pioneering study, Taylor et al. (1983) analysed obsidian clasts from what they called “very young” (≤ 2000-yr-old) rhyolite eruptions from Newberry caldera, Medicine Lake and the Inyo Domes chain. These authors observed a large variation within individual eruptive sequences, with H_2O content decreasing with the progress of the eruption. H_2O concentrations up to 3.1 wt.% were measured in obsidians from the explosive deposits. Furthermore, they identified an apparent boundary between H_2O content from explosive and effusive deposits at ~0.4 wt.%. Eichelberger et al. (1986) further investigated the abundance of this volatile species in effusive deposits by drilling in a 600-yr- old obsidian dome of the Inyo Domes (Ca). The authors reported values in the range of 0.1 to 0.4 wt.%, consistent with previous studies. Newmann et al. (1988) were the first to examine the volatile geochemistry (H_2O and CO_2) of a rhyolite eruptive sequence by infrared spectroscopy (FTIR). The authors were able to analyse obsidians from a well-defined stratigraphic sequence related to the 1340 A.D Mono Craters eruption (US). They reported H_2O values ranging from 0.5 to 2.6 wt. % for the explosive deposits, while glasses from effusive activity showed values <0.4 wt.%. The maximum and mean observed H_2O contents tend to decrease with increasing stratigraphic height (i.e., as the eruption progressed) and by first time, a significant variability in H_2O concentration within each stratigraphic horizon of the pyroclastic deposits was reported. These deposits were later investigated also by Barnes et al. (2014) and Gardner et al. (2017), finding similar ranges of H_2O contents. Dunbar and Kyle (1992) measured H_2O concentrations in 6500 - 20000 yr-old rhyolite tephra deposits from the Taupo Volcanic Zone in New Zealand by applying KFT. H_2O contents obtained for these sequences were between 0.2 and 2.5 wt.%. However, the authors reported some technical limitations for the determination of H_2O contents <0.4 wt.%. For that reason, their results are not shown in Fig. 2.1. More recently, Rust and Cashman (2007) investigated the origin of obsidian pyroclasts related to the 650 A.D Newberry volcano eruption. The authors characterized obsidians textures and volatiles contents (H_2O and CO_2) by performing a detailed sampling of a 2.65 m thick fallout deposit. Their results from infrared spectroscopy measurements showed that H_2O contents range between 0.1 and 1.5 wt% and, although an overall decrease of H_2O with eruption progression was observed, the volatile depletion trend is not as evident as those described in previous studies. Rhyolite obsidian H_2O contents were also reported in many other studies in which the goal was not the characterization of H_2O during eruptive events per se but the performance of experiments (Bagdassarov and Dingwell, 1993; Bagdassarov et al., 1996, Stevenson et al., 1997; Ryan et al., 2015; von Aulock et al., 2017). Even though the large number of measurements and detailed characterization of H_2O content in diverse rhyolite deposits around the world, the lack of direct observation of these events did not allow for precise time constraints on the observed hydrous geochemical trends and stratigraphic patterns.

On the other hand, despite pumices (i.e., vesicular glass) being by far more abundant in rhyolite deposits than obsidians (Newmann et al., 1988; Rust and Cashman, 2007, Watkins et al., 2012), H_2O content data on this pyroclastic component is scarce. This might be probably related to the ease of these porous samples to incorporate significant amounts of secondary H_2O in relative short time. Among the few exceptions, Eichelberger and Westrich (1981) found that pumices contained a broader range of H_2O content (0.5–2 wt.%) than the co-eruptive obsidians, a fact they attributed to the presence of secondary H_2O. Newman et al. (1988) reported 3.07 wt.% H_2O for a pumice from Mono Craters, also a value higher than any of the measured in the obsidian chips. Dingwell et al. (2016) characterized the H_2O content distribution in a 8.7 Ma old tube pumice from the Ramadas Volcanic Center (Altiplano, Argentina), finding values between 4.8 and 5.5 wt.%. The authors estimated that only between 0.86 and 1.01 wt.% of that H_2O was magmatic. Giachetti and Gonnermann (2013) provided values ranging from 0.92 to 3.01 wt.% for pumices from Medicine Lake, Glass Mountain. Unlike the case of obsidians, to date no systematic study exists about residual magmatic H_2O content preserved in pumices during the evolution of an eruption.

2.1.3.1 Recent rhyolite eruptions

The eruption of Chaitén, in 2008, and of Cordón Caulle later in 2011, generated vast amount of fresh rhyolite glass (Castro and Dingwell, 2009; Alfano et al. 2011; Castro et al., 2013). Castro et al. (2012a) were the first to measure the concentration of H_2O retained in obsidians from 2008 Chaitén eruption. By using synchrotron-FTIR, the authors analysed almost 200 pyroclasts, spanning the entire eruptive interval. According to their measurements, total H_2O contents preserved in explosive products range from 0.1 to 1.4 wt.%, while the dome extruded in May 2008 present H_2O contents <0.4 wt.%. Magmatic CO_2 was not detected in any of the analysed samples. Castro et al. (2014) performed Thermal Conversion Element Analyzer (TCEA) mass spectrometry measurements to analyse H_2O_t and H-isotopic composition over a variety of 2008 Chaitén and 2011 Cordón Caulle eruptive products. Chaitén eruptives exhibited similar bulk H_2O (0.1–1.6 wt.%) than the ones reported by Castro et al. (2012a). H_2O preserved in obsidian bombs ranges from 0.22 to 1.59 wt.%, with an average H_2O content of 0.9 wt.%. The authors also found that in most of the cases, tuffisites (i.e., pyroclastic channels) were drier than their hosting obsidians. Furthermore, they provided the first H_2O values of recently-erupted Plinian pumice fragments (bombs and fallout deposits). Interestingly, all the values were consistently around 0.7 wt.%. On the other hand, the products of Cordón Caulle eruption were found to be significantly drier, both pumices and obsidians. H_2O contents reported for these eruptives were uniformly low (<0.35 wt.%), in agreement with the values reported by Schipper et al. (2013). No systematic differences in either δD or H_2O exist for the various eruptive phases and products of this eruption. For that reason, this study will focus only on the deposits related to 2008 Chaitén eruption.

2.2 Methodology

2.2.1. Sampling strategy

Deposits formed during each of the three eruptive phases of 2008–2010 Chaitén volcano eruption were sampled in several field campaigns spanning 2008 to 2016. Samples were collected at variable distances from the vent, both inside and outside the caldera, and comprise: distal Plinian tephra fallout, PDC deposits and volcanic bombs (explosive phase), a tephra cone developed around the vent during the hybrid activity and the lava dome (effusive phase) (Fig. 2.2).

A tephra fallout deposit from the explosive phase was sampled twice, first in June 2008, shortly after the onset of the eruption, and later in February 2016. Samples were collected from the same area of the Amarillo River, some 15 km SW of the volcano (Fig. 2.2). According to Alfano et al. (2011), this deposit corresponds to the Plinian activity that took place during 3 May 2008. The fallout deposit sampled in 2016 was 20 cm thick at the location and it was in contact with the pre-2008 soil (Fig. 2.3A). Samples were collected every 2 cm, following the same criterion than Prof. Jonathan Castro when sampled the deposit in June 2008. Once in the laboratory, samples were sieved and glassy, bubble-free, obsidian chips >250 µm selected with the aid of an optical microscope.

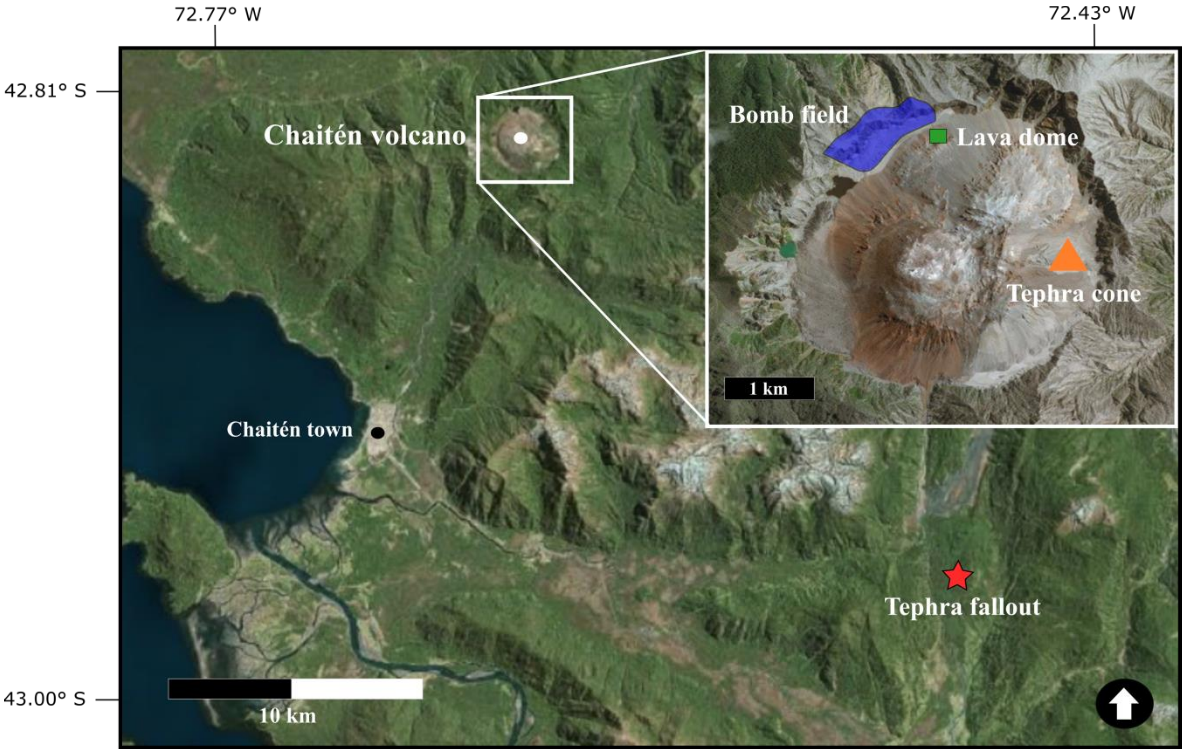

Fig. 2.2 Satellite image showing the location of the study area and the sampling spots. In the upper right corner, a detailed image of Chaitén volcano.

The obsidian and pumice bombs were collected from an area of highly cratered land located to the north of the Chaitén dome and within the caldera during several field campaigns between 2010 and 2016 (Fig. 2.2). Due to the regular occurrence of rock falls from the lava dome, only bombs embedded in the PDC deposit were sampled in its vicinity (Fig. 2.3B). Faced with the logistic impossibility of whole-bomb collection, the main strategy consisted of sampling centimetric-size fragments with no evidence of alteration. Nevertheless, 15 complete specimens were brought to the lab for further investigations. Following the same criteria, material from the earliest extruded lava lobe (May, 2008; Pallister et al., 2013), which is exposed on the northern end of Chaitén caldera was collected (Fig. 3.3C). A sample of a lava dome mapped by Pallister et al. (2013) as part of the pre-2008 lava dome was also obtained.

Regarding the transitional phase, a section of a tephra cone overlying the 2008 and pre-historic lava domes and exposed in the SE, was sampled. The outcrop presents a thickness of 4.25 m and, based on textural characteristics, a number of stratigraphy layers were defined (Fig. 3.3D). All the layers were sampled. Once in the laboratory, the bulk material sampled was dried, sieved and glassy pyroclasts (i.e., obsidians and pumices) >1 mm hand-picked.

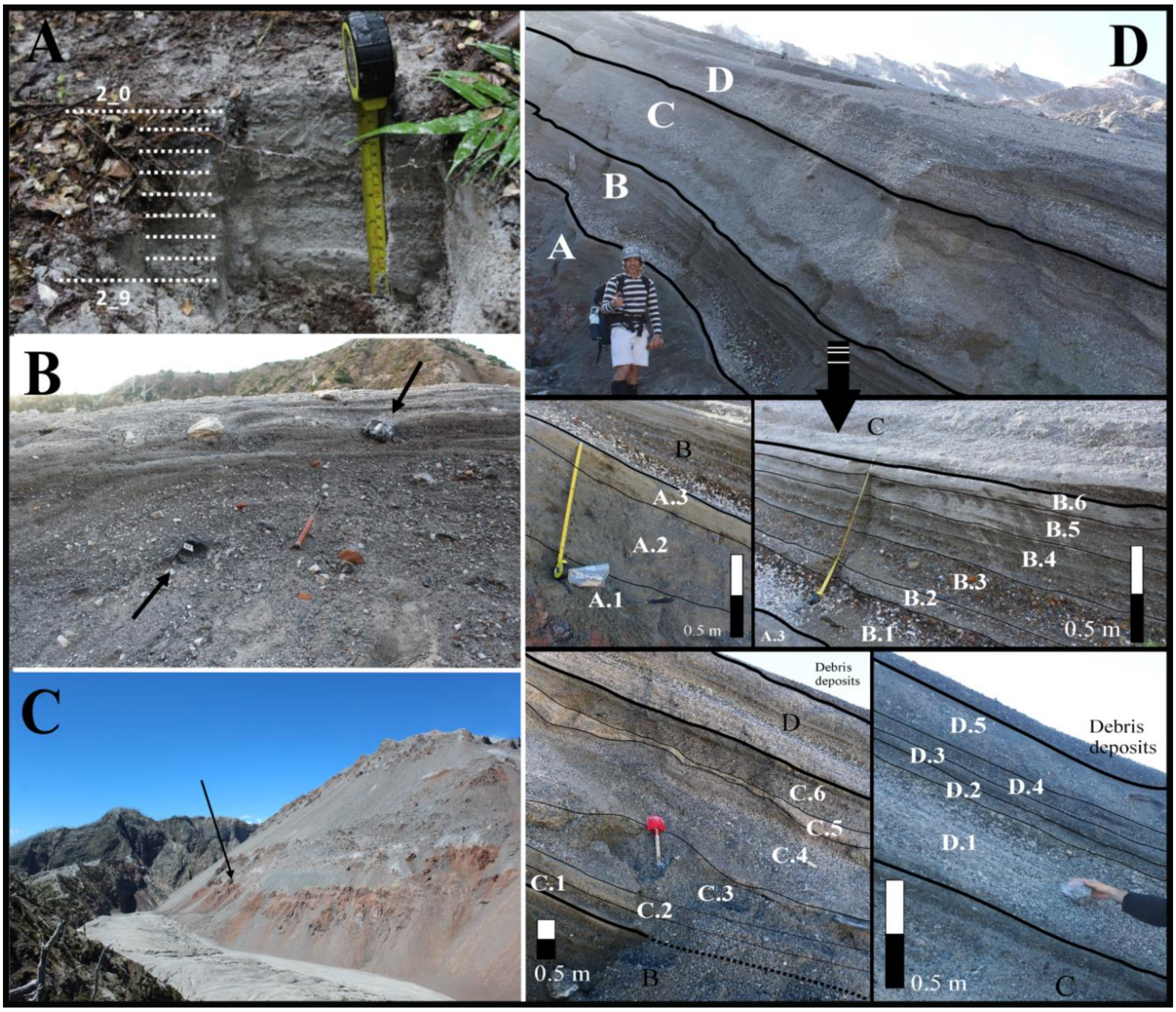

Fig. 2.3. Samples collected from the three eruptive phases (explosive, A–B; effusive, C and transitional, D). A) Ash deposit in the Río Amarillo area. Each dot line represents a horizon from which a sampled was collected. B) Arrows point two obsidian bombs sampled from a PDC deposited (inside the caldera) during the first week of activity. C) North face of the lava dome complex. Black arrow points the lava lobe extruded in May 2008, from which a sample was taken. D) Stratigraphic section of the tephra cone built during the transitional phase. Four main layers (A, B, C and D), and a series of sub-layers were identified.

2.2.2 H_2O content determination

A set of samples from the different deposits described above were selected to analyze their H_2O contents. H_2O concentrations in bubble-free (<5%) glassy samples (i.e., obsidians) were obtained by applying Fourier Transform Infrared (FTIR) spectroscopy. High porosity represents a limitation for this analytical technique. For that reason, Differential scanning calorimetry-Thermogravimetric analysis (DSC-TGA) was used as a complementary technique to obtain H_2O contents of pumices.

2.2.2.1 FTIR measurements

A total of 493 obsidian samples were analyzed by FTIR to determinate their H_2O contents (Table 2.1). In addition to total H_2O_t, hydrous species concentrations were also discriminated. The method also allows for quantification of CO_2, but it was not detected in any FTIR experiments. Measurements were carried out at the facilities of the Institute für Geowissenschaften at the Johannes Gutenberg University (JGU) following the protocols described by Castro et al. (2012a) and von Aulock et al. (2014). Samples were embedded in epoxy, sectioned into thin wafers with a Buhler slow speed saw, and then doubly polished with diamond-impregnated lap wheels. Spectra were acquired using a Nicolet Continuum FT-IR Microscope attached to a Nicolet 6700 FT-IR bench, with a KBr-beamspliter, a MCT/A detector and a 15x objective. Measurements were performed in transmission mode, on the doubly polished wafers that ranged from 95 to 500 µm thick. Wafer thicknesses were measured using a digital Mitutoyo® ball micrometer, with a precision of ~1 µm. Between 4 and 38 spots were measured on each bomb and lava sample, while for the tephra fallout and transitional cone samples 2 measurements were performed on different spots of the sample. Size of the analyzed samples was 1 to 2 mm and 500 µm to 1 mm for the transitional cone and Plinian fallout deposits, respectively. Between 256 and 512 scans were collected at each single spot at 4 cm^{-1} spectral resolution, with some few exceptions in which 1026 scans were collected in order to increase the signal/noise ratio. Background spectra comprising the infrared signal of a sample-free aperture were collected every 10 min and subsequently used by the onboard Omnic software to background-correct each unknown sample spectra. Absorbance values (A) in conjunction with absorption coefficients (ε; Ihinger et al., 1994; Withers and Behrens, 1999) and the Beer-Lambert law were used to determine the concentration (ω) of each hydrous species in weight fraction:

$$\omega = \frac{A.M}{\varepsilon.l.\rho} \quad (2.3)$$

where M is the molar mass of the absorber, l the path length (i.e., thickness) and ρ the density. The absorbance of the hydroxyl (OH^-) peak at 4512 cm^{-1} and molecular water (H_2O_m) peak at 5200 cm^{-1} were used to quantify individual and bulk hydrous components. When not saturated (i.e., peak heights less than 1 absorbance unit), the total water (H_2O_t) peak at 3750 cm^{-1} was also used, and this provided an independent control on the bulk H_2O values obtained by summing the concentrations of the two hydrous species. A glass density value of 2300 kg m^{-3} was assumed for all the samples. This value is based on an average

Chaitén rhyolite glass density and it is in agreement with values measured with a 1mL Witeg® pycnometer.

Table 2.1 Summary of FTIR measurements on obsidian samples

Eruptive phase	**Deposit**	**N° samples analysed**	**N° total measurements**
Explosive	Bomb field	69	528
	Tephra 2008	58	120
	fallout 2016	91	184
Transitional	Pyroclastic cone	274	551
Effusive	Lava dome	2	10
Total		*493*	*1393*

2.2.2.2 DSC-TGA measurements

Differential scanning calorimetry-Thermogravimetric analysis (DSC-TGA) was performed at the Ludwig Maximilian University (LMU), Germany. The instrument used was a STA 449 C Jupiter®, which allows for simultaneous DSC-TGA analysis. Pumice samples were hand-picked from different stratigraphic layers of the transitional cone (Fig. 2.3D). Prior to the analysis, samples were oven-dried at 60°C. Pyroclast with a weight between 20 and 30 mg were placed in a tared platinum cup on the DSC-TGA sample beam and heated from room temperature (~21°C) to 1100°C at a constant rate of 25° C min^{-1}. A total of 11 samples were analyzed. A second measurement was performed on several samples to confirm that samples lost the totality of their volatiles during the experiments. Measurements were carried out by Dr. Kai-Uwe Hess.

2.2.3 Electron Probe Microanalysis (EPMA)

A total of 12 obsidian samples spanning the complete eruptive sequence (from explosive to effusive) were selected to analyze their major element glass compositions. Measurements were performed with the electron microprobe available at the Institute für Geowissenschaften-University of Mainz. Following the standard preparation procedure, all the samples were first polished and then carbon coated. For the measurements, a 10 µm spot was used with a beam current of 60 nA for Cl, F, S and P, and 4 nA for all other elements, with counting times of 50–200s per analysis. During the measurements, Na peaks were counted first to avoid significant migration during the run.

2.3 Results

Chaitén obsidians exhibit a wide range of H_2O_t contents (0.1 to 3.44 wt.%), significantly expanding the upper H_2O limit reported by Castro et al. (2012a, 2014). The dome obsidians have the lowest H_2O concentrations. Measurements revealed that the sample collected from the lava lobe extruded in May 2008 preserves 0.13 wt.% of this volatile species, while the one mapped as part of the pre-2008 dome has retained 0.3 wt.%. Figure 2.4 shows H_2O content distributions for the obsidian clasts from the different pyroclastic deposits studied. Obsidian bombs (Fig. 2.4A) present the narrowest H_2O range (0.57 to 1.77 wt.%) and values define an unimodal right-skewed distribution, with a peak in ~0.6 wt.% and a mean of 0.92 wt.%. The most interesting aspect of this graph is how the absence of bombs containing less than 0.5 w.t.%, defines a sharp lower limit for the H_2O content distribution of these pyroclasts. Distributions of H_2O retained in obsidians from tephra fallout deposits associated with the explosive (Fig. 2.4B) and transitional (Fig. 2.4C) phases show a higher degree of symmetry than the observed for the bombs (Fig. 2.4A). Nevertheless, the distribution for Plinian fallout glasses is slightly skewed to the right, showing a longer tail to high H_2O contents. Maximum H_2O value observed in the glasses from the transitional cone is 2.7 wt.%, while for the tephra fallout deposit obsidians with up to 3.44 wt.% H_2O were measured. Average H_2O contents are similar for both set of samples (~1.1 wt.%). A distinctive feature shared by both distributions is their strong bimodality, associated with the presence of a second mode at H_2O ~0.2 wt.%. Interestingly, in each series the two modes are clearly defined and separate by a sharp decrease in H_2O between 0.4 and 0.5 wt.%. When distributions observed in Fig 2.4A–C are compared with values reported in previous studied for effusive and explosive rhyolite glasses (Fig. 2.4D), it is possible to observe that the distribution of H_2O in bombs as well as the main modes of the transitional cone and Plinian fallout data sets overlap with the distribution for explosive products. In the same way, the secondary peaks observed in these two last deposits at H_2O ~0.2 wt.% coincide with the H_2O distribution characteristic for effusive rhyolites. Thus, it is likely that samples with H_2O <0.5 wt.% observed in Fig. 2.4B and C, represent fragments of the pre-existing dome through which the 2008 eruption developed. In this sense, these samples represent lithic fragments and not primary 2008 magmatic components. In the case of the transitional phase, these obsidians could also be juvenile degassed material associated with the lava dome that was being extruded simultaneously with the occurrence of explosive activity.

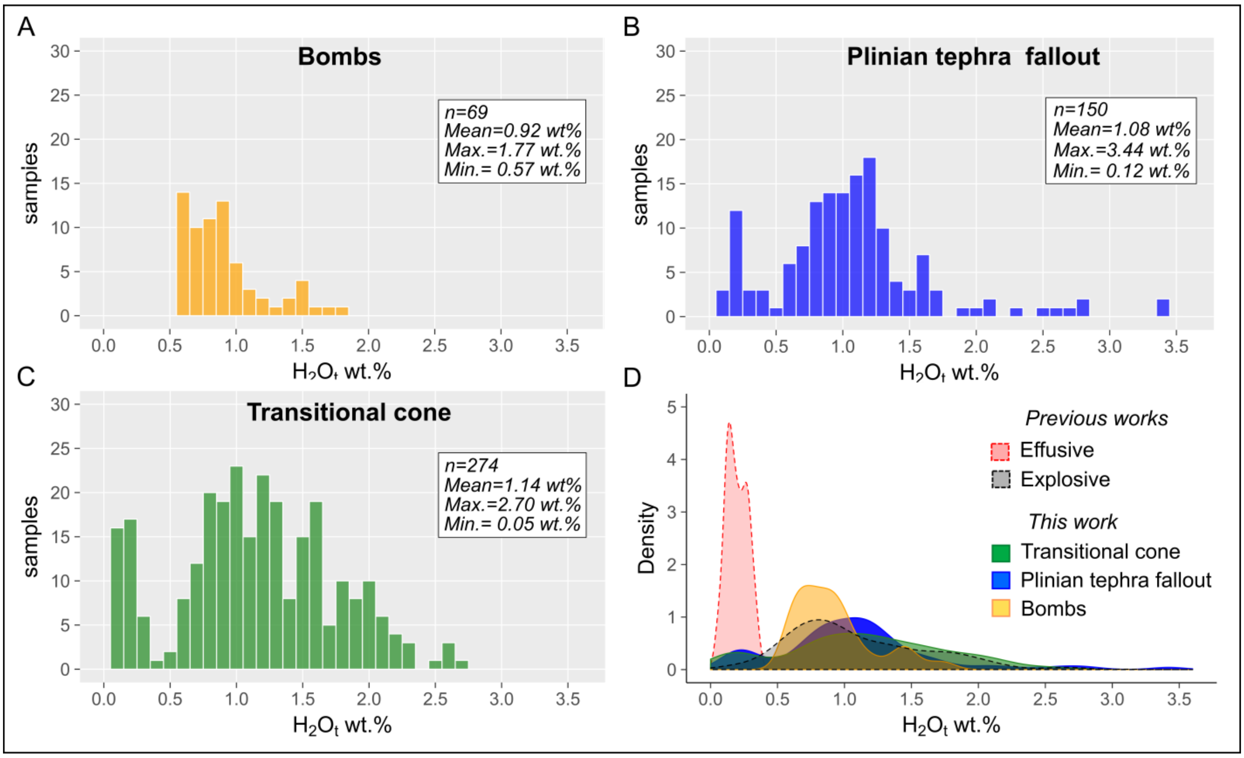

Fig. 2.4. H_2O_t content distribution of 2008 Chaitén pyroclastic obsidians erupted during the explosive (A–B) and transitional (C) phases. Graph D shows a comparison between density curves of these measurements with the H_2O reported for rhyolite glasses in previous studies (Fig. 2.1). The amount of H_2O was determined by FTIR, following the procedure described in section 2.2.2.1. For the complete list of measurements see Appendix A.

Box plots in Fig. 2.5 provide additional elements for the comparison of the distributions observed for the different deposits. Fig. 2.5A shows the same data that was presented in Fig. 2.4. The different degrees of symmetry of the distributions can be clearly identified from the comparison between mean and median values. As described above, symmetry of the distributions increased from bombs to transitional phase glasses. The dispersion of the distributions also increased in this way, as indicated by the inter-quartile box sizes. Box plots also allow for the identification of outliers. While for the bombs all the values >1.47 wt.% are considered outliers (n = 3), for the Plinian tephra fallout distribution the outliers are all the values >2.04 wt.% (n = 10). No outliers for the transitional cone are observed. In figure 2.5B, the same box plots for the three different deposits are shown, but excluding the glasses with H_2O <0.5 wt.%. When these data points are not considered, both, Plinian fallout and transitional cone data sets show skewed-right distributions. At the same time, the exclusion of the driest glasses results in a lower degree of dispersion of the distributions. As a consequence, the number of outliers increases. In this case, all the samples from the tephra fallout and transitional cone data sets with H_2O content >2.01 (n = 11) and 2.64 wt.% (n = 1), respectively, are considered outliers. As no obsidian bombs with

H_2O values >0.5 wt.% were identified, no changes in the distribution is observed for this data set.

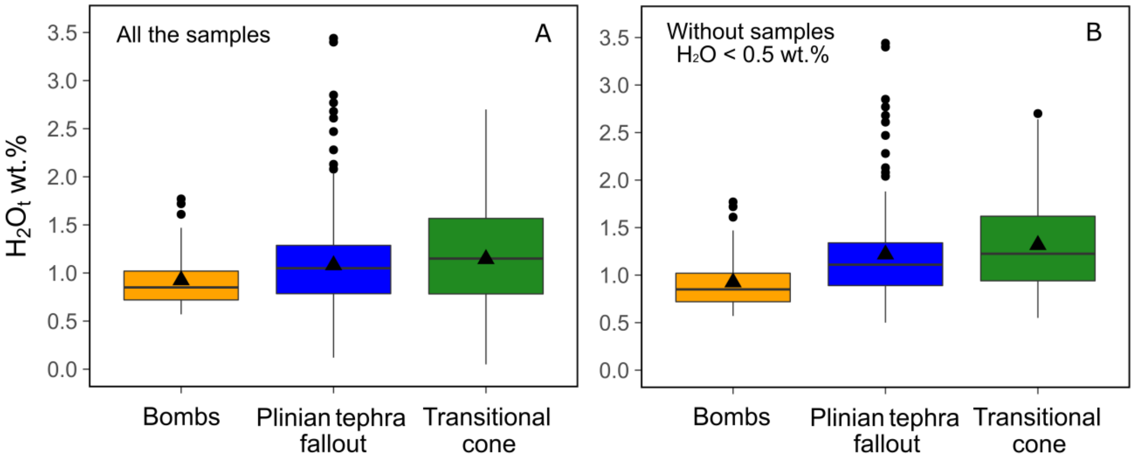

Fig. 2.5 Box plots of H_2O data from the different deposits shown in Fig. 2.4. Each box plot is constructed from five values: the smallest value, the first quartile (Q1), the median (Q2), the third quartile (Q3), and the largest value. Outliers are plot as individual points (black dots) and represent values that are larger than Q3 plus 1.5 times the inter-quartile (Q3–Q1) range or smaller than Q1 minus 1.5 times the inter-quartile range. The median is represented as a thick horizontal black line inside each box, while black triangles shown the mean for each set of values.

Figure 2.6A shows the concentrations of H_2O_m and OH^- groups that are dissolved in the glasses from the different deposits studied. Obsidian pyroclasts from the Plinian tephra fallout and transitional cone deposits contain more OH^- at fixed total H_2O content than the obsidian bombs. At the same time, differences between glasses from the first two aforementioned deposits are observed at H_2O_t >1.6 wt.%, as evidenced by the larger dispersion of data at higher OH^- and H_2O_m contents. On closer inspection, Fig. 2.6A reveals that there is a group of samples from the transitional cone that lie out of the main trend, showing a larger range of H_2O_m content for a certain OH^- concentration. With the exception of this last feature, the speciation data is in agreement with the one reported by Castro et al. (2012a), as shown in Fig 2.6 (B–D). In all the cases, trends from both studies overlap and show similar degree of dispersion. Furthermore, these figures (Fig. 2.6B–D) demonstrate how the results of this study extend the range of H_2O contents measured in each deposit. Castro et al. (2012a) attributed the different H_2O species ratio observed between the deposits to their distinct thermal histories, related to different magma ascent and cooling histories. The authors verified their hypothesis by providing cooling rate calculations based on Zhang et al. (2000). Results showed average cooling rates of 500 K s^{-1} for the pyroclasts from the Plinian tephra fallout and transitional cone deposits, 1 K s^{-1} for tuffisite bombs and 0.01 K s^{-1} for effusive obsidians.

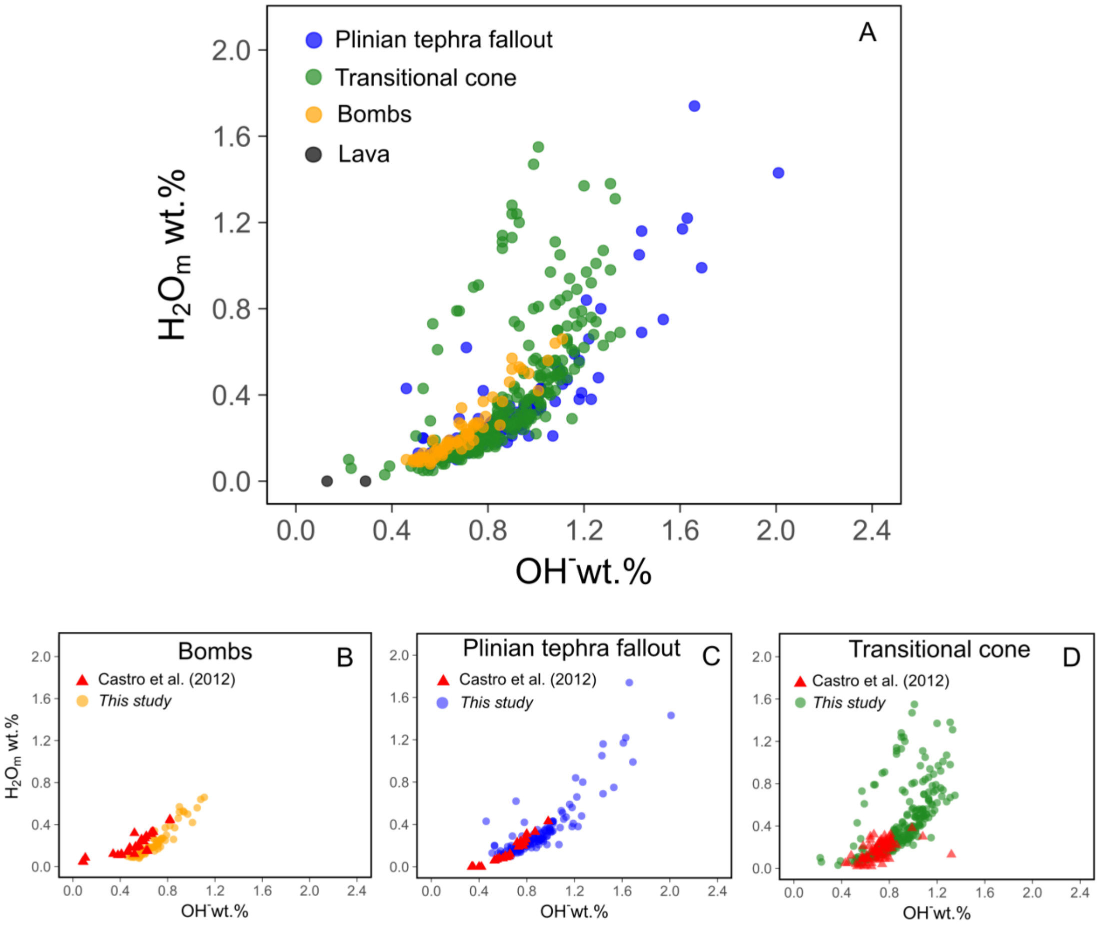

Fig. 2.6 Hydrous speciation in Chaitén obsidians as determined by FTIR. In A, the speciation data obtained for the different group of samples is shown. In B to D, H_2O species for each set of pyroclastic obsidians are compared with H_2O speciation data published by Castro et al. (2012a). Each dot represents an average of 2 to 38 punctual measurements (see Appendix A for details). Error bars are smaller than respective symbols.

Pumice samples collected from the transitional cone deposits showed a loss in mass relative to the initial mass sample of 0.65 to 1.68 wt.%, when heated during the DSC-TGA experiments (Table 2.2). Due to the fact that no evidence of CO_2 was detected during the FTIR measurements, all the weight loss is attributed to the release of H_2O. These results will be further analyzed in the discussion.

Table 2.2 H_2O content of pumice samples from the transitional phase measured by DSC-TGA

Stratigraphic unit	**Sample**	**H_2O released pre-Tg (wt.%)**	**H_2O released post-Tg (wt.%)**	**Total H_2O* released (wt.%)**
D	D4_p2	0.04	0.51	**0.65**
	D4_p1	0.37	0.62	**1.09**
C	C6_p1	0.3	0.69	**1.09**
	C4_p2	0.37	0.63	**1.10**

	C4_p1	0.32	0.5	**0.92**
	C1_p1	0.53	0.8	**1.43**
B	B4_p2	0.62	0.87	**1.59**
	B4_p1	0.88	0.77	**1.75**
	B2_p1	0.88	0.7	**1.68**
A	A1_p2	0.38	0.77	**1.25**
	A1_p1	0.78	0.89	**1.77**

* Values were corrected by adding 0.10 wt.% to account for unextracted H_2O in glasses after heating (Leschik et al. 2004)

Glass chemistry is a useful tool to distinguish between deposits from different sources and volcanic events (e.g., Fontijn et al., 2014). In Fig. 2.8, glass compositions of samples from the different eruptive phases of 2008 Chaitén eruption are shown. For ease of comparison, values were normalized to the composition of an obsidian bomb representative of the explosive phase.

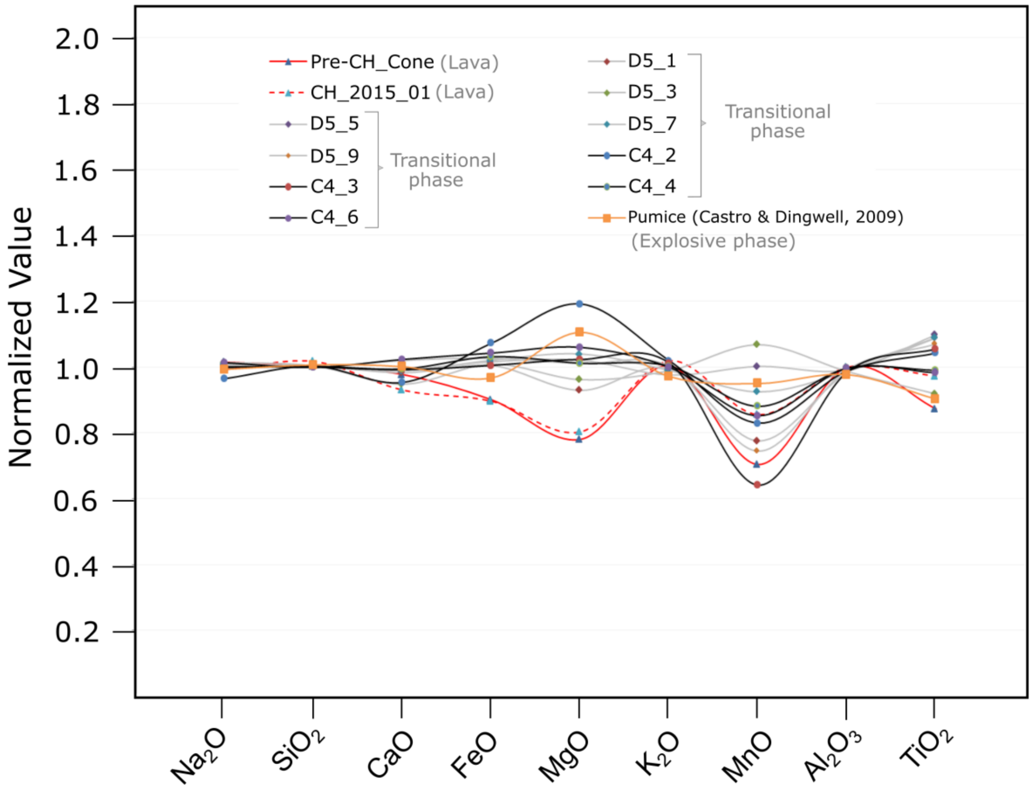

Fig. 2.7. Glass composition of the 2008 Chaitén eruptives. Values are normalized to the composition of an obsidian bomb (CH_2016_04) for ease of comparison between products of the different eruptive phases. Each curve represents an averaged value of 3 to 6 measurements. A complete list of the EMPA analysis can be found in Appendix B.

All glasses measured are rhyolite in composition, with similar SIO_2, Al_2O_3, Na_2O, CaO and K_2O values irrespective of the eruptive phase. Subtle differences are observed for FeO, TIO_2, while variations are larger for MgO and MnO. However, no apparent correlation is observed between these variations and eruption progression (i.e., position in the stratigraphic record). The large amplitude of the curves at MgO and MnO can be explained as an artifact due to the manner in which the results were plotted. In particular, since MgO and MnO are both of low concentration, an even minor fluctuation in their values could represent a relatively large difference with the obsidian bomb used as a reference. Figure 2.8 also includes a pumice from the explosive phase measured in Castro and Dingwell (2009), which composition is within the range of the ones measured in this study. Furthermore, the values obtained for the different products are in agreement with the EPMA analysis presented by Amigo et al. (2013). Altogether, this indicates that all the samples are derived from the same magma source.

2.4 Discussion

Each of the deposits that represent the three eruptive phases observed during 2008 Chaitén eruption preserves specific H_2O ranges preserved in their glasses. As introduced in section 2.1.3, evolution of H_2O during the progression of an eruption was already studied in some Holocene rhyolite eruptions throughout the Pacific Northwest (USA). However, due to the lack of direct observations, before the eruption of Chaitén in 2008 precise constraints on the time of deposition of the different eruptive products was missing. In this sense, this eruption gave us the opportunity, for the first time, to associate the deposits, and hence their preserved H_2O, with a precise timeline of their eruption. This allows for the study of H_2O content evolution during the 2008 Chaitén event, at the same time that offers a platform rooted in observation to go back and reinterpret some of the many rhyolite eruptions that occurred in the late Holocene.

2.4.1 Magmatic or secondary H_2O?

A necessary first step to any interpretation of the results is to elucidate whether the H_2O measured in the glasses is magmatic or if there are also contributions from meteoric sources. This is particularly relevant in light of the high values obtained (up to 3.5 wt.%) for some of the glasses from the explosive and transitional phases. Considering the slow diffusivity of H_2O at low temperature (10^{-24} and 10^{-21} m^2 s^{-1}; Giachetti and Gonnermann, 2013) and the short time elapsed between sample deposition and collection (<8 yrs.), the extensive incorporation of H_2O into the glass chemical network seems highly unlikely. Oxygen isotope composition measured by Castro et al. (2014) on a lava dome sample also ruled out the presence of meteoric H_2O. Nevertheless, Chaitén eruptives were exposed to a wet environment once ejected into the atmosphere, as this volcano is located in a region with an average annual rainfall of ~2400 mm. This might be particularly relevant for the case of pumices, which higher specific surface areas could facilitate the incorporation of significant amounts of H_2O by adsorption.

2.4.1.1 Hydrous speciation

The analysis of H_2O species provides a relatively simple and powerful tool to shed light on the origins of the H_2O retained in volcanic glasses. As described above, the relative abundance of OH^- and H_2O_m is determined by K_{eq} (Eq. 2.2), which defines the equilibrium species concentration for a certain set of conditions. Any perturbation to this equilibrium will lead to compensation by the interconversion reaction (Eq. 2.1). Importantly, the speed of this reaction decreases with falling temperature (Zhang et al., 1991; 2007). If H_2O_m enters the melt at magmatic temperatures, Eq. 2.1 will act rapidly to convert that H_2O_m into OH^-. However, at lower temperatures, the interconversion rate is considerably slower and it will become negligible once the glass transition is crossed. The temperature at which this occurs is named the temperature of apparent (or last) equilibrium (T_{ae}). In a scenario of low-to-negligible interconversion rate, all the H_2O_m that enter the melt/glass structure will remain as H_2O_m. In this extreme case, we have the scenario of meteoric hydration. As a consequence, this will give to $OH:H_2O_m$ ratios that differ (they will be smaller) from those expected under equilibrium conditions (Eq. 2.2).

The data was examined for evidence of disequilibrium speciation. The hydrous speciation data from the different deposit, as determined by FTIR, was compared with the equilibrium speciation model developed by Nowak and Behrens (2001):

$$K_{eq} = 27.98 \exp(\frac{-4210}{T+273.15}) \quad (2.4)$$

For the calculations, the procedure implemented by Mitchell et al. (2018) was followed. In their work, the authors used the systems of equations provided by Zhang and Ni (2010):

$$[H_2O_t] = \frac{\frac{C_W}{18.015}}{\frac{C_W}{18.015}+\frac{(100-C_W)}{W}} \quad (2.5)$$

$$[H_2O_m] = \frac{C_{H_2Om}}{C_W}[H_2O_t] \quad (2.6)$$

$$[OH] = 2([H_2O_t] - [H_2O_m]) \quad (2.7)$$

$$[O] = 1 - [H_2O_m] - [OH] \quad (2.8)$$

where square brackets denote molar fraction, C_w is H_2O_t in wt.% and W the weight of the dry melt per mole of oxygen. Based on the XRF data presented in Table 3.2, W assumed a value of 32.5 g mol^{-1}. Rearranging the equilibrium equation (Eq. 2.2) in terms of [H_2O_t] (Eq. 2.5), the concentration of H_2O_m in wt.% (C_{H2Om}) can be calculated for a given H_2O_t (wt.%) and temperature:

$$C_{H_2O_m} = \frac{C_w(K_{eq}(2[H_2O_t]-1)+\sqrt{K_{eq}}\sqrt{K_{eq}(1-2[H_2O_t])^2-16([H_2O_t]-1)[H_2O_t]-8[H_2O_t]})}{2(K_{eq}-4)[H_2O_t]} \quad (2.9)$$

As mentioned in the introduction of this chapter, K_{eq} depends on temperature (see also Eq. 2.4). In order to cover the complete spectrum of possible K_{eq} values and realistic scenarios, equilibrium speciation was estimated for a range of temperatures. The upper limit selected was the maximum eruptive temperature estimated by Castro and Dingwell (825°C) while the lower limit considered the lowest experimental glass transition temperature (T_g found for H_2O rich rhyolite with a cooling rate <1 K min^{-1} (Giordano et al., 2005).

Figure 2.8 provides the results obtained from this comparison. Most of the data from the different deposits show OH^-:H_2O_m ratios that correspond to equilibrium speciation between 700–500°C.

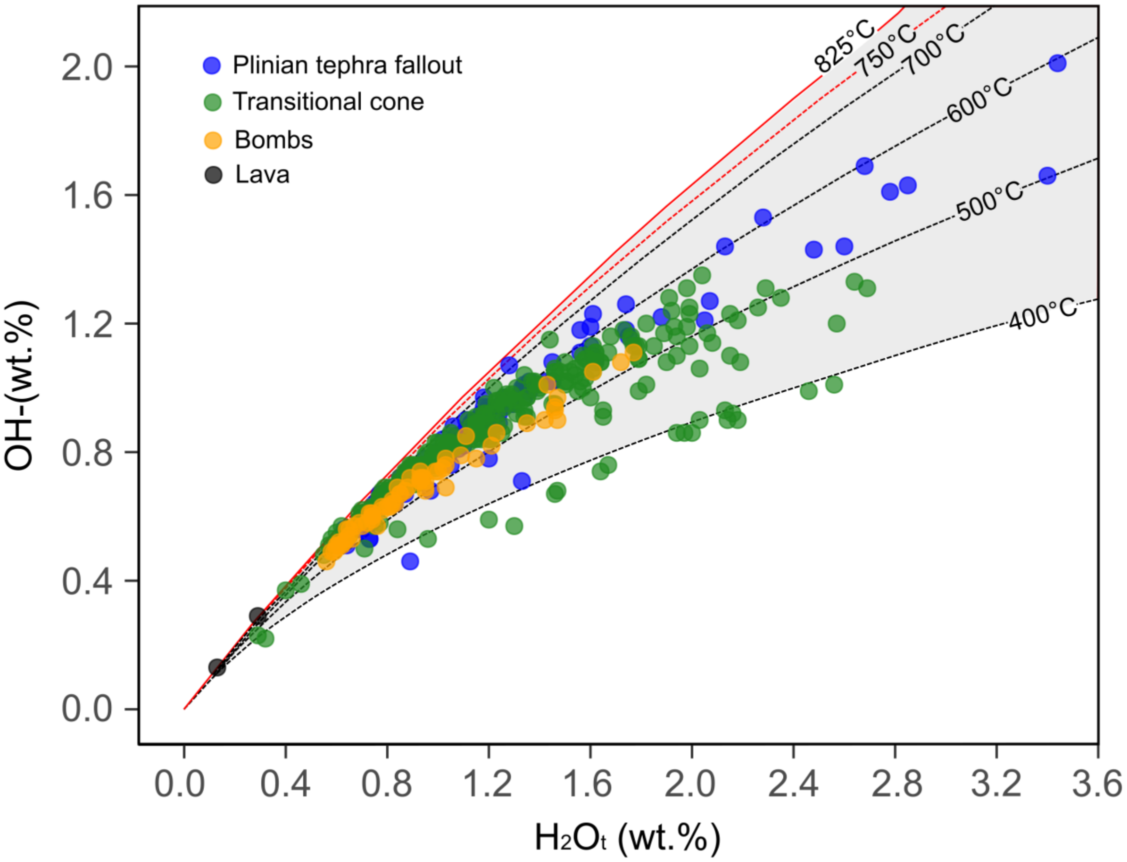

Fig. 2.8 Comparison of H_2O speciation data from the different deposits of Chaitén with the equilibrium speciation model of Nowak and Behrens (2001). The grey area represents equilibrium speciation for a range of temperatures between 400 and 825°C. Red lines are the equilibrium speciation conditions for Chaitén eruptive temperatures estimated by Castro and Dingwell (2009).

The sharpest trend is defined by the bombs, which exhibit equilibrium speciation consistently coincident with T_g = 500°C over the complete range of $H_2O_{t,}$.The lower apparent equilibrium temperatures of these samples in comparison with the other two series are is in agreement with the lower cooling rates estimated for these pyroclasts by Castro et al. (2012a). Figure 2.8 also shows that towards higher H_2O_t values, samples from the Plinian fallout and transitional cone deposits tend to present hydrous species ratios corresponding to lower T_g. This feature is not surprising, since the presence of higher H_2O_t content in a melt, will decrease its T_g (Giordano et al., 2008). Another distinctive feature of Fig. 2.8 is the higher degree of dispersion observed for the data with H_2O_t >1.6 wt.%. This could be explained by differences in cooling rates within a particular deposit. As shown in the supplementary Fig. S.1 of Castro et al. (2012b), cooling rates estimated for each deposit comprise a wide range of values. The authors attributed this to different transport history, grain size, or residence time in the conduit of the samples. However, there is a group of samples that could not be explained by cooling rates differences. Some 17 samples from the transitional cone lie entirely outside the equilibrium speciation field, showing equilibrium speciation lower than T_g = 400°C. This strongly suggests the addition of H_2O_m that was not re-equilibrated.

One possible explanation for the anomalous H_2O_m values observed in this group of samples from the transitional cone is the incorporation of secondary H_2O after deposition. However, considering that all the samples were collected from a single stratigraphic section (Fig. 2.2) that was deposited in a short period of time (<20 days), it seems highly unlikely that only a few proportion of the glasses were hydrated. An alternative explanation might be the occurrence of re-incorporation of H_2O_m by bubble resorption. McIntosh et al. (2014) proposed that bubble resorption may occur during the quench from melt to glass as H_2O solubility increases with decreasing temperature. Furthermore, the authors mentioned that this might be an extended process that affects all the melts with bubbles that undergo quenching. As for the first option, this mechanism of H_2O enrichment might not be appropriate for explaining the pattern observed in Fig. 2.8. The gap observed for data between 500° and 400°C might indicate that the mechanism, from which H_2O was incorporated, operated only in a fraction of the samples. In support to this idea, it is worth noting that 10 out of the 17 samples belong to layer B1. Watkins et al. (2012) proposed an alternative explanation for bubble resorption than includes a pressure increase in the volcanic conduit prior to eruption. Such a mechanism could satisfactorily explain the occurrence of anomalous H_2O_m for a restrict group of layers. Nevertheless, future works should investigate evidence of water resorption as H_2O diffusion profiles as well as the correlation between H_2O species and textural characteristics of the deposits.

2.4.1.2 2008 vs. 2016 ash fallout deposits

The 2008 Chaitén eruption provided the unique opportunity of collecting fresh obsidian glass shortly after its deposition. Likewise, subsequent sampling of same deposits allows for a longitudinal study -research method in which data is gathered for the same subjects repeatedly over a period of time- of the influence of the environmental conditions on the H_2O retained in the glass. Figure 2.9 compares H_2O measurements performed in glasses collected from the same spot (and same tephra fallout deposit) in 2008 and 2016. As revealed by Fig. 2.9A, H_2O distributions are almost identical, with 2016 samples showing values slightly higher. Even though at a first glance this could be attributed to some H_2O gain due to rehydration, H_2O species concentrations show no evidences of incorporation of secondary H_2O (Fig. 2.9B). As pointed out previously, during rehydration H_2O is expected to be adsorbed and diffused into the glass structure as H_2O_m. However, when H_2O_m - OH^- trends defined for both datasets are compared, they overlap, with no evidence of higher H_2O_m in the 2016 glasses at fixed OH- value. Thus, the difference in bulk H_2O observed in Fig. 2.9A might be related to minor differences in the stratigraphic position of the analysed samples (see Section 2.4.2). In conclusion, these results suggest that no measurable amount of secondary H_2O was incorporated in the rhyolite obsidians in the time elapsed between both sampling campaigns.

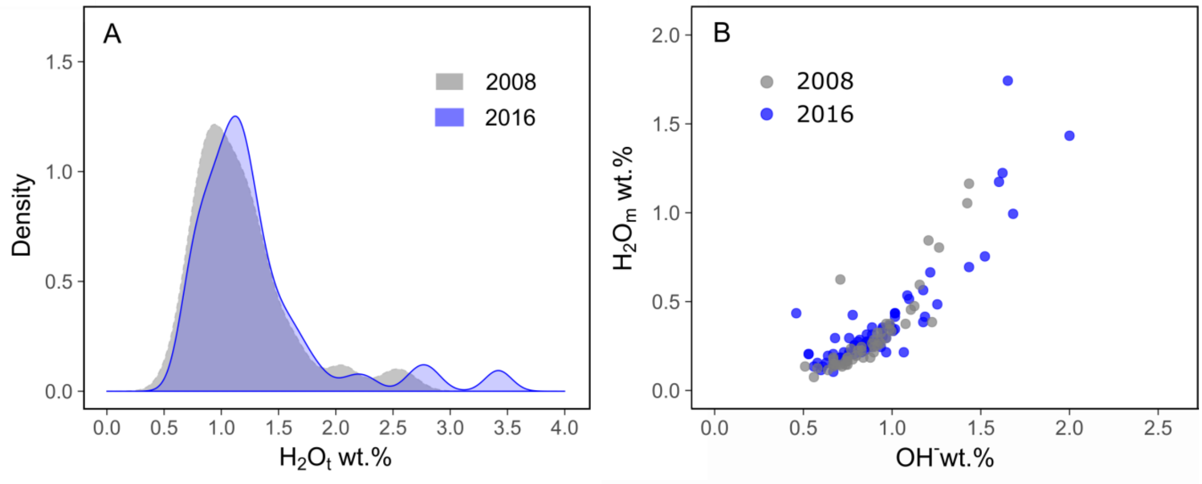

Fig. 2.9 Comparison of H_2O content in glasses from the same Plinian fallout deposit sampled in 2008 (grey) and 2016 (blue). In (A), the H_2O_t content distributions of both set of samples are compared. Graph B shows the concentration of H_2O and OH^- groups retained in these glasses. Glasses with H_2Ot <0.5 wt.% were excluded from the plots. For details about sampling location reader is referred to section 2.2.1.

2.4.1.3 DSC-TGA measurements

The amount of H_2O incorporated to the non-vesicular glasses in the time frame between the eruption and sample collection appears to be insignifcant. However, high porostiy of pumices, calculated in 43 to 80% by Alfano et al., (2012), might have allowed the absorption of secondary water by the glass surface. Unfortunately, textural characteristics of pumices impose a challenge for the use of point-based measurement techniques (e.g., FTIR). For that reason, bulk sample methods, like TGA, are usually preferred instead. During TGA, the loss of adsorbed H_2O occurs at lower temperatures that the loss of magmatic H_2O.

Eichelberger and Westrich (1981) reported two different temperatures of maximum volatile release rate when performing TGA, 300° and 600°C, for pumices and obsidians, respectively. More recently, Giachetti et al. (2015) identified that most of the secondary H_2O is released at temperatures <480°C, while the release of magmatic H_2O took place at T >600°C. Furthermore, the authors proposed that the maximum mass rate associated to primary H_2O occurs approximately at the estimated sample T_g. However, they also highlighted the influence of the heating rate on the released temperature.

As reported in Table 2.2, total H_2O released by pumices from the transitional phase during TGA measurements range between 1.67 and 0.55 wt.%. In Fig. 2.10A and B, mass evolution as a function of temperature is shown for the 11 analysed samples. In addition to TGA, simultaneous DSC measurements allowed for the estimation of T_g, which for these pumices assume an average value of 560°C. Fig 2.10C shows the calculated amount of H_2O released before and after crossing T_g. Following Giachetti et al. (2015) and assuming that all the weight loss after T_g is mainly due to primary H_2O exsolution, it is possible to obtain a first approximation of the amount of primary and secondary H_2O contained by the samples. Excluding sample D4_p1, which shows mass loss only at T >T_g, all the other samples released between 30 and 55% of its H_2O before T_g. Subtracting these percentages to the total H_2O released suggests that pumices preserve between 0.6 and 1 wt.% of magmatic H_2O. Interestingly, values of estimated primary H_2O are in the range of values reported by Castro et al. (2014) (~0.7 wt.% for the explosive phase). However, these should be considered as maximum magmatic H_2O concentration values, since if the applied heating rate was too fast, some of the secondary H_2O might have been released after T_g (e.g., Sodeyama et al., 1999). Further measurements at lower heating rates are needed to evaluate the influence of this parameter on the weight loss curves.

Despite the uncertainties, TGA measurements demonstrated that, unlike the obsidians, pumices show evidences of post-eruptive hydration. The different degrees of hydration (different slopes in Fig. 2.10A–B) might be in part attributed to differences in samples vesicularity.

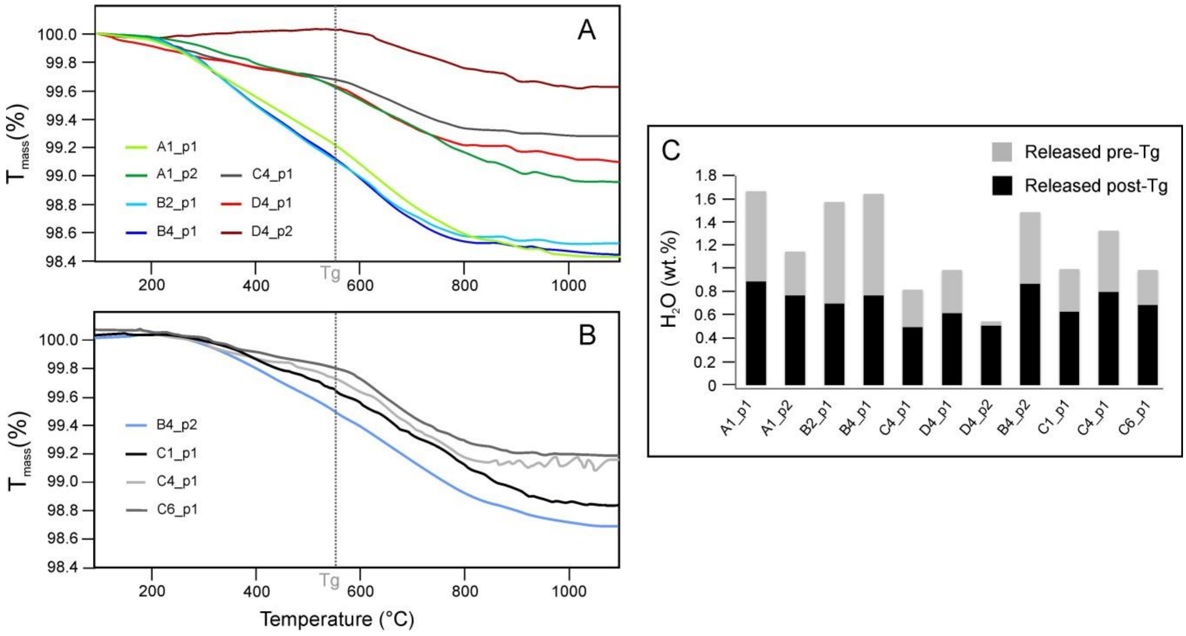

Fig. 2.10 Mass loss as a function of temperature for the pumices of the transitional phase as recorded during the DSC-TGA experiments. Measurements were divided between plot A and B to simplify the figure. Tg as estimated by DSC analysis is represented which the vertical grey dot line. In C, a detalied of the H_2O_t assumed to be realeased during heating before and after crossing the glass transition temperature (T_g).

2.4.2 H_2O content evolution during 2008 Chaitén eruption

The results of this study show that H_2O content in the melt varied during the course of the Chaitén eruption. This confirms earlier evidence found in many deposits of Holocene rhyolite eruptions. Figure 2.11 and 2.12 show the H_2O content evolution of 2008 Chaitén eruption as recorded in the transitional cone and the Plinian tephra fallout deposits, respectively. Together with the raw data (grey dots), both figures display the predicted mean estimates from a model ran in R (R Core Team, 2013). This analysis was carried out using the statistical packages ‘lme4’ (Bates et al., 2014) and ‘arm’ (Gelman and Yu-Sung, 2015) in a Bayesian framework with non-informative prior probability distribution of the estimates. A Gaussian error distribution was assumed, which was confirmed for all response variables after visual inspection of model residuals. Subsequently, the ‘sim’ function was used to simulate values from the posterior distributions of model parameters. The 95% credible interval around the mean were extract (Gelman and Hill, 2007), representing the uncertainty around the estimates. From the figures, a statistically meaningful difference between groups can be assumed if the credible interval of one group (i.e. stratigraphic layer) does not overlap with the mean estimate of the other.

A first look to the data displayed in Fig. 2.11A reveals a gradual decrease in H_2O_t with the progression of eruption. This can be identified both, from the raw data and the mean estimated by the model. A difference of ~1 wt.% in the mean H_2O content is observed between the basal (1.73 wt.%) and top (0.72 wt.%) layers. At the same time, three sub-trends can be identified along the sequence (A1 to B3 and B4 to C3 and C4 to D5). These fluctuations in H_2O might be indicative of heterogeneities in the volatile content of the magma. Alternatively, they could be related to different degassing mechanism—with associated different efficiencies—operating during the evolution of the eruption. An additional interesting feature of Fig. 2.11A is the occurrence of "H_2O content windows" within stratigraphic horizons. These windows, defined by the H_2O content distribution of each layer, also shift with stratigraphic position, showing narrower ranges with eruption progress. While at the base of the sequence ΔH_2O is 1.48 wt.%, at the top the difference between maximum and minimum H_2O preserved in the glasses is only 0.57 wt.%. It is also important to remark, that the observed H_2O windows demarcate clear H_2O gaps with respect to effusive obsidians (see Fig. 2.3C).

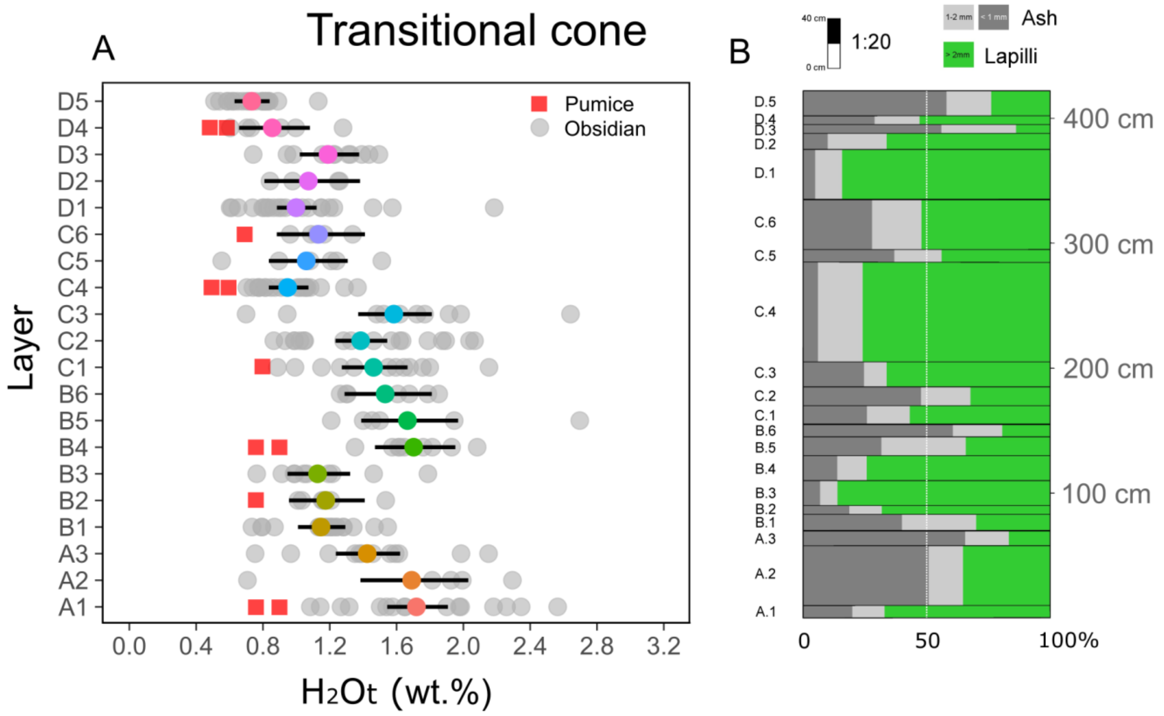

Fig 2.11.A H_2O_t variations in the transitional cone deposits as a function of stratigraphic position. Grey dots represent average glass H_2O content for individual chips. Colour dots represent the median value while black horizontal bars are their 95% credible intervals. See main text for the description of the statistical approach. Glasses with H_2O_t <0.5 wt.% were excluded from the analysis and in order to simplify the chart they are not shown. The vertical axis is not scaled. For stratigraphic heights and thicknesses of the different layers, see plot B. A photo of this stratigraphic section is shown in Fig. 2.3D. Red squares represent pumice H_2O_t as determined by DSC-TGA.

Even though data sets are smaller, similar features are recognized in the stratigraphic sequences related to the Plinian fallout deposits (Fig. 2.12). Unfortunately, in these cases the sampling strategy was not based on a geological criterion, making the detailed comparison with the results from Fig. 2.11 not possible. Finally, in Fig. 2.11A the results of the DSC-TGA measurements on pumices are shown. Interestingly, all the samples show H_2O contents that coincide with the lower limit of the H_2O window defined for that layer. Although more measurements are needed to statistically analyse this occurrence, preliminary results might be suggesting a relationship between the residual H_2O contents preserved in vesicular and non-vesicular glasses.

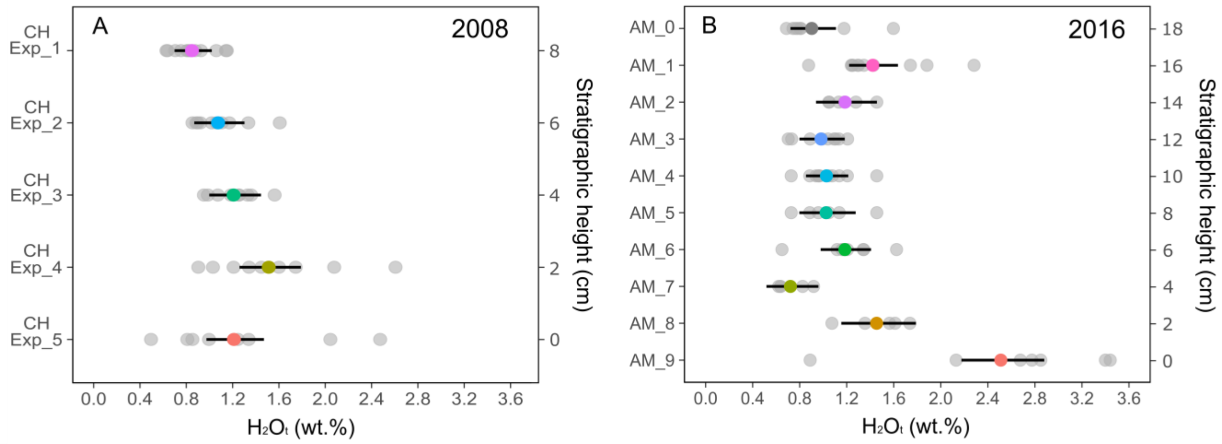

Fig 2.12 H_2O_t variations in the Plinian tephra fallout deposit sampled in 2008 (A) and 2016 (B) as a function of stratigraphic position. Grey dots represent average glass H_2O for individual chips. Colour dots represent the median value while black horizontal bars are the 95% credible interval. The same statistical approach than for the analysis of the Transitional cone glasses was followed. Although plots are scaled, the spatial correlation between the two set of samples is not possible. A photo of the deposit sampled in 2016 is shown in Fig. 2.3A. As for the case of Fig. 2.11, glasses with H_2O_t <0.5 wt.% were excluded from the analysis and are not show.

A strikingly similar pattern of H_2O content distribution and evolution throughout a sequence to the one presented in Fig. 2.11, was observed by Newmann et al. (1988) in the deposits of 1340 A.D Mono Craters eruption (see their Fig. 3). The H_2O data presented by Rust and Cashman (2007) from 1300 B.P. Newberry volcano eruption also presents a range of H_2O values for each layer. However, the upper and lower boundaries as well as a general H_2O depletion trend are not as evident as in the previously described sequences. In the light of the results of this study, it might be convenient to reanalyse the results of Rust and Cashman (2007) excluding the data with H_2O <0.5 wt.%. Both, Newmann et al. (1988) and Rust and Cashman (2007), offer different explanations for the observed range of H_2O within single pyroclastic layers, which are strongly related to the origin of the obsidians itself Newman et al. (1988) suggested that obsidians represent fragments of the glassy margins of the volcanic conduit. In their model, the authors explained the range of H_2O contents within a stratigraphich layer as the results of glassy material sampled (by erosion) at different depths (i.e., different pressures) by the “fragmentation front”. In this way, the maximum H_2O content of each layer records the maximum depth reached by the fragmentation surface, while the H_2O depletion trend in the sequence indicates the shallowing of the fragmentation level through time. Contrary to this interpretetation, Rust and Cashman (2007) argued that obsidian pyroclasts provide limited constraints of the fragmentation level. Furthermore, the authors proposed multiple origins for the obsidians of Newberry eruption. More recently, Gardner et al. (2017) proposed that obisdians originate from sintering of small glass/melt fragments in the conduit. As can be seen, there is no agreement among scientist about the origin of obsidians. Finding an explanation to the formation of obsdians necessarily need to include an explanation to the braod range of H_2O concentrations preserved in the glasses and the different degassing mechanisms that take place during an eruption. For that reason, in order to provide a robust interpretation of the mechanisms underlying obsidian formation during 2008 Chaitén eruption and also of the H_2O depletion patterns observed in the different deposits, further investigation on the pyroclasts textures and isotopic compositions is required. Elucidating the origin of Chaitén osidians includes the challenge of explaining how obsidians can preserve up to 3.4 wt.% H_2O, considering the fact that pre-eruptive H_2O at storage levels was estimated in 4 wt.% by Castro and Dingwell (2009).

2.5 Conclusions

A total of 493 obsidian samples from different deposits representative of each of the three phases of 2008–2010 Chaitén eruption were analyzed for their H_2O contents by FTIR. Results show bulk H_2O contents between 0.5 and 3.44 wt.%, with specific ranges for each deposit. Obsidian bombs show the narrowest range (0.5–1.77 wt.%), while H_2O retained in the glasses from the Plinian tephra fallout and transitional cone deposits reach values up to 2.7 and 3.44 wt.%, respectively. The lowest H_2O concentrations were measured in the lava dome obsidians (<0.3 wt.%). Altogether, the distributions of H_2O in Chaitén eruptives are in agreement with the ones observed in glasses associated with explosive and effusive activity from previous rhyolite eruptions in other regions. Furthermore, this study has identified a sharp boundary at ~0.5 wt.% that separates H_2O contents preserved in explosive and effusive products.

Following a multi-methodological approach, the origin of the H_2O preserved in the glasses was constrained. The analysis of hydrous species revealed that most of the H_2O retained in the glasses show no evidence of significant incorporation of secondary (meteoric) water. The extensive influence of bubble resorption seems also highly unlikely. However, disequilibrium speciation observed in a group of 17 samples highlight the need for further investigations. The comparison between glasses from the same tephra fallout deposit sampled twice, in 2008 and 2016, supports the magmatic origin for the H_2O preserved in the obsidians, including the samples from the Plinian Fallout deposits with H_2O up to 3.4 wt.%. This is somehow surprising, since the pre-eruptive H_2O at storage levels was estimated in 4 wt.% by Castro and Dingwell (2009). On the other hand, DSC-TGA measurements on 11 pumices showed that this porous pyroclasts were probably hydrated during the time elapsed between their eruption and collection. TGA results offer a maximum H_2O content estimation for these samples, which range from 0.5 to 0.9 wt.%.

Finally, the evolution of H_2O content was analyzed in three stratigraphic sections (two from the Plinian tephra fallout and one from the transitional cone). Similar features were identified in all the cases, with H_2O decreasing from base to top in each sequence. Internally, H_2O sub-trends were recognized in each sequence. However, the most striking finding was the occurrence of “H_2O content windows” within stratigraphic horizons, defined by upper and lower H_2O content values. These water content windows shift with stratigraphic position and demarcate clear H_2O gaps with respect to effusive obsidians. Overall a well-defined trend of H_2O depletion from the explosive to the effusive deposits is observed for the 2008–2010 Chaitén eruptive cycle.

Chapter 3

High temperature-0.1 MPa experiments with rhyolite glasses

3.1 Introduction

Heating natural rhyolitic obsidian glasses at atmospheric pressure above their glass transition temperatures results in the growth of bubbles (Murase and McBirney, 1973), which indicates that H_2O is retained in the volcanic glass since the time of quench. This observation has enabled scientists to experimentally investigate H_2O exsolution and bubble growth kinetics, from nucleation to coalescence and collapse. Since the pioneering study of Murase and McBirney (1973), a considerable amount of effort was invested to understand the physical and chemical processes related to gas exsolution and vesiculation in rhyolitic systems. Bagdassarov and Dingwell (1993) performed 0.1 MPa, high-temperature experiments (1200–1400°C) on calc-alkaline rhyolite with H_2O content ranging between 0.14 and 0.2 wt.% to investigate the kinetics of foaming as a result of the internal stress of gas expansion. After that, Bagdassarov et al. (1996) investigated the vesiculation of a peralkaline rhyolite melt with 0.14 wt.% H_2O in the temperature range of (650–950°C) through optical and dilatometric methods, demonstrating that a “time lag” exists between the moment of supersaturation and the beginning of the vesiculation process. These workers, furthermore, parameterized the competing regimes of viscous- and diffusion-controlled bubble growth through the use of Peclet (Pe) number quantifications. With a similar approach, Stevenson et al. (1997) studied the effects of temperature and viscosity on the kinetics of bubble growth and vesiculation at 520–624°C in high water content calc-alkaline obsidians (~1.8 wt.%). Navon et al. (1998) explored the kinetics of bubble growth at atmospheric pressure and 375–460°C in hydrated rhyolitic melts with 5 wt.% H_2O, common content for pre-eruptive storage conditions. Most recently, Ryan et al. (2015) investigated the expansion and degassing behavior of “dry” rhyolitic glasses (~0.11 wt.%) at temperatures between 900 and 1100°C. Based on these experiments, a 1-atm, H_2O solubility model was developed permitting the prediction of water concentration in hydrous glass from porosity data. Von Aulock et al. (2017) heated cylindrical cores of obsidian with 0.12–0.16 wt.% H_2O to 950°C to understand degassing and outgassing procceses in closed and open systems.

These previous studies provide a good basis for understanding vesiculation in effusive products, since these usually retain magmatic water contents up to about 0.3 wt.% (e.g., Eichelberger et al., 1986; Castro et al., 2005). The applicability of these studies to understanding H_2O-temperature conditions found in explosive eruption deposits -as the ones described for 2008–2010 Chaitén eruption in Chapter 2- is as of yet unexplored and arguably limited, since the pyroclastic glasses produced in explosive rhyolite eruptions are so much more water-rich and explosive fragmentation requires that the samples do not remain coherent during the course of bubble growth. Accordingly, a range of parameter space from H_2O contents ranging from 0.20 to 1.8 wt.% was identified (Fig. 3.1). Here the existing gap is spanned by performing experiments at eruption-relevant temperatures and applying a new methodological approach that allowed observing and monitoring the complete duration of the experiments. Taking obsidian glass drilled from bombs and lava dome samples of 2008–2010 Chaitén eruption as starting material, and through a series of high-temperature, 0.1 MPa vesiculation experiments, new insights into the response of silicic melts to degassing are demonstrated.

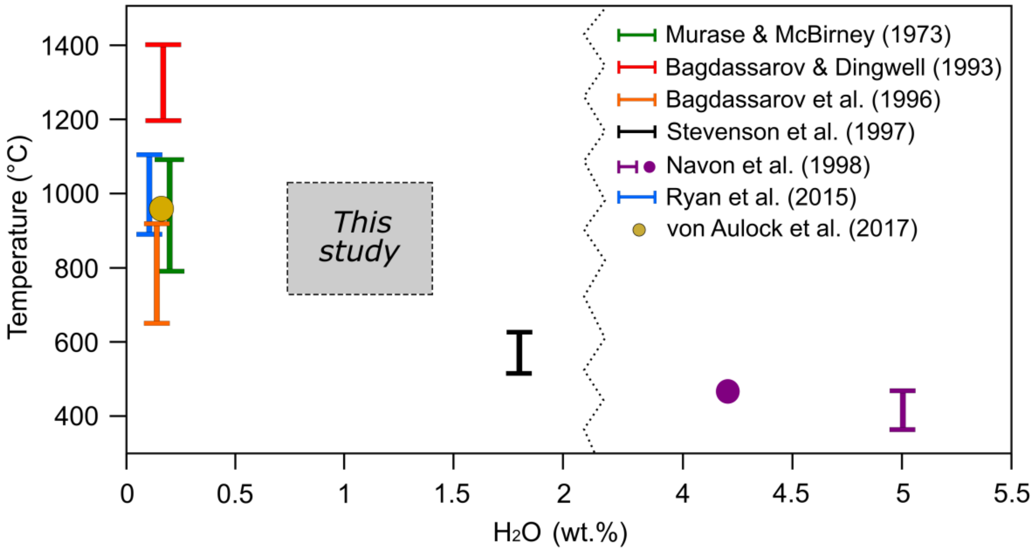

Fig. 3.1. Previous high-T, 0.1 MPa experiments performed on obsidian glass and the experimental gap identified that this work spanned.

3.2 Methodology

3.2.1 Samples

Samples for the experiments comprise decimeter-sized obsidian bombs collected during field campaigns in 2010 and 2015 from an area of highly cratered land located to the north of the Chaitén dome and within the caldera. Due to the impossibility of detecting H_2O contents in the field, sampling was made based on the appearance of fresh glass and the absence of alteration. Materials from the 2008 lava dome complex were also collected, specifically on the earliest erupted lava lobe (May, 2008), which is exposed on the northern end of Chaitén caldera (see Fig. 2.3 in the previous chapter).

3.2.2 Experimental and Analytical Methods

3.2.2.1. Sample characterization and preparation

The obsidian samples were first analyzed by Fourier transform infrared spectroscopy (FTIR) to determinate their H_2O contents. Measurements were carried out at the facilities of the Institute für Geowissenschaften at the Johannes Gutenberg University (JGU) and a detailed description of this methodological procedure is provided in Chapter 2 (see section 2.2.2.1). Magmatic CO_2 was below detection limits in all samples. The results of FTIR measurements guided the selection of 4 samples for experimental investigation (Table 3.1). Three of these samples are obsidian bombs (CH_2015_02, CH_2015_05 and CH_2011_5) containing between 0.75 and 1.4 wt.% H_2O and the other sample is a relatively dry lava dome obsidian (CH_2015_01; 0.13 wt.% H_2O). It is assumed that all the H_2O measured in the samples is of magmatic origin, an interpretation that is supported by the results shown in Chapter 2.

Table 3.1. Experimental conditions and H_2O contents

Sample	**OH^-** (4512 cm-1)	**H_2O_m** (5200 cm-1)	**H_2O_t**	**T (°C) range**	**N° experiments**
CH_2015_01	0.12 ± 0.02	- [a]	**0.13** ± 0.01[b]	766-1032	12
CH_2015_02	0.60 ± 0.06	0.15 ± 0.06	**0.75** ± 0.12	728-1001	22
CH_2015_05	0.66 ± 0.10	0.31 ± 0.07	**0.97** ± 0.17	746-1024	42
CH_2011_05	0.88 ± 0.09	0.52 ± 0.03	**1.40** ± 0.13	741-901	18

Note: complete list of experiment conditions and results in Supplementary Table 1.

[a] Absorbance peak not detected.

[b] H_2O content calculated from 3750 cm^{-1} peak.

Table 3.2. Bulk composition of Chaitén samples obtained by X-Ray Fluorescence Analysis.

Sample	CH_2015_01 **(0.13 wt.%H_2O)**	CH_2015_02 **(0.75 wt.%H_2O)**	CH_2015_05 **(0.97 wt.%H_2O)**	CH_2011_5 **(1.40 wt.%H_2O)***	**Average composition***
SiO_2	74.43	74.23	73.98	75.6	**74.41** (±0.55)
Al_2O_3	13.94	13.89	13.86	13.9	**13.89** (±0.03)
Fe_2O_3(t)	1.55	1.55	1.53	1.5	**1.54** (±0.02)
MnO	0.06	0.06	0.06	0.05	**0.06** (±0.004)
MgO	0.16	0.16	0.15	0.26	**0.18** (±0.04)
CaO	1.47	1.47	1.46	1.46	**1.46** (±0.01)
Na_2O	4.16	4.16	4.13	4.04	**4.12** (±0.04)
K_2O	3.02	3	3	2.93	**2.99** (±0.03)
TiO_2	0.15	0.15	0.15	0.14	**0.15** (±0.003)
P_2O_5	0.05	0.05	0.05	0.06	**0.05** (±0.004)
Cr_2O_3	0.001	0.001	n.d	n.d	**0.001** (±0.002)
SO_3	0.005	0.006	0.008	n.d	**0.01** (±0.001)
Total	99.24	99.62	99.53	99.9	**99.52** (±0.21)

**Average value reported by Castro and Dingwell (2009) that represent the composition of CH_2011_05 (1. 40 wt. %)*

Under the optical microscope, all glassy samples are texturally isotropic, with microlite and bubble contents lower than 5%. The only exceptions are some micrometric-width flow bands having a locally higher concentration of microlites. Bulk X-ray fluorescence analyses (XRF) performed in all the samples indicate homogeneous major element composition, consistent with values published by Castro and Dingwell (2009) (Table 3.2). For this reason, an average value of bulk composition will be considered for further calculations.

3.2.2.2 Experimental procedure

Heating experiments were performed on cylindrical obsidian cores drilled from the bomb and/or lava sample interiors with a diamond-coring device. Cores had an initial diameter of 9 mm and an average height of 3.5 mm. Size was measured with a precision digital caliper (σ ± 0.01 mm) and the samples were weighed with a high-precision balance (σ ± 0.01 mg). The ends of the cores were ground flat and polished to avoid irregularities. Before running the experiments, all the glassy cores were carefully inspected under a microscope for preexisting fractures, and the ones showing damage, significant bubble contents (>1 vol.%) or tuffisite veins were discarded.

A total of 94 experiments at 0.1 MPa and variable temperature (728–1032°C) as well as across a range of H_2O contents (0.13–1.4 wt.%; Table 3.1 and Fig. 3.2) were conducted. Owing to the wide range of H_2O contents, the experiments comprise the first analysis of the behavior of the full spectrum of degassing levels observed in rhyolitic glasses produced during 2008 Chaitén eruption, but also in many other similar systems (e.g., Inyo Domes; e.g., Castro and Mercer, 2004).

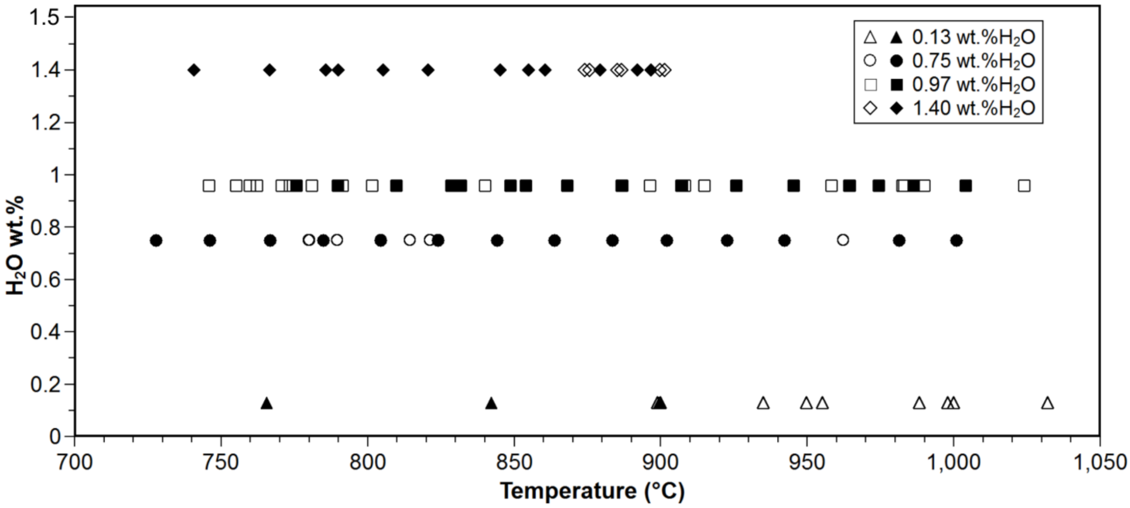

Fig. 3.2. Experimental series ran at different temperature and H_2O conditions. Each symbol represents a single experiment. Filled symbols represent experiments with a standard dwell time of 27 minutes. Unfilled symbols represent experiments with dwell time longer (up to 3 days) or shorter (1 minute) than standard dwell time. (More details about experimental conditions are shown in Appendix C).

The experimental results were grouped into three H_2O-content regimes, each of which showed clearly distinct behavior upon heating: (1) the low H_2O domain, with 0.13 wt.%

and represented by the lava dome sample (CH_2015_01), (2) the intermediate domain, composed of CH_2015_02 and CH_2015_05 with 0.75 and 0.97 wt.% H_2O and (3) the high-H_2O content domain, represented by CH_2011_05 with 1.4 wt.%.

The cores, initially at room temperature (~25°C), were placed on a stage inside a Nabertherm® LT24/12 box furnace that was pre-heated to the target temperature (see Appendix C for the complete list of experiment conditions and results). Each experiment was run for a total of 27 minutes, which provided a consistent time frame to analyze the potentially different behaviors. The only exceptions to the 27–min experimental run-time were: 1) the experimental series CH_2015_01, which, due to the low H_2O content of these samples, required longer times in order to observe a significant response to the heating process, and 2) experiments on sample CH_2011_05 were run at significantly shorter times, because, due to its very high H_2O content, obsidians exploded within minutes of sample insertion into the furnace. A second set of complementary experiments was also performed over variable durations—long and short dwell times—in order to quantify the response times of the obsidian to heating within the first minutes and to therefore establish a lag time (t_{lag}; the time between sample insertion and the moment the first expansion or change in volume is recognized). Long dwell time experiments were used as well to determine equilibrium conditions for low H_2O-T experiments of the intermediate H_2O content domain. Some of these experiments also served as a calibration on the heating rates of obsidians for different target temperatures. Once the experimental dwell time was reached, samples were manually removed and set on insulation to cool within seconds to room temperature.

The furnace permits real-time observation of the sample through a 15 X 15 cm sapphire window (Fig. 3.3A). The evolution of the experiments was monitored by using two cameras, one (EX-F1 CASIO® camera) was used to record the experiment at High Definition (HD) and 60 fps, and the second recorded at high-speed (Edgertronic®), which permitted digital capture of important fast phenomena—e.g., pyroclast ejection during explosions— (Fig. 3.3B).

Special effort was focused on obtaining precise values of the experimental sample temperature. Given the presence of a strong thermal gradient within the oven (between the bottom and the top and front and back of the furnace), its temperature was additionally measured with a chromel-alumel K-type thermocouple (Omega® KMQXL) inserted through the back of the furnace and located a few centimeters from the sample. A systematic difference of ~10°C between the furnace temperature as read on the controller display and the K-type thermocouple was repeatedly observed. As the furnace thermometer is located at the top of the inner chamber, the temperature values reported for the experiments correspond to the ones measured with the thermocouple probe. In addition, an infrared thermometer (Optris® CS laser 2MH-SF) was used to track the temperature evolution on a laser-defined spot (~3 mm in diameter) on the front surface of the sample. As this measurement was made through the sapphire window, the infrared sensor was adjusted to account for the transmissivity of the window and variable emissivity of the sample, which arose due to vesiculation and attendant sample color change from black to grey. In general, very small differences (<5˚C) were observed between the thermocouple and IR thermometer readings. A series of experiments were performed on the same sample type (CH_2015_01, 0.13 wt.% H_2O) in order to constrain timescales for sample heating. Experiments were run twice to check reproducibility. Measurements at a temperature range spanning the experimental conditions (740–975°C) showed that samples need between 98 and 80 seconds to reach the target temperature (Fig 3.4). At higher target T, time needed for the sample to reach thermal equilibrium is shorter.

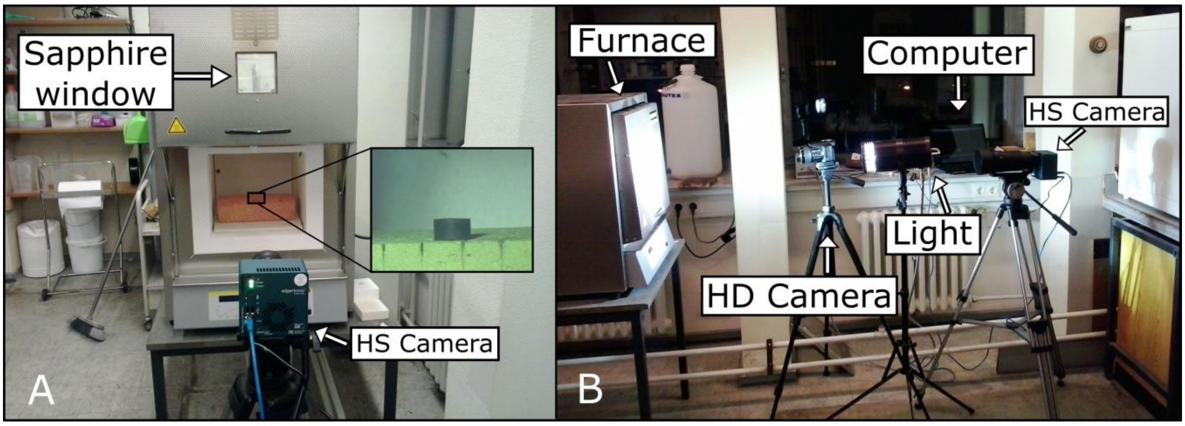

Fig. 3.3. Experimental setup A) Frontal view of the furnace. B**)** View of the complete experimental setup, including the furnace, two cameras (High Speed (HS) and High Definition (HD) cameras), and an external source of light.

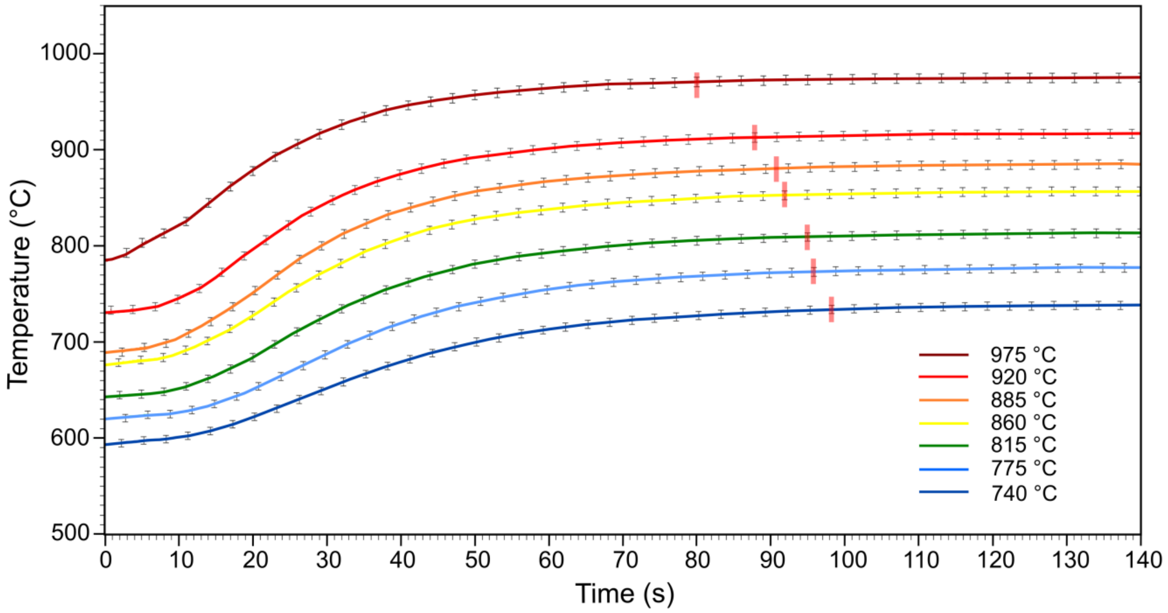

Fig. 3.4. Curves showing timescales for sample heating at different target temperatures.

All video recordings were analyzed with ImageJ software (Abramoff et al., 2004). The sample's initial cross-sectional area as observed front-on was used as a control parameter for tracking the growth evolution through time. The 2D borders of the expanding sample were digitized in successive video frames by using the pen tool in ImageJ. Owing to the change of color and size of the samples during the vesiculation and growth of obsidian (from black to light brown/whitish), that affect the definition of the area boundaries, two errors were calculated. During the onset of experiments (before expansion) the initial edge-detection error (black sample) is about 1.7%, whereas for more advanced stages of expansion (light brown to whitish) it was 1.4%.

To complement the information obtained from the 2D analysis of the videos, post-experiment volume of the samples that did not experience fragmentation was also measured with a density determiner water pycnometer (gravity cup). The equation $\phi = \Delta V/V_f$, where V_f is the final volume, yields the final porosity of the samples with σ ± 1%. The instrument was calibrated by measuring the volume of steel spheres of different size and comparing the values obtained with their theoretical volumes ($V_{sphere} = \frac{4}{3}.\pi.r^3$). Calibration showed precision of the instrument increases with volume. An overestimation of ~7% in porosity was observed for V ~0.25 cm^3 while for V ~4 cm^3 it was ~1.4%. Additionally, two foamed samples from the 1.4 wt. % H_2O content series were scanned with a Procon X-Ray computed µ-tomography system at the University of Mainz in order to document the size and 3D structure of vesicles. The scan resolution (~5–10 µm voxel edge length) prevented adequate base images to produce sharp 3D models, however, 2D sections through CT stacks were adequately sharp for bubble size distribution and number density measurements. Finally, a binocular microscope was used to characterize bubble size distributions during the initial stages of vesiculation in a subset of experiments from the 0.97 wt.% H_2O series.

3.3. Results

Three types of behavior were identified in the experiments as a result of different H_2O-temperature experimental combinations (Fig. 3.5): A) expansion + equilibrium, B) expansion + shrinking and C) expansion + fragmentation. Expansion is defined here as the measurable increase in sample volume after some dwell period due to vesiculation. Equilibrium is defined as the state reached whereby vesiculation stops and the sample volume remains constant. Shrinking, by contrast, is the tendency for the sample to decrease in volume after it has expanded. Fragmentation is the sudden explosive response of the sample resulting in innumerable particles.

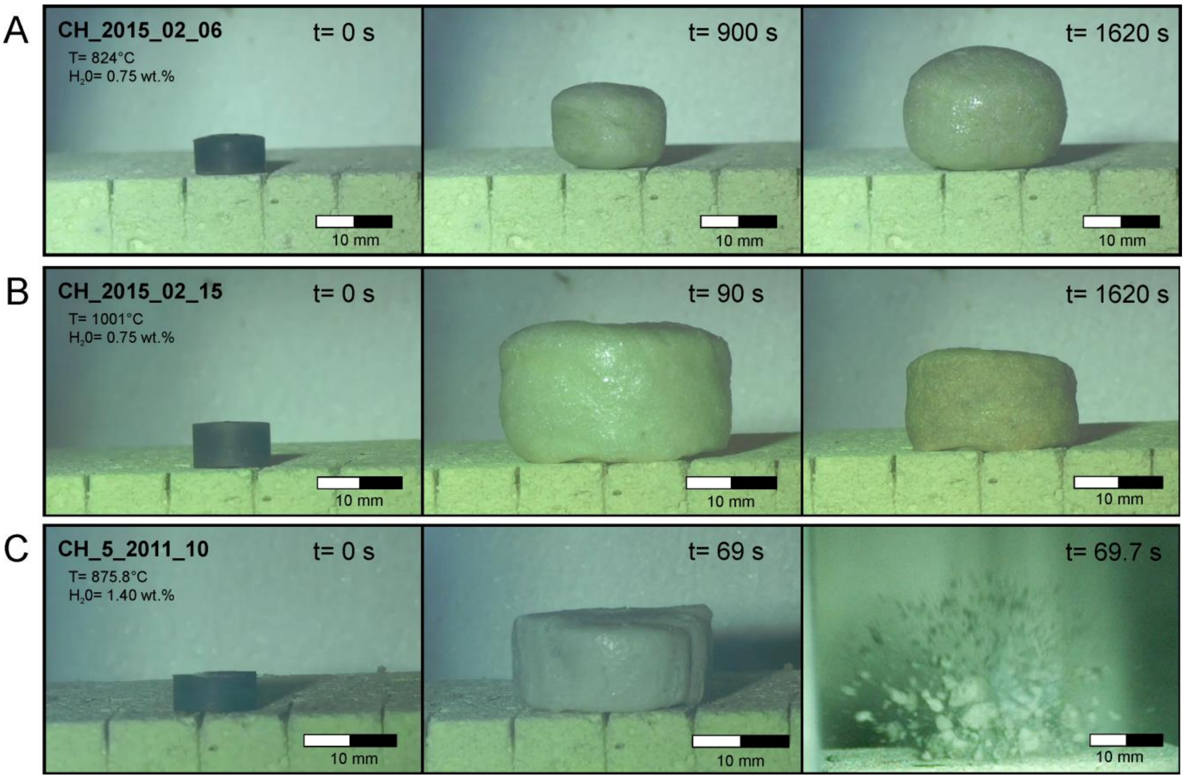

Fig. 3.5. Three different vesiculation behaviors identified through video analysis. A) Expansion + equilibrium (constant volume). B) Expansion + shrink. C) Expansion + fragmentation.

After an initial time lag (Toschev, 1973), defined as the time need for the system to heat above the calorimetric glass transition (between 709 and 547°C for Chaitén samples; Giordano et al. (2008)) all the experimental samples expanded due to the gas exsolution (vesiculation), causing the consequent volume increase. For samples showing behaviors A and B, a deceleration in the expansion rate was identified after certain time. Finally, for the case of behavior A, the growth of vesicles and expansion stopped and samples reached the "equilibrium state". In the case of behavior B, after reaching the maximum expansion, shrinkage of the samples occurred. For its part, behavior C is characterized by a continuous expansion that is disrupted when the sample explosively fragments. It is important to note that fragmentation always occurred at a stage in expansion at which samples had not reached the equilibrium state

The three classes of behaviors are reconstructed as a function of time (t) and changing sample area (A/A_0; where A and A_0 correspond to the final and initial cross-sectional areas, respectively) in Figure 3.6. Characteristic sigmoidal shapes are found for behaviors A and B, similar to bubble growth and cumulative volume curves previously documented in experiment studies by Murase and McBirney (1973), Bagdasarov et al. (1996), Stevenson et al. (1997) and Navon et al. (1998). In contrast to previous studies, however, these experiments reveal for the first time the transition from expansion to fragmentation as shown by the steep truncated paths in Fig. 3.6D and generally expressed the type C experiments.

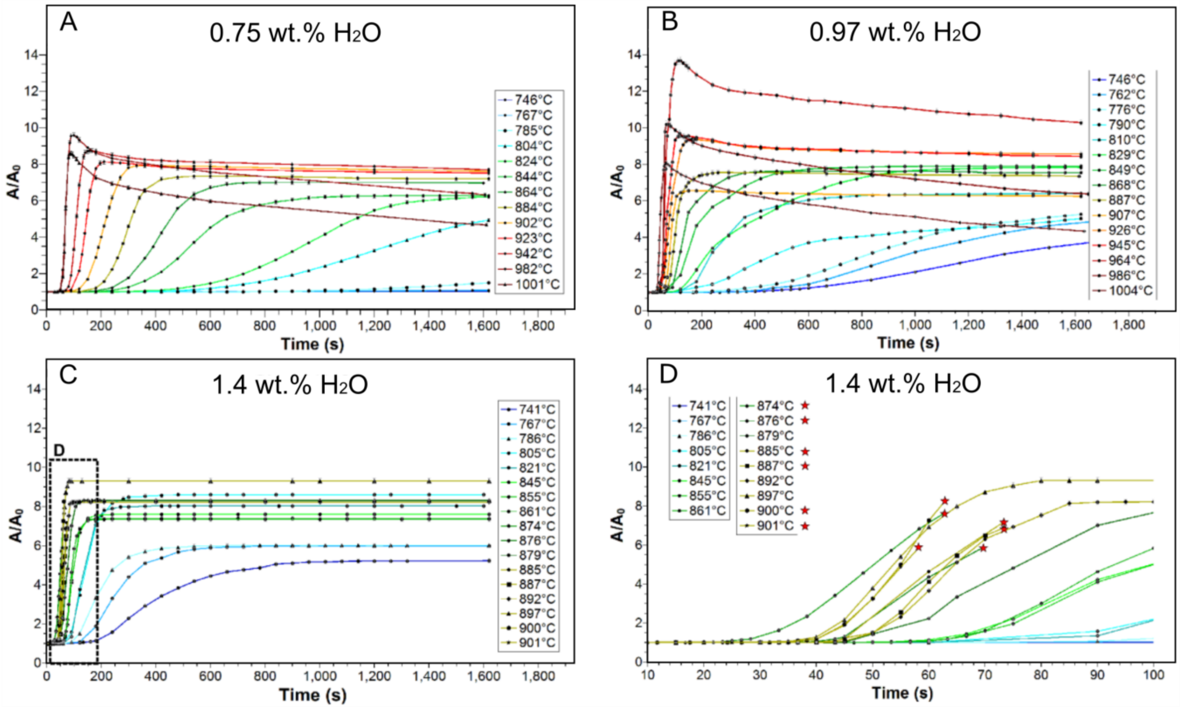

Fig. 3.6. Evolution of sample area for the intermediate and high-H_2O contents experimental series. Each dot represents a video frame in which the area was manually measured. The colors of the curves represent the different temperatures, which are color coded to allow the comparison between the different series. Frames A and B depict expansion + equilibrium, and expansion + shrinking behaviors respectively. In both cases, after an exponential growth phase, the curves show a deceleration and the development of a sigmoidal shape. After that, some samples reach their maximum size and equilibrate, represented by the curve plateaus at long times. For the highest T experiments of these two series, a decrease in the A/A_0 ratio was observed, corresponding to shrinking of the sample. Graphs C and D depict area evolution of the high-H_2O domain samples; in these expansion + equilibrium and expansion + fragmentation behaviors are represented. Graph D is a close up view of the first 100 seconds of the high-H_2O domain experiments, where the fragmentation of the cores was observed for T's >874˚C. Red stars represent the points of fragmentation.

Figure 3.7 illustrates the correlation between initial H_2O content and obsidian vesiculation behavior, specifically, whether the sample reaches the equilibration state, grows and then shrinks, or grows and then explodes. In general terms, the higher the initial H_2O content, the lower the temperature and shorter the time lag before the onset of exsolution and expansion. At higher initial H_2O contents, the temperature range over which behavior A occurs is furthermore larger. Behavior B was only identified in both intermediate H_2O content series, with shrinkage of samples occurring some 20˚C lower temperature when initial H_2O

content is 0.75 wt.%. Behavior C was observed only for the high H_2O series (1.4 wt.%), at temperatures higher than 874°C. Interestingly three out of nine experiments at T >874°C did not explode, however, this is attributed to pre-existing cracks in the samples that may have helped bleed off vapor during expansion. The high-T condition of explosive fragmentation was confirmed in an additional set of experiments, which are presented in Chapter 4. Lastly, the driest obsidians (0.13 wt.% H_2O) exhibited no change in volume during the standard dwell time (27 minutes).

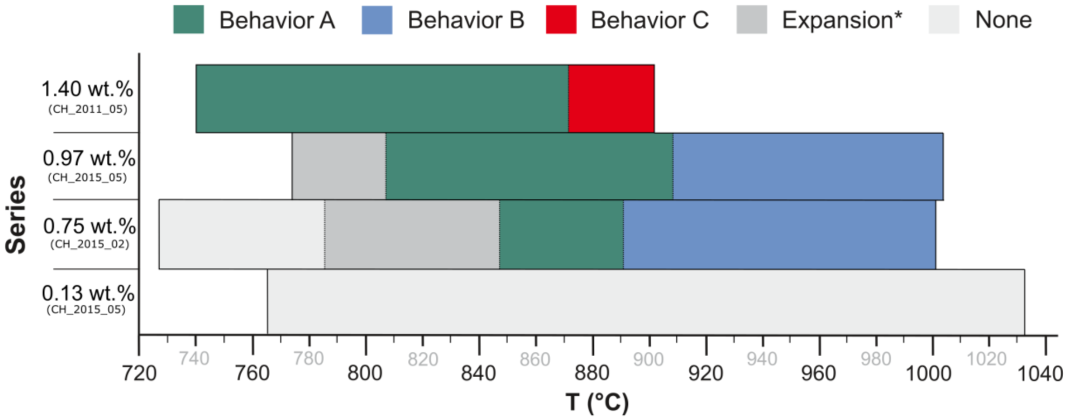

Fig. 3.7. Different behaviors observed at different temperature and H_2O experimental combinations during standard 27 minutes-long experiments: A) Expansion + equilibrium (constant volume). B) Expansion + shrink. C) Expansion + fragmentation. (*) Dark gray represents samples which did not complete the expansion process in the 27 minutes timeframe.

The temperature dependency of obsidian expansion becomes clearer when looking in detail at the individual vesiculation curves for each series Fig. 3.6 (A–D). An increase in the angle of the slope, which reflects an increase in the sample's expansion rate, occurs from low to high temperature. Temporal information on expansion is also represented in Fig. 3.8, where the natural log of the growth time (t_{gw}) is plotted as a function of reciprocal temperature. Growth time follows an exponential behavior, with values converging at high temperatures. In addition, t_{gw} differences of up to two orders of magnitude were found within each single series. As is the case with the growth rates (i.e., the A/A_0 slopes in Fig. 3.6), this broad range of t_{gw} reflects, in part, the dependency of H_2O solubility on temperature, more specifically its inverse or retrograde nature (e.g., Ryan et al., 2015).

Fig. 3.8 also highlights the importance of initial H_2O in controlling the timescale of the exsolution process. For example, at the same experimental target temperature (~875°C), samples showing behavior C needed less than 70 seconds to explosively fragment while obsidian cores from the intermediate H_2O-content series required much longer times (480–540 s) just to reach equilibrium conditions. This difference in time between series reflects the profound influence of H_2O content on the fundamental process of chemical diffusion and melt viscosity, both of which, control rates of bubble growth. The results of volume measurements also show the close connection between melt H_2O content, temperature and bubble growth rates. As observed in Figure 3.9, volumes (V_f/V_i) increase with temperature until the point in which behavior B takes place. Interestingly, samples from the high and intermediate H_2O domains (in particular 1.4 and 0.97 wt.% H_2O series), reach final volumes that are about the same ($V_f/V_i > 15$). To quantify volume expansion rates, changes in volume through time ($\Delta V/\Delta T$) were analyzed for experiments of different series at a similar temperature (~875°C). To determine ΔV, the difference between initial and maximum achieved volumes was measured and thus, the growth rates are linear-averaged values. Volume expansion rates of 0.006, 0.009 and 0.029 $cm^3\ s^{-1}$ were calculated for the 0.75, 0.97 and 1.4 wt.% series, respectively. Even though they represent averaged values, and from the A/A_0 curves we can clearly recognize changes in the rates within single experiments, these values offer us a first impression of the effect of H_2O content on bubble growth rate.

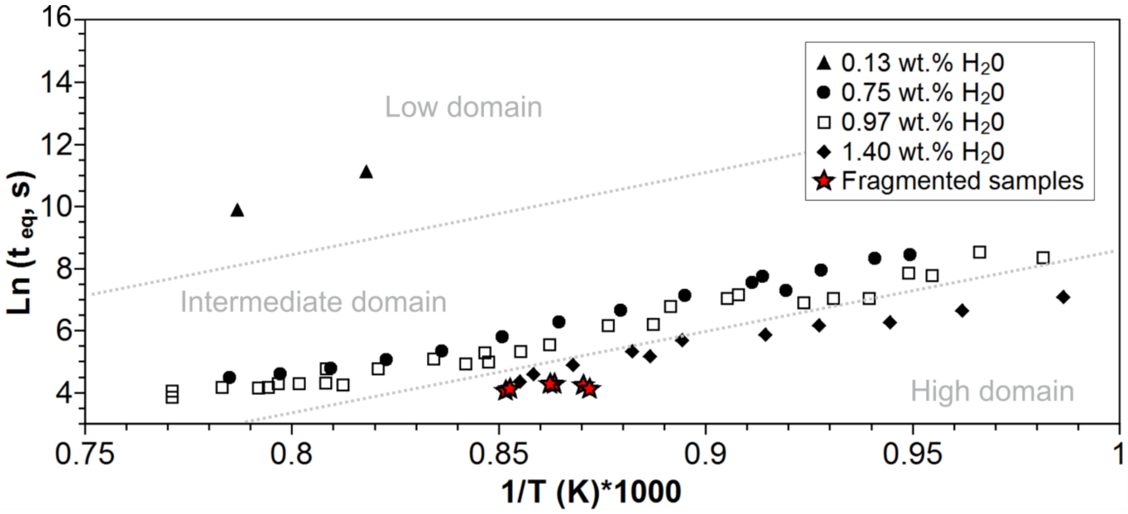

Fig. 3.8. Growth time (t_{gw}) as a function of reciprocal temperature for the different H_2O series. The growth time for the samples showing behavior A was estimated as the time needed for the sample to reach equilibrium (constant volume). In the case of behavior B, it was considered as the maximum A/A_0 before shrinkage begins. For samples showing behavior C (red stars), it is the time between the beginning of the experiments and the occurrence of fragmentation.

Regarding final porosity (ϕ), the experimental products show trends that reflect the volume development for different experimental series (Fig. 3.9). The maximum porosities for many experiments are >90% and, for values below this maximum, there is a clear dependency on temperature and H_2O content. All of the porosities measured for the 1.4 wt.% series (in samples that did not experience fragmentation) represent equilibrium conditions and increase until the fragmentation temperature (T >874°C) is reached. In the case of the intermediate domain series, although the increasing trend is observed, porosity reduction up to 4.5 (for series 0.75 wt.%) and 8.5% (for series 0.97 wt.%) were measured at

T >960°C. Samples from the lower T experimental regime of these series (T <800°C) did not reach equilibrium conditions and highlight ϕ's additional dependency on dwell time.

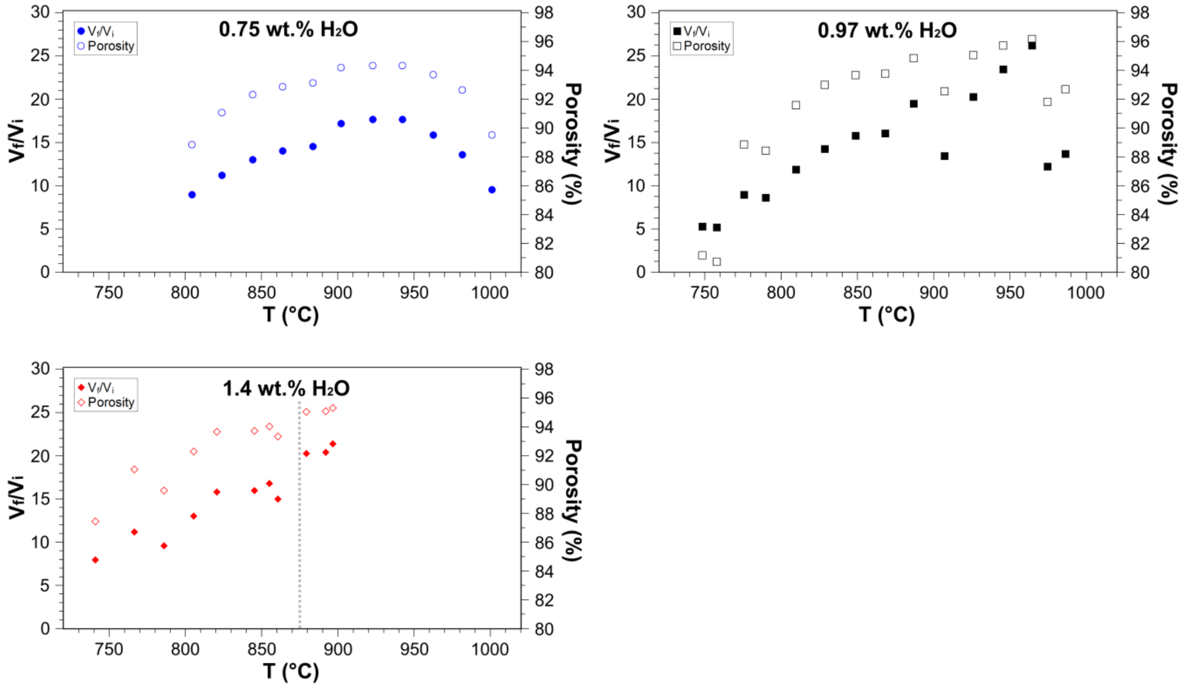

Fig. 3.9. Final/initial volume ratio (V_f/V_i) and porosities values for the experimental series during experiments with standard dwell time (27 minutes). The 0.13 wt.% series is not represented because no change in the measured property was detected during that period of time. Gray dash line represents temperature at which first fragmentation of a sample was observed. The samples from the 1.40 wt.% series plotted to the right of the dash line correspond to the 3 out of 9 experiments that did not experience fragmentation at T >874°C.

In order to characterize final bubble sizes of experimental products, fragments of two foamed samples of the 1.4 wt.% H_2O series were scanned with a Procon X-Ray CT system. Samples of experiments ran at low and high-temperature were selected to bracket the experimental conditions. A bubble size distribution was built up from sub-selecting three separate areas or stack slices from the CT data and using Image J to measure the maximum 2D diameters of bubbles in specific slices through the volume. No correction for stereological effects to get a 3D diameter was done. Results in Fig. 3.10, show mean bubble size values decreased from to 136 to 96 µm with increasing temperature (741–897°C). Although these values might not be representative of all the experimental products, they provide first-order magnitude values that are helpful to characterize bubble size distribution for the experimental conditions explored in this study.

Finally, Fig. 3.11 shows the surface textures of the experimental products and how these vary across the different experimental series. Textures of the 0.13, 0.75 and 0.97 wt.% (not pictured) samples comprise smooth surfaces (Fig. 3.11A–B). The 0.13 wt.% series in particular, developed a shiny outer "skin", consisting of a glassy rind, much like those observed in other vesiculation studies (e.g., Ryan et al., 2015; von Aulock et al, 2017). In contrast, the products of the high-H_2O series developed rough surfaces with irregular to polygonal cracks (Fig. 3.11C) and resembling breadcrust textures on volcanic bombs. This phenomenon was also reported by Stevenson et al. (1997) in their vesiculation experiments on compositionally similar high-H_2O content obsidians (H_2O = 1.5 wt. %, T = 520–624 °C). As it was observed through the furnace window, these cracks formed while the samples were in the expansion stage, confirming that this surface behavior is in fact related to the growth history of the samples rather than being a post-experiment (e.g., cooling and contraction-controlled) process. The different surface textures might be indicative of dissimilar stresses generated within the samples during expansion and vesiculation.

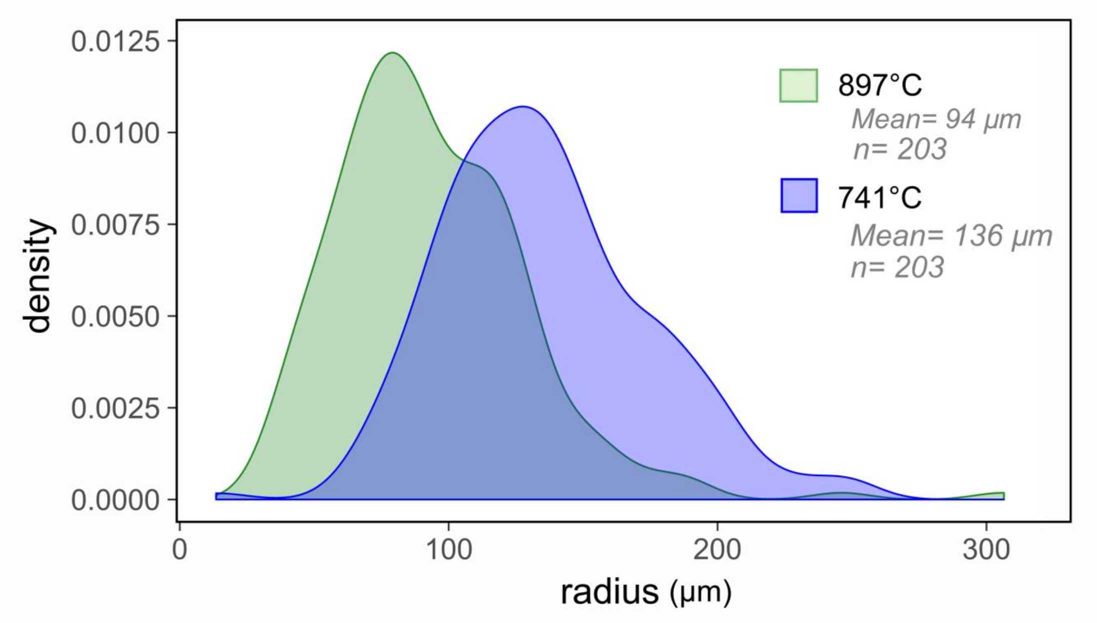

Fig. 3.10. Bubble size distribution in two foamed high-H_2O experiment samples (1.4 wt.%) at low (741°C) and high (897°C) experimental temperature.

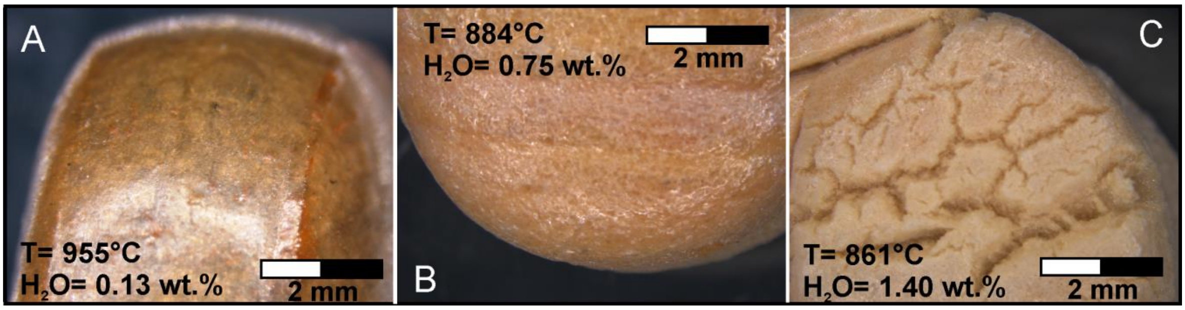

Fig. 3.11. Images acquired with an optical microscope showing surface textures of different experimental products. There is a systematic change in the surface texture from glassy skins observed on low-H_2O-content experiments (A) to rough surfaced at intermediate H_2O contents (B), to a fractured crust on the high H_2O content samples (C).

3.4. Discussion

The varied responses of obsidians to being heated to magmatic temperatures (i.e., behaviors A, B and C) demonstrate the complexity of H_2O exsolution kinetics in rhyolitic melts. The occurrence of these behaviors very clearly follow specific H_2O-temperature conditions and are the result of the decompression rate, viscous deformation of the melt, and diffusivity of H_2O. In particular, the wide range of vesiculation and fragmentation timescales, as well as textures of the experimental products, illustrate how temperature and H_2O strongly influence bubble growth and therefore eruptive dynamics. What is perhaps most striking about this experimental dataset is the observation that explosive fragmentation behavior correlates to *both* initial H_2O content and temperature. The following discussion will be focused on interpreting the different vesiculation behaviors as a function of magmatic intensive parameters, T and P_{H2O}, while the analysis and interpretation of fragmentation behavior observed in the 1.4 wt.% H_2O experiments will be addressed in Chapter 4.

3.4.1 Onset of vesiculation

Experimental heating of hydrous obsidians above their glass transition temperatures releases intrinsically dissolved H_2O from the melt and drives bubble nucleation and growth. Bubble nucleation, the critical first step in the foaming process, requires that the melt is sufficiently supersaturated in H_2O. All of the samples used for these experiments contain H_2O well in excess of the value expected at 1-atm. (~0.05 wt.%; Ryan et al., 2015) and thus were supersaturated at all conditions. The manner of bubble nucleation depends strongly on the presence of microlites in the melt, which act to lower the nucleation energy barrier and prompt heterogeneous nucleation (e.g., Mangan and Sisson, 2000). The presence of ubiquitous microlites in all of our starting materials implies that bubbles in the experiments nucleated heterogeneously.

Formation of bubble nuclei during experiments cannot be tracked with the existing experimental setup because newly nucleated bubbles are exceedingly small at their critical radius $\sim 10^{-9}$ m (Mangan and Sisson, 2000). Furthermore, these small bubbles, even if grown into the 10’s of μm’s range, would contribute little to expansion of the obsidian core caused by bubble growth. For example, the bubble number density in high-H_2O experiments is on the order of 10^6 cm^{-3}. The number density of bubbles was measured by assigning each bubble’s center area (same samples that were used for bubble size distribution analysis, Fig. 3.10) a point in Image J and then having the program count those points. The total number of points was divided by the effective area of glass in the image (this equal to the total image area minus the area occupied by thresholded grey matter in the image). These 2D number densities were corrected to 3D values using the formulation of Peterson (1996). Assuming these values represent an initial nucleation pulse at the onset of experiments, the bubbles would have to have been >10 µm to generate an observable 5% volume increase; recall that a 5% increase in the sample area establishes the onset of measureable vesiculation. Thus, the volume increase observed in experiments is overwhelmingly due to bubble growth rather than nucleation.

Once nucleated, bubbles will grow and expand. Measurements performed in a subset of experiments of the 0.97 wt.% H_2O series (Fig. 3.12), show how bubble size distribution evolves during the first stages of the vesiculation process. By the time the sample reached a ~5% increase in its volume, mean bubble size is 7µm, and it quickly double its size in the next ~20 seconds. Although growing times are expected to be different for each H_2O-T experimental condition, Fig.3.12 shed light on the first moments of bubble growth, and provides bracketing values for further calculations. Bubbles grow by both diffusive mass transfer and gas expansion due to the vapour pressure gradient between bubbles and the atmosphere (ΔP) and viscous melt deformation to accommodate the increase in gas volume.

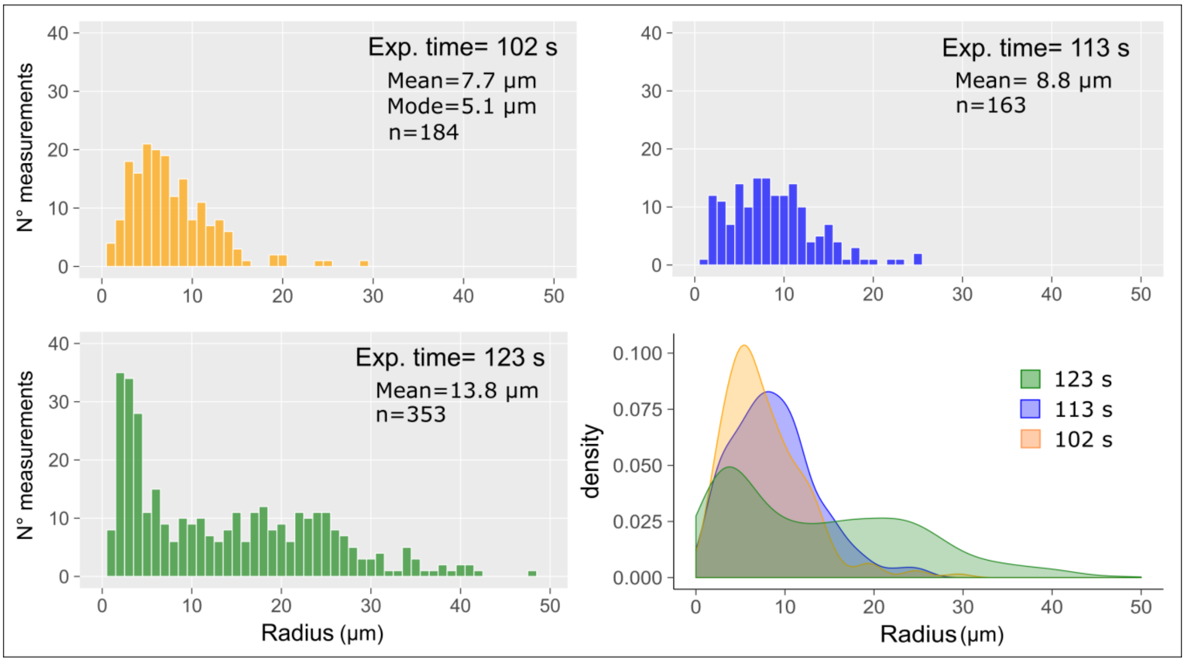

Fig. 3.12. Bubble size distribution at the first stages of vesiculation process in a subset of experiments of the 0.97 wt.% H_2O series. Three experiments were performed at 795°C and variable durations (102 to 123 seconds). The shortest time chosen to run the experiments corresponds with the expected t_{lag} at *Pe* = 1. To obtain these BSD, experimental products were first embedded in epoxy, sectioned into thin wafers with a Buhler slow speed saw, and then doubly polished with diamond-impregnated lap wheels. Images of the existing bubbles were acquired with the assistance of a binocular microscope and their sizes measured with ImageJ.

3.4.2 Vesiculation regimes

Diffusive mass transport and viscous deformation during bubble growth are controlled by the silicate melt's temperature and H_2O concentration, as both of these variables strongly influence the H_2O diffusivity coefficient and viscosity (Zhang and Behrens, 2000; Giordano et al., 2008). Accordingly, it is somewhat expected that the variably hydrous samples displayed well-defined ranges of expansion behavior that follow temperature intervals. One way to characterize different vesiculation regimes is through comparing the relative importance of H_2O diffusion and viscous melt deformation on bubble growth. In non-dimensional terms, the Peclet number (*Pe*) weighs the characteristic timescales of diffusion ($\tau_d = {R^2}/{D}$) and viscous deformation timescale ($\tau_v = {\eta}/{\Delta P}$) via the following expression (e.g., Lyakhovsky et al., 1996):

$$Pe = \frac{\Delta P . R^2}{\eta . D} = \frac{\tau_d}{\tau_v} \quad (3.1)$$

where ΔP is the overpressure inside a bubble of radius *R*, η the viscosity of the melt and *D* is the composition- and temperature-dependent H_2O diffusion coefficient (Zhang and Behrens, 2000). According to Bagdassarov et al. (1996), *Pe* = 1 represents a transition between these authors' so-called diffusion-limited (at relatively high-T) and viscosity-limited (relatively low-T) growth regimes. This is to say that when *Pe* >1, the timescale of diffusion limits bubble growth, while for *Pe* <1, viscous melt deformation limits the kinetics of the vesiculation process. Note, however, that under certain experimental conditions, it will be the smaller of the two timescales—i.e., the faster process—that will control bubble expansion during the course of an experiment. For example, *Pe* >>1 indicates $\tau_d >> \tau_v$ and thus, diffusive contributions to the growing bubble will be negligible for a certain time compared to bubble growth by vapour expansion and viscous relaxation of the pressure differential, ΔP. This may lead to high degrees of H_2O supersaturation in the melt (e.g., Gonnermann and Manga, 2007). By contrast, for *Pe* <<1 conditions, $\tau_d << \tau_v$, i.e., diffusion keeps pace with the decrease in H_2O solubility driven by decompression and, owing to rather sluggish viscous deformation, the system may become critically overpressurized (Gonnermann and Manga, 2007). Consequently, large and small *Pe* regimes are sometimes termed as "viscosity-controlled" and "diffusion-controlled", respectively (e.g., Toramaru, 1995; Lyakovsky et al., 1996; Navon et al., 1998; Lensky et al., 2004). This terminology will be used to refer high- and low-*Pe* regimes from here on out.

It is clear from the *Pe* formula (Eq. 3.1) that large *Pe's* stem from high ΔP and relatively low melt viscosities, conditions that are fostered by high initial H_2O content and temperature. In contrast, low *Pe* is fostered by relatively small ΔP (low initial P-H_2O) and high viscosity (low T). Unfortunately, the value of ΔP in the experiments is *a priori*, unknown. However, if it is assumed that ΔP is the difference between the hypothetical pressure at which the initial dissolved H_2O would be in equilibrium (i.e., at the solubility limit) with the melt and the ambient pressure (i.e., 1-atm in all experiments), a maximum values of *Pe* that may have governed vesiculation is obtained (Fig.3.13 and Table 3.3). Clearly *Pe's* determined this way could be in error if in fact the bubble pressure is initially less than that of the dissolved H_2O content. In addition, diffusivity (*D*) also plays a role in *Pe*, varying sympathetically with temperature and H_2O content (e.g., Zhang and Behrens, 2000), but *D* variations impact *Pe* slightly less than ΔP and viscosity. Similarly, bubble radius is rather restricted to a small range (~5–100 µm) in our experiments (Fig. 3.10 and 3.12). Therefore, over the course of a vesiculation experiment, it is expected the Pe's decrease as the melt-H_2O steadily decreases during H_2O exsolution and bubble growth and the viscosity concomitantly rises.

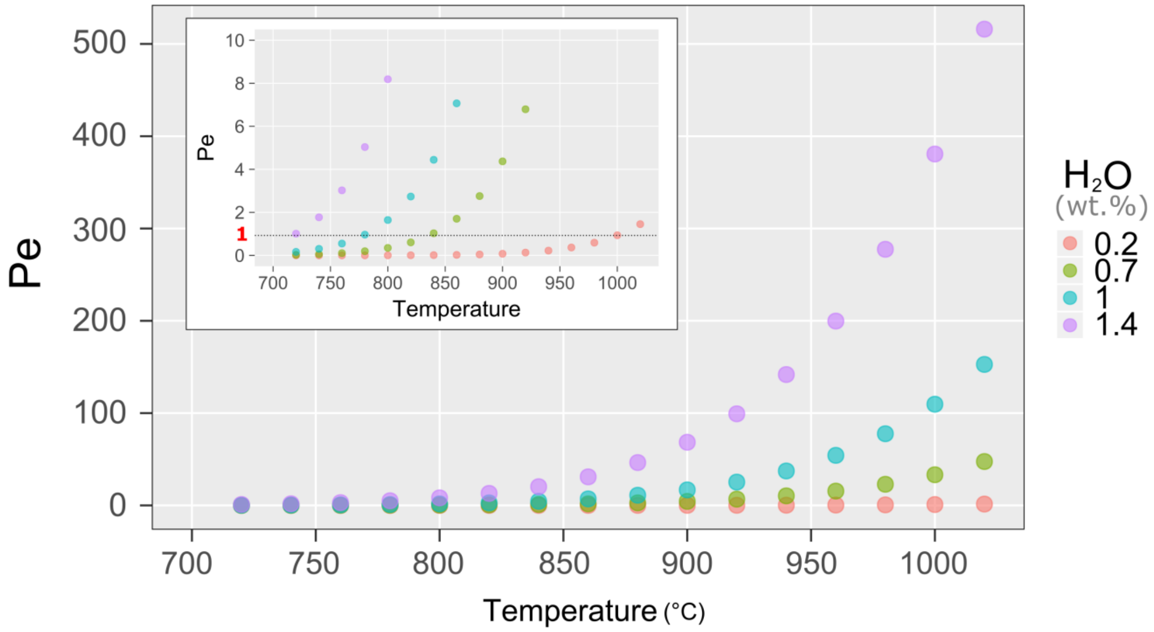

Fig. 3.13. Peclet number estimations for the different H_2O content series. In the upper left corner, a close up view of Pe values <10. It is important to observe the different temperatures at which the experimental series transition from viscosity- (*Pe* <1) to diffusion-controlled (*Pe* >1) regimes. *Pe* = 1 is represented, in the upper right corner plot, by an horizontal dotted line. Assumptions made and parameters used for calculations are described in Table 3.3 as well as in the main text.

Table 3.3. Calculated *Pe* numbers for a range of T and H_2O experimental conditions

H_2O (wt.%)	**T (°C)**	**Δ P $^{(a)}$ (MPa)**	**Radius$^{(b)}$ (µm)**	**$\log_{10} \eta$ $^{(c)}$ (Pa s^{-1})**	**Diffusivity $^{(d)}$ (µm^2 s^{-1})**	***Pe* estimated**
1.4	780	14.2	5	7.8	1.5	**5**
	880	17.1	5	6.6	3.5	**46**
1.0	780	7.4	5	8.3	1.2	**0.96**

	880	8.9	5	7.0	2.7	**11**
0.7	780	3.8	5	8.9	0.9	**0.2**
	880	4.5	5	7.4	2.0	**2.7**
0.4*	780	1.2	5	9.6	0.5	**0.02**
	880	1.4	5	8	1.2	**0.4**

(a) Based on Newman and Lowenstern (2002) solubility model

(b) Obtained from Giordano et al. (2008)

(c) Calculated from Ni and Zhang (2008)

(d) Navon et al. (1998)

* Hypothetical Pe numbers not based on our starting H_2O contents

The experimental parameter space over which bubble growth is controlled by viscosity versus diffusion can also be defined by plotting the natural log of the time lag (t_{lag}) vs. reciprocal temperature (Fig. 3.14; e.g., Bagdassarov et al., 1996). However, it must be noted that this parameterization only categorizes bubble nucleation and growth during the earliest stages and does not describe the entire expansion history of our samples, since t_{lag} was time-limited after 5% growth. That said, Bagdassarov et al. (1996) used this parameterization to quantify the activation energies associated with H_2O diffusion and viscous deformation during the onset of vesiculation in rhyolitic obsidians. Similar to what these authors observed, the data from this study plot into distinct temperature ranges, and those for 0.75 and 0.97 wt.% series (Fig. 3.14B–C) comprise two linear arrays distinguished by different slopes. The linear segments, steeply sloping at low-T and shallow at high-T, are divided by a kink whose position is offset to lower temperatures as water content increases (i.e., from 0.75 wt. % to the 0.97 wt. %). The 1.4 wt.% H_2O experimental series is not kinked as all its values plot on a single line (Fig. 3.14A). This suggests that experiments at 1.4 wt.% H_2O did not reach low enough temperatures to delineate a more steeply sloping segment.

Bagdassarov et al. (1996) showed that kinked plots in t_{lag}-1/T space characterize two bubble growth regimes, using their terminology: 1) high-T, diffusion-limited growth represented by the shallow sloping segment, and 2) low-T, viscosity-limited growth demarcated by the steeper-sloping segment. The activation energies (*Ea*) corresponding to H_2O-diffusion and viscous deformation are in turn proportional to the slopes of the arrays at high and low temperatures, respectively. Specifically *Ea*'s are obtained from linear fitting of the form:

$$\ln \tau_{lag} = ln\,(\tau_0) + \left(-\frac{Ea}{R}.\frac{1}{T}\right) \quad (3.2)$$

where R is the ideal gas constant and τ_0 represents a fitting parameter.

The experimental data yields *Ea*'s of 205 and 208 kJ mol^{-1} for the 0.75 and 0.97 wt.% H_2O series, at T's less than 897° and 802°C, respectively, while for higher temperatures, fitting returns *Ea*'s of 85 and 78 kJ mol^{-1}, respectively (Fig. 3.14). These *Ea*'s are similar with those obtained for compositionally similar rhyolitic melts (Bagdassarov et al., 1996; Stevenson et al. 1997; Zhang and Behrens, 2000), which confirms that despite different experimental configurations and conditions, the activation energies for diffusion and viscous flow are somewhat constant. The 1.4 wt.% H_2O series yields *Ea* of 81 kJ mol^{-1}, consistent with the high-T *Ea*'s of the other two lower-H_2O series.

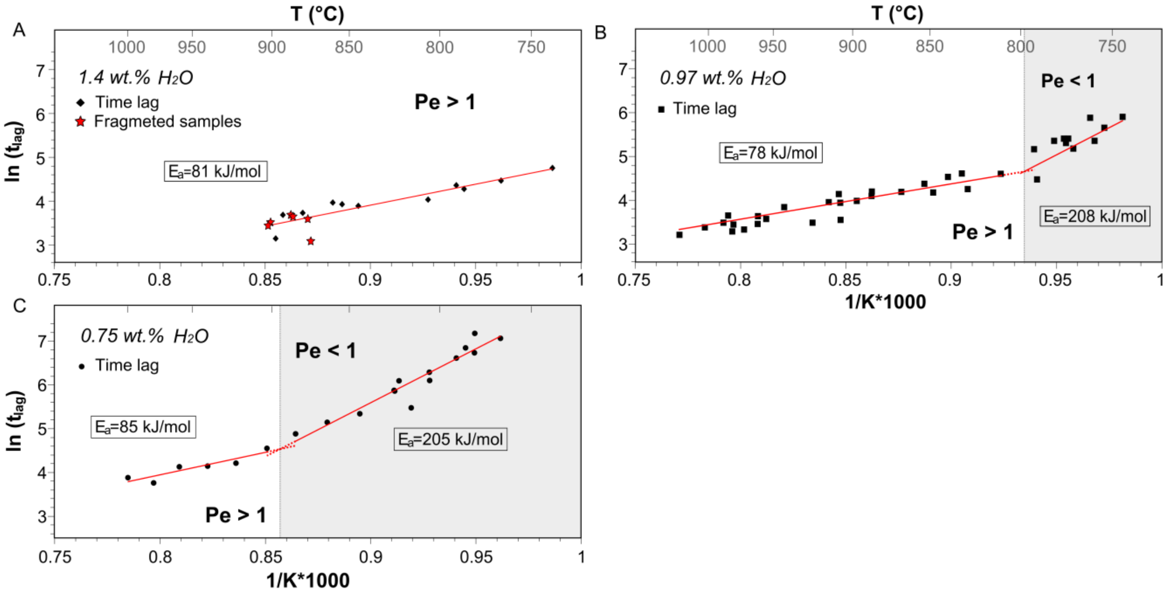

Fig. 3.14. Plots of the natural logarithm of the lag time (tl_{ag}) versus reciprocal temperature for the high (A) and intermediate (B–C) H_2O experimental series. T_{lag} was obtained graphically by documenting the time at which a measurable increase in the sample area (5%) occurred during initial foaming. In contrast to the highest H_2O content series, which has a single linear segment, the two lower H_2O content series depict "kinks" in the t_{lag} relation, indicating a temperature dependent transition across diffusion- and viscosity-limited expansion behavior. The activation energies for diffusion and viscous flow are shown as Ea values in boxes.

Following on the work of Bagdassarov et al. (1996), the kinked plots in t_{lag}-1/T space are interpreted to record two bubble growth regimes, corresponding to viscosity and diffusion controlled conditions. The positions of the transition from *Pe* >1 to *Pe* <1 in intermediate H_2O content series, i.e., where *Pe* = 1, provides a way to independently estimate the early ΔP stored in bubbles. More specifically by assigning *Pe* = 1 and rearranging the *Pe* formula (Eq. 1), we have:

$$\Delta P = \frac{\eta . D}{R^2} \quad (3.3)$$

Unfortunately this overpressure formulation cannot be directly apply to the 1.4 wt.% H_2O series, since its t_{lag} plot does not display a kink. However, the values derived for the two intermediate H_2O content series, whose *Pe* = 1 positions are at 800˚C and 900˚C, do provide limiting overpressure estimates. Thus, considering the average bubble radius in these experiments at the onset of vesiculation (R~5 μm; Fig. 3.12) and appropriate viscosity and H_2O-diffusivity values, the bubble overpressures at 800˚C (at 0.97 wt.% H_2O) and 900˚C (at 0.75 wt.% H_2O) would be on the order of 4.6 and 4.0 MPa, respectively. These values are comparatively lower than the overpressures estimated assuming that initial bubbles formed with a vapour pressure equal to the solubility limit (~7.7 to 5.9 MPa). We expect that the overpressure in the 1.4 wt.% experiment series would be even higher given that H_2O correlates to higher ΔP (e.g., note relative $\Delta P's$ of 0.97 and 0.75 wt.% experiments).

Experimental and numerical studies demonstrate that high *Pe* (>1) conditions lead to exponential bubble growth in time, and square-root-of-time or parabolic growth trajectories at small *Pe* (Toramaru, 1995; Navon et al., 1998; Lyakovsky et al., 1996). The sigmoidal forms of the experimental A/A_0 vs. time plots manifest both exponential and parabolic components of bubble growth (Fig. 3.6 and Fig. 3.15). At short times, the concave-up segments indicates that sample expansion is purely exponential, a reflection of the viscosity control on bubble growth at large *Pe* (Toramaru, 1995; Navon et al., 1998). After some period of time, which is indicated geometrically by the inflection point in the growth curve, expansion rate slows and then resembles a parabolic law. Viewed macroscopically, the growth curves demonstrate accelerating (early) and decelerating (late) components. This prompts the question: what is the physical significance of the expansion rate change?

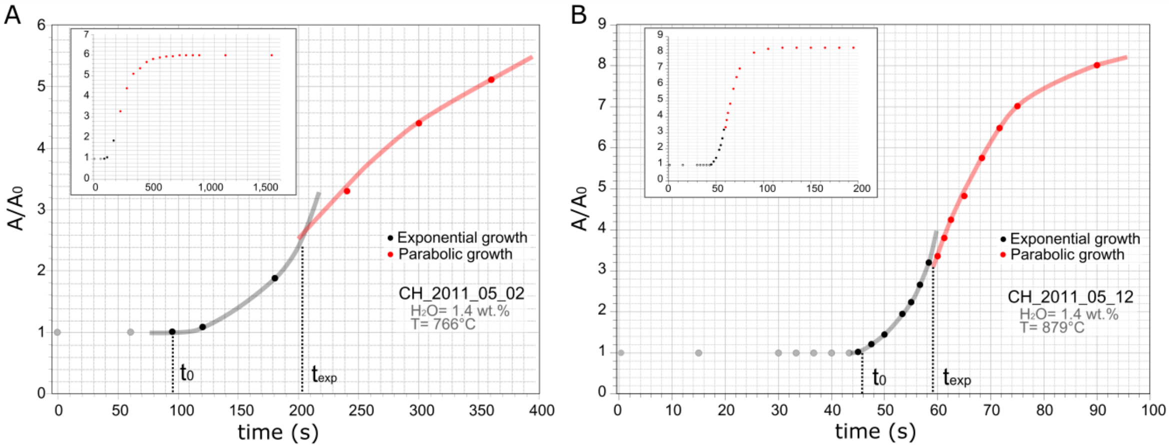

Fig. 3.15. Exponential and parabolic growth segments for two samples of the 1.4 wt.% H_2O series that did not experience explosive fragmentation (behavior A). Each dot (black and red) represents a video frame in which the area was manually measured. While T_0 corresponds with measured t_{lag} (see Appendix C), t_{exp} coincides with the inflection point of the sigmoidal curve. The inflection point was determined graphically by inspecting the growth traces directly on graphs. In the upper left corner of each plot, the complete growth evolution of the sample is represented.

Interestingly, explosive fragmentation in type-C experiments occurred only when the foamed samples were just emergent from the exponential growth segment, exploding after just tens of seconds (~20–30 s) of foaming (Fig. 3.16). Qualitatively, this suggests that a late-stage pressurization due to prolonged vesiculation in the low-*Pe*, diffusion-controlled realm—as is often ascribed to overpressure-induced explosions in lava domes (Sato, 1992; Navon et al., 1998; Gonnermann and Manga, 2007)—is not the only mechanism driving fragmentation in our experiments. Instead, the explosions seem to manifest initial overpressure that was not fully relieved by viscous bubble growth. Hence, it is the initial high-H_2O content and the incipient shift between growth regimes that may in part be critical for pushing foaming into fragmentation.

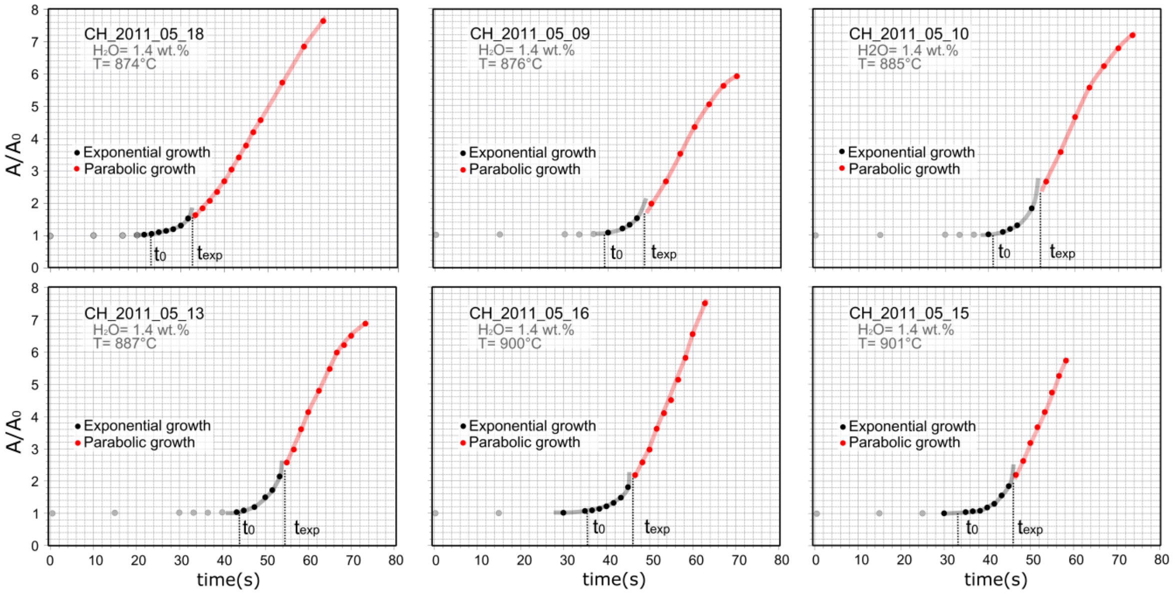

Fig.3.16. Exponential and parabolic growth segments for the 1.4 w.t% H_2O samples that experienced explosive fragmentation (behavior C). For the construction of the graphs, the same procedure as the one described in Fig. 3.15's caption was followed. Detailed information about the duration of exponential and parabolic growth segments can be found in Table 3.4.

Table 3.4. Exponential and parabolic growth times of experiments showing behavior C. Values were measured graphically from Fig. 3.16.

Experiment	Temp (°C)	t_0	t_{exp}	Exponential growth (s)	Parabolic growth (s)	Time fragmentation (s)
CH_2011_05_18	874	23	33	9	30	63
CH_2011_05_09	876	39	49	10	21	70
CH_2011_05_10	885	41	52	11	21	73
CH_2011_05_13	887	44	55	11	19	73
CH_2011_05_16	900	36	46	10	17	63
CH_2011_05_16	901	33	46	13	12	58

The observation that the most H_2O-rich (1.4 wt% series) experimental samples exhibit both explosive *and* coherent foaming behavior—depending on temperature—suggests that in addition to high initial vapour overpressure (high *Pe*), the dynamics of expansion may also be at play in promoting fragmentation behavior (e.g., Lensky et al., 2004; Gonnermann and Manga, 2007). In particular, the timescales of expansion are very different between exploding (e.g., <30 secs at 880˚C) and non-exploding (e.g., >200 secs at 780˚C) 1.4 wt.% H_2O experiments (Fig. 3.6 and 3.8). With temperature being the only difference underpinning these two distinct expansion times, it is proposed that temperature dependencies of viscosity (>1 order of magnitude difference; Giordano et al., 2008) and the solubility vapour pressure (about 3 MPa higher at 880˚C; Newman and Lowenstern, 2002) conspire to drastically change the viscous deformation timescale ($\tau_v = {}^{\eta}/_{\Delta P}$= 0.21s at 880˚C vs. 4.4s at 780˚C). This, in turn, facilitates significantly faster viscous expansion rates in the H_2O-rich, high-T experiments. For all intents and purposes, foam expansion rate is analogous to a sample's decompression rate, in so far that a prescribed amount of P-V work is done by the expanding clast over the a defined amount of time (e.g., Kaminsky and Jaupart, 1997). Therefore, in addition to the *Pe*, a characteristic decompression rate appears to dictate whether experiments exhibit coherent foaming, or foaming to fragmentation behavior (e.g., Lensky et al., 2004; Gonnermann and Manga, 2007). This will be addressed in detail during the next chapter.

3.5. Conclusions

Through a robust set of experiments (94), this study bridges the existing gap for 1-atm, high-temperature experiments with rhyolite glasses and provides new insights into the degassing and vesiculation dynamics of rhyolite magmas with eruptive-relevant H_2O contents. A novel experimental setup permitted to monitor and record the complete duration of the experiments. Post-experimental video analysis has revealed 3 types of behaviors of the samples: a) expansion followed by equilibrium (constant volume), b) expansion followed by shrinking and c) expansion followed by explosive fragmentation. The occurrence of these behaviors very clearly follow specific H_2O-temperature conditions and, as shown here, are the result of variations in expansion rates, viscous deformation of the melt and diffusivity of H_2O. In particular, the wide range of vesiculation and fragmentation timescales, as well as textures of the experimental products, illustrate how temperature and H_2O strongly influence bubble growth and therefore eruptive dynamics.

Explosive behavior was identified exclusively in samples with H_2O = 1.4 wt.%, and at temperatures higher than 874°C. For samples with H_2O <1.4 wt.%, no fragmentation was observed, even at higher temperatures (up to 1030°C), well above the estimated pre-eruptive temperature (~825˚C) of the 2008 Chaitén rhyolite. In samples that did not experience fragmentation, porosities of up to ~90% were measured. Surface textures identified in the samples also correlate with the different observed behaviors. Finally, it was possible to characterize vesiculation regimes associated to the different behaviors observed.

In particular, *Pe* and t_{lag} permitted to define viscous and diffusion regimes that controlled bubble growth during the experiments. Interestingly, in contrast to the models proposed for lava dome explosions (e.g., Navon and Lyakhovsky, 1998), the explosions in these experiments seem to manifest initial overpressure that was not fully relieved by viscous bubble growth.

Chapter 4

Explosive fragmentation of rhyolite magma: an experimental perspective

4.1 Introduction

Magmatic fragmentation in highly-silicic systems involves brittle fracture of a magma body and, as it was mentioned in the introductory chapter, it can be seen as either a bottom-up or top-down driven process (Cashman and Scheu, 2015). A number of mechanisms have been proposed for just how brittle failure of magma occurs (e.g., McBirney and Murase, 1970; Sparks, 1978; Alidibirov and Dingwell, 1996a; Dingwell, 1996; Papale, 1999; Zhang, 1999; Alidibirov and Dingwell, 2000). Most models consider that silicic melts behave viscoelastically under stress, that is, they show different material responses to stress when subjected to variable temperatures and timescales of deformation. Dingwell and Webb (1989) parameterized this behavior and showed that brittle (elastic) and viscous-response fields are separated by the relaxation time curve, also termed the glass transition. For fragmentation to occur, magma (initially in the viscous regime) can cross the glass transition dynamically by being deformed at a rate higher than the melt's relaxation rate, which defines a critical rate above which stress cannot be dissipated by viscous flow. Another mechanism to drive fragmentation is for the overpressure to increase beyond that of the strength of the melt, the so-called tensile-strength-limiting condition (Zhang, 1999).

Given the difficulty (and danger) of directly observing magmatic fragmentation, the development of experiments has greatly improved our understanding of fragmentation and its underlying mechanisms. Significant progress has been made for the case of Vulcanian-type activity, in which fragmentation is thought to be driven by instantaneous decompression (Alidibirov and Dingwell, 1996a,b; Alidibirov and Dingwell, 2000; Martel et al., 2000, 2001; Spieler et al., 2004, Kueppers et al., 2006). However, to date, explosive degassing from rhyolite volcanoes has only been scarcely experimentally investigated with natural materials. High-pressure and temperature (PT) autoclave experiments involving rapid decompression of vesicular rocks into a low-pressure chamber utilize an externally supplied gas as an exsolved-volatile equivalent, and when a diaphragm ruptures between the high- and low-pressure sections, a decompression shock wave fragments the sample (Alidibirov and Dingwell, 1996a,b). As a consequence, these experiments indicate how pre-existing porosity and the gas-pressure gradient influence the “fragmentation threshold” of bubbly melts (Martel et al., 2000, 2001; Spieler et al., 2004). However, because the pressurizing gas is introduced to an already porous sample, such experiments cannot shed light on how bubble growth may drive fragmentation (e.g., Sparks, 1978; Papale, 1999). To date, however, no experimental studies have induced explosive fragmentation from bubble growth in silicic melts. Consequently, there has been a disconnect between experimental constraints on bubble growth (see section 1.1.1 and references therein) and observations of the fragmentation process itself.

In Chapter 3, the results of a series of high-T, 0.1 MPa experiments performed on natural pyroclastic obsidians erupted during Chaitén volcano's 2008 explosive Plinian phase were presented. These obsidians, like those of many other rhyolite systems (e.g., Mono Craters, CA; Newman et al., 1988), preserve a range of magmatic H_2O contents (~1.4 to 0.13 wt.%) that reflect various amounts of degassing from what was initially much more hydrous melt (~4 wt. %; Castro and Dingwell, 2009). As it was shown, and despite the natural samples being partially degassed relative to pre-eruptive conditions, these obsidians still contain sufficient H_2O to vesiculate, and in some cases fragment, when heated at 1-atm. This means that 1-atm. vesiculation behavior of obsidian can reveal critical elements of the explosive degassing process, which in turn can be used to better understand different low-pressure "degassing environments" within a silicic eruption.

In this chapter, a detailed analysis of the explosive behavior (behavior C) observed in the high-T, 0.1 MPa experiments is presented. In addition, these results are compared with a separate set of high-P experiments performed in a fragmentation bomb. Finally, all these experimental results are discussed in the context of 2008 Chaitén eruption.

4.2 Methodology

To explore the fragmentation mechanisms involved in the disruption of highly-silicic melts, the experiments presented in Chapter 3 (High-T, 0.1MPa) were complemented with a set of high pressure experiments performed in a fragmentation bomb at the LMU.

4.2.1. High Temperature-0.1 MPa experiments

The experimental setup and procedure followed for these experiments was already described in Chapter 3. However, in addition to the experiments presented in that chapter, a complementary set of experiments was carried out to further characterize the pyroclastic material generated (Table 4.1). Unfortunately, the original design of the experimental setup was not optimal for samples recovery (Fig. 4.1A). In addition to the loss of material, especially the finest fraction, the exposure of the resultant pyroclasts to temperatures above glass transition for extended periods of time (until the furnace cooled down), made the setup not suitable for post-experimental textural analysis. To overcome this limitation, an ash collector was designed and developed in cooperation with SCHOTT® (Fig. 4.1B). The collector consists in a 150x240x280 mm glass box, made of Quarzal®, which is a slip cast, fused silica material (99.6 wt.% SiO_2) that has an excellent thermal shock resistance. One side of the box was replaced with a 3mm thick removable window, which allows not only for the insertion of the sample, but also for observation of the experiment evolution. The window material is fused silica glass (JGS1), which has a transmissivity that matches with the IRwavelength of the laser used to monitor sample surface temperature evolution. Additionally, the collector has a 3 mm hole in the back that permits the introduction of a thermocouple.

Table 4.1. Experimental conditions and post-experimental analysis performed.

Experiment	T(°C)	GSD analysis	Particle velocity tracking
CH_2011_05_09	876	No	Yes
CH_2011_05_10	885	No	Yes
CH_2011_05_13	887	No	Yes
CH_2011_05_15	901	No	Yes
CH_2011_05_16	900	No	Yes
CH_2011_05_18	874	No	Yes
CH_2011_05_19*	879	Yes	No
CH_2011_05_20*	890	Yes	No
CH_2011_05_21*	897	No	Yes

* Complementary set of experiments, not presented in Chapter 3.

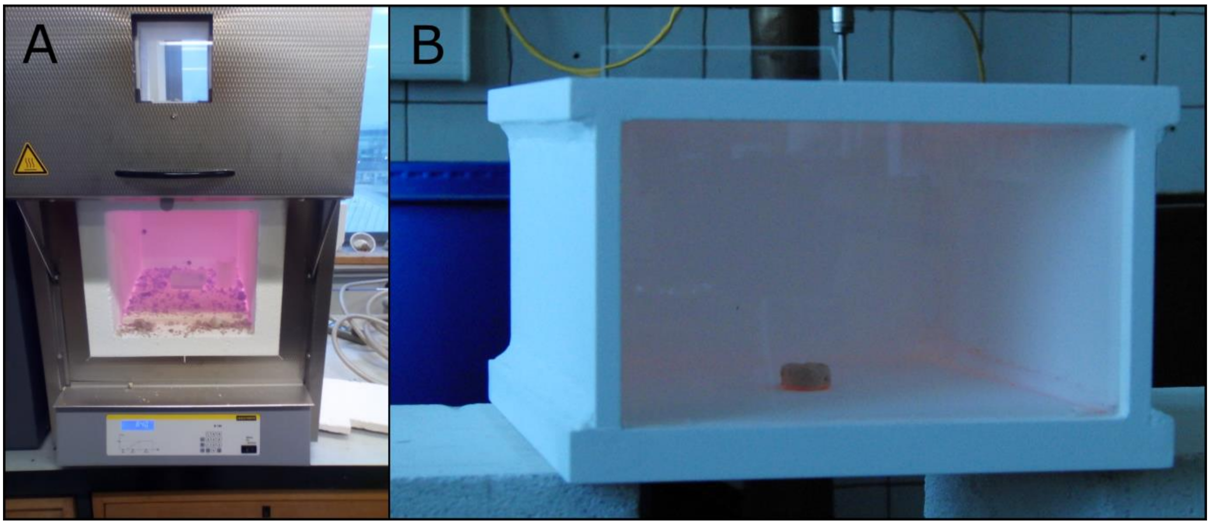

Fig. 4.1. A) Photo of the furnace at JGU after a series of high-T, 0.1 MPa fragmentation experiments. It is possible to observe the resultant pyroclastic material covering the floor of the furnace. B) Glass box developed to collect pyroclastic material generated during an experiment. A 15 mm-width foamed obsidian sample placed inside the collector provides a scale.

To perform this complementary set of experiments, the ash collector was placed inside the furnace at room temperature and then heated up to the target experimental conditions (Table 4.1). Before running the experiment, time was given for the ash collector interior to reach thermal equilibrium with the furnace inner chamber. This was monitored by using two chromel-alumel K-type thermocouples, one to measure the temperature inside the collector and other the one outside (furnace interior T). Once thermal equilibrium was reached, the sample was inserted into the collector, the window closed and the experiment recorded following the methodology described in the previous chapter. Upon completion of the experiment, the box was immediately removed with the assistance of a steal shovel and cooled down with compressed air. After ~1 minute, the temperature inside the ash collector was below sample's glass transition temperature.

Unfortunately, due to the limited amount of obsidian glass with 1.4 wt.% H_2O available, it was possible to performed only 2 experiments with the improved setup (Table 4.1). Nevertheless, the ash collector was successfully tested with other samples (that are not of interest of this thesis), proving its utility for future research.

4.2.2. High Pressure–variable Temperature shock-tube experiments

4.2.2.1. Sample characterization

Samples for the experiments were obtained from a single, decimeter-sized, pumice bomb (Fig. 4.2A). The bomb was collected during a field campaign in November 2016 from the northern outer rim of the Chaitén caldera and it represents part of the material erupted during the initial explosive phase of the 2008 eruption.

The pumice exhibits a texture composed of tubular bubbles (Fig. 4.2B) and an open-porosity value of 55%. Porosity was measured with a Quantachrome Ultrapyc 1200e helium-pycnometer at LMU, and this value represents an average obtained from 5 independent measurements. Due to the experimental procedure followed, open porosity is the only porosity value relevant for these experiments. H_2O content of this sample, determined by DSC-TGA is ~0.70 wt.% (see Chapter 2).

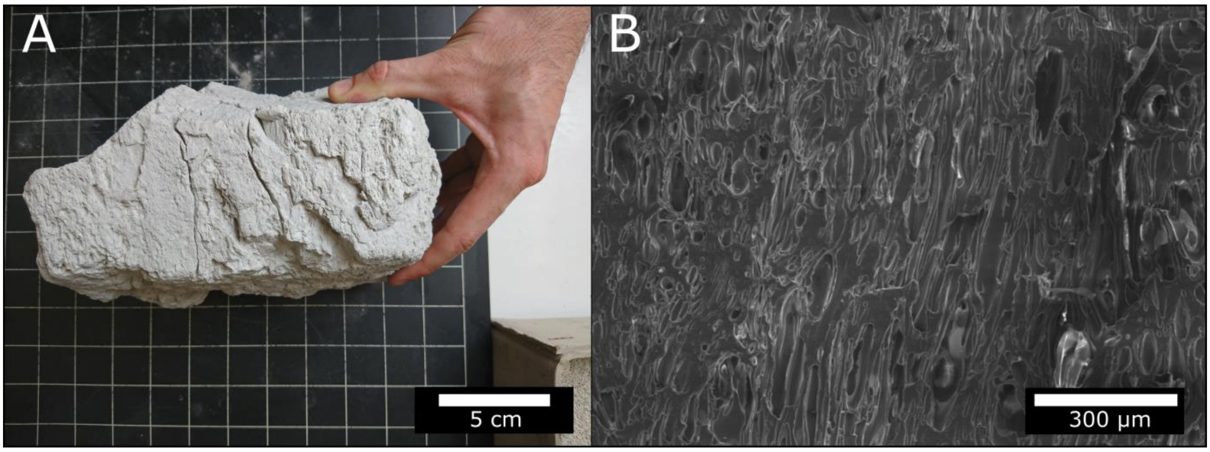

Fig. 4.2. A) Pumice bomb used for the high-P experiments. B) SEM image showing the pore morphology of the pumice.

4.2.2.2. Experimental procedure

High-P experiments were performed in the fragmentation bomb available at the laboratories of LMU (Fig. 4.3). This experimental apparatus consists of three main units (Fig.

4.3B): a) a shock-tube (made of Nimonic 105 alloy), which allows for high P-T conditions, b) a diaphragm system, composed of 3 diaphragms that open at a relative pressure differential, and c) a low-pressure tank (atmospheric conditions). A cylindrical Plexiglas tube at the base of the low-P tank allows for direct visual observation and high-speed video filming of the experiments.

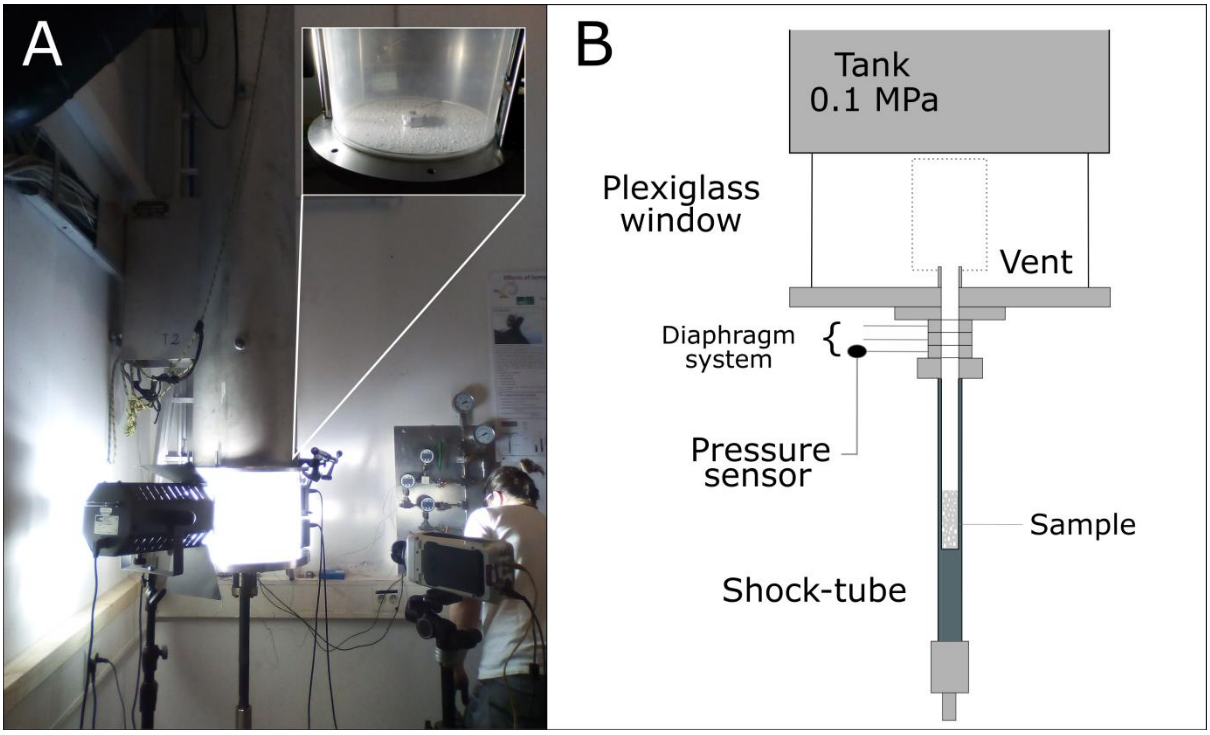

Fig. 4.3. Experimental setup for the high-P experiments. A) Photo of the fragmentation bomb. External source of light is used to record high speed videos of the experiments. In (B), a detailed description of the experimental apparatus is presented (not to scale). The grey dot-lined rectangle indicates the camera field of view (Modified from Cigala et al., 2017).

Cylindrical cores drilled from the pumice with a diamond-coring device were used as starting material. Cores had an initial diameter of 25 mm and two different lengths, 30 and 60 mm. Size was measured with a precision digital caliper (σ ± 0.01 mm) and the samples were weighed with a high-precision balance (σ ± 0.01 mg). The ends of the cores were ground flat and polished to avoid irregularities. As for the case of the obsidian cores, before running the experiments all the samples were carefully inspected for preexisting fractures, and the ones showing damage were discarded.

Once the sample was placed inside the shock-tube, the system was pressurized. The set-up permits precise and reproducible pressurization of the sample. The shock-tube was pressurized with an external gas (Argon). Two different initial overpressures were applied during the experiments, 10 and 15 MPa. Experiments were carried out at two different temperatures, 25°C (room T) and 500°C.This temperature range, below sample T_g, was used in order to avoid heating-induced physical changes in the samples. High experimental temperature was achieved by using an external tube furnace. Temperature inside the shock-tube was monitored with a K-type thermocouple located at the bottom of the sample. Before decompression, sample was in thermal equilibrium with the surrounding gas phase. To ensure this, sample was held at target conditions for 10 minutes before triggering decompression. Pressurization of the uppermost diaphragm over its strength induces its failure and triggers system depressurization. Decompression is instantaneous, triggering fragmentation. As a consequence, a mixture of gas and sample fragments is ejected into the low-P tank. Upon decompression, the expanding gas phase is rapidly cooled. After allowing time to settle (~2h), the experimentally generated particles were carefully collected for grain size distribution (GSD) analysis. The experiments were filmed with a Phantom high-speed camera (V711) at 10,000 fps. The camera was connected to a pressure sensor, which records pressure drops and triggers the recording. These experiments were performed with the assistance of Dr. Ulrich Kueppers.

A total of 9 high-P experiments were conducted at a variable set of conditions (Table 4.2). Parameters modified include: pressure (10 and 15 MPa), temperature (25 and 500°C), and sample (30 and 60 mm) length. Additionaly, in two of the experiments the length of the low-P tank was modified from 3 to 1 m. The goal of these experiments was to explore the effect of the tank length on the final grain size distribution observed. Although this goal is irrelevant to the research focus of this thesis, the results of these experiments were used to test the reproducibility of certain experimental results (e.g., pressure-velocity relation).

Table 4.2. Experimental conditions and post-experimental analysis performed.

Experiment	T °(C)	P (Mpa)	Cylinder length (mm)	GSD analysis	Particle velocity tracking
CH_P2_1	25	10	31.5	Yes	Yes
CH_P2_2	500	15	61.2	Yes	Yes
CH_P2_4	25	15	60.4	Yes	Yes
CH_P2_5	500	10	60	Yes	Yes
CH_P2_6	25	15	30	Yes	Yes
CH_P2_7	25	10	59.4	Yes	Yes
CH_P2_8	25	10	30.4	Yes	Yes
CH_P2_9	500	15	30.4	Yes	Yes
CH_P2_11	25	15	29.8	Yes	Yes

4.2.3 Post-experimental analysis

The design of both experimental setups (low and high-P experiments) permitted filming fragmentation experiments with high speed cameras (Fig.4.4 and 4.8). Post-experimental video analysis allowed precise timing of explosions as well as estimation of fragment velocities and ejection directions. For this, a number of particles (between 50 to 200) were manually tracked in each experiment by using MTrackJ, an ImageJ plug-in. Velocity was evaluated by measuring the distance of single particles in five consecutive scaled frames and averaging the velocity for this time interval. No perceptible acceleration or deceleration could be detected during that time frame.

Experimental products were collected to analyze their grain size distributions (GSD). The pyroclastic material generated both in the fragmentation bomb and inside the ash collector at JGU (see Table 4.1 for details), was carefully collected with the aid of a brush and sieved. Sieving was performed at half-Φ steps ($\Phi = -\log_2 d$, with d = particle diameter in mm), spanning the grain size range from 32 to 0.06 mm. Samples were sieved dry, with an average sieving duration of 20 s per sieve class. Samples were weighed before and after sieving with a high precision digital balance. In all cases, weight loss was <1 wt.%. Particles <0.06 mm were collected and weight together as one class.

Scanning Electron Microscopy (SEM) was performed on a Zeiss DSM 942 to image the internal texture and structures of experimental products (Fig. 4.5). Images were collected in Secondary Electron (SE) mode on carbon-coated samples at different magnifications.

4.3. Results

In the following section, the results obtained from the experiments performed in both experimental setups are presented and evaluated independently. Particle velocities, grain size distributions and textural characteristics of the experimentally produced pyroclasts are presented. In section 4.4, these results are compared and discussed in the context of 2008 Chaitén eruption.

4.3.1 High-T, 0.1 MPa experiments

Explosive fragmentation of samples during High-T, 0.1MPa was observed only for the high H_2O series (1.4 wt.%), at temperatures higher than 874°C (see Fig. 3.7 in previous chapter). This behavior is characterized by a continuous expansion of the sample that is disrupted after (~20–30 s) of foaming when it explosively fragments. Fragmentation always occurred at a stage in expansion at which samples had not reached the equilibrium state. As mentioned in Chapter 3, three out of nine experiments performed at T >874°C did not explode. Nevertheless, the complementary set of experiments presented in this chapter, confirmed their reproducibility and the high-T condition of explosive fragmentation.

Figure 4.4 shows an image sequence of the first 0.22 ms of an explosion captured by high speed imaging. As can be observed in this figure, sample exploded from a central point, breaking into innumerable fragments of different sizes. This fragmentation mode was identified in most of the experiments. However, in two of them, fragmentation started from a side of the samples. This might be a consequence of H_2O content heterogeneities in the sample or the presence of pre-existing internal structures, which could have conditioned the stress distribution.

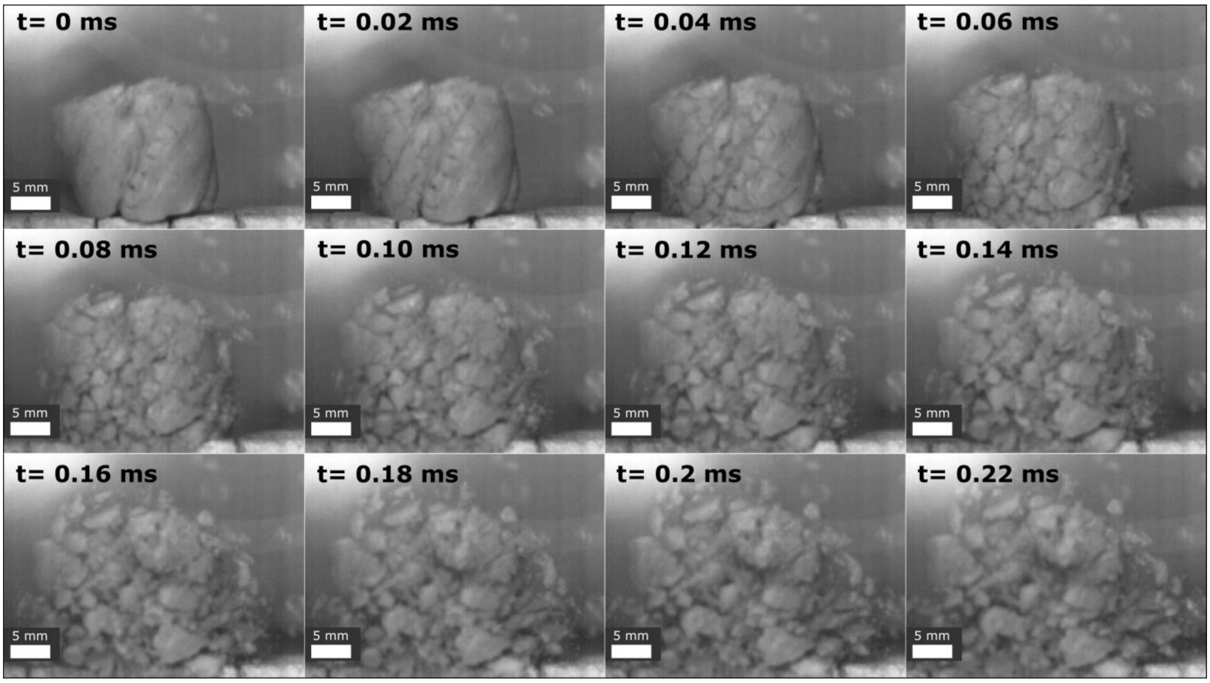

Fig.4.4. Image sequence showing the first 0.22 ms of a high-T, 0.1 MPa fragmentation experiment performed at 897°C (CH_2011_05_21). This video was captured with a NAC HX-3 high-speed camera with a Zeiss 100 mm macro lens that allows for higher frame rate and shutter speed. Frame rate for this video was 50,000 fps. Videos of the complementary set of 0.1 MPa experiments presented in this chapter were recorded by Dr. Jacopo Taddeucci, from INGV (Italy).

The frame-by-frame tracking of sample fragments permitted the calculation of their velocities during the first instants after fragmentation (Fig. 4.5). In all the cases, a non-linear decay of particle velocity was observed, with values becoming asymptotic towards zero after ~3 ms. After 10 ms, the totality of the particles ejected by the explosion were out of the camera visual field. Maximum velocities measured in the experiments ranged from 43 to 58 m s^{-1} (see Table 4.3). No clear correlation between maximum particle velocity and experimental temperature was observed.

The resulting pyroclastic material of these explosions developed rough surfaces with irregular to polygonal cracks (Fig. 4.6A). On the microscopic scale, these clast exteriors comprise microbrecciated surfaces just a few µm's thick (Fig. 4.6C). No glassy rinds were found in the fragments. These samples instead cracked while they were in the expansion stage, confirming that this surface behavior is linked to the samples' growth history rather than post-experiment cooling and contraction. In Fig. 4.6B, the abundance of relatively thin (~2–5 µm) septa between large vesicles (~100 µm average radius) indicates encroachment of neighboring bubbles on one another and consequent melt film deformation between those bubbles (highlighted with white arrows)

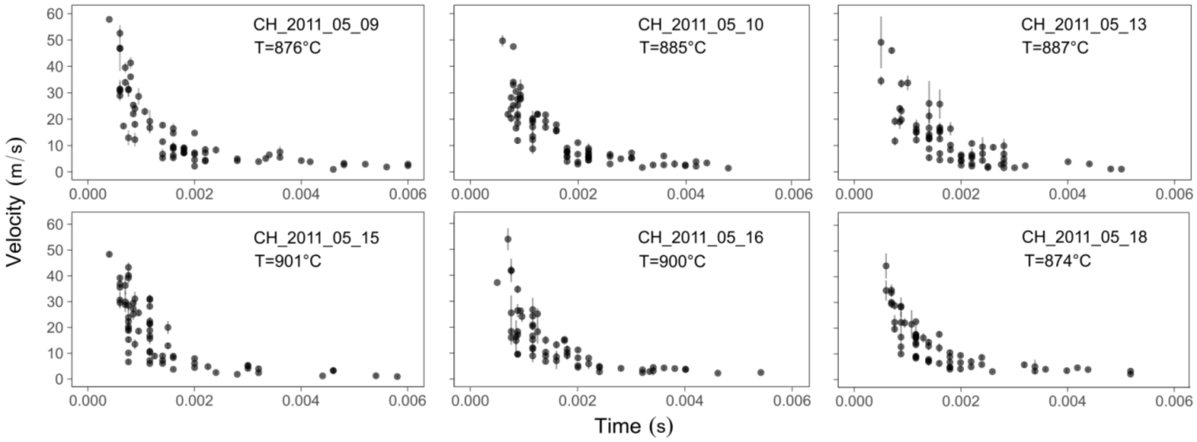

Fig. 4.5. Temporal evolution of particle velocity for the experiments of series CH_2011_05 (1.4 wt. % H_2O) that experienced explosive fragmentation. Each black dot in the plots represents an average velocity based on particle displacement measured in five consecutives frames. Between 50 and 70 particles were tracked for each experiment. Most of the error bars are smaller than related symbol.

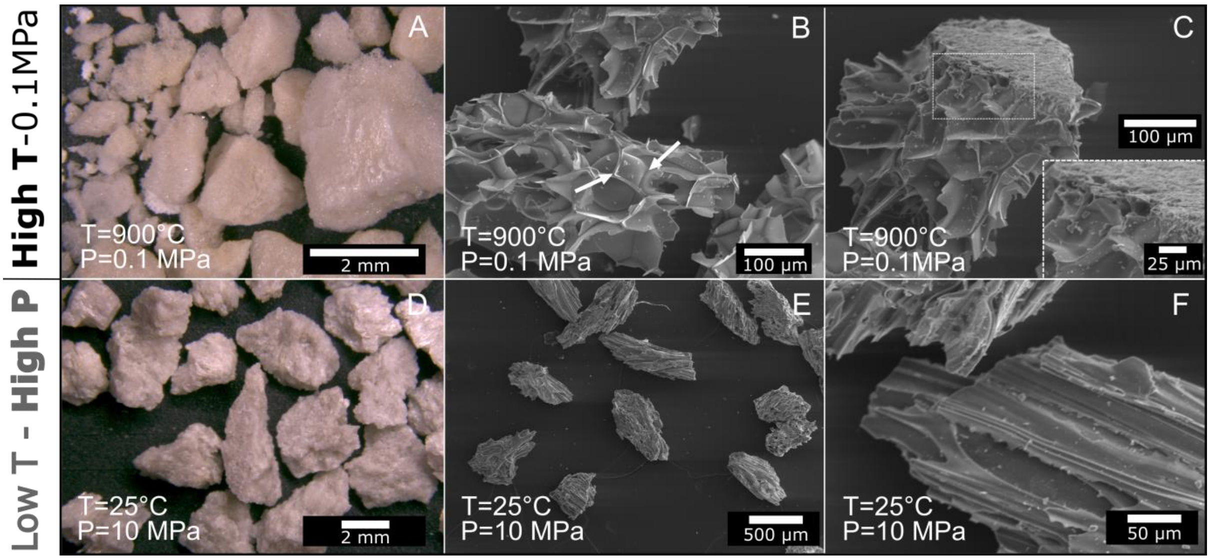

Fig. 4.6. Images acquired with an optical microscope (A and D) and SEM (B–C and E–F) showing surface and internal textures of the products obtained from the two different experimental setups. Image B shows bubbles and septa developed during 0.1 MPa experiments. In (C), the surface texture of an exploded fragment is displayed with the inset view providing high magnification of this rough textured surface Image E and F show the elongated and angular shape of the ash generated in the fragmentation bomb. The close up view of a pyroclast offered by image F, allows for the identification of the original tube porosity.

Figure 4.7 presents the grain size distribution of two experiments performed inside the ash collector. While the experiment CH_2011_05_19 (blue histogram) shows a defined non-Gaussian particle size distribution, a similar trend cannot be clearly identified for the case of experiment CH_2011_05_20 (pink histogram). In particular, a strikingly high value of the class Φ = 3 can be identified, which might be attributed to the fragmentation mode showed by this particular experiment. Unfortunately, the lack of material (i.e., obsidian bomb with H_2O = 1.4 wt.%) precluded repetition of the experiment to check reproducibility. Another limitation for the analysis of the grain size distribution of the high-T, 0.1 MPa experiments is the small amount of material used (<0.8 gr). On the positive side, the ash collector showed a material recovery capacity >95%, which makes it attractive for future experiments.

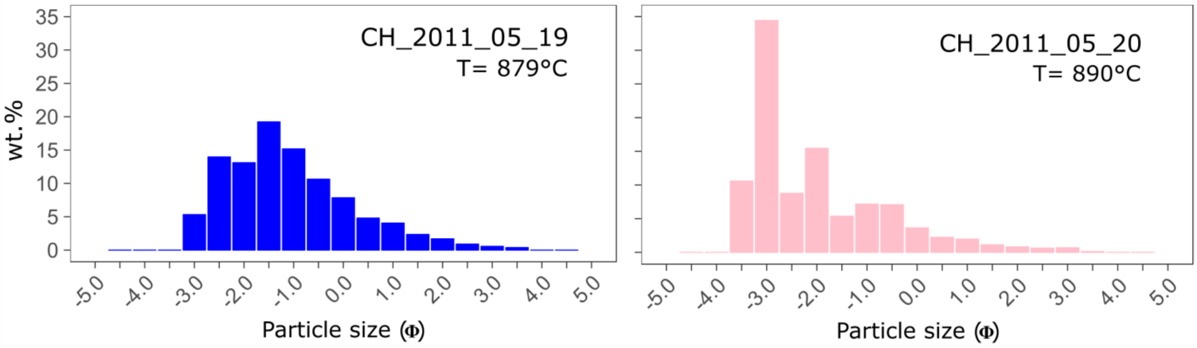

Fig. 4.7. Grain-size distribution of two high-T, 0.1 MPa experiments performed inside the ash collector. The height of the columns represent the wt.%-values for each sieving class. Φ = 4.5 represents all the material <0.06 mm.

4.3.2 High-Pressure experiments

All the samples exposed to rapid pressure differentials at the selected experimental conditions (Table 4.2) experienced explosive fragmentation. Once the set of diaphragms are disrupted and the pressurized autoclave is linked to the low-pressure tank, the sample is exposed to a sudden pressure drop. If this pressure differential is higher than the sample fragmentation threshold (see Spieler et al., 2004), the sample will fragment. As a consequence, the resultant gas-particle mixture is ejected in the low-pressure tank (Fig. 4.8). In all the experiments, the gas stored above the sample was the first phase to be observed in the camera field of view. The gas phase is visible due to condensation under illumination. Depending on the experimental conditions, the first particles were identified between 3.5 and 7.9 ms after the gas front was detected. For all the cases, the highest concentration of particles was observed during the first ~15 ms of the experiment.

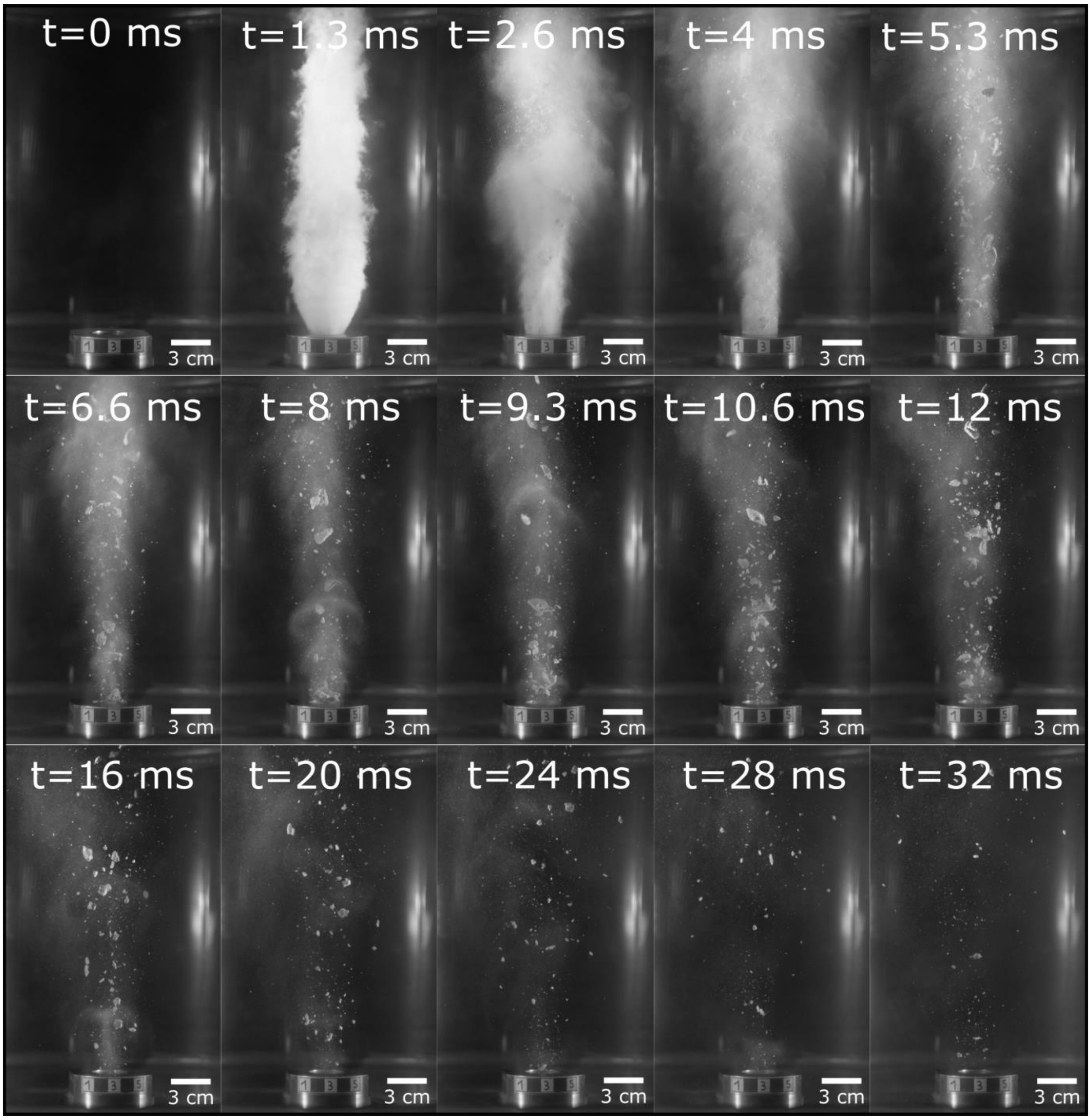

Fig. 4.8. Sequence of still-frames showing the first 32 ms of a high-P, low-T experiment performed in the fragmentation bomb. High-speed imaging at 10,000 fps allowed for the observation, first of the outflow of the gas front and then the gas-particle mixture. After 12 ms, most of the gas was released. Specific conditions for this experiment were 10 MPa and 25°C (experiment CH_P2_7).

Fig. 4.9 and 4.10 show particle exit velocity vs. time for a combination of experimental parameters. The maximum velocities measured range from 151 to 234 m s^{-1}, with the highest velocity values recorded always at the onset of the experiment. As in the case of the high-T, 0.1MPa experiments, a non-linear decay of particle velocity is observed. However, in these experiments the decay time was longer, with values becoming asymptotic towards zero after ~20 ms. Decay time and the shape of the velocity curve are slightly different for each experiment, depending on the combination of experimental variables considered. Nevertheless, in all the cases particle velocity decay time was larger than for the

0.1 MPa experiments. When the velocity vs. time curves of both types of experiments are compared (high-P vs 0.1 Mpa), although their overall shape is the same, the curve defined by the cluster of individual particle velocity measurements is more scatter for the 0.1 MPa experiments (Fig. 4.5) This might be a consequence of the experimental setup characteristics. While in the fragmentation bomb the particles travel all in one direction and can be tracked once they are ejected through the vent, in the furnace experiments the fragments expand radially, making it difficult to establish a common starting point to measure their velocities.

In Fig. 4.9, the velocity evolution of ejected pyroclasts is evaluated as a function of pressure and temperature. Higher particle peak velocities were measured for higher initial pressure differentials (i.e., ΔP). When experiments presenting the same initial pressure are compared, the highest velocities are observed at higher temperature. These results are in agreement with the ones reported by Martel et al. (2000) and, more recently, by Cigala et al. (2017). The effect of sample initial length in the observed velocity was also evaluated (Fig. 4.10). Results show that higher velocities are obtained when longer cylinders are used. As in Fig. 4.9, the same effect of initial pressure on particle velocities can be recognized. Regarding the texture of the experimental products, fragments exhibit plate-like shapes (Fig. 4.6D-F). This shape was already observed in several previous studies performed in the fragmentation bomb (e.g., Alidibirov and Dingwell, 1996a; Martel et al. 2000) and is a consequence of the fragmentation mechanism operating during sample disruption (Alidibirov and Dingwell, 2000). Experimental pyroclasts preserve the original tube-pore morphology and show angular outlines (Fig. 4.6F), confirming sample brittle response to sudden decompression.

Grain size distributions of the pyroclastic material generated during the instantaneous decompression experiments were also analyzed (Fig 4.11 and 4.12). Results are evaluated considering the same experimental parameters that were considered for the analysis of particle exit velocities (Fig. 4.9 and 4.10). As a common feature, all the grain-size plots exhibit a non-Gaussian particle size distribution. In addition, the histograms show that higher experimental pressures produce larger amounts of ash, as well as a decrease in the grain-size of the most abundant particle class. Similar results were reported by Kueppers et al. (2006) in a study in which the authors explored the fragmentation efficiency of explosive eruption with a similar experimental setup that the one used here. Regarding the effect of temperature, in Fig. 4.11 it is possible to recognize a reduction of the coarsest pyroclastic fraction when experimental temperature is higher. This was reported also by Aldibirov and Dingwell (1996a). Grain size distributions analysis of the experiments in which the sample length was modified (Fig. 4.12) show that Mdϕ was lower in those cases in which used cylinder were shorter. A lower Mdϕ implies a larger grain size reduction. However, this trend is not as clear as the previously described (P-T related).

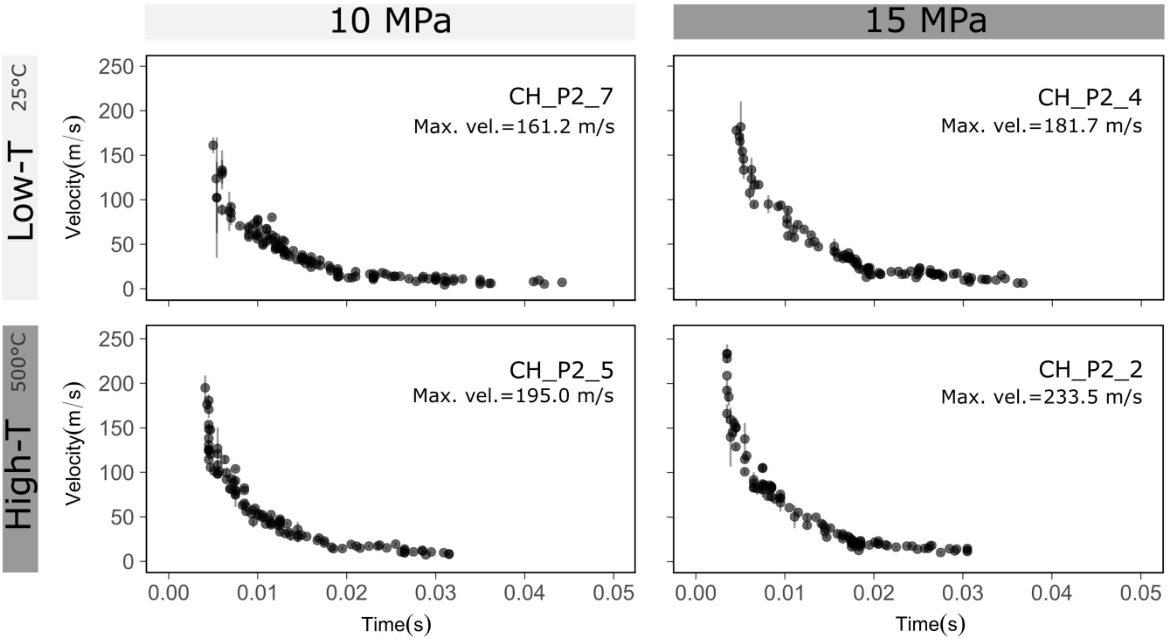

Fig. 4.9. Temporal evolution of particle velocity for a series of experiments performed in the fragmentation bomb at variable P-T conditions, and constant sample length (60 mm). Between 100 and 120 particles were tracked per video covering the entire duration of particle ejection. Most of the error bars are smaller than related symbol.

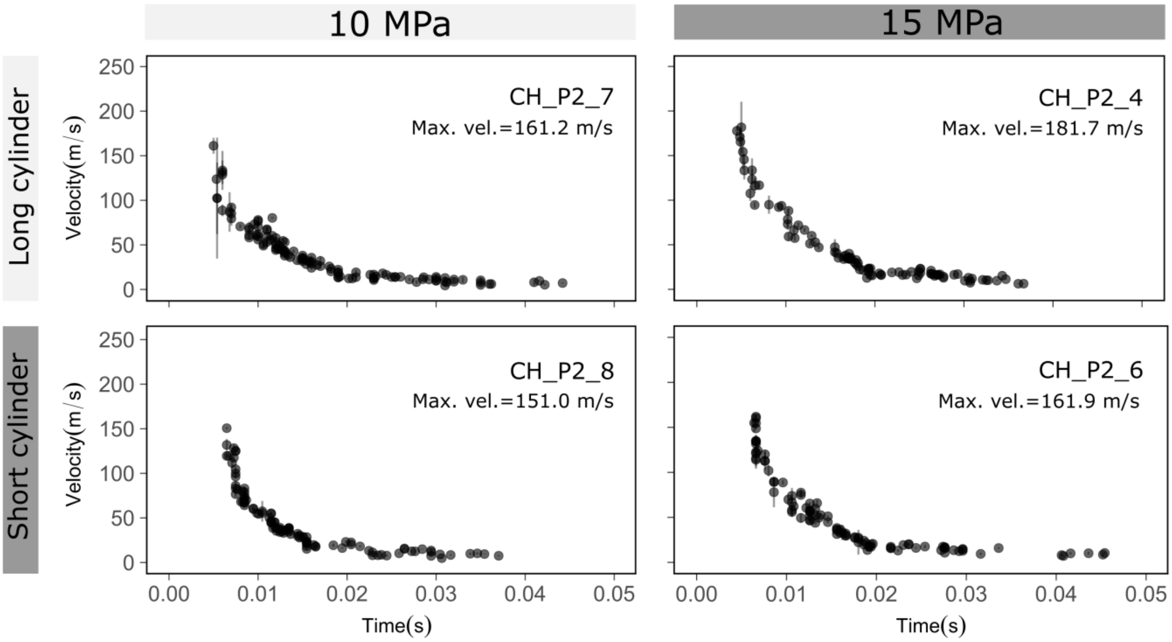

Fig. 4.10. Temporal evolution of particle velocity for a series of experiments performed in the fragmentation bomb at variable P and sample length (60 mm), and constant temperature (25°C). Between 100 and 120 particles were tracked per video covering the entire duration of particle ejection. Most of the error bars are smaller than related symbol

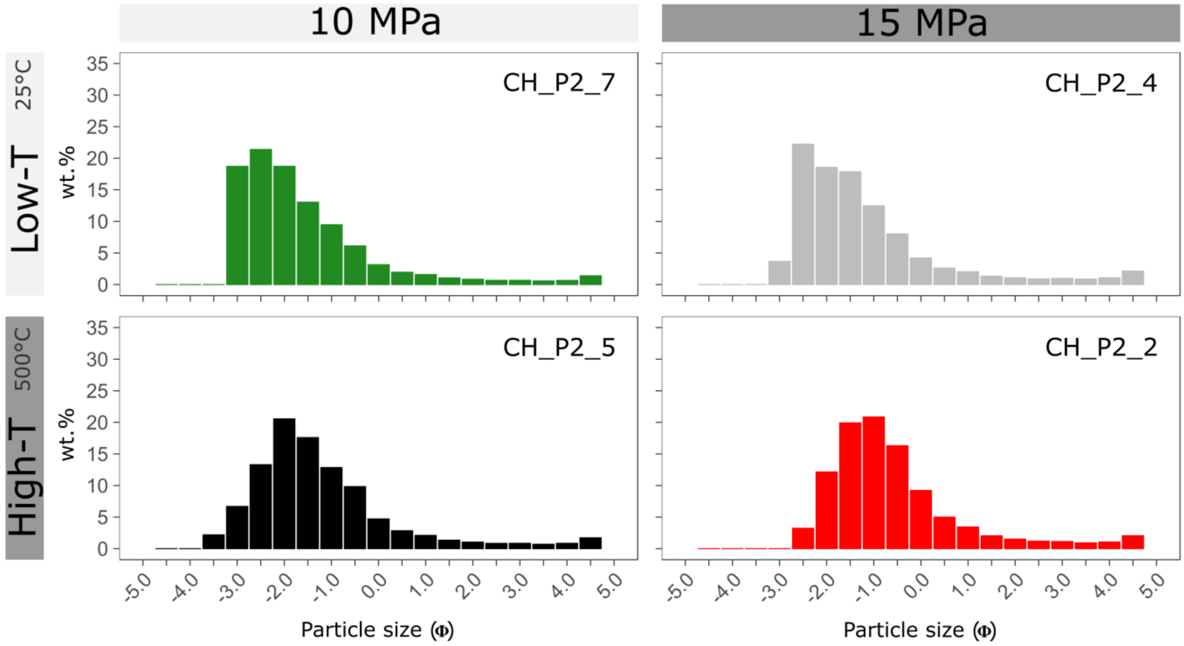

Fig. 4 .11. Grain-size distributions for a series of experiments performed in the fragmentation bomb at variable P-T conditions and constant sample length (60 mm). The height of the columns represent the wt.%-values for each sieving class. Class Φ = 4.5 represents all the material <0.06 mm. Temporal evolution of particle exit velocity of these experiments is presented in Fig. 4.9.

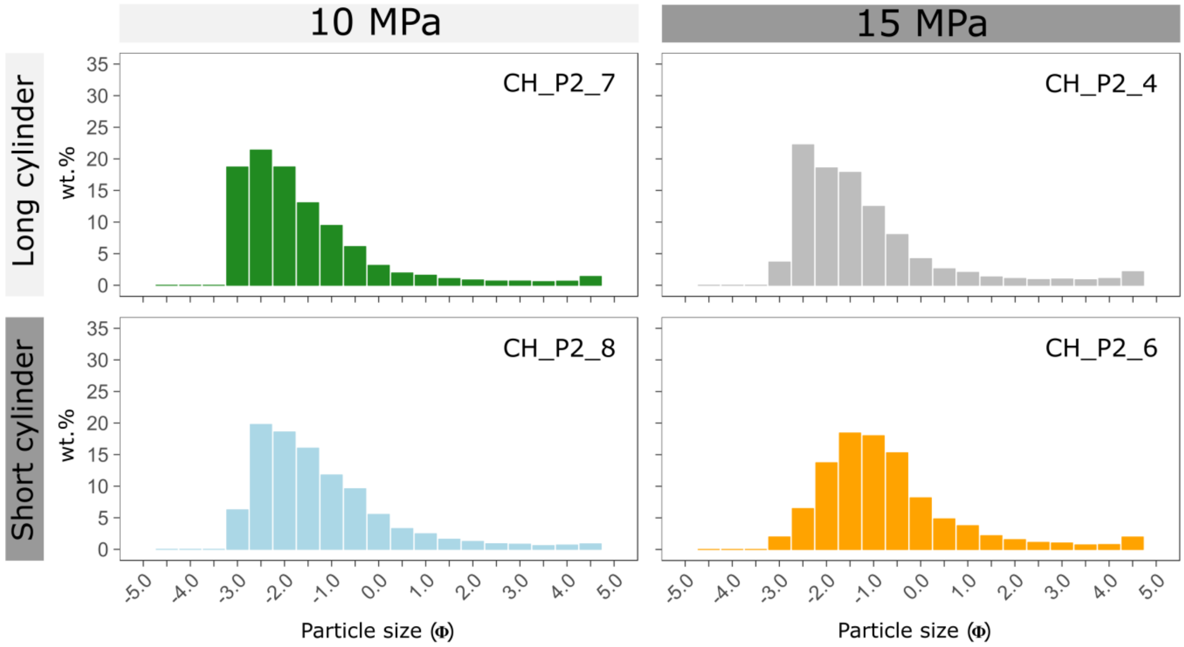

Fig.4 .12. Grain-size distributions for a series of experiments performed in the fragmentation bomb at variable P and sample length (30–60 mm), and constant temperature (25°C). The height of the columns represent the wt.%-values for each sieving class. Class Φ = 4.5 represents all the material <0.06 mm. Temporal evolution of particle exit velocity of these experiments is presented in Fig. 4.10.

4.4 Discussion

The high temperature-0.1 MPa experiments provide an unprecedented view of fragmentation at eruption-relevant temperatures and H_2O contents. During these experiments, sample fragmentation was induced as a consequence of bubble growth. This mechanism differs from the one simulated with the fragmentation bomb, in which sample disruption is driven by the rapid release of the gas externally introduced. In the following section, this finding is discussed and interpreted in the context of existent fragmentation theories. After that, the results of both set of experiments are compared and discussed in the framework of 2008 Chaitén eruption.

4.4.1. High Temperature-0.1 MPa experiments

4.4.1.1 From Foam to Fragments: why samples of the 1.4 wt.% H_2O series explode?

As discussed in Chapter 3, it is both the absolute H_2O content and the time evolution of bubble vapor pressure (i.e., the expansion rate), moderated by temperature, that are critical for driving fragmentation during the experiments. Because there appears to be a very clear decompression rate dependence on explosive fragmentation in our experiments (see discussion below), brittle behavior is interpreted to stem from the exsolution and expansion of retained magmatic H_2O. This, in turn suggests that bubble growth, driven by internal vapor pressure, imposed sufficiently high strain rates to push the melt's deformation response into the brittle field (e.g., Dingwell, 1996; Papale, 1999; Gonnermann and Manga, 2003). Indeed, many eruption models consider that silicic melts behave viscoelastically under stress, that is, they may cross the glass transition when sufficiently high rates of deformation (e.g., Dingwell and Webb, 1989; Dingwell, 1996).

As shown by Papale (1999) and more recently Gonnermann and Manga (2003), the viscous-to-brittle transition can be predicted by the Maxwell relation:

$$\frac{dv_z}{dz} > k\frac{1}{\tau} = k\frac{G_\infty}{\eta_s} \quad (4.1)$$

where *dv_z/dz* is the elongational strain rate ($\dot{\gamma}$), *k* is a constant that assumes a value of 0.01 and corrects for the onset of brittle magma failure and τ is the melt's structural relaxation time, defined as the quotient of the relaxed melt shear viscosity (and the shear modulus (G_∞). G_∞ is assumed to be constant at $\log G_\infty = 10 \pm 0.5$ (Dingwell and Webb, 1989). In principle, when the elongational strain rate is greater than the last term on the right hand side of equation 4.1, the so-called relaxation rate (τ^{-1}), fragmentation will occur.

In order to confirm that the brittle threshold was exceeded, bulk elongational strain rates, $\dot{\gamma}$, was estimated by video analysis of 0.75, 0.97 and 1.4 wt.% H_2O experiments and compared them to the theoretical melt relaxation rates (τ^{-1}) that dictate the brittle fragmentation criterion (Eq. 4.1; Fig. 4.13). Elongational strain rates were determined by dividing the horizontal change in length (i.e., l_f-l_i) of foamed samples by the initial lengths (l_i) to achieve a fractional elongational strain value and in turn, divided this value by total growth time determined from A/A0 vs. t curves (Fig. 3.6). Analysis of expansion behavior in videos, namely tracking of the velocities of the sample margins along three directions shows that the direction of measurement is unimportant in that tests of the horizontal, vertical, and head-on diagonal growth velocities are all within a factor of two of one another. As the H_2O contents of the samples at the time of fragmentation were not known *a priori*—fragments were too small to be analyzed by FTIR and KFT—melt relaxation rates were calculated for exploding clasts using a range of viscosity values consistent with H_2O contents between ~1.0 and 0.05 wt.% H_2O. The lower limit for τ^{-1} in non-exploding experiments was calculated by assuming that these samples equilibrated to 1 atm pressure, which employs a melt viscosity consistent with very low H_2O at T-0.1 MPa (~0.05 wt.%; Ryan et al., 2015).

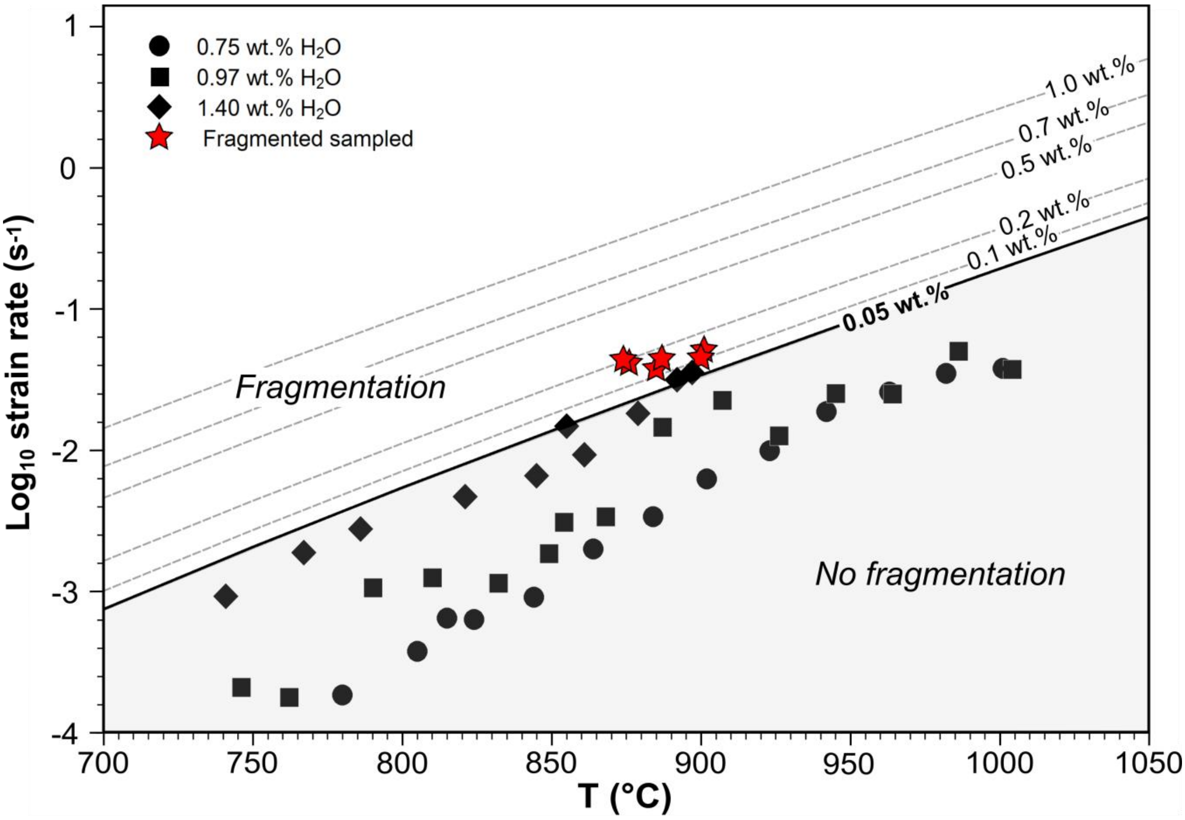

Fig. 4.13. Elongational strain rates measured derived from observed sample expansion rates (see text) for intermediate and high H_2O experimental series. Red stars represent samples that explosively fragmented. Uncertainties in both temperature and strain rate are less than the size of the symbols (~10% of the measurement). Solid black and dashed grey lines represent melt relaxation rates calculated based on Chaitén rhyolite melt viscosity derived from composition in Table 2 and for different H_2O contents. The bold black line (at 0.05 wt.% H_2O) divides the fields where explosive fragmentation and foaming + equilibrium (No fragmentation) are expected to occur.

According to Fig. 4.13, which plots experiment elongational strain rates versus temperature, samples that explosively fragmented had strain rates in excess of the predicted threshold for melts with 0.1 to 0. 2 H_2O wt.%. This result is consistent with independent fragmentation predictions based on conduit models (Gonnermann and Manga, 2003). The non-fragmenting obsidians (with 0.75 and ~1 wt.% H_2O) expanded at strain rates one to two orders of magnitude lower.

Another implication of the results shown in Fig. 3.14 is that explosively fragmented experimental samples should have residual H_2O contents between 0.1 and 0.2 wt.%. While these values appear low compared to average H_2O contents (~0.7 wt.%) measured in natural Chaitén Plinian pumice (see Chapter 2), they are consistent with the relatively higher experimental temperatures that yielded them. For example, if the strain rate values experienced by these fragmented samples are extrapolated to the 0.7 wt.% H_2O relaxation rate curve, associated T's are between 785 and 805°C, very much in line with estimates of with Chaitén's 2008 eruptive T (780–825°C; Castro and Dingwell, 2009). This is further discussed in Chapter 6.

Bubble-scale strain during thinning of the melt films between adjacent bubbles provides an independent check on the critical strain rates needed to fragment the sample and can link bubble-scale growth to strain localization leading to fragmentation. Stretched inter-bubble melt films are abundant in the exploding samples (Fig. 4.5B). As bubbles get close to one another they begin to interact and exert strain on the melt between them (Fig. 4.5B; Castro et al., 2012b). In this way, the stretching of the melt film is coupled to the growth of the bubbles. To assess deformation rates in inter-bubble melt films, the melt-film thinning model of Castro et al (2012b) was used, which relates the bubble growth rate to a film stretching rate (cf. Fig. 7 in Castro et al., 2012b). This method requires an estimate of the bubble growth rate for two equal-sized bubbles that are in contact with one-another and exerting elongational strain on an inter-bubble melt film. An average bubble growth rate was assessed by using the mean bubble radius (R) measured on CT scans of a high water content experiment (Fig. 3.10) and this value (~100 µm) combined with the average time to explosion (t ~20 sec) yields a growth rate of about 4 µm sec^{-1}. Results of the model reveal that inter-bubble melt films would have experienced strain rates on the order of 10^{-1} to 10^{-2} s^{-1}, which is entirely consistent with strain rate estimates derived from the bulk expansion rates of vesiculated samples.

Finally, It was noted that while fragmentation could also occur by bubble overpressure exceeding the tensile strength of magma (Alidibirov and Dingwell 1996; Spieler et al., 2004), which for crystal poor bubble-bearing rhyolite at eruptive conditions has been estimated about 5 to 10 MPa (Martel et al., 2000, 2001), the lack of explosive fragmentation in low-temperature yet hydrous foaming experiments means that this mechanism may have been of second order importance.

4.4.1.2. Foam expansion as an analogous of magma decompression

When natural obsidians with variable H_2O content are heated at temperatures above their glass transitions, H_2O exsolves and samples vesiculate. Together, diffusion and bubble expansion drive P-V (i.e., pressure-volume) work that the bubbly melt does against the atmosphere by foaming. Vesiculation is, for all intents and purposes, analogous to the decompression that occurs in natural volcanic conduits when bubbly melts rise or when individual pyroclasts expand after fragmentation events (Kaminski and Jaupart, 1997; Castro et al., 2012b). Therefore, it might be valuable to calculate the decompression rates that operated during the experiments.

As it is not possible to know the exact pressure evolution of bubbles (see discussion in Chapter 3), it is difficult to constrain a critical fragmentation-inducing decompression rate. It might be important, however, to estimate and compare the decompression rates for the intermediate (0.75 and 0.97 wt.%) and high (1.4 wt.%) H_2O series. Assuming a linear decompression rate, an initial and final pressure value need to be considered. The initial overpressure is assumed to be the solubility-controlled P-H_2O (Newman and Lowenstern, 2002), while final pressure assumes two different values. For the samples that did not explode (and reached equilibrium conditions), a final pressure of 0.1 MPa was assumed. For the exploding samples of the 1.4 wt.% series, a final (pre-fragmentation) pressure of ~2.5 MPa was estimated. In order to estimate the overpressure developed in the samples at the moment of fragmentation (1.4 wt.%; T ≥874°C), a reformulated version of Turcotte et al. (1990) equation by Taddeucci et al. (2004) was applied:

$$V = (nRT)^{0.5}\ln\left(\frac{P_{frag}}{P_{atm}}\right) \quad \text{(Eq. 4.2)}$$

where V is the pyroclast exit velocity, n is the mass fraction of exsolved volatiles, P_{frag} is the pressure at fragmentation; P_{atm} is the atmospheric pressure; R is the specific gas constant and T is temperature. Based on the concept that maximum pyroclast velocities at the conduit oulet during an explosive eruption is mainly controlled by pressure difference between the gas in the bubbles and the atmosphere, Turcotte model (and others, for example, Wilson, 1980, Woods, 1995; Alatorre-Ibargüengoitia et al., 2010) were developed to quantify this overpressure.

Maximum pyroclast velocities were measured by video analysis (Fig. 4.6), while R assumes a value of 461 J Kg^{-1} K^{-1} for H_2O. A value of 1.2 wt. % of exsolved H_2O ($n = 0.012$) was considered for the calculations based on sample residual water content estimated in Fig. 4.13. Overpressures (i.e., the fragmentation minus atmospheric pressure) obtained for our experiments are in the order of 0.1 MPa (Table 4.3). It is important to note that this is a conservative value because it was assumed that the samples experienced no leak during their growth prior fragmentation. On the other hand, if a scenario in which most of the gas escaped from the sample is assumed (through crack and fractures) almost immediately after its exsolution (n = 0.001), overpressures expected in the samples are in the order of 0.8 MPa.

Table 4.3. Sample overpressures (minima) estimated for the moment of fragmentation

Experiment	Temperature (°C)	Max. velocity (m/s)	P_{frag} (MPa)	ΔP (MPa)
CH_2011_05_09	876	58	0.21	0.11
CH_2011_05_10	885	50	0.19	0.09
CH_2011_05_13	887	49	0.18	0.08
CH_2011_05_15	901	47	0.18	0.08
CH_2011_05_16	900	53	0.19	0.09
CH_2011_05_18	874	43	0.17	0.07

Although the model of Turcotte et al. (1990) was developed for Vulcanian explosions, the fact that it does not consider the presence of a rigid caprock, together with the assumption that particles remain in thermal equilibrium, make it suitable for the 1-atm experiments presented here. Note that the samples do not exhibit a hard exterior shell (Fig. 4.5.C) akin to a caprock and are subject to constant temperature at the time of expansion and explosion. However, it should be recognized that the calculations here provided, are absolute *minimum* values. Alatorre-Ibargüengoitia et al. (2010) postulated that some of the energy in the overpressurized bubbles will in fact be partitioned into energy required to rupture the melt. Furthermore, these authors proposed that the pressure prior to magma disruption ($P_{pre\text{-}frag}$) can be estimated by considering this value as the sum of the effective pressure (P_{frag}) available for particle ejection and the fragmentation threshold (P_{th}) of the magma. This latter value can be derived from the equation proposed by Spieler et al. (2004), which relates effective tensile strength (σ) and porosity (ϕ) ($P_{th}= \sigma/ \phi$). For the case of these experiments, P_{th} ranges between 2.3 and 2.5 MPa. The sum of calculated P_{th} and P_{frag} pressures yields $P_{pre\text{-}frag}$ values ranging from 2.4–2.6 MPa. These values, along with P_{frag} (derived from particle velocities), bracket the range of possible final overpressure (pre-fragmentation). For P_{th} estimations, a final porosity values of 80-85% is considered and an effective tensile strength of 2MPa assumed (Spieler et al., 2004; Alatorre-Ibargüengoitia et al., 2010). Porosity was measured with a density determiner water pycnometer (Fig. 3.9) and confirmed by 2D image analysis on image slices extracted from CT stacks.

Once initial and final pressure were estimated, they were then divided by a decompression timescale, which it was taken as the duration of the parabolic growth segment assessed graphically on sample expansion curves (see Navon et al., 1998; section 3.4.2.). In this way, a maximum decompression rate leading to fragmentation was estimated. These estimations assume that the bubbles initially formed with the full H_2O complement in the melt phase. These calculations yield a range of decompression rate for the exploding samples of about 0.5–1.2 MPa sec^{-1} (Fig. 4.14).

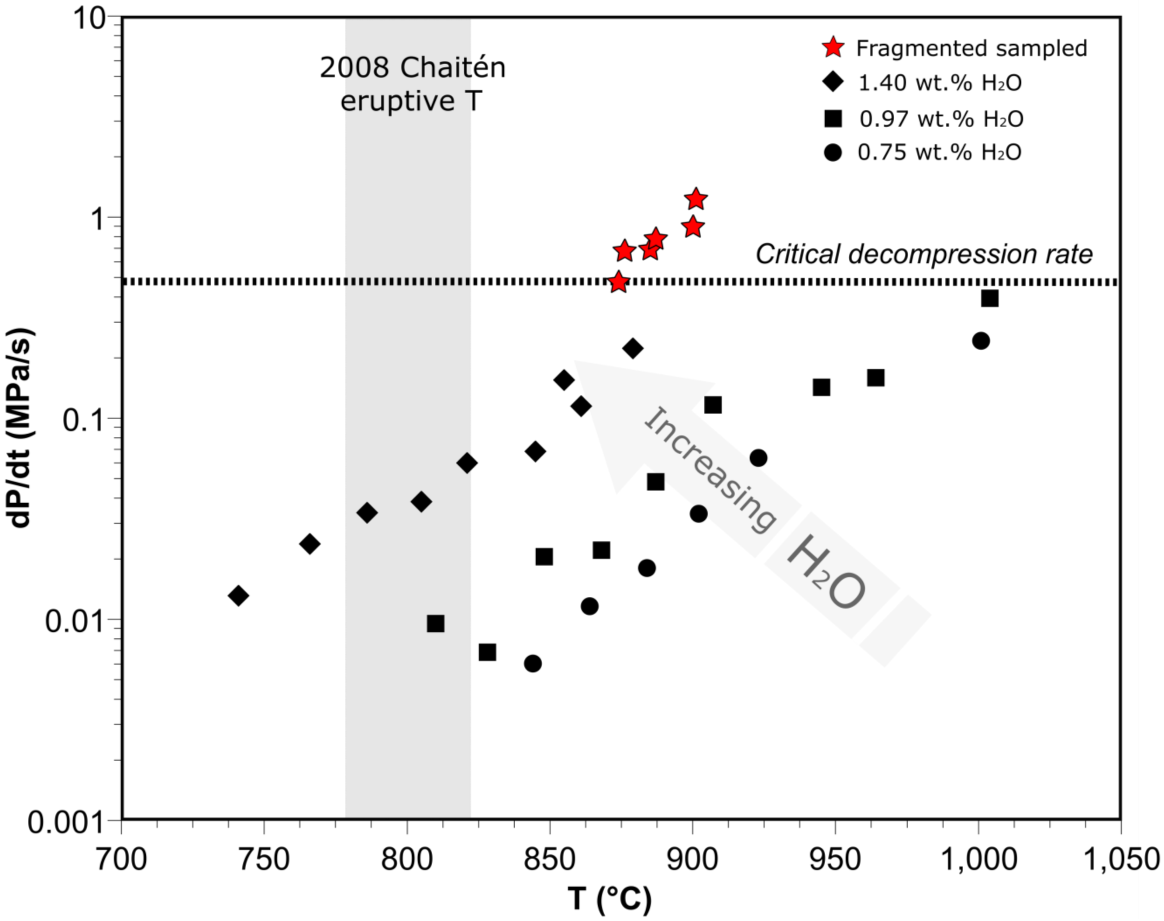

Fig. 4.14. Calculated decompression rates for representative experiments of intermediate and high-H_2O series. Red stars represent samples that explosively fragmented. Dashed black lines represent the critical decompression rate necessary for sample to explosively fragment. The dark grey area represents the range of eruptive temperatures estimated for 2008 Chaitén eruption by Castro and Dingwell (2009). Uncertainties in both temperature and decompression rate are less than the size of the symbols. See text for description of decompression rate calculations.

By comparison, the decompression rates for non-exploding, low-T experiments of the 1.4 wt.% series, are about an order of magnitude smaller. These results demonstrate that even though a parcel of melt may be significantly hydrous, it may not explode during foaming due to slow and effectively restricted expansion and consequently not exceeding a critical decompression rate. However, as rhyolite magmas often contain several wt.% H_2O prior to eruption (e.g., Castro and Dingwell, 2009), and therefore are much more hydrous than our experimental samples, critical decompression rates may in fact be achieved at lower eruption temperatures than implied by our experiments. Clearly, in addition, magma parcels with >2 wt.% H_2O would potentially fragment as well, provided they are subject to a large enough pressure gradient to foster high decompression rates. These results corroborate the finding that elongational strain rates of exploding versus non-exploding samples also differ by at least an order of magnitude.

4.4.2 Fragmentation experiments and the 2008 Chaitén eruption

As shown in section 4.3.1, particle velocities observed in the fragmentation bomb experiments are influenced by several parameters. By modifying the initial experimental conditions (i.e., temperature, pressure and sample length), differences in the maximum velocities up to 90 m s^{-1} were obtained. The highest maximum velocity was measured in the experiment performed at 500°C, initial overpressure of 15 MPa and sample length of 60 mm. Nevertheless, despite the differences observed, all these velocities are at least 100 m s^{-1} higher than the ones obtained during the high-T, 0.1 MPa explosions (Fig. 4.15).

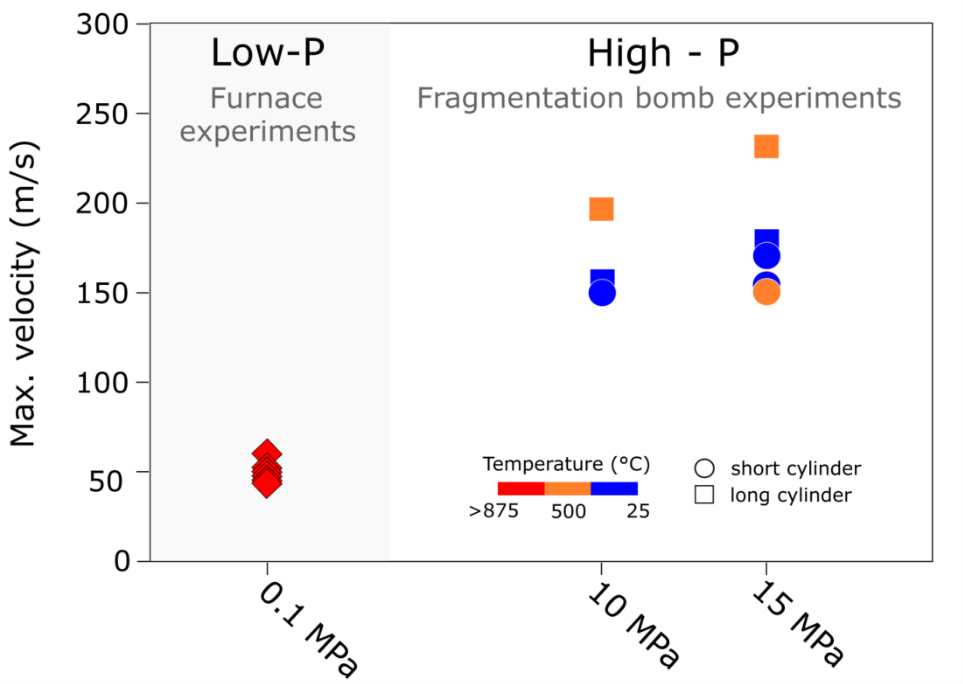

Fig. 4.15 Comparison between maximum particle velocities obtained for the different experimental setups. The x-axis is not scaled.

Together with the differences in particle velocities, it is important to notice that these experimental setups simulate two different fragmentation mechanisms. The fragmentation bomb experimental apparatus, first used by Alidibirov and Dingwell (1996a) to explore the fragmentation behavior involved in 1980 Mount St. Helens eruption, has become a well-established setup to investigate fragmentation due to bubble overpressure triggered by rapid decompression. On the other hand, the experiments performed at JGU provide a view of brittle fragmentation induced by volatile exsolution and bubble growth, which so far, had been only simulated with numerical models (e.g., Papale, 1999; Polacci et al., 2004). This prompt the question: which of these experiments, if any, is representative of the explosive activity observed during 2008 Chaitén eruption?

The initial pressures (10 and 15 MPa) selected to perform the experiments in the fragmentation bomb are in the range of the initial overpressure estimated (solubility-controlled P-H_2O; Newman and Lowenstern, 2002) for the 0.1 MPa experiments that experienced explosive fragmentation. At the same time, H_2O content of the samples used for the 0.1 MPa experiments are representative of the values observed in the deposits (Chapter 2). Therefore, experimental conditions of both sets of experiments are within the range of P-H_2O conditions of 2008 Chaitén eruption. Regarding temperature, it is important to note that the highest temperature used in the fragmentation bomb experiments is below the eruptive temperatures estimated by Castro and Dingwell (2009) (750–825°C). As shown in this and previous studies (e.g., Cigala et al., 2017), particle velocity increases with temperature. Thus, the velocities estimated here provide a minimum velocity value for the velocities expected in 2008 Chaitén eruption. Regardless the differences between experimental and eruptive temperatures, and consequent variation in the velocities (and GSD), experimental conditions of both sets of experiments and their results still reproduce two different fragmentation mechanisms and can be used to better understand the fragmentation dynamic during Chaitén eruption

Alfano et al. (2012) explored the eruptive dynamics of Chaitén eruption by analysing the textural characteristics of lapilli-size pumices erupted during the 6 May, 2008, climatic phase. In their study, the authors reported bulk porosity ranging between 43 and 80%, with relative open porosity varying between 70 and 86% of these values. According to aspect ratio measurements, vesicles show a high degree of elongation and modal diameter between 50 and 80 µm while estimated BNDs are in the order of $9x10^4$ to $1.3x\ 10^5$ mm^{-3}. In this sense, the pumice used in the fragmentation bomb experiments is representative of the material erupted during the early stages of 2008 Chaitén eruption. Based on these textural features, Alfano et al. (2012) suggested that vesiculation was homogenous, occurred over a very short time and relatively late during magma ascent. The authors propose that vesicle nucleation and growth was virtually inhibited by magma fast ascent—enabled by its low viscosity—and the absence of microcrystals, allowing large portions of the magma body to reach shallow crustal levels highly saturated in water. Once the magma reached shallow levels, the presence of the pre-2008 lava dome acted as a plug, causing pressure to increase. Its failure triggered homogeneous vesiculation, the built up of overpressure in the bubbles and finally magma fragmentation. This hypothesis of early explosive eruptive stages characterized by dome disruption, sudden magma decompression and consequent violent explosions is also supported by the large amounts of lithic fragments (~80%) in the deposits described by Alfano et al. (2011).

In this scenario, fragmentation bomb experiments appear to be the most suitable to reproduce the fragmentation mechanism dominant during the Plinean phase of the eruption. By using the BND (Bubble Number Density) decompression rate meter method developed by Toramaru (2006), Alfano et al. (2012) estimated decompression rates between 8 and 12 MPa s^{-1}, with fragmented mixture (gas + particles) exit velocity between 330 and 1180 m s^{-1}. The experiments performed at the fragmentation bomb suggest that velocities of individual pyroclasts might have been significantly lower. As discussed earlier in this chapter, the ideal maximum velocity reached by the fragments at the conduit outlet depends mainly on the pressure differential between gas and atmosphere and on the initial amount of volatiles. Unfortunately, the data collected about obsidian bombs in the field is not enough to validate the results obtained in the experiments with any of the available models (e.g., software EJECT! by Mastin (2001)).

When pumice textural characteristics reported by Alfano et al. (2012) are compared with the products of the 0.1 MPa, High-T experiments, the latter show higher porosity (5 to 15%), larger bubbles (mode = 90 µm) and lower BDN (~10^3 mm^{-3}). All these characteristics are in agreement with a scenario dominated by heterogeneous nucleation, as postulated in the previous chapter (section 3.4.1). At the same time, it is worth noting that decompression rates associated with samples that fragmented explosively are one order of magnitude lower than values obtained by Alfano et al. (2012). This might also help explain the differences in bubble sizes observed. In this sense, it is expected that samples with higher initial H_2O contents than the one used here, would experience higher decompression rates and, therefore, form smaller bubbles.

Due to its experimental design, the 0.1 MPa, high-T experiments can shed light on low-pressure degassing environments. This includes tuffisites, which are active pyroclastic channels that cross-cut magma-filled volcanic conduits and enable outgassing of magma to the atmosphere (Tuffen et al., 2003). The opening and closing of tuffisites may impose intermittent pressure drops of (1–15 MPa) on the hydrous melt, and tuffisite’s vertical connectivity (to 500 m; Castro et al., 2014), suggests that melt parcels would indeed be subject to rapid decompression to atmospheric levels. Evidences of these degassing structures are ubiquitous in Chaitén bombs and also in the obsidian lava dome (Castro et al. 2012a).

In summary, experimental and field evidence suggest that both fragmentation mechanisms might have been responsible of the explosive activity observed during 2008 Chaitén eruption. During the initial explosive phase, fast ascent of “crystal-free” magma, together with the progressive failure of the pre-existing lava dome and consequent exposure of magma to sudden pressure drops, might have conspired to trigger magma fragmentation due to bubble overpressure. As the eruption progressed, slower ascent rate might have enabled the formation of microlites, promoting heterogeneous bubble nucleation. In addition, degassing might have favoured shear-induced magma fracturing, leading to the occurrence of tuffisites. These pyroclastic channels, in turn, facilitated the exposure of still hydrous melt parcels to low pressure, contributing to a scenario in which fragmentation occurred due to strain rates (bubble growth-related) exceeding melts relaxation rates. Recent findings of Wadsworth et al. (2018) support this eruption evolution. The authors predict that during early stages of the eruption, magma behaviour resided in the viscous field. As a consequence, conduit-scale shear fracturing was not likely to be a dominant component during the initial Plinian explosive activity. Instead, they suggest fragmentation due to bubble overpressure as the dominant mechanism. As the eruption progressed, and magma degassed, the eruption transitioned into a mixed viscous-brittle regime and ash generation occurred simultaneously with the emplacement of a lava dome.

4.5 Conclusions

Two different fragmentation mechanisms were simulated by using the experimental setups at JGU and LMU. While in the fragmentation bomb (LMU) magma fragmentation is caused by gas overpressure exceeding melt tensile strength (e.g., Spieler et al., 2004), the 0.1 MPa experiments performed at JGU shed light on fragmentation mechanisms in which magma disruption is a consequence of strain rates directly stemming from bubble growth overcoming the structural relaxation timescale of the melt (e.g., Papale, 1999).

The 0.1 MPa, high-temperature experiments provide the first observations on explosive fragmentation due to experimental vesiculation of hydrous rhyolite melt at eruption-relevant temperatures and H_2O contents. Samples with initial H_2O contents of 1.4 wt.% exposed to T’s >874°C will expand at sufficiently high rates to explosively fragment. Image analysis permitted the estimation of associated strain and decompression rates that lead to magma fragmentation. On the other hand, even though the experiments at LMU do not yield novel results, the widespread use of this technique for the study of magmatic fragmentation offer a reference framemork for the comparison of both sets of experiments. Among the most relevant findings from this comparison, highlights the difference in measured pyroclastic velocities of up to 150 m s^{-1}, which should be considered as a lower limit difference for the velocities expected during the intial stages of 2008 Chaitén eruption.

Experimental results were interpreted in the context of 2008 Chaitén eruption. The fragmentation bomb experiments seem to be more appropriate to simulate the early stages of the eruption, characterized by the failure of the pre-existing lava dome, violent explosions and Plinian activity. On the other hand, fragmentation mechanism simulated in the 0.1 MPa experiments may reproduce better the explosive activity observed during the transitional phase of the eruption, in which explosive and effusive activity occurred simultaneously. Results show that exposure of significantly hydrous and hot melt parcels to low pressure will in and of itself result in fast deformation and decompression rates necessary for melt disruption. This process will likely aid magma degassing in the conduit environment or in newly opened melt-hosted fractures that act as low pressure sinks for outgassing (tuffisites; Castro et al., 2012a).

Finally, these results help explain the H_2O content distributions in 2008 Chaitén pyroclastic obsidian deposits described in the Chapter 2 of this thesis, as well as the ones observed in other rhyolitic eruptions (e.g., Mono Craters, Newman et al., 1988; Rust et al., 2004).

Chapter 5

Long-lasting impacts of rhyolite eruptions: ash resuspension events

5.1. Introduction

Hazards and impacts associated with dispersal and sedimentation of primary volcanic tephra during eruptions are well documented in the literature (e.g., Horwell and Baxter, 2006; Wilson et al., 2012; Guffanti and Tupper, 2014; Jenkins et al., 2015). Worthy of note are also the tools from the social sciences used to characterize and identify public awareness, perceptions and behavior around volcanoes, including preparedness related to primary tephra fallout (e.g., Greene et al., 1981; Johnston et al., 1999; Paton et al., 2001; Gregg et al., 2004; Bird, 2009; Bird and Gísladóttir, 2012). Social science research is also used in post-event impact assessments, where eye-witness accounts provide scientists with invaluable physical data not recorded in the geological record (e.g., Wilson et al., 2011; Craig et al., 2016b). However, less attention has been devoted to characterization of ash as a secondary hazard after it has been resuspended by winds. Despite the relative dearth of research on ash resuspension, the phenomenon has been documented in several areas during and after volcanic eruptions (Table 5.1).

Defined as "ash storm" by Bitschene et al. (1995), ash resuspension events are prone to occur under specific meteorological and environmental conditions such as strong winds, low soil moisture and lack of vegetation (e.g., Leadbetter et al., 2012; Wilson et al., 2011). Particles begin to move by creeping, saltation and suspension when the wind reaches a threshold friction velocity (Bagnold, 1941), which depends on soil and ash textural and morphological characteristics (i.e., grain size, density, surface roughness, degree of compaction; Sivakumar, 2005). Saltation is the dominant mechanism during initial stages of ash resuspension, with particles first being lifted and then transferring their kinetic energy when falling back to the surface and thus promoting a chain reaction (Shao et al., 1993) that liberates stationary ash particles from the surface. Once the threshold friction velocity is exceeded, sediment suspension may become stable causing large-scale ash remobilization. Ash travelling in suspension can affect areas several hundred kilometers away from the primary depositional area (e.g., Alexander, 1934; Miller, 1934; Wilson et al. 2011; Folch et al., 2014). This long-lasting phenomenon, unlike most primary tephra fallouts, does not have a point source of emission (i.e., a single volcanic vent), but is typically sourced from wide areas, and can occur in both young (e.g., Thorsteinsson et al., 2012; Wilson et al., 2013) and old deposits (e.g., Hadley et al., 2004; Mingari et al., 2017). The term tephra is considered here in the sense of Thorarinsson (1944)—a collective term used to describe all particles ejected from volcanoes irrespective of size, shape and composition. Wind remobilization typically affects the ash fraction of tephra deposits, but terms like "volcanic ash" are often used common languagel to describe all sizes of volcanic particles. Since this study involved survey interviews of farmers who may not use grain size terms consistent with those of scientists, in the following sections “ash fallout/deposits” and “tephra fallout/deposits” are considered to be equivalent.

Remobilization of tephra deposits was first reported by Alexander (1934) and Miller (1934), affecting the city of Buffalo (USA) on 12-13 November 1933. Characterization of the particles deposited and meteorological conditions led the authors to propose Alaska as the source of this volcanic ash. Hadley et al. (2004) reported an ash resuspension event related to the 1912 Novarupta eruption (Katmai volcanic cluster, Alaska) on 20-21 September 2003 and highlighted its hazardous nature to aviation. The Alaska Volcano Observatory reported several remobilization events related to this deposit over the last 14 years, with most events taking place during boreal spring and fall and affecting areas up to 250 km downwind (Wallace et al., 2015). Novarupta tephra deposits are still remobilized more than 100 years after its deposition. Following the 1980 Mount Saint Helens eruption (USA), Hobbs et al. (1983) described ash resuspended over eastern Washington State and provided the first measurement of the concentration of this particulate material in the atmosphere. Iceland is another important source of volcanic sediments that are frequently subjected to intense aeolian processes and resuspension (Dagsson-Waldhauserova et al., 2013). Thorsteinsson et al. (2012) and Leadbetter et al. (2012) identified ash resuspension events during and shortly after the 2010 Eyjafjallajökull eruption (14 April to 20 May) and performed the first systematic ground-based measurements of air quality (i.e., concentration of Particulate Matter (≤ 10 μm, (PM_{10})) at locations around the volcano). Leadbetter et al. (2012) made the first attempt to model these events. Arnalds et al. (2013) registered over 30 erosive events on Eyjafjallajökull tephra deposited between June and October 2010, including an extreme episode that transported 11,802 kg m^{-1} at sustained wind speeds between 14.1 and 22.5 m s^{-1} and gusts up to 38.7 m s^{-1}. Lastly, applying morphological, textural and compositional analysis, Liu et al. (2014) characterized a resuspended ash deposit on Reykjavik following a blizzard in March 2013 and identified multiple sources—the 2010 Eyjafjallajökull and 2011 Grímsvötn deposits.

In the southern hemisphere, Patagonia is another region where conditions for ash resuspension are often reached. After the eruption of Mount Hudson (Chile) in 1991, Scasso et al. (1994) described deposits of remobilized ash at several locations east of the volcano, while Inbar et al. (1995) analyzed the chemical and physical characteristics of the airborne ash. The Global Volcanism Program (GVP) reported wind remobilization of Hudson’s tephra from shortly after the 12-15 August 1991 eruption until late March 1992 (GVP, 1991a,b,c; GVP, 1992). More recently, ash resuspension events related to the 2008-2010 Chaitén volcano (Craig et al., 2016b) and 2011-2012 Cordón Caulle (Wilson et al., 2013; Folch et al., 2014; Craig et al., 2016a,b; Elissondo et al., 2016; Ulke et al., 2016 and Panebianco et al., 2017) eruptions were reported in the Argentinian Patagonia. The same phenomenon was described by Reckziegel et al. (2016) after the short eruption of Calbuco volcano in 2015 (Chile). In the Argentinian/Chilean region of La Puna, Collini et al. (2015) noted the occurrence of a resuspension event shortly after the eruption of Lascar in 1993 (Chile). Also in La Puna, on 13 June 2015 the Volcanic Ash Advisory Centers (VAAC) in London and Buenos Aires identified a plume of ash in the vicinity of Nevados Ojos del Salado volcano (Chile/Argentina). After discarding the volcano as the source of the ash, they related it to resuspension of relict pyroclastic deposits from an eruption of Cerro Blanco volcano some 4300 years ago (Collini et al., 2015; Mingari et al., 2016).

Table 5.1 Summary of reported ash resuspension events.

Volcanic eruption (onset)	**Resuspension event**	**Affected area (distance, km)**	**Particle Matter (PM)*[1] [µg/m^3]**	**References**
Alaska*	12–13 Nov. 1933	Buffalo (USA) (>4000)		Alexander (1934); Miller (1934)
Novarupta (06.06.1912)	20–21 Sep. 2003	Gulf of Alaska (USA) (230)		Hadley et al. (2004)
	2003–2005 2010–2015	Shelikof Strait, Kodiak Island Gulf of Alaska (250)		Wallace et al. (2015)
Mount St. Helens (18.05.1980)	23 May 1980	Eastern Washington (USA) (125–225)	14 PM$_2$ /250.5*[2]	Hobbs et al. (1983)
Eyjafjallajökull (14.04.2010)	7 May–6 Jun 2010	Vik (40)	13157/ 1231	Thorsteinsson et al.(2012)*[4]
		Heimaland (50)	4000/>1000	
		Hvolsvöllur (35)	-/~500	
		Reykjavík (125)	-/2000	
	23 May–2 Jul 2010	Heimaland (50)	4161	Leadbetter et al.(2012)*[5]
		Hvolsvöllur (35)	1900	
		Grensàsvegur (120)	1413	
		Hvaleyrarholt (125)	1726	
	21 Sep 2010–16 Feb 2011	Drangshildardalur (12)	1900	
	Jun–Oct 2010	10 km from the crater		Arnalds et al. (2013)
	6–7 Mar 2013	Reykjavík (125)		Liu et al. (2014)
	18 Sep 2012	Kirkuæbjarklaustar (75)		
	22–23 Aug 2013	Siglufjördur (285)		
	12 Nov 2013	South of Eyjafallajökull (<15)		
Grìmsvötn (21.04.2011)	6–7 Mar 2013	Reykjavík (225)		Liu et al. (2014)
Cerro Blanco (2300 BCE)	13 Jun 2015	“Bolsón de Fiambalá” area (~100)		Collini et al. (2015) Mingari et al. (2017)
Mount Hudson (08.08.1991)	16–23 Aug 1991	*No specifications*		GVP (1991b)
	Sep 1991	Comodoro Rivadavia (400)		GVP (1991a)
		Río Gallegos (770)		
		Puerto Deseado		

		Puerto San Julian Atlantic Ocean (1000) Mar del Plata (>1500)		GVP (1991c)
	21 Mar 1992	Comodoro Rivadavia (400) Malargüe (1300)		GVP (1992)
	1991–1992	XI region (Chile) - Santa Cruz province (Argentina)	3768–6000 part./l*^{3}	Inbar et al. (1995)
	1991–2011	(120–570)		Wilson et al. (2011)
Lascar (30.01.1993)	23 April 1993	Puna región (Argentina) (50–100)		Collini et al. (2015)
Chaitén (01.05.2008)	Feb 2009	Esquel – Pilcaniyeu (110–250)		Craig et al. (2016b)
Cordón Caulle (04.06.2011)	Jun 2011–Mar 2012	Bariloche – Ing. Jacobacci (100–250)		Wilson et al. (2013)
	Aug 2011	Ingeniero Jacobacci (250)		
	4–5 Mar 2012	Ingeniero Jacobacci (250)	919/ 625	
	14–18 Oct 2011	Buenos Aires (1400)	252	Folch et al. (2014)
	Jun 2011–Jan 2012	Villa La Angostura (50)	~600/ ~300	Elissondo et al. (2016)
		Ingeniero Jacobacci (250)	~1500 / ~1100	
	Jun 2011–Mar 2012	Villa La Angostura - Ingeniero Jacobacci (50-250)		Craig et al. (2016a)
	Jun 2011–Dec 2012	Patagonian Steppe (200–260)		Panebianco et al. (2017)
Calbuco (22.04.2015)	2–3 May 2015	Neuquén province (200–250)		Reckziegel et al. (2016)

* Volcanic system is not specified.

*^{1} When not clarified PM refers to PM_{10}

*^{2} Total Mass Concentration of Particles obtained via aircraft airbone sampling.

*^{3} Values reported as particles per liter.

*^{4}The first value reported corresponds to the maximum 10 min average concentration while the second is the maximum 24 hour average.

*^{5} Values reported as hourly averages

Little assessment, however, exists of impacts of resuspension events on human health, infrastructure, economic activities and, in general, on communities as integrated and complex systems. Sixteen years after the 1991 Mount Hudson eruption, Wilson et al. (2011) examined the long-term environmental, social and economic consequences of ash resuspension events in the southern Patagonia Steppe. The authors identified several impacts on farming activities, including farmland buried under ash dunes, abraded vegetation, contaminated feed supplies and, tooth abrasion, gastrointestinal problems, blindness, impeded movement and exhaustion in livestock, causing the abandonment of some farming activities and farms. Wilson et al. (2011) also showed that ash resuspension events can extend the effects of primary tephra fallout for several years. This was corroborated by Craig et al. (2016a,b) in their studies on impacts on agricultural activities after tephra falls in Patagonia. Recent ash resuspension events reported in Iceland (Table

3.1) aroused great concern about the possible consequences of long term exposure to high airbone concentrations of thoracic (≤10 μm) and respirable (≤4 μm) size particles on human health (Leadbetter et al., 2012). These critical grain size classes were defined by the Quality of Urban Air Review Group (1996). Although the potential impacts of long term exposure are known (Horwell and Baxter, 2006), no epidemiological survey has been carried out in areas affected by this secondary ash hazard. The only published study (Carlsen et al., 2015), found that high levels of PM_{10} due to volcanic ash during non-eruptive periods increased the number of emergency hospital visits for cardiorespiratory causes in adults in Reykjavík. To our knowledge, however, no study has examined people's perception, awareness and preparedness related to ash resuspension events.

In this chapter, aspects of natural and social sciences are combined to characterize ash resuspension events associated with the 2011–2012 Cordón Caulle deposits and assess the impact on a farming community in the Argentinian Patagonian steppe (i.e., Ingeniero Jacobacci, Fig. 5.1). The impacts of ash resuspension are compared to those of primary tephra fallout. Furthermore, farmers' perception and knowledge in relation to these hazardous events were assessed. At the same time, the information they provided was used to complete the description of the physical phenomenon, based on measurable physical parameters (i.e., rainfall, wind velocity).

5.2. Area of study

The area of Ingeniero Jacobacci was severely affected during the 2011–2012 Cordón Caulle eruption, despite the fissure system being ~250 km distant (Fig. 5.1; Gaitán et al., 2011). Furthermore, the prevailing environmental conditions (i.e., low vegetation coverage and low precipitation rates) of the region around Ingeniero Jacobacci make it especially susceptible to post-eruptive ash resuspension events. Located in the Department of 25 de Mayo, in Rio Negro province, Argentina, Ingeniero Jacobacci is in the Argentinian Patagonian Steppe (Fig. 5.1A) and has a population of 6261 inhabitants (INDEC, 2010). The closest main cities are Bariloche (210 km), General Roca (350 km) and Viedma (700 km), capital of the province. Next, we summarize the main social, economic, meteorological and environmental aspects that established a baseline to understand the population and environmental conditions of our study area.

5.2.1. Social and economic aspects

Ingeniero Jacobacci was founded in 1917 as a consequence of the arrival of the railway that today connects the city with Bariloche and Viedma. However, the area was already populated before that time by indigenous communities (Mapuches and Tehuelches).

Between 1878 and 1885 the Argentinian government launched military campaigns to exterminate the existing indigenous communities and take control of their lands. As a result of those campaigns, vast areas of the Patagonia were incorporated within the incipient Argentinian State. Farming activity in the area began soon after this period and expanded rapidly. Due to the historical process of land occupation, different categories of farmers and scales of farming activities can be recognized in the area, ranging from relatively small ones practicing subsistence cattle-farming to big landowners with several thousands of hectares and animals (LADA, 2010). Although improvements in legislation have recognized some indigenous rights, tension for the possession of the land between remaining indigenous communities and the Argentinian State still persists (Murgida and Gentile, 2015).

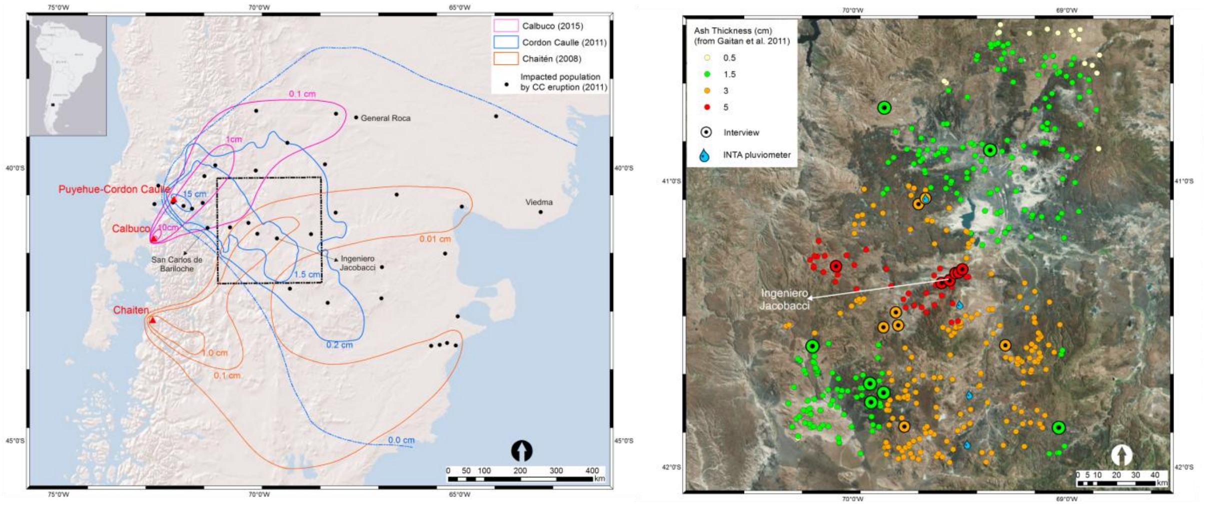

Fig.5.1. Location of the study area. A) Isopach maps of the tephra deposits of the last three eruptions that affected the region: 2008–2010 Chaitén (Alfano et al., 2011; Watt et al., 2009), 2011–2012 Cordón Caulle (modified from Gaitán et al., 2011) and 2015 Calbuco (Van Eaton et al., 2016) eruptions. The rectangule indicates the location of the study area. B) Zoom on the study area. The colored dots show the locations of farms in the study area (Census INTA, 2016), while black dots indicate farms involved in the present study. Different colors indicate tephra thickness deposited according to Gaitán et al. (2011).

Farming is the main economic activity in the study area and it developed as extensive, low-intensity livestock farming on arid/semi-arid grazing lands. Production consists mainly of sheep (Merino breed) and goats (Angora and Criolla breeds) for wool exportation and, on a smaller scale, cattle are bred for meat production. According to the last census carried out by INTA in 2016, 508 families live in the rural area of Ingeniero Jacobacci (Fig. 5.1B). The city of Ingeniero Jacobacci functions as a service center for the farmers, providing access to banking, a hospital, agricultural institutions and an agricultural cooperative. The main source of employment in the city is the municipal government, while mining-related activities represent an important complementary source of employment.

5.2.2. Meteorological and environmental aspects

The Argentinian Patagonian steppe is a low relief region with hills, plateaus and plains. The area under study experiences a climate comprising four seasons, characterized by changes in temperature, wind conditions and precipitation (Fig. 5.2).

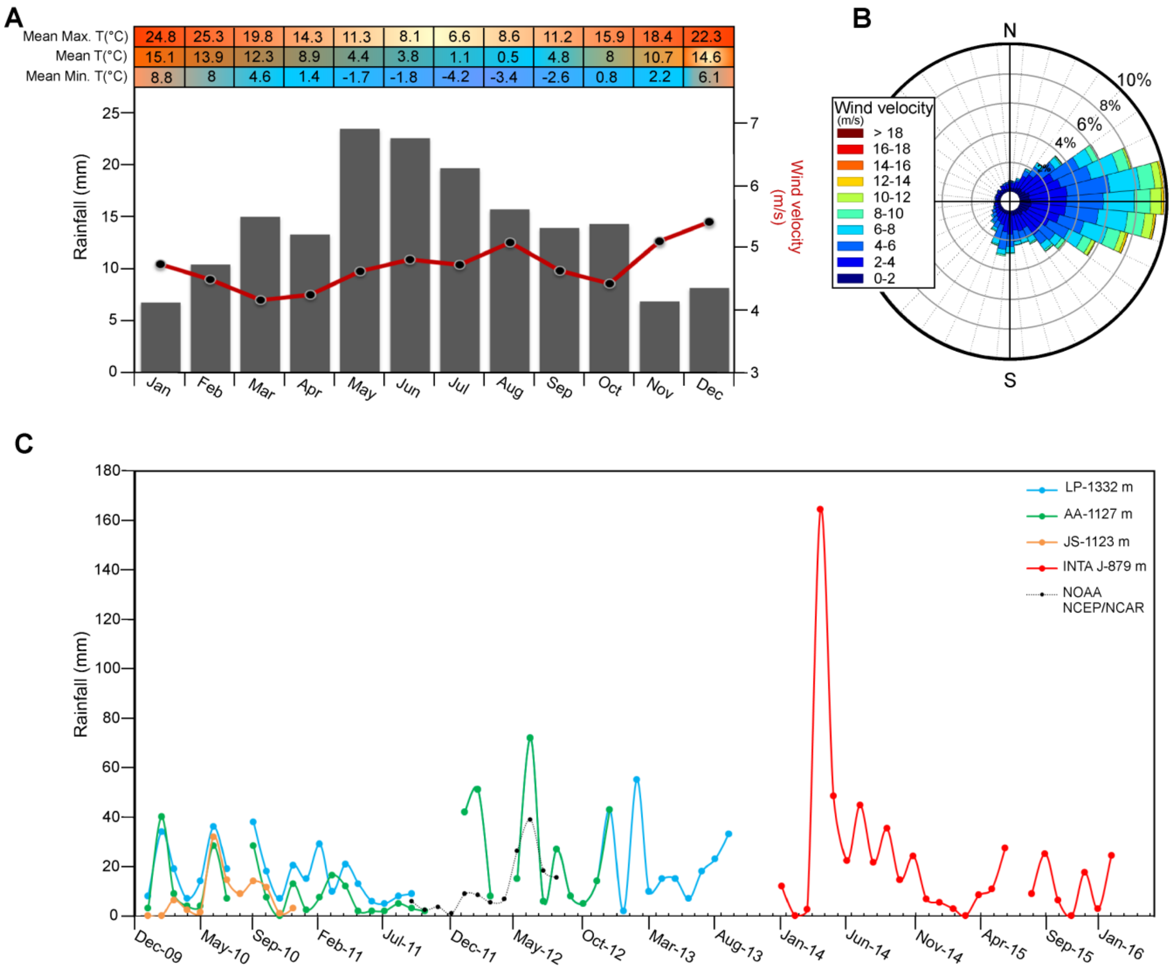

Fig. 5.2. Meteorological characteristics of the study area. A) Columns represent monthly distribution of rainfall for the period 1941–2005 (Source: Station Emiliano Criado—900 m.a.s.l). Red line represents monthly mean wind velocity for the period 2011-2016 obtained from ERA-Interim Re-Analysis of the ECMWF (European Center for Medium-range Weather Forecasts) dataset. At the top, monthly temperatures averaged for the period 1982-1990 (Source: INTA-DPA). B) Wind direction and velocity for the period 2011-2016. C) Rainfall for the period December 2009 - February 2016. LP, AA and JS are pluviometers. INTA J is emplaced in the city of Ingeniero Jacobacci. Grey dot line represents data of Elissondo et al. (2016) for the period September 2011–July 2012 (NOAA NCEP/NCAR).

According to the UNEP (1992) Aridity Index, it can be classified as an Arid/Semi-arid region. Annual median temperature is 8.2°C; however, large daily and seasonal fluctuations exist. Winds prevail from the west with an annual mean velocity of 4.7 m s^{-1}. Summer and winter are the windiest seasons, with maximum mean velocities of 5.4 m s^{-1} reached in

December; while lowest wind velocities occurred in fall (4.16 m s^{-1} in March). The historical annual precipitation is 170 mm (1941–2004) with most rainfall occurring between April and September (Fig. 5.2A). Unfortunately, rainfall data for the area is discontinuous. Nevertheless, data from pluviometers emplaced by INTA in farms located at different altitudes allows for a first characterization of the precipitation regime during the last 6 years (2010–2015). These values are supplemented in Fig. 5.2C with the ones published by Elissondo et al. (2016). Since 2007 the region has been affected by a severe drought (INTA-EEA, 2011).

5.2.3. Volcanic activity and its impacts

The influence of post-glacial volcanic activity in the Patagonian steppe can be recognized in the geological record (Fontijn et al., 2014). Tephra layers identified in a paleolake sequence in the vicinity of Ingeniero Jacobacci (~20 km to the north) by Tatur et al. (2002) show how these events have impacted the region at least during the last 14,000 years. The active Andean volcanic front is located approximately 200 km west of the study area (Fig. 5.1A). According to the GVP (http://volcano.si.edu/), in the segment between 39° and 43°S, a total of 25 volcanoes are considered to be active, some of which have erupted explosively during the last decades. The 2008-2010 Chaitén and 2011–2012 Cordón Caulle eruptions were the two most explosives taking place in this segment, developing extensive volcanic plumes and dispersing tephra all over this region (Watt et al., 2009; Alfano et al., 2011; Pistolesi et al., 2015; Fig. 5.1A). On a minor scale, the 2015 eruption of Calbuco affected the northern sector of Patagonia (Reckziegel et al., 2016; Romero et al., 2016; Van Eaton et al., 2016; Fig. 5.1A). On 22 April 2015, and preceded only by three hours of a sudden increase in its seismic activity, Calbuco volcano erupted explosively, producing a 15 km high eruption column (SERNAGEOMIN, 2015a). After two short but energetic and highly explosive phases, the activity of the system decreased, giving rise to the alternation of smaller explosions and periods of quiescence. The eruption was over by the end of May (SERNAGEOMIN, 2015b). In the following sections, the main impacts of these eruptions are described, putting special emphasis on the study area.

5.2.3.1. 2008–2010 Chaitén eruption

Chaitén volcano, located 310 km southwest of Ingeniero Jacobacci, produced vast amounts of tephra during the first weeks. Impacts were severe at a local, regional and global scale. A wide area of the Argentinian Patagonia was affected by the dispersion and deposition of fine ash. According to the isopach map developed by Watt et al. (2009), our study area was covered with 0.1 to 0.5 mm of volcanic material (Fig. 5.1). Martin et al. (2009) evaluated the environmental effects (i.e., on air, water and vegetation) of the eruption in Argentina. They reported ash resuspension-related problems in Esquel city, but triggered by anthropogenic activity (i.e., vehicular traffic). Although there is no specific study carried out in Ingeniero Jacobacci, Craig et al. (2016b) identified pastoral and horticultural impacts in the Patagonian Steppe related to the primary tephra fallout. They also reported wind remobilization of tephra deposits, which exacerbated the impacts of primary tephra fallout on farming activities and increased the affected area.

5.2.3.2. 2011–2012 Córdon Caulle eruption

The 2011–2012 Cordón Caulle eruption emitted about 1 km^3 of tephra (Pistolesi et al., 2015) and prevailing westerly winds in the region caused most of the primary tephra to be deposited in nearby Argentina (Fig. 5.1A), causing disruption to various economic and other human activities in several localities (Wilson et al., 2013; Craig et al., 2016a,b; Elissondo et al., 2016). According to Gaitán et al. (2011), 3 to 5 cm of tephra was deposited in Ingeniero Jacobacci (Fig. 5.1B). Their measurements were performed at some time during the first two months after the onset of the eruption while Pistolesi et al. (2015) measured about 6.5 cm in July 2011. Electricity, water supplies, communications, road traffic, school and administrative activities were significantly disrupted in Ingeniero Jacobacci (Wilson et al., 2013; Elissondo et al., 2016).

Farming activities were also seriously affected by the primary tephra fallout. According to Jacobacci municipality, livestock losses were estimated at 40–60% for a total herd of 225,000 sheep and 60,000 goats. Craig et al. (2016a) reported starvation and gastrointestinal blockages as the main cause of mortality. Other problems reported include eye irritation, teeth abrasion and difficulties in breathing. Due to the lack of uncovered pasture, supplemental nourishment with forage and grains was implemented. In their report, Wilson et al. (2013) pointed out that birth rates went down from 60% to 10–30% and that there were instances of livestock being sold and moved to other areas. Contamination of wool with tephra adversely impacted the health of animals as well as in the quality and profitability of woolen products (Aguirre, 2012; Easdale et al., 2014).

In addition to the impact of widespread dispersal of primary tephra fallout during the eruption, Ingeniero Jacobacci was significantly affected by the remobilization of primary ash immediately after its deposition and during several months after the climactic phase (e.g., Folch et al., 2014). A team from the Argentinian Geological Survey (SEGEMAR) monitored air quality in the city between September 2011 and July 2012, and measured concentrations exceeding the daily exposure limit (Elissondo et al., 2016). These events prolonged the effects observed during primary tephra fallout, reducing visibility, interrupting mobility of vehicles, delaying urban clean-up activities and increasing water demand (Craig et al., 2016a).

5.2.3.3. 2015 Calbuco eruption

Although Calbuco volcano is located at the same latitude as Ingeniero Jacobacci, the tephra plume of this short eruption was mainly dispersed towards the NE and, in consequence, no primary tephra fallout was reported in our study area. Reckziegel et al. (2016) reported several ash resuspension events related to the 2015 Calbuco eruption deposits; however, according to the authors these events affected a region located more than 200 km north of our study area.

5.3. Methodology

Four sources of data were used to understand ash resuspension events and their impacts on people. These resources include: 1) available meteorological data, 2), in-person interviews with people living in the study area since the 2011–2012 eruption of Cordon Caulle (i.e., eye-witnesses); 3) newspaper articles detailing the eruption, resuspension and impacts; and 4) field observations in the impacted region. Collectively, these data was used to characterize the phenomenology of ash resuspension events in the study region of the Patagonian Steppe. Prior to the in-person interviews, informed consent of respondents was obtained, following the institutional review board requirements for research on human subjects.

A sample survey research was carried out by using a written questionnaire to guide in-person interviews. A 41 item questionnaire was developed based on that used by Bird and Gisladóttir (2010). The questionnaire combined both open and closed-ended questions. It was developed in Spanish, taking special effort to avoid ambiguity and following a logical order. The questionnaire was structured in four sections. Section 1 gathered personal information about the interviewee. Section 2 addressed issues related to the initial phases of the 2011 Cordón Caulle eruption and the primary tephra fallout while Section 3 focused on subsequent ash resuspension events. Sections 2 and 3 were subdivided in two sub-sections, focusing on: (A) the characteristics of the events and, (B) impacts of the phenomena under consideration. Section 4 contained questions related to the 2015 Calbuco eruption. As this latter eruption occurred during the development of the questionnaire, it was considered valuable to expand ther analysis to capture the influence of this event on the sample population. Several items in Section 3B that inquired about support and assistance provided to the farmers during and after the eruption are omitted from the analysis as they are beyond the scope of this chapter.

A total of 21 In-person interviews were conducted during the first week of February 2016. Local farmers were interviewed and, when possible, their farms were visited to make field observations, documenting impacts and environmental conditions. However, due to the long distances between farms and poor accessibility, some of the interviews were conducted in Ingeniero Jacobacci (city) with farmers who were in town on business. A local employee of the ‘Cooperativa Indígena Ganadera’ (i.e., farmers cooperative) served as a Field Coordinator to the project, providing assistance in identifying farms and farmers (based on the fact that these farmers had come to Ingeniero Jacobacci to run their errands) and facilitating access to them during the interview campaign. Before starting the interview phase, it was verified that the purposive sample represented a good cross section of the farms across the spatial extent of the study area and consisted of a mixture of small and large farms being affected by variable accumulation of ash (Fig. 5.1). Only one farmer refused to participate, arguing that he was already interviewed once and there was no direct benefit for him.

The first question asked respondents was ‘Did you live here during the 2011 Cordón Caulle eruption?’ This screening question acted as a filter to verify the farmer’s suitability to the purpose of the research. In case of a negative answer, Section 2 of the questionnaire was skipped. The interviews were conducted in Spanish by a native speaker from the research team. Although the questionnaires were filled-in by the research team during the interviews, each one was audio recorded so that the conversations could be transcribed and analyzed. These transcriptions provided the opportunity to revisit each interview to ensure the accuracy of recorded responses in each questionnaire. The average time of each interview was 47 minutes. Completed questionnaires were subsequently coded and entered into the software SPSS v19® (Statistical Package for the Social Sciences) and answers checked to detect missing data and errors made during the interviews.

Newspapers were used as a complementary source of information. Although information derived from a newspaper analysis may not have the same rigour as a measurement or a social survey, their usefulness to complement hazard characterization and impact assessments has been demonstrated (e.g., Elissondo et al., 2016). Due to the fact that interviews were carried out almost five years after the onset of the eruption, newspapers are also used to verify facts given by interviewees. After a detailed examination of national, provincial and local newspapers, it was found that the provincial newspaper *Diario de Rio Negro* offered the most detailed descriptions. While news about the 2011 Cordón Caulle eruption travelled around the country (and the world) during the first two weeks, subsequent ash resuspension events that occurred in Ingeniero Jacobacci did not receive attention from the national mass media. The short term nature of media coverage is consistent with other disasters and events. For that reason, only *Diario de Río Negro* was considered for the analysis presented here. Search of news was online, using key words (i.e., Cordón Caulle, ceniza, viento, Jacobacci, Linea Sur). A database with news matching the search was created and information about characteristics of ash resuspension events and related impacts extracted (i.e., duration, reported wind velocity, visibility, impacts on accessibility, telecommunications, electricity supply and school activities).

Field observations (i.e., aspects of the deposit, erosion/accumulation features) were also an important component to characterize the geological evidence of ash resuspension events. Visits to the farms, when possible, were also fundamental to validate the data about impacts and mitigation measures obtained from the questionnaires.

5.4. Results

5.4.1 Farmers: main demographics

Of the 21 farmers interviewed, 19 were small-scale producers while 2 were owners of big farms. This is representative of the ratio large:small-scale producers in the area (~1:10; LADA, 2010). The mean age of the farmers was 53.6 (± 12.3) years. Almost two-third of them (62%; n = 13) recognized themselves as descendants of or belonging to an indigenous community. In the majority of cases, the respondents were strongly rooted in the area. Most of the farmers (86%; n = 18) have lived there since birth. Only one respondent had lived in Ingeniero Jacobacci for less than 10 years and all of them were living in the area when Cordón Caulle erupted. With respect to the highest level of education completed, 71% finished primary school, 14% high school, 9% tertiary education and only 1 had obtained a university degree.

Table 5.2 summarizes the agricultural activities practiced among the respondents. Some 19 out of 21 people interviewed possess grazing lands in which they primarily practice extensive low-intensity farming of sheep (88%; n = 18) and goats (57%; n = 12; Fig. 5.3A). Some 52% (n = 11) declared cattle farming; however, the scale of production is considerably smaller than for the previous two. Even though the percentages for poultry and horse farming are also high, with few exceptions the first one is only for self-consumption, while horses are used for daily farming activities. A group of small farms devoted to pig production was identified in the outskirts of the urban area of Ingeniero Jacobacci (Fig. 5.3B). There are no farms with big extensions of cultivated land; however, 24% mentioned that they grow vegetables for self-consumption, mostly in greenhouses (Fig. 5.3C). Although all declared that farming is their main source of income, over half of the respondents (57%) indicated that they had supplementary sources of income, such as a retirement pension or urban job.

In order to understand the importance that farmers might give to primary tephra fallout and resuspension events compared to other events in their community, the open question: ‘List the three main problems you face in your community’’ was asked. Answers were subsequently coded and grouped in different categories. In total, environmental related problems were mentioned 20 times, governance issues 16 times and economic problems five times. Surprisingly, almost five years after the eruption, and from a total of 63 possible answers (3 problems times 21 respondents), ash related problems were only mentioned twice. Other environmental problems such as mining and waste management were mentioned an equal number of times. From the answers obtained, it seems that the actual main concern among farmers is drought, as nearly half of the respondents (n=10) mentioned water-related problems. Only 6 farmers did not mention any environmental related problem. The following question, however, specifically asked about environmental problems, to which five respondents mentioned drought. Two of them also mentioned ash and only one did not identify any environmental problems. This result shows that whether upon prompting respondents about environmental problems or not, drought was the critical hazard on their minds, not resuspended ash.

Table 5.2 Current agricultural activity practiced.

Agricultural activity	Percent of cases (%)
Grazing land	90
Sheep	88
Poultry	71
Equidae	67
Goats	57
Cattle	52
Pigs	33
Crops	24
Other	5

Fig. 5.3. Farming styles. A) Typical farm of the area devoted mainly to sheep and goat farming. On the right side of the picture, the farmyard can be observed next to the house. B) Pig farming in the outskirts of Ingeniero Jacobacci town. C) Greenhouse for self-consumption constructed with the assistance of INTA.

5.4.2. Ash resuspension events

The remobilization of ash deposited by 2011–2012 Cordón Caulle eruption began shortly after the first plume arrived in the area (5 June; Elissondo et al., 2016) and continued during the years that followed the end of the eruption in 2012. All of the interviewed farmers identified the occurrence of ash-related events after the end of what they defined as the “main eruption”. At the beginning of Section 2 the respondents were asked, ‘What was the duration of the 2011 Cordón Caulle eruption?’ The purpose of this question was to see if the farmers were able to define the duration of the eruption and also distinguish the ash resuspension events from the primary fallout. Results are shown in Fig. 5.4A, together with the chronology of the eruption. Nearly half of the respondents (43%, n = 9) defined the main eruption in the time frame of the purely explosive phase of Cordón Caulle (first 10 days). Two of them considered that the eruption was still ongoing in April 2012, when OVDAS reported minor explosions and ash plumes lower than 1 km, and only one defined the duration of the eruption longer than it actually was. Some 24% (n = 5) defined the eruption as a <2 day long event. Despite the different durations defined for the eruption, most of the farmers agreed that the remobilization of ash started almost “immediately” after the ash impacted Ingeniero Jacobacci.

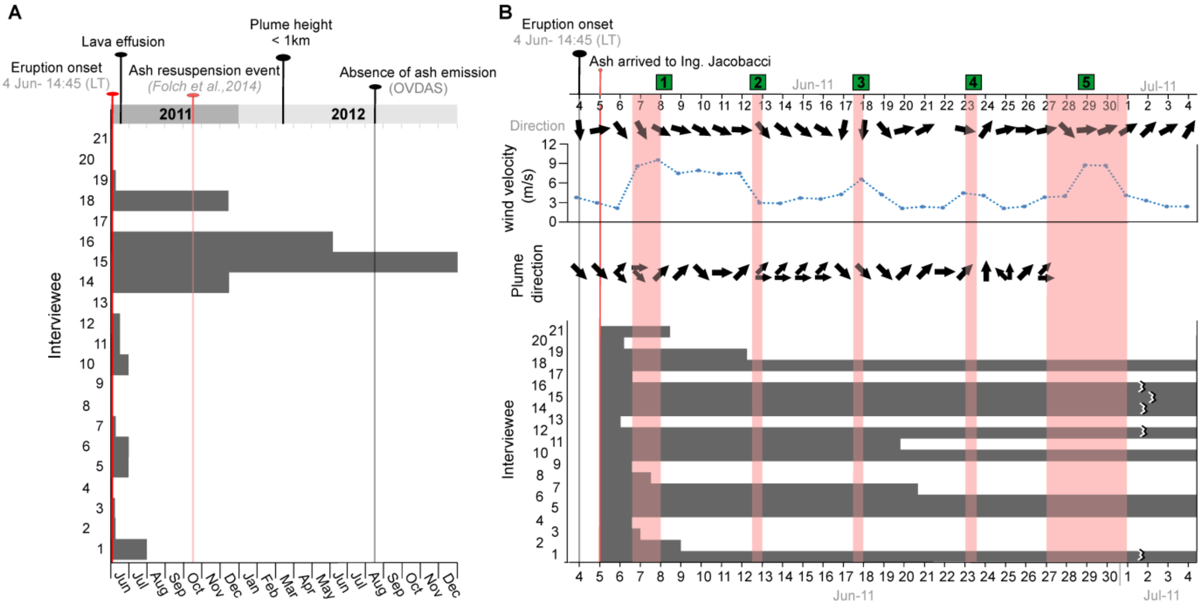

Fig. 5.4. A) Responses to the question: ‘What was the duration of 2011 Cordón Caulle eruption?’ B) Zoom into the first month of the eruption. From top to bottom: mean daily wind direction (North to top of page) and velocity (from ERA-Interim Re-Analysis of the ECMWF dataset), plume direction and height (from Ellisondo et al., 2016) and responses to the question about eruption duration. In green boxes, the event code number (See Appendix D).

According to farmers’ descriptions of the eruption, something similar to snowflakes started falling and covering the landscape in the earliest hours of 5 June. Media reported the onset of a wind storm on the night of 6 June, which continued the next day, resuspending the ash deposited during the first day (event 1). According to the newspaper, the wind reached velocities higher than 28 m s^{-1}. Wind data from ERA-Interim Re-Analysis of the ECMWF dataset shows a marked increase for 6 June, reaching a daily average velocity of

9.5 m s^{-1} on 7 June (Fig. 5.4B). Considering the reported plume dispersion direction, Ingeniero Jacobacci was affected simultaneously by primary ash fallout and resuspension during those days. During the first month of the eruption four other resuspension events were reported by the provincial media, the longest with a duration of four days (event 5). Two of them (events 3 and 5) coincided with marked increases in daily wind velocity. This is not the case for events 2 and 4, which do not match with wind peaks. However, the purely resuspension nature of these events can be deduced from the volcanic plume direction observed during those days (E-NE).

With regard to resuspension events described by the respodents, when they were asked 'Are these events still occurring', some 95% (n = 20) answered in the affirmative. However, the same number of respondents agreed that the frequency and intensity of these events had decreased with time, as discerned from a follow-up question where it was asked, 'Did the frequency and the intensity (amount of ash, duration and extension) of these events decrease with time?' Although this was a closed-ended question, during the conversation most of respondents mentioned that frequency abruptly decreased after the first two years. At least half of them also described a rainfall event that took place during the first half of 2014 as the turning point. When looking at the data from pluviometers (Fig 5.2C), a peak is recognized in 2014. Between 2 and 8 April 2014, a big storm affected North Patagonia, causing mud flows and damage to roads and houses all around the region. In one week, the area of Ingeniero Jacobacci received 132 mm of rain, and in sum, rainfall in April was almost the same as the annual historical precipitation for the area. Moreover, respondents were asked to indicate, 'What was the frequency of occurrence of these events (ash resuspension)?', to which 20 of the respondents concurred that before the change in frequency, events had an occurrence greater than once per month.

As can be seen from Fig. 5.5, a total of 28 ash resuspension events were identified based on the newspaper article analysis (See Appendix D). Even though the lack of news about resuspension events after 11/11/2013 cannot be unequivocally interpreted as the absence of events after that date, the remarkable decrease in reported events are in agreement with the interviewees descriptions. A closer inspection to Fig. 5.5A reveals a good agreement between the distribution of resuspension events reported and the windiest months, in particular after September 2011. From the rainfall anomalies plot (Fig. 5.5B), the deficit of rainfall and the persistent drought conditions during the three years following the eruption can be recognized. The scenario changed in April 2014, with 8 months of rainfall above the historical average. Rainfall data are shown here in terms of anomalies instead of absolute values to highlight that the area was being simulateneously affected by both hydrometeorological hazard and ash resuspension (please refer to Fig. 5.2 for absolute values of monthly rain accumulation).

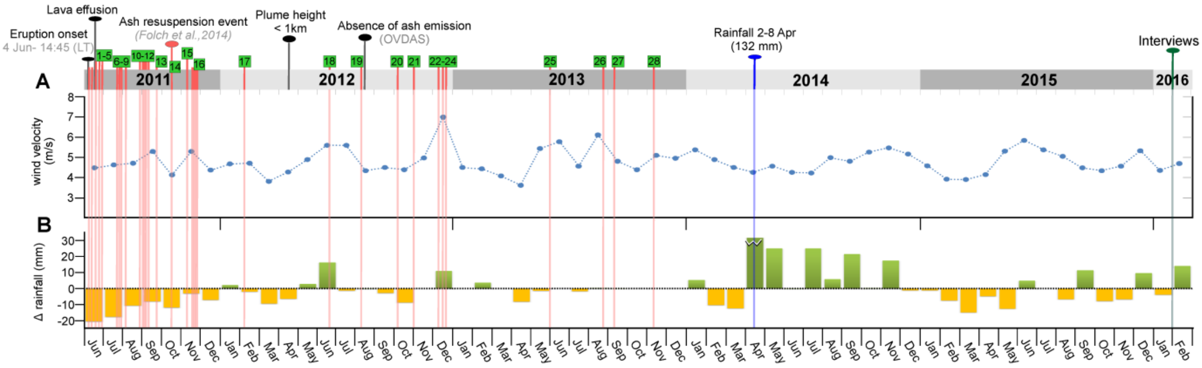

Fig. 5.5. Chronology of events (2011–2016): wind, rainfall anomalies and resuspension events. Light red vertical bars represent ash resuspension events reconstructed by newspaper analysis. In green boxes, the event code number (see Appendix D). A) Monthly mean wind velocity obtained from ERA-Interim Re-Analysis of the ECMWF dataset. B) Rainfall anomalies: difference between historical precipitation (1941–2005) and rainfall for the period under consideration. Light green bars are months with rainfalls above the average value while orange columns show months with rainfalls below the historical average.

Farmers were asked, ‘Does the occurrence (amount of ash, duration and extension) of these events change as a function of the season?’ Responses are shown in Fig. 5.6 and compared with wind and available rainfall data for the period 2011–2015. Interestingly, more than 80% (n = 17) of respondents believe these events are seasonally-controlled and almost without exceptions they agreed that they are more common during austral spring and summer. During these seasons, winds are strong and rain is scarce. Similar wind conditions are reached during the end of fall and beginning of winter, however, this is the wettest period of the year. Together, these results support the observation that, although wind is a necessary factor to trigger ash resuspension, rain acts as a first order control (inhibitor) for the occurrence of events involving the resuspension of ash.

Aspects related to the characteristics of the deposits (primary and secondary, if any) and the modification of the landscape through time were also addressed. For these purposes, first the farmers were asked to define, ‘What was the average thickness of ash accumulated in each event?’ Although answers were not precise (vague estimations), most of the farmers mentioned thicknesses ranging from a millimeter to a centimeter. Three of the respondents described how the events did not leave any deposit. Secondly, they were asked, ‘Have you noticed any specific accumulation/erosion processes (in your farm)?’

All of the respondents identified the occurrence of erosion processes in their farm. From the set of options we gave them (not mutually exclusive), 91% (n=19) of respondents reported a non-uniform distribution of ash deposits in their farms. Just over half of them (52%) reported a decrease of ash thickness with time, while only one identified a local increase of the ash deposited. During a visit to some of the farms, accumulation of ash was identified in areas protected from wind in gullies and small valleys (Fig. 5.7A). When examing the deposits in detail, it is possible to identify a discontinuous ash layer of 2–3 cm thickness that corresponds to the primary fallout and on the top, a layer presenting cross-bedded structures where the ash is already mixed with non-volcanic material. Ash deposits can also be found, as small pockets, downwind of pastures and bushes (Fig. 5.7B). Figures. 5.7C and 5.7D illustrate the two main scenarios described by farmers regarding these events: (a) storms or days with persistent high winds, where ash is remobilized massively and visibility is severely affected and (b) local and short duration dust devils. According to many of the respondents, the second ones are the main way by which ash has been remobilized during the last years (and even now). In summary, the availability of ash and wind are a necessary condition for putting ash in suspension in the atmosphere; however, rain seems to be the key player in controlling its occurrence.

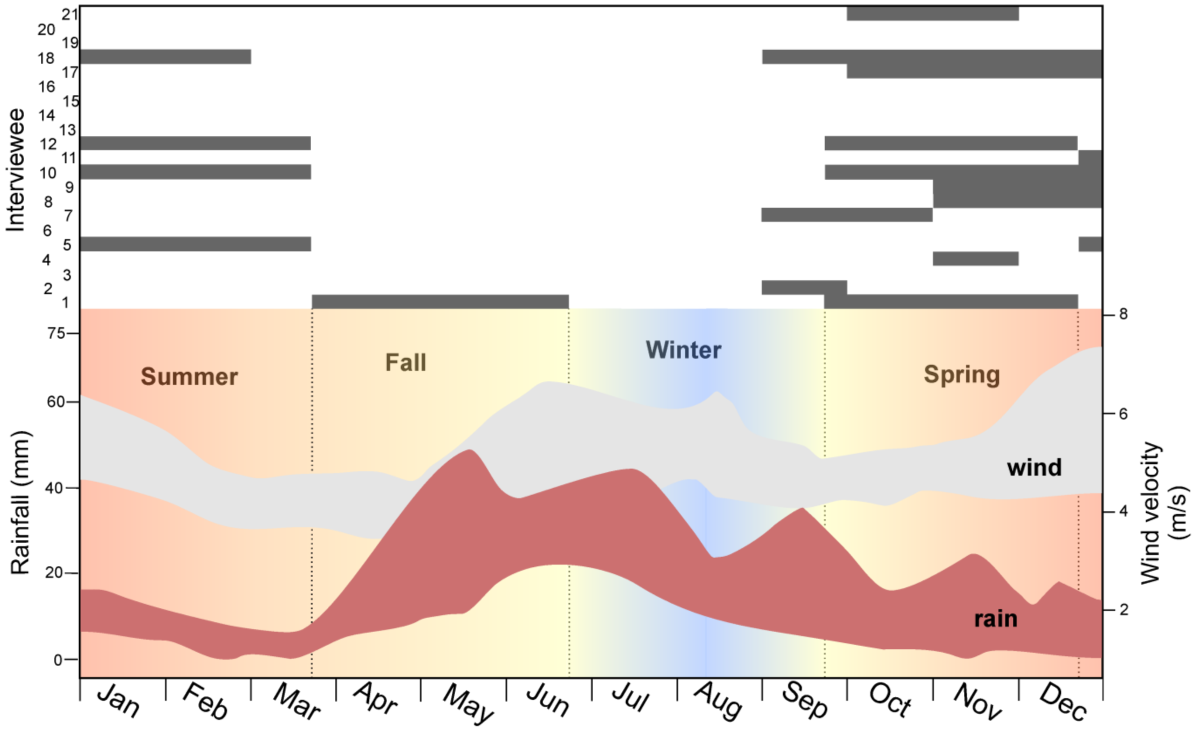

Fig. 5.6. Seasonal variability**:** comparison between answers to the question 'Does the occurrence of these events change as a function of the season? When are they most common?' and seasonal variability of wind and rainfall in Ingeniero Jacobacci. Wind range was obtained considering mean wind velocity for the period 2011–2015 from the ERA-Interim Re-Analysis of the ECMWF dataset. In the case of rainfall, monthly values from Elissondo et al. (2016) and pluviometer INTA_J were considered for the periods (2011–2012) and (2014–2015), respectively. Colored background is a qualitative representation of seasonal variability of mean temperature.

Farmers' understanding of the origin and causes of resuspension events was also explored by asking them, 'What are, in your opinion, the sources of generation of these events?' Overall, their knowledge about this secondary hazard is high. Answers show that the farmers perceive ash resuspension as complex events that depend on a combination of several factors. Only two respondents considered that an ongoing eruption is necessary for the occurrence of these events. All respondents selected wind as one of the responsible factors. Most of them also selected the lack of precipitation (77%, n = 16) and the existence of volcanic ash deposit in the ground (81%, n = 17). A small number of respondents (11%) indicated the effect of vegetation as one of the causes. One famer attributed these events to the will of God.

Fig. 5.7. Field evidences. A) Geoform of accumulation detected in a valley nearby Ingeniero Jacobacci city. At the low right corner a cross section of the deposit is shown. B) General view of a hillslide covered with low vegetation (pastures and bushes). White patches downwind is remaining ash from 2011 Cordón Caulle eruption. A closer view of this can be found at the upper right corner. C) Feeding sheep with forage during an ash resuspension event on the 05/09/2011 (credits: Fermín Franco). D) Farmers transporting dead bodies of sheep in the same farm than in picture a on the 03/10/2011 (credits: Fermín Franco). Arrows point to dust devils occuring in the horizon.

5.4.3. Impacts: ash resuspension events vs. primary tephra fallout

The short-term impact of the Cordon Caulle eruption on urban (Wilson et al., 2013; Elissondo et al., 2016) and agricultural facilities (Craig et al., 2016a, b) was already assessed, but the visit to the area almost five years after the eruption allowed for an evaluation of its long-term impact and, in particular, of the effects of ash resuspension events.

In a first set of questions, impacts of primary tephra fallout on farming activities were assessed by asking, ‘What impact did the ash have on vegetation growth in grazing lands?’ during the main phase of the eruption. The same question was repeated in Section 3, for periods of ash resuspension events. From the comparison of the responses, the most interesting result is the opposite short–long term effect that farmers perceive on their farming activities (Fig.5.8A). While immediate impact was evaluated as negative by all of the farmers possessing grazing lands (91%), 76% (n = 16) of them indicated that during the subsequent years after the eruption there was an increased yield of grazing areas. From this 76%, some 69% (n = 11) mentioned the precipitations of April 2014 as the starting point of the vegetation recovery, while 19% (n = 3) attributed it to the low levels of cattle-grazing during the first years after the eruption. In Fig. 5.9, two pictures taken at the same farm in 2011 (A) and 2016 (B), illustrate the evolution and recovery of vegetation and landscape.

It was also asked, ‘What was the impact on livestock?’ of both primary ash fallout during the eruption and during ash resuspension. Results are shown in Fig.5.8B and the first interesting point that arises is that all the farmers declared that their livestock suffered some kind of impact due to primary ash fallout, while less (75%) reported impacts during resuspension events. Nearly all farmers (20 of 21) reported death of livestock associated with primary fallout. Rates of mortality reported by respondents matched estimations of local authorities (40-60%; Wilson et al., 2013) and affected small and large scale farmers in the same way. On the other hand, only two farmers reported death of livestock due to ash resuspension events. Interestingly, one of them was the farmer who mentioned no livestock died due to primary ash fallout. This farmer is devoted to pig and poultry farming, and reported deaths of chickens after resuspension events. The other farmer mentioned his livestock died during 2011, but recorded no deaths in 2012.

Although there are documented cases of evacuation of livestock after the eruption (Craig et al., 2016b), only one of the respondents evacuated livestock to the locality of Valcheta (~340 km to the east). Less than a quarter of respondents (19%, n = 4) housed their livestock during the main phase of the eruption and only one undertook this measure when ash storms took place.

Among the impacts of ash on livestock during the whole period, the most mentioned by farmers were: teeth abrasion, obstruction of digestive tract with ash, eye irritation and blindness, difficulties in breathing, miscarriage and problems with reproduction. Among the farmers that possessed goats and sheep, there was a general consensus that goats were more resilient, especially the breed Criolla. One of the poultry farmers reported that turkeys and geese were more resilient than chickens. However, he also mentioned all three species experienced reduced reproduction rates. Regarding the non-farming animals, many respondents reported more fox attacks to livestock and related them to the decrease of hare populations in the area.

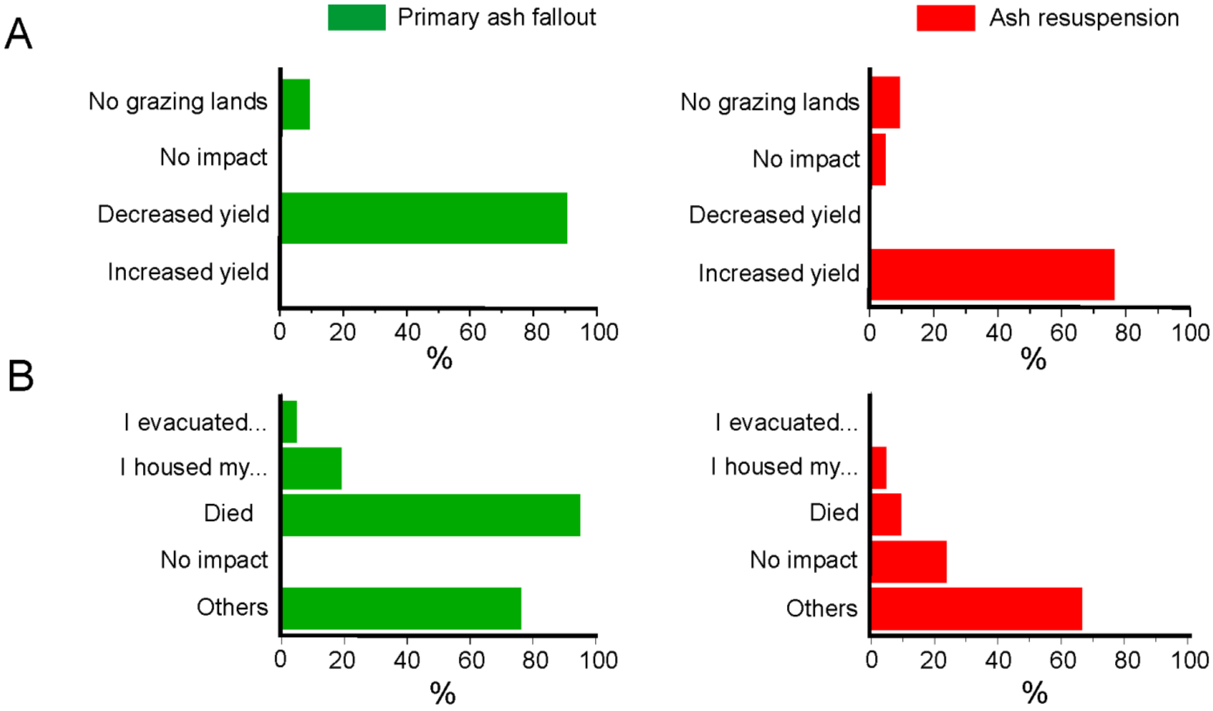

Fig. 5.8. Impacts on farming activities: A) Answers to question ‘What impact did the ash have on vegetation growth in grazing land?’ due to primary ash fallout (question 16.A) and resuspension events (question 28.A). Answer ‘No grazing lands’ accounts for farmers that did not pose grazing lands. B) Answers to question ‘What was the impact on livestock?’ due to primary ash fallout and resuspension events. Answers labeled ‘I evacuated/I housed…’ refer to the different farming animals. Detailed information about answer ‘Other’ is provided in the main text.

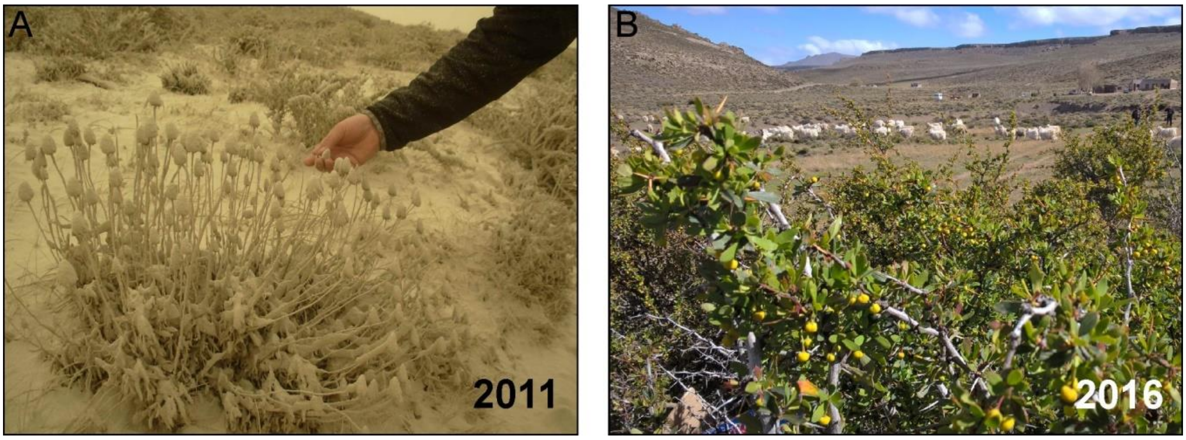

Fig. 5.9. Comparison of the state of vegetation and landscape between 2011 and 2016. Photos taken at the same farm in September 2011 (A) and November 2016 (B) (Credits: Jazmín Miguel).

In order to understand impacts on farms and the sale of farm products the respondents were asked, ‘Have you experienced any issues in selling farm produce to suppliers due to the occurrence of these events?’ Although a frequent answer was ‘…we didn’t have anything to sell’, a number of issues were identified. The main problem was related to wool production. Its quality was severely dimished by ash contamination and as a related problem, damage of tools was a frequently reported during shearing. A pig producer reported to have difficulties in selling his products, apparently because customers were concerned about the quality of the products from the area after the 2011-2012 Cordón Caulle eruption.

After asking about the impacts, it was also inquired whether farmers adapted or changed their farms to mitigate the effects of these events. To do so, respondents were asked, ‘What, if any, changes have you made to your farm, after the Cordón Caulle 2011 eruptions, to deal with the impact of ash storms? (e.g., structural measures, change of crop type or farming practices)’. Almost half of respondents (43%, n=9) declared having improved protection of water catchment areas (i.e., wells and waterholes). In some cases, concrete structures were built while in other areas only nylon was used for the protection (Fig. 5.9).

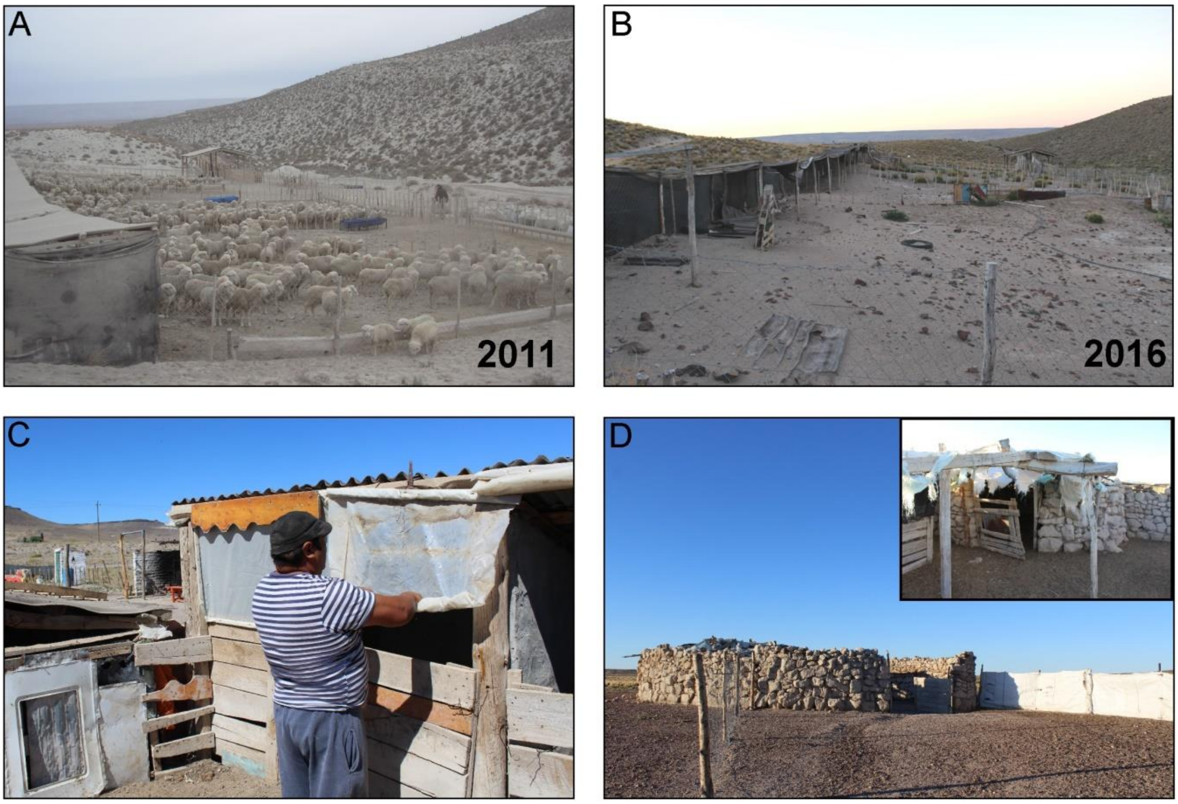

Fig. 5.10. Ash hazard mitigation measures: A,B) Photos taken at the same location shortly after the eruption (A) and during our visit (B). On the left side of it is possible to observe the drinking and feeding troughs installed after the begining of the eruption. C) Windows of pig farm stalls protected with nylon. D) Farmyard for sheep and goats reinforced with stone and with an internal close shelter.

Respondents also indicated that they increased the frequency of clean-up activities. During the first month after the eruption, supplementation with forage and grains was a common practice. For that purpose, in many farms drinking and feeding troughs were installed (Fig. 5.10A). However, most of them were abandoned once livestock was able to feed again with natural pastures (Fig. 5.10B). Additional modifications mentioned were the improvement of farmyards, covering their open areas with nylon (Fig. 5.10C) or reinforcing the walls (Fig. 5.10D). Only three respondents declared that they did not make any change to their farms.

Although no questions about volcanic events occurring before 2011 Cordón Caulle eruption were asked, during the interviews some farmers mentioned spontaneously the eruption of Chaitén in 2008. In all the cases, their comments described how the impact of that event was reduced in comparison with what occurred in 2011.

Impacts of primary ash fallout and ash resuspension events on farmers and the influence on their personal health, wellbeing and behavior were also explored. First, we asked them to define different level of impacts in relation to the 2011–2012 eruption using a 5-point Likert scale (Table 5.3). Almost three quarters of respondents indicated an extreme impact of the eruption on their emotions. More than half of respondents indicated a moderate impact on health while, for the other aspects, results were less homogenous.

Table 5.3. Answers to the question: 'On a scale ranging from 1 (no impact) to 5 (extreme impact), please indicate in which level the eruption impacted on:'

	1	2	3	4	5
	No impact (%)	*A little impact (%)*	*Moderate impact (%)*	*Great impact (%)*	*Extreme impact (%)*
…your house?	5	10	29	29	29
…your health and the health of your family?	9	14	**52**	14	10
…your finantial situation?	9	**33**	29	14	14
…you and your family emotionally?	0	9	5	14	**71**

Finally, after exploring impacts and memories associated with the eruption and resuspension events, respondents were asked, 'In your opinion, which events were the worst: the primary ash fall related to 2011 Cordón Caulle event or the subsequent ash storms? Why?' Almost two-thirds of the respondents (62%, n = 13) expressed the main eruption was the worst, while 29% (n = 6) felt ash resuspension events were worse. The remaining 10% (n = 2), weighted the effect of both phenomenon as similar. When asked, 'Have you ever considered the option of moving to another place as a result of the occurrence of these events?', answers were almost equally divided. Some 57% (n = 12) answered in the affirmative, while 43% (n = 9) said they have never considered that option. We then asked the ones that considered moving from the area, ‘Why have you not moved yet?’ Reasons given by respondents were diverse. Some of them decided to stay after receiving support (i.e., livestock—sheep and goats) from provincial and national institutions. Others mentioned their bond with the area as a reason for staying while a few took it as a personal challenge. In addition, when talking about this last topic with interviewees, it was pointed out several times that young generations were leaving the farms and moving to the city.

5.4.4 The influence of 2015 Calbuco eruption

Due to the location of Calbuco volcano, the 2015 eruption could have easily affected our study area. However, due to strong SW winds, no significant ash deposition occured in Ingenerio Jacobacci (Fig. 5.1A). This was confirmed by interviewees answers in Section 4. The totality of respondents agreed that the eruption did not affect their farms. It was remarkable that all the respondents remembered the name of the volcano (even though Calbuco volcano is only about 100 km south of Cordon Caulle volcano) and the approximate date of the eruption. When respondents were asked about the occurrence of ash resuspension events after the eruption, all agreed that there were no changes in the frequency or pattern of occurrence of ash resuspension events in the area. This is supported also by the lack of reported events by media (Fig. 5.5A).

5.5. Discussion

During the last five years, ash resuspension events have captured the attention of a growing sector of the scientific volcanological community mostly due to its long-lasting and widespread impact. The eruption of Cordón Caulle in 2011, together with the Eyjafjallajökull eruption in 2010, provided the opportunity to observe the complete cycle, from the onset of the eruption to the dispersion, deposition and subsequent re-insertion and transport of volcanic ash into the atmosphere. The magnitude, recurrence and impacts of this last phenomenon led to first attempts to model them (Leadbetter et al., 2012; Folch et al., 2014 and Liu et al., 2014). Even though the models used were developed for mineral dust emission, results obtained from modeling volcanic ash are promising because the model outcomes are in good agreement with field observations. However, the authors recognized that the lack of data on soil properties and meteorological conditions at a local scale are still one of the main limiting factors in the modeling processs. Whereas experiments can contribute to a better understanding of the role of these variables (e.g., Del Bello et al., 2018), there is still a need for detailed field investigations and characterization of the phenomenology of these events. This information is also fundamental to assess the potential impacts of these events and, in consequence, necessary for governments to develop tools to cope with them.

5.5.1. Phenomenology of ash resuspension events

Resuspension of ash in Ingeniero Jacobacci started almost immediately after its deposition and during the first weeks the area was affected simultaneously by primary ash fallout and resuspension. There is consensus about the primary importance of wind and soil moisture in ash remobilization processes (e.g., Wilson et al., 2011, Leadbetter et al., 2012; Folch et al., 2014); however, accurate information about this last parameter is usually absent for recent fallout deposits (Leadbetter et al., 2012; Folch et al., 2014). As a result, in some numerical simulations, precipitation rate is used instead of soil moisture (e.g., Leadbetter et al., 2012; Liu et al., 2014); while in other cases an arbitrary value is chosen (e.g. Folch et al., 2014). Unfortunately, meteorological data for the study area are incomplete. Rainfall records are discontinuous and there are no wind data from meteorological stations in the region to carry out a high-resolution analysis of these variables. Nevertheless, wind data from the ERA-Interim Re-Analysis of the ECMWF (European Center for Medium-range Weather Forecasts) datasets was combined with reported events by media to obtain a first-order characterization of the role played by this variable in our system (Fig. 5.11). Wind data is presented as four daily values (at 0, 6, 12 and 18 hs) and represents an altitude of 10 m above the surface. Even if events reported by newspapers do not always allow us to precisely constrain events in time, in particular the end of the event, it is interesting to note how all the resuspension events shown in Fig. 5.11 correspond to peaks in surface wind velocity.

Wind velocities reported by media for the events shown in Fig. 5.11 are between 8.3 (event 11) and 25 m s^{-1} (event 12 and 21), with most of the events occurring with velocities higher than 19.4 m s^{-1} (Table 5.4). For these events, surface wind velocities from the ERA-Interim Reanalysis of the ECMWF datasets reached maximum values of ~13.0 m s^{-1}. Similar values were reported by Arnalds et al. (2013) for resuspension of Eyjafjallajökull 2010 volcanic ash. For the events 11 and 16, with reported durations of several days, wind velocities reached values down to 2.5 and 1.9 m s^{-1}, respectively. Considering that for both cases these low values coincide with the beginning of the events, this may be reflecting the inaccuracy of newspaper data to constrain the duration of the events.

Rainfall data from pluviometers are monthly averages and consequently it is not possible to correlate them with daily wind data. However, for the period September 2011–July 2012, averaged values every two days are available and shown in Fig. 5.11. Precipitation for those months was low and in only two cases there was a certain amount of rain (1mm) during a reported resuspension event (events 11 and 12). Interesting to note is that event 12 matched with conditions of relative low wind velocities and a rainfall peak. Even though this could be also attributed to an inaccuracy in media reports, it also opens the question about the effect and response time of the soil to rainfall (e.g., rainfall threshold to inhibit resuspension, local infiltration rates). Unfortunately, due to the lack of high-temporal resolution data for the area (i.e., wind and rainfall) no further interpretations can be made.

Table 4 Wind velocities: comparison between ERA-Interim Re-Analysis of the ECMWF dataset and newspapers. For detailed information about the events (i.e., duration, reported wind velocity and reported impacts) see Supplementary Material 2.

Wind velocity (m s^{-1})

	ERA-Interim Re-Analysis of the ECMWF dataset			Newspaper
Event	Max.	Min.	Average	
11	12.2	2.5	6.9	<13.9
12	9.6	5.2	6.5	>25
13	7.7	3.4	5.2	8.3
14	11.7	3.5	6.6	19.4
15	9.3	5.1	6.9	-
16	13.4	1.9	7.3	>19.4
20	12.2	6.1	7.8	>19.4
21	11.7	7.0	9.0	>25
22	13.2	5.8	8.9	>19.4
23	12.04	6.4	9.1	-
24	12.2	3.8	7.4	>19.4

However, the influence of the (lack of) rain in controlling the occurrence of ash resuspension events becomes evident when looking at the seasonal distribution of events (Fig. 5.6). As pointed out earlier, and although similar wind conditions are reached in summer and winter, most of the resuspension events occurred during summer and spring—the driest seasons. Seasonal control of resuspension events was also reported by Wallace et al. (2015) for the 1912 Novarupta-Katmai deposits. The seasonal control can also be recognized in the study area by looking at the distribution of reported events in Fig. 5.5, in particular for 2012–2013. The situation is slightly different for 2011. Even though many resuspension events were reported between September and December, 63% of the events reported by media in 2011 took place during winter (June to August). This could be attributed to two factors: the deficit of precipitations related to the drought that was affecting the area since 2007 and the availability of ash deposit. Supporting the first factor, Fig. 5.5B shows that a rainfall deficit was at its highest level during the first months of the eruption. Regarding the second factor, Panebianco et al. (2017) indicated that the highest mass transport rates in our study area occurred during the first seven months after the eruption. After that period, the authors identified a decrease in the mass transport rate, which they attributed to the depletion of ash deposit in the system.

Topography is another factor that needs to be considered. It was already pointed out by Liu et al. (2014) that it could be a source of error when modeling resuspension events. Recent findings of Panebianco et al. (2017) suggest that relief was controlling the erosion rates in the Patagonian Steppe. Although the results from this study are qualitative, similar conclusions can be extracted. Farmers identified different accumulation and depletion areas associated with topography. This was validated by visiting some of the farms during the field campaign (Fig. 5.7).

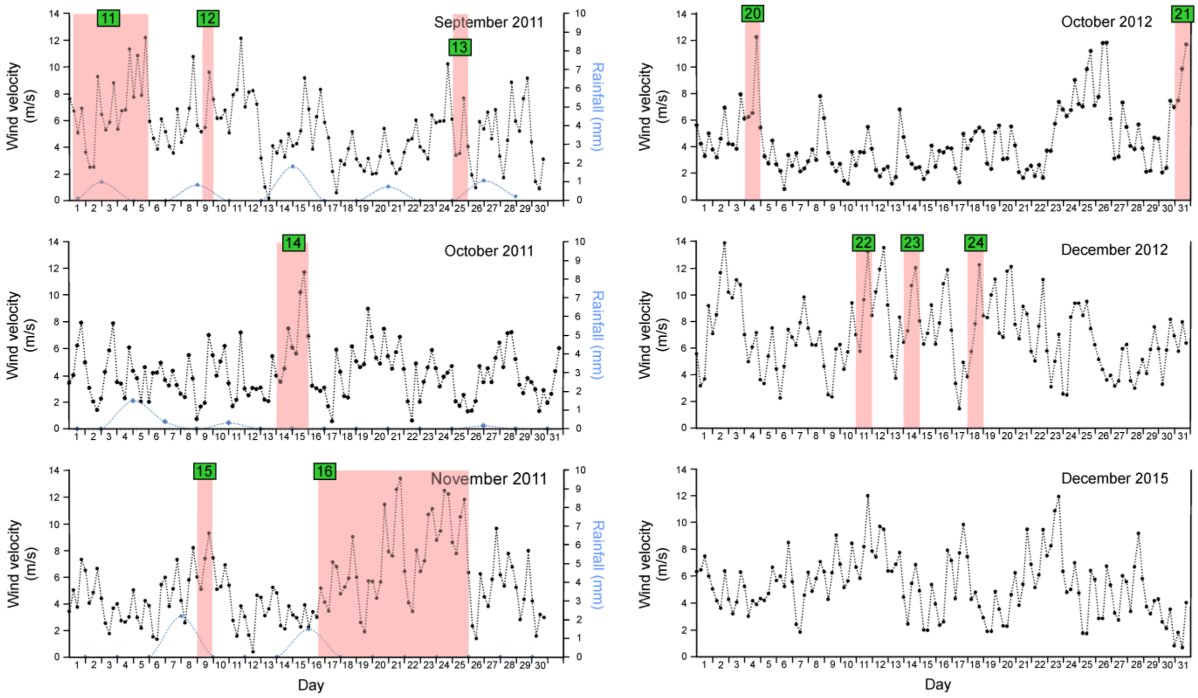

Fig. 5. 11. Wind velocity (at surface level ~10 m height) and resuspension events reported by media for selected months during the period September 2011–December 2012. Wind data for December 2015 is shown to serve as a comparison with the earlier months in which ash resuspension events were reported. In green boxes, the event code number (See Supplementary Material 2). Rainfall from Elissondo et al. (2016) is shown, when available.

The timescale for the decay in frequency of events observed from the media analysis matched with the one reported by Panebianco et al. (2017). Grouping all the evidence, it is possible to describe an initial scenario in which ash was remobilized massively and the controlling parameters were (lack of) precipitations (i.e., below the historical average) and availability of ash. Once the eruption decreased its explosivity, depletion of ash supply due to wind remobilization and the increase of precipitation may have led to a gradual decrease in the frequency and magnitude of resuspension events. The extraordinary precipitation event of April 2014 and the associated flash-flood may have induced a massive remobilization of an important amount of the remaining ash in the system. The increase of rainfall after this event may have contributed to increased soil cohesion making it less susceptible to suspension by wind (Fécan et al., 1998). Since then, and during windy days, local and short-duration dust devils can be observed, which put into suspension the remaining ash accumulated in specific areas. Comparison of wind profiles (Fig. 5.5A and Fig. 5.11) shows that wind conditions for the area have not changed in the period under study.

5.5.2. Impacts

The visit to the area around Ingeniero Jacobacci almost five years after the eruption allowed for an evaluation of the impact of the Cordón Caulle eruption beyond the primary tephra fallout of 2011.

It is recognized that the short-term impact on the farming community was highly negative. The “unexpected” ash fallout deposit that covered the area of Ingeniero Jacobacci caused the collapse of productivity of the farming system, even though the area was previously affected in a much reduced way by 2008 Chaitén eruption. Furthermore, as Wilson et al. (2011) observed for the case of Mount Hudson, resuspension events extended the negative effects of the eruption. However, the quick recovery of the environment described above, was also reflected in the incipient recovery of the farming community. Evidence of this could be manifested by the results of question 11, which revealed that after five years only two farmers consider ash-related events as a current problem. Answers obtained from questions exploring feelings also showed how main impacts on emotions were associated with the scenario that took place during the first week/month after the beginning of the eruption.

The results obtained in this study in relation to the impact of the primary ash fallout are in agreement with those reported by previous studies in the area (Wilson et al., 2013; Craig et al., 2016a,b and Elissondo et al., 2016). For the case of livestock, impacts reported by farmers are hard to exclusively attribute to primary fallout or resuspension events. Regarding the impacts on grazing lands, it is interesting to observe how a high number of respondents recognized a recovery and increase in yield of grazing areas in the long-term. Many of the farmers attributed this to the precipitations of 2014. The positive long-term effect of volcanic ash in soils has been already reported for other areas in Patagonia (e.g., Wilson et al., 2011). In addition to the positive effect of rain, ash remobilization may have contributed to the observed recovery. Three farmers attributed it to the low levels of cattle-grazing during the first years after the eruption. This observation necessarily suggests that we should consider the pre-existing context of the area before the eruption took place. The practice of subsistence cattle-raising without land planning strategies in the area has led to the overload of lands and its consequent degradation (Murgida et al., 2015). This situation was amplified by the existing drought that has been affecting the area since 2007. Craig et al. (2016b) recognized that this situation contributed to increased vulnerability of the farms systems. Although they did not present specific results for Ingeniero Jacobacci, the authors mentioned that this environmental condition was already the reason why impacts on farming activities were more extensive in the Patagonian Steppe after the 2008 Chaitén eruption. In addition, some respondents mentioned that young generations were leaving the farms and moving to the city. Even though this could be partially attributed to the situation after the eruption, Murgida et al. (2015) showed that migration of young people from the farms to the city was already occurring before the eruption. According to data from the national Census, between 2001 and 2010 the rural population in the Department of 25 de Mayo decreased 30%.

Overall, the results of this research suggest that the eruption adversely impacted farming life of an already highly vulnerable community, and that the ash fallout and associated resuspension events amplified the effect of an existing natural hazard that had already been affecting the area for years— the drought.

5.6. Conclusions

This study has shown the importance of a multidisciplinary approach to understand hazardous processes, such as ash resuspension, and their associated impact in the context of a multi-hazard scenario involving a volcanic eruption and prolonged drought and overgrazing. Furthermore, it was demonstrated the usefulness of interviews for capturing in-depth information on people’s knowledge and experiences related to ash resuspension events. Combining their results with measurable physical parameters (i.e., rainfall, wind velocity), it was possible to reconstruct and characterize the phenomenology of ash resuspension events in an area of the Patagonian Steppe. Interviews demonstrated also their importance for the assessment of primary ash fallout and resuspension events impacts on farming activities and farmers emotions.

The results of this research show that, although wind is a necessary factor, rainfall and ash availability play a first order control on the occurrence and persistence in time of ash resuspension events. It was observed that after the first six months, frequency of massive ash remobilization events was gradually decreasing until the beginning of 2014. Although the precipitation event of April 2014 can be considered as the turning point for the system evolution, the gradual decrease in frequency may be attributed to the availability of ash. This may also explain why deposits from massive eruptions such as Novarupta (i.e., Katmai, Alaska in 1912) are still remobilized after more than one hundred years, while smaller eruptions such as Mount St. Helens in 1980 (and Cordón Caulle) have shown shorter periods of time of associated ash resuspension activity.

It was also identified that seasonal variability has a direct influence on the spatial distribution of ash resuspension events. Most of them occurred during the austral spring and summer, the driest seasons of the year. Although winter shows similar wind conditions, the higher amounts of precipitation may have played a key roll in inhibiting the occurrence of these events. Moreover, the presence of pre-existing hydrometeorological hazards, such as drought, and the occurrence of long-return period events, such as the exceptional precipitations of April 2014, demonstrate the importance of assessing ash resuspension events in a multi-hazard scenario context.

Another important finding of this research is that, although the short-term impact of ash resuspension was highly negative, the environment and the farming community are showing signs of recovery after five years. Farmers reported that grazing lands are showing an increased yield and the volume of ash deposited in the fields has decreased. Remaining accumulations of ash can be found in low wind velocity areas like gullies and downwind side of bushes. On the other hand, it was found hard to attribute impacts on livestock exclusively to primary fallout or resuspension events. The main reason for this is that resuspension events began almost simultaneously with the arrival of the volcanic plume. This suggests as well that both hazards pose similar impacts. An interesting finding with implications for agricultural planning was the identification of different resiliencies in farming animals. Goats, and in particular the breed Criolla, showed more resilience than sheep, while for poultry, turkeys and geese adapted better to this stressful scenario than chickens. Different levels of resilence were also reported for non-farming animals. Regarding mitigation measures, and although some improvement have been made in the farms, it is important to point out that many of the structures built immediately after the eruption have not been maintained.

Finally, this study highlights the need to improve the existing meteorological networks in areas prone to resuspension events. This is particulary important in the Patagonian Steppe, where meteorological conditions and volcanic activity in the Andes range combine to increase the probability of occurrence of ash resuspension episodes in the future. Future research should concentrate also in the quantification of the physical parameters discussed here (i.e., wind velocity, rainfall and soil moisture, ash availability) and needed to model resuspension events. It is of primary importance to link them with the experimental and numerical model variables such as wind friction velocity (U*), soil moisture and precipitation rate.

Chapter 6

Summary and conclusion

Taking the unique opportunity afforded by 2008–2010 Chaitén and 2011–2012 Cordón Caulle eruptions, this thesis shed light on the characteristics and dynamics of long-lasting rhyolite events. Combining field work, analytical techniques, experiments and also tools from social sciences, several aspects of these eruptions were studied. While the 2008 Chaitén eruption was selected as a case of study to learn about physical processes related to magma degassing and fragmentation dynamics, the eruption of Cordón Caulle provided the opportunity to look to aspects related to hazards and impacts of these long-lasting events.

As promised in the introductory chapter, H_2O was a central topic of this thesis. In Chapter 2, a detailed analysis of the H_2O preserved in glasses from 2008–2010 Chaitén eruption revealed the evolution of this volatile species during the eruption. By applying FTIR, almost 500 obsidians from time-constrained deposits representative of each of the three eruptive phases (i.e., explosive, transitional and effusive) were measured. This is the largest data set analyzed so far for a single volcanic event. Results show that obsidians from Chaitén exhibit a wide range of H_2O_t contents (0.1 to 3.44 wt.%), significantly expanding the upper H_2O limit reported by Castro et al. (2012a, 2014). The lowest concentrations were found in obsidians from the lava domes (0.1–0.3 wt.%) while the narrowest range is shown by the obsidian bombs (0.5–1.77 wt.%). The highest H_2O values were measured in the glasses from the Plinian tephra fallout and transitional cone deposits, which retained up to 2.7 and 3.44 wt.% H_2O, respectively. Altogether, the distributions and mean H_2O values in Chaitén eruptives are in agreement with the ones observed in glasses associated with explosive and effusive activity from previous rhyolite eruptions in other regions. Interestingly, by compiling measurements from previous works (Fig. 2.1), this study has identified a sharp boundary at ~0.5 wt.% that separates H_2O contents preserved in explosive and effusive products. This boundary is also clearly identified in the H_2O distribution observed for Chaitén. Based on these observations, a re-analysing of the existing published data on H_2O in rhyolite glasses (e.g., Newman et al., 1988; Rust and Cashman, 2007) is suggested.

A critical aspect related to the interpretation of H_2O retained in glasses is the discrimination between magmatic and secondary H_2O. For that reason, in this study a multi-methodological approach was followed in order to constrain the origin of the H_2O measured. First, the data was examined for evidence of disequilibrium speciation by comparing the hydrous species ratio in the glasses (OH^-:H_2O_m) with the equilibrium model of Nowak and Behrens (2001). Results revealed that most of the glasses show no evidence of significant incorporation of secondary (meteoric) H_2O. The extensive occurrence of bubble resorption (e.g., Watkins et al., 2012; McIntosh et al, 2014) seems also highly unlikely. However, disequilibrium speciation observed in a group of 17 samples highlight the need for further investigations. In particular, future work should focus on looking for H_2O disequilibrium profiles around bubbles and micro-fractures. Secondly, the comparison between glasses from the same volcanic deposit sampled twice, in 2008 (shortly after the eruption) and 2016, was performed. These results support the magmatic origin for the H_2O preserved in the obsidians of Chaitén, including the samples from the Plinian Fallout deposits with H_2O up to 3.4 wt.%. Finally, DSC-TGA measurements on 11 pumices showed that, unlike obsidians, this porous pyroclasts were probably hydrated during the time elapsed between their eruption and collection. TGA results offer a maximum H_2O content estimation for these samples, which range from 0.5 to 0.9 wt.%. To better constrain the total amount of magmatic vs. meteoric H_2O, this study should be repeated applying different heating rates.

Overall, non-vesicular glasses shows a defined H_2O depletion trend —from explosive to effusive deposits— for the 2008–2010 Chaitén eruptive cycle. The evolution of H_2O content was analyzed in three stratigraphic sections (two from the Plinian tephra fallout and one from the transitional cone). Similar features were identified in all the cases, with H_2O decreasing from base to top in each sequence. Internally, H_2O sub-trends were recognized in each sequence. However, the most striking finding was the occurrence of "H_2O content windows" within stratigraphic horizons, defined by upper and lower H_2O content values. These water content windows shift with stratigraphic position and demarcate clear H_2O gaps with respect to effusive obsidians. At the base of the sequence ΔH_2O is 1.48 wt.%, while at the top the difference between maximum and minimum H_2O preserved in the glasses is only 0.57 wt.%. Similar patterns were observed in other rhyolite systems, as Mono Craters and Newberry volcano, raising the question about the existence of any parameter(s) controlling the H_2O distribution observed in the different deposits. To address this, the experiments presented in Chapter 3 and 4 were performed.

Taking obsidian glass drilled from bombs and lava dome samples of 2008–2010 Chaitén eruption as starting material, a series of high-temperature, 0.1 MPa vesiculation experiments were carried out in order to explore the response of silicic melts (with different wt.% H_2O) to degassing at different temperatures. Experiments showed that when hydrous rhyolitic obsidians from Chaitén are experimentally heated above their glass transition temperatures at ambient 1 atm-conditions, two different behaviors result, depending on starting H_2O concentration and temperature: obsidians vesiculate to stable or quasi-steady state foams when H_2O is $\leq$1 wt.% for a wide range of temperatures (728–1032˚C), but will explode within just tens of seconds (<30 secs) of the foaming process when H_2O is 1.4 wt.% and T is >874˚C. Whether a foaming sample remains coherent or explodes depends on two interrelated factors, the Peclet number (*Pe*) —a dimensionless ratio of diffusive and viscous timescales— and the timescale or rate of decompression, which is dictated in part by the H_2O-vapour pressure gradient between bubbles and atmosphere. At or above 1.4 wt.% H_2O, and for a range of permissible Chaitén eruption temperatures, *Pe* is large (>10), meaning viscous deformation aiding vapour expansion is the dominant mode of growing bubbles. Consequently, vesiculation can proceed rapidly due to high initial overpressure and low melt viscosity, until the point is reached that the melt deforms at a rate greater than its relaxation rate, resulting in fragmentation. Below 1.4 wt.% H_2O and for temperatures equal to or lower than Chaitén's eruption, decompression and deformation rates, inferred from experimental clast expansion and bubble growth behavior, are at least an order of magnitude smaller than the explosive cases, which is insufficient for critical melt-rupturing. *Pe* estimations highlight the first order influence of temperature and H_2O content on physical degassing behavior. Since the starting H_2O content and temperature dictate many the parameters that govern bubble growth—pressure gradient, melt viscosity, and chemical diffusivity—these experiments shed light on what limits fragmentation in natural eruptions and offer an alternative explanation for H_2O contents measured in pyroclastic deposits from Chaitén and other rhyolite centers (e.g., Newman et al., 1988; Rust et al., 2004; Castro and Gardner, 2008). In essence, pyroclastic obsidian H_2O contents could reflect temperature and P-H_2O limitations on fragmentation. Interestingly, explosive behavior occurs above Chaitén's estimated eruption temperature (~780–825˚C). This temperature discrepancy implies that in the actual 2008 eruption, explosive fragmentation was fuelled by magma bearing higher H_2O contents than the one using for running the experiments. Coherent with that inference, H_2O content distributions for Plinian and transitional cone deposits show that Chaitén's pyroclastic obsidians preserved up to 2.6 wt% H_2O (excluding outliers, see Fig. 3.5). Unfortunately, the narrow range of H_2O contents preserved in the obsidian bombs of Chaitén (Fig. 3.4A) impedes the performance of experiments with higher H_2O concentrations using natural samples. An alternative that should be considered for future works is the experimental hydration of Chaitén glasses. At the same time, this research should be extended to a broader range of compositions (i.e., other silicic volcanic systems) in order to validate these findings at a larger scale.

Results from these experiments also show that foam expansion under low-P, high-T-H_2O conditions can foster strain rates in excess of the melt's relaxation rate and thus drive fragmentation (Fig. 4.13). Thus, in addition to rapid magma ascent (and high magma supply rates), rapid clast expansion under low pressure conditions may also be important for explosive magma fragmentation. In this sense, these experiments may shed light on degassing dynamics of low-pressure environments, such as the ones associated with tuffisites (Tuffen et al., 2003). These features have been observed to erupt copious ash, lapilli and bombs during hybrid explosive-effusive activity (e.g., Schipper et al., 2013). The opening and closing of tuffisites may impose intermittent pressure drops of (1–15 MPa) on the hydrous melt, and tuffisite's vertical connectivity (to 500 m; Castro et al., 2014), suggests that melt parcels would indeed be subject to rapid decompression to atmospheric levels.

Other relevant degassing scenarios include explosive pyroclast expansion above the fragmentation level in shallow conduits, or the rise of pyroclasts in eruptive plumes involving significant volatile exsolution as melt-H_2O solubility decreases under exceedingly low external pressures (~0.1 MPa; e.g., Kaminsky and Jaupart, 1997; Polacci et al., 2004). Together with the decompression experiments performed in the fragmentation bomb that are shown in Chapter 4, the results of this thesis provides insights in the evolution and dynamics of 2008-2010 Chaitén eruption. In addition, the similar patterns observed in the H_2O distribution of other rhyolite deposits, may allow making the findings of this thesis extensive to many other silicic systems.

A natural progression of the work presented in this thesis is to incorporate the parameter decompression rate to the experiments. Martel et al. (2000, 2001) had already foamed H_2O-oversatured rhyolites at high-T and P in a fragmentation bomb device. However, during their experiments, the authors triggered sample fragmentation (by sudden decompression), only after enabling the sample enough time to vesiculate at the target P-T (hence solubility-) conditions. In this way, the experiments allowed for the investigation of the effect of the magnitude of the decompression, porosity, and pore morphology on the fragment shape and size distribution. However, up to date, no experiments have tried to simulate explosive fragmentation by allowing vesiculation of melt due to sample decompression at eruptive relevant P-T-H_2O conditions. In this sense, the results of the 0.1 MPa experiments here presented provide a parameter space that future research could explore to shed light on vesiculation dynamics that take place in the last hundred of meter of volcanic conduits during an eruption.

Finally, Chapter 5 reminds us of the importance of understanding the mechanisms underlying the occurrence and dynamics of long-lasting rhyolite eruptions. These events can produce vast amounts of ash, with associated consequences and impacts on the environments and communities. In the study presented in that chapter, special effort was invested in the characterization of a secondary hazard associated with ash: wind-remobilization events and ash storms. The parameters responsible of controlling the occurrence of these events were identified, as well as their frequency and dynamics. At the same time, the impacts of these events on a farming community in the Argentinian Patagonian Steppe were evaluated by combining tools from natural and social sciences. Results show that although, the short-term impact of ash resuspension was highly negative, the environment and the farming community are showing signs of recovery after five years.

Bibliography

Abramoff, M.D., Magalhães, P.J., Ram, S.J. (2004). Image processing with ImageJ. Biophotonics international, 11(7), 36-42.

Aguirre, A. (2012). Estudio del impacto de las cenizas volcánicas en el proceso de esquila en una unidad productiva del centro norte de la provincia del Chubut, Ganadería. Junio (2012), pp. 199-202

Alatorre-Ibargüengoitia, M. A., Scheu, B., Dingwell, D. B., Delgado-Granados, H., Taddeucci, J. (2010). Energy consumption by magmatic fragmentation and pyroclast ejection during Vulcanian eruptions. Earth and Planetary Science Letters, 291(1-4), 60-69.

Alexander, A. E. (1934). The dustfall of November 13, 1933, at Buffalo, New York, J. Sediment. Petrol., 4(2), 81–82.

Alfano, F., Bonadonna, C., Gurioli, L. (2012). Insights into eruption dynamics from textural analysis: the case of the May, 2008, Chaitén eruption. Bulletin of Volcanology, 74(9), 2095-2108.

Alfano, F., Bonadonna, C., Volentik, A.C., Connor, C. B., Watt, S.F., Pyle, D.M., Connor, L.J. (2011). Tephra stratigraphy and eruptive volume of the May, 2008, Chaitén eruption, Chile. Bulletin of Volcanology, 73(5), 613-630.

Alidibirov, M., Dingwell, D.B. (1996a). Magma fragmentation by rapid decompression. Nature, 380 (6570), 146.

Alidibirov, M., Dingwell, D.B. (1996b). An experimental facility for the investigation of magma fragmentation by rapid decompression. Bulletin of Volcanology, 58(5), 411-416.

Alidibirov, M., Dingwell, D.B. (2000). Three fragmentation mechanisms for highly viscous magma under rapid decompression. Journal of Volcanology and Geothermal Research, 100(1-4), 413-421.

Alloway, B.V., Pearce, N.J., Moreno, P.I., Villarosa, G., Jara, I., De Pol-Holz, R., Outes, V. (2017). An 18,000 year-long eruptive record from Volcán Chaitén, northwestern Patagonia: Paleoenvironmental and hazard-assessment implications. Quaternary Science Reviews, 168, 151-181.

Amigo, A., Lara, L.E., Smith, V.C. (2013). Holocene record of large explosive eruptions from Chaitén and Michinmahuida Volcanoes, Chile. Andean Geology, 40(2).

Anovitz, L. M., Cole, D. R., Fayek, M. (2008). Mechanisms of rhyolitic glass hydration below the glass transition. American Mineralogist, 93(7), 1166-1178.

Arnalds, O., Thorarinsdottir, E.F., Thorsson, J., Waldhauserova, P.D., Agustsdottir, A.M. (2013). An extreme wind erosion event of the fresh Eyjafjallajökull 2010 volcanic ash. Scientific reports, 3, 1257.

Ayele, A., Jacques, E., Kassim, M., Kidane, T., Omar, A., Tait, S., King, G. (2007). The volcano–seismic crisis in Afar, Ethiopia, starting September 2005. Earth and Planetary Science Letters, 255(1-2), 177-187.

Bacon, C.R., Newman, S., Stolper, E. (1992). Water, CO_2, Cl, and F in melt inclusions in phenocrysts from three Holocene explosive eruptions, Crater Lake, Oregon. American Mineralogist; (United States), 77.

Bagdassarov, N.S., Dingwell, D.B. (1993). Deformation of foamed rhyolites under internal and external stresses: an experimental investigation. Bulletin of volcanology, 55(3), 147-154.

Bagdassarov, N.S., Dingwell, D.B., Wilding, M.C. (1996). Rhyolite magma degassing: an experimental study of melt vesiculation. Bulletin of volcanology, 57(8), 587-601.

Bagnold, R.A. (1941). The physics of blown sand and desert dunes. London: Methuen. Progress in physical geography, 18(1), 91-96.

Barclay, J., Riley, D.S., Sparks, R.S.J. (1995). Analytical models for bubble growth during decompression of high viscosity magmas. Bulletin of Volcanology, 57(6), 422-431.

Barnes, J. D., Prather, T. J., Cisneros, M., Befus, K., Gardner, J. E., Larson, T. E. (2014). Stable chlorine isotope behavior during volcanic degassing of H 2 O and CO 2 at Mono Craters, CA. Bulletin of Volcanology, 76(3), 805.

Bates, D., Mächler, M., Bolker, B., Walker, S., 2014. Fitting linear mixed-effects models using lme4. J. Stat. Softw.

Behrens, H., Romano, C., Nowak, M., Holtz, F., & Dingwell, D. B. (1996). Near-infrared spectroscopic determination of water species in glasses of the system MAlSi3O8 (M= Li, Na, K): an interlaboratory study. Chemical geology, 128(1-4), 41-63.

Bird, D.K. (2009). The use of questionnaires for acquiring information on public perception of natural hazards and risk mitigation–a review of current knowledge and practice. Natural Hazards and Earth System Sciences, 9(4), 1307-1325.

Bird, D.K., Gísladóttir, G. (2012). Residents' attitudes and behaviour before and after the 2010 Eyjafjallajökull eruptions—a case study from southern Iceland. Bulletin of volcanology, 74(6), 1263-1279.

Bitschene, P.R. (1995). Environmental impact and hazard assessment of the August 1991 eruption of Mt. Hudson (Patagonian Andes). In: Bitschene PR, Menida J (eds) The August 1991 eruption of the Hudson Volcano (Patagonian Andes): a thousand days after. Cuvillier, Gottingen, pp 2–15

Blank, J.G., Stolper, E.M., Carroll, M.R. (1993). Solubilities of carbon dioxide and water in rhyolitic melt at 850 C and 750 bars. Earth and Planetary Science Letters, 119(1-2), 27-36.

Bonadonna, C., Cioni, R., Pistolesi, M., Elissondo, M., Baumann, V. (2015a). Sedimentation of long-lasting wind-affected volcanic plumes: the example of the 2011 rhyolitic Cordón Caulle eruption, Chile. Bulletin of Volcanology, 77(2), 13.

Bonadonna, C., Pistolesi, M., Cioni, R., Degruyter, W., Elissondo, M., Baumann, V. (2015b). Dynamics of wind-affected volcanic plumes: The example of the 2011 Cordón Caulle eruption, Chile. Journal of Geophysical Research: Solid Earth, 120(4), 2242-2261.

Burnham, C. W. (1975). Water and magmas; a mixing model. Geochimica et Cosmochimica Acta, 39(8), 1077-1084.

Bursik, M. (1993). Subplinian eruption mechanisms inferred from volatile and clast dispersal data. Journal of Volcanology and Geothermal Research, 57(1-2), 57-70.

Carn, S.A., Pallister, J.S., Lara, L., Ewert, J.W., Watt, S., Prata, A.J., Villarosa, G. (2009). The unexpected awakening of Chaitén volcano, Chile. Eos, Transactions American Geophysical Union, 90(24), 205-206.

Cashman, K.V., Scheu, B. (2015). Magmatic fragmentation. In The Encyclopedia of Volcanoes (Second Edition) (pp. 459-471).

Castro, J.M., Mercer, C. (2004). Microlite textures and volatile contents of obsidian from the Inyo volcanic chain, California. Geophysical Research Letters, 31(18).

Castro, J. M., Gardner, J.E. (2008) Did magma ascent rate control the explosive-effusive transition at the Inyo volcanic chain, California? Geology, 36(4), 272-282.

Castro, J.M., Dingwell, D.B. (2009). Rapid ascent of rhyolitic magma at Chaitén volcano, Chile. Nature, 461(7265), 780-783.

Castro, J.M., Cordonnier, B., Tuffen, H., Tobin, M.J., Puskar, L., Martin, M.C., Bechtel, H.A. (2012a). The role of melt-fracture degassing in defusing explosive rhyolite eruptions at volcán Chaitén. Earth and Planetary Science Letters, 333, 63-69.

Castro, J.M., Burgisser, A., Schipper, C.I., Mancini, S. (2012b) Mechanisms of bubble coalescence in silicic magmas. Bulletin of Volcanology, 74, 2339-2352.

Castro, J.M., Schipper, C.I., Mueller, S.P., Militzer, A.S., Amigo, A., Parejas, C.S., Jacob, D. (2013). Storage and eruption of near-liquidus rhyolite magma at Cordón Caulle, Chile. Bulletin of Volcanology, 75(4), 702.

Castro, J.M., Bindeman, I.N., Tuffen, H., Schipper, C.I. (2014). Explosive origin of silicic lava: Textural and δD–H 2 O evidence for pyroclastic degassing during rhyolite effusion. Earth and Planetary Science Letters, 405, 52-61.

Carlsen, H.K., Gislason, T., Forsberg, B., Meister, K., Thorsteinsson, T., Jóhannsson, T., Oudin, A. (2015). Emergency hospital visits in association with volcanic ash, dust storms and other sources of ambient particles: a time-series study in Reykjavík, Iceland. International journal of environmental research and public health, 12(4), 4047-4059.

Cembrano, J., Lara, L. (2009). The link between volcanism and tectonics in the southern volcanic zone of the Chilean Andes: a review. Tectonophysics, 471(1-2), 96-113.

Cigala, V., Kueppers, U., Peña Fernández, J. J., Taddeucci, J., Sesterhenn, J., Dingwell, D. B. (2017). The dynamics of volcanic jets: Temporal evolution of particles exit velocity from shock-tube experiments. Journal of Geophysical Research: Solid Earth, 122(8), 6031-6045.

Cioni, R., Pistolesi, M., Rosi, M. (2015). Plinian and subplinian eruptions. In The Encyclopedia of Volcanoes (Second Edition), 519-535.

Clarke, A.B., Ongaro, T.E., Belousov, A. (2015). Vulcanian eruptions. In The Encyclopedia of Volcanoes (Second Edition), 505-518.

Collini, E., Osores, M.S., Folch, A., Viramonte, J.G., Villarosa, G., Salmuni, G. (2013). Volcanic ash forecast during the June 2011 Cordón Caulle eruption. Natural hazards, 66(2), 389-412.

Collini, E.A., Mingari, L., Reckziegel, F., Bustos, E., Baez, W., Andrioli, M., Folch, A. Alexander, P. Viramonte, J.G. (2015). Satellite images uncertainty: eruption or resuspension? The importance of the multidisciplinary approach. The case of June 13th, 2015 Ojos del Salado false volcanic eruption. In World Meteorological Organization 7th International Workshop on Volcanic Ash, Anchorage, Alaska, 19-23 October, 2015.

Coombs, M. L., Gardner, J. E. (2001). Shallow-storage conditions for the rhyolite of the 1912 eruption at Novarupta, Alaska. Geology, 29(9), 775-778.

Craig, H., Wilson, T., Stewart, C., Outes, V., Villarosa, G., Baxter, P. (2016a). Impacts to agriculture and critical infrastructure in Argentina after ashfall from the 2011 eruption of the Cordón Caulle volcanic complex: an assessment of published damage and function thresholds. Journal of Applied Volcanology, 5(1), 1.

Craig, H., Wilson, T., Stewart, C., Villarosa, G., Outes, V., Cronin, S., Jenkins, S. (2016b). Agricultural impact assessment and management after three widespread tephra falls in Patagonia, South America. Natural Hazards, 82(2), 1167-1229.

Dagsson-Waldhauserova, P., Arnalds, O., Olafsson, H. (2013). Long-term frequency and characteristics of dust storm events in Northeast Iceland (1949–2011). Atmospheric Environment, 77, 117-127.

Davis, M. J., Ihinger, P. D., Lasaga, A. C. (1997). Influence of water on nucleation kinetics in silicate melt. Journal of Non-Crystalline Solids, 219, 62-69.

Del Bello, E., Taddeucci, J., Merrison, J. P., Alois, S., Iversen, J. J., Scarlato, P. (2018). Experimental simulations of volcanic ash resuspension by wind under the effects of atmospheric humidity. *Scientific reports*, *8*(1), 14509.

Denton, J. S., Tuffen, H., Gilbert, J. S., Odling, N. (2009). The hydration and alteration of perlite and rhyolite. Journal of the Geological Society, 166(5), 895-904.

Dingwell, D.B., Webb, S.L. (1989). Structural relaxation in silicate melts and non-Newtonian melt rheology in geologic processes. Physics and Chemistry of Minerals, 16(5), 508-516.

Dingwell, D. B., Webb, S. L. (1990). Relaxation in silicate melts. European Journal of Mineralogy, (4), 427-449.

Dingwell, D.B. (1996). Volcanic dilemma: flow or blow?. Science, 273(5278), 1054.

Dingwell, D.B., Holtz, F., Behrens, H. (1997). The solubility of H2O in peralkaline and peraluminous granitic melts. American Mineralogist, 82(3), 434-437.

Dingwell, D.B. (2010). Experimental Volcanology: 2010 and 2020. In AGU Fall Meeting Abstracts (Vol. 1, p. 04).

Dingwell, D. B., Lavallée, Y., Hess, K. U., Flaws, A., Martí Molist, J., Nichols, A. R., Schillinger, B. (2016). Eruptive shearing of tube pumice: pure and simple.

Dobson, P.F., Epstein, S., Stolper, E.M. (1989). Hydrogen isotope fractionation between coexisting vapor and silicate glasses and melts at low pressure. Geochimica et Cosmochimica Acta, 53(10), 2723-2730.

Duhart, P., Moreno, H., Basualto, D., Mella, M., Muñoz, J. (2009). Erupción en curso del volcán Chaitén: productos, impactos y colapso parcial de domos del 19 de febrero de 2009. In Congreso Geológico Chileno (No. 12).

Dunbar, N. W., Kyle, P. R. (1992). Volatile contents of obsidian clasts in tephra from the Taupo Volcanic Zone, New Zealand: Implications to eruptive processes. Journal of volcanology and geothermal research, 49(1-2), 127-145.

Durant, A.J., Villarosa, G., Rose, W.I., Delmelle, P., Prata, A.J., Viramonte, J.G. (2012). Long-range volcanic ash transport and fallout during the 2008 eruption of Chaitén volcano, Chile. Physics and Chemistry of the Earth, Parts A/B/C, 45, 50-64.

Eichelberger, J. C., Westrich, H. R. (1981). Magmatic volatiles in explosive rhyolitic eruptions. Geophysical research letters, 8(7), 757-760.

Eichelberger, J.C., Carrigan, C.R., Westrich, H.R., Price, R.H. (1986). Non-explosive silicic volcanism. Nature, 323(6089), 598-602.

Eichelberger, J.C. (1995). Silicic volcanism: ascent of viscous magmas from crustal reservoirs. Annual Review of Earth and Planetary Sciences, 23(1), 41-63.

Elissondo, M., Baumann, V., Bonadonna, C., Pistolesi, M., Cioni, R., Bertagnini, A. Gonzalez, R. (2016). Chronology and impact of the 2011 Cordón Caulle eruption, Chile. Natural Hazards and Earth System Sciences,16(3), 675-704.

Fanara, S., Botcharnikov, R. E., Palladino, D. M., Adams, F., Buddensieck, J., Mulch, A., Behrens, H. (2015). Volatiles in magmas related to the Campanian Ignimbrite eruption: Experiments vs. natural findings. American Mineralogist, 100(10), 2284-2297.

Fécan, F., Marticorena, B., Bergametti, G. (1998). Parametrization of the increase of the aeolian erosion threshold wind friction velocity due to soil moisture for arid and semi-arid areas. In Annales Geophysicae (Vol. 17, No. 1, pp. 149-157). Springer-Verlag.

Fenn, P. M. (1977). The nucleation and growth of alkali feldspars from hydrous melts. The Canadian Mineralogist, 15(2), 135-161.

Fierstein, J., Hildreth, W. (1992). The plinian eruptions of 1912 at Novarupta, Katmai national park, Alaska. Bulletin of Volcanology, 54(8), 646-684.

Friedman, I., Long, W., Smith, R.L. (1963). Viscosity and water content of rhyolite glass. Journal of Geophysical Research, 68(24), 6523-6535.

Fogel, R.A., Rutherford, M.J. (1990). The solubility of carbon dioxide in rhyolitic melts; a quantitative FTIR study. American Mineralogist, 75(11-12), 1311-1326.

Folch, A., Mingari, L., Osores, M.S., Collini, E. (2014). Modeling volcanic ash resuspension. Application to the 14-18 October 2011 outbreak episode in Central Patagonia, Argentina. Nat. Hazards Earth Syst. Sci, 14, 119-133.

Fontijn, K., Lachowycz, S.M., Rawson, H., Pyle, D.M., Mather, T.A., Naranjo, J.A., Moreno-Roa, H. (2014). Late Quaternary tephrostratigraphy of southern Chile and Argentina. Quaternary Science Reviews, 89, 70-84.

Gaitán J.J., Ayesa J.A., Umaña F., Raffo F., Bran D.B. (2011). Cartografía del área afectada por cenizas volcánicas en las provincias de Río Negro y Neuquén. http://inta.gob.ar/documentos/cartografia-del-area-afectada-por-cenizas-volcanicas-en-las provincias-de-rio-negro-y-neuquen/.

Gardner, J.E., Hilton, M., Carroll, M.R. (1999). Experimental constraints on degassing of magma: isothermal bubble growth during continuous decompression from high pressure. Earth and Planetary Science Letters, 168(1-2), 201-218.

Gardner, J. E., Denis, M. H. (2004). Heterogeneous bubble nucleation on Fe-Ti oxide crystals in high-silica rhyolitic melts1. Geochimica et Cosmochimica Acta, 68(17), 3587-3597.

Gardner, J. E., Llewellin, E. W., Watkins, J. M., & Befus, K. S. (2017). Formation of obsidian pyroclasts by sintering of ash particles in the volcanic conduit. Earth and Planetary Science Letters, 459, 252-263.

Gelman, A., Hill, J., 2007. Data Analysis Using Regression and Multilevel/Hierarchical Models. Cambridge University Press

Gelman, Andrew, Yu-Sung, S., 2015. arm: Data Analysis Using Regression and Multilevel/ Hierarchical Models. R Package Version 1.8-5. URL. http://CRAN.R-project.org/ package=arm.

Gerlach, D.C., Frey, F.A., Moreno-Roa, H., Lopez- Escobar, L. (1988). Recent volcanism in the Puyehue- Cordón Caulle region, southern Andes, Chile (40.5°S): Petrogenesis of evolved lavas: Journal of Petrology, v. 29, p. 333–382.

Giachetti, T., Gonnermann, H. M. (2013). Water in volcanic pyroclast: Rehydration or incomplete degassing?. Earth and Planetary Science Letters, 369, 317-332.

Giachetti, T., Gonnermann, H. M., Gardner, J. E., Shea, T., & Gouldstone, A. (2015). Discriminating secondary from magmatic water in rhyolitic matrix-glass of volcanic pyroclasts using thermogravimetric analysis. Geochimica et Cosmochimica Acta, 148, 457-476.

Giordano, D., Nichols, A. R., & Dingwell, D. B. (2005). Glass transition temperatures of natural hydrous melts: a relationship with shear viscosity and implications for the welding process. Journal of Volcanology and Geothermal Research, 142(1-2), 105-118.

Giordano, D., Russell, J.K., Dingwell, D.B. (2008). Viscosity of magmatic liquids: a model. Earth and Planetary Science Letters, 271 123-134.

Global Volcanism Program. (1991a). Report on Cerro Hudson (Chile). In: McClelland, L (ed.), Bulletin of the Global Volcanism Network, 16:8. Smithsonian Institution. http://dx.doi.org/10.5479/si.GVP.BGVN199108-358057.

Global Volcanism Program. (1991b). Report on Cerro Hudson (Chile). In: McClelland, L (ed.), Bulletin of the Global Volcanism Network, 16:9. Smithsonian Institution. http://dx.doi.org/10.5479/si.GVP.BGVN199109-358057.

Global Volcanism Program. (1991c). Report on Cerro Hudson (Chile). In: McClelland, L (ed.), Bulletin of the Global Volcanism Network, 16:11. Smithsonian Institution. http://dx.doi.org/10.5479/si.GVP.BGVN199111-358057

Global Volcanism Program. (1992). Report on Cerro Hudson (Chile). In: McClelland, L (ed.), Bulletin of the Global Volcanism Network, 17:3. Smithsonian Institution. http://dx.doi.org/10.5479/si.GVP.BGVN199203-358057.

Gonnermann, H.M., Manga, M. (2003). Explosive volcanism may not be an inevitable consequence of magma fragmentation. Nature, 426(6965), 432.

Gonnermann, H.M., Manga, M. (2007). The fluid mechanics inside a volcano. Annu. Rev. Fluid Mech., 39, 321-356.

Gonnermann, H.M. (2015). Magma fragmentation. Annual Review of Earth and Planetary Sciences, 43, 431-458.

Greene, M., Perry, R., Lindell, M. (1981). The March 1980 eruptions of Mt. St. Helens: Citizen perceptions of volcano threat. Disasters, 5(1), 49-66.

Gregg, C.E., Houghton, B.F., Johnston, D.M., Paton, D., Swanson, D.A. (2004). The perception of volcanic risk in Kona communities from Mauna Loa and Hualālai volcanoes, Hawaii. Journal of Volcanology and Geothermal Research, 130(3), 179-196.

Guffanti, M., Tupper, A. (2014). Volcanic Ash Hazards and Aviation Risk. Volcanic Hazards, Risks and Disasters, Elsevier, Waltham, MA, 87-108.

Hadley, D., Hufford, G.L., Simpson, J.J. (2004). Resuspension of relic volcanic ash and dust from Katmai: still an aviation hazard. Weather and forecasting, 19(5), 829-840.

Hamilton, D. L., Burnham, C. W., Osborn, E. F. (1964). The solubility of water and effects of oxygen fugacity and water content on crystallization in mafic magmas. Journal of Petrology, 5(1), 21-39.

Hantke, G. (1940). Das Vulkangebiet zwischen den Seen Ranco und Puyehue in Sued-Chile: Bulletin of Volcanology, v. 7, p. 75–83

Hess, K. U., Dingwell, D. D. (1996). Viscosities of hydrous leucogranitic melts: A non-Arrhenian model. American Mineralogist, 81(9-10), 1297-1300.

Hildreth, W., Fierstein, J. (2012). The Novarupta-Katmai Eruption of 1912: Largest Eruption of the Twentieth Century: Centennial Perspectives (p. 259). US Geological Survey.

Hobbs, P.V., Hegg, D.A., Radke, L.F. (1983). Resuspension of volcanic ash from Mount St. Helens. Journal of Geophysical Research: Oceans, 88(C6), 3919-3921.

Horwell, C.J., Baxter, P.J. (2006). The respiratory health hazards of volcanic ash: a review for volcanic risk mitigation. Bulletin of Volcanology, 69, 1-24.

Horwell, C.J., Michnowicz, S., Le Blond, J. (2008). Report on the mineralogical and geochemical characterisation of Chaitén ash for the assessment of respiratory health hazard. University of Durham-IVHHN-Natural Environmental Research Council (unpublished).

Hurwitz, S., Navon, O. (1994). Bubble nucleation in rhyolitic melts: Experiments at high pressure, temperature, and water content. Earth and Planetary Science Letters, 122(3-4), 267-280.

Ihinger, P. D. (1991). An experimental study of the interaction of water with granitic melt (Doctoral dissertation, California Institute of Technology).

Ihinger, P. D., Hervig, R. L., McMillan, P. F. (1994). Analytical methods for volatiles in glasses. Reviews in Mineralogy and Geochemistry, 30(1), 67-121.

Ihinger, P. D., Zhang, Y., Stolper, E. M. (1999). The speciation of dissolved water in rhyolitic melt. Geochimica et Cosmochimica Acta, 63(21), 3567-3578.

INDEC (2010). Censo Nacional de Población, Hogares y Viviendas 2010.

INTA-EEA Chubut (Estación Experimental Chubut) 2011 Estado de situación y recomendaciones para enfrentar los efectos de la sequía y la ceniza en la provincia del Chubut (04/10/2011), INTA, Ministerio de Agricultura, Ganadería y Pesca, 5 pp., available at:http://inta.gob.ar/sites/default/files/script-tmp-recomendaciones_sequa_ceniza_chubut_octub_2011.pdf

Jaupart, C., Allègre, C.J. (1991). Gas content, eruption rate and instabilities of eruption regime in silicic volcanoes. Earth and Planetary Science Letters,102(3), 413-429.

Jay, J., Costa, F., Pritchard, M., Lara, L., Singer, B., Herrin, J. (2014). Locating magma reservoirs using InSAR and petrology before and during the 2011–2012 Cordón Caulle silicic eruption. Earth and Planetary Science Letters, 395, 254-266.

Jenkins, S.F., Wilson, T.M., Magill, C., Miller, V., Stewart, C., Blong, R., Costa, A. (2015). Volcanic ash fall hazard and risk. Global Volcanic Hazards and Risk. doi, 10(1017), 173-222.

Jicha, B.R., Singer, B.S., Beard, B.L., Johnson, C.M., Moreno-Roa, H., Naranjo, J.A. (2007). Rapid magma ascent and the generation of ^{230}Th excesses in the lower crust at Puyehue-Cordón Caulle, Southern Volcanic Zone, Chile: Earth and Planetary Science Letters, v. 255, p. 229–242.

Johnston, D.M., Bebbington Chin-Diew Lai, M.S., Houghton, B.F., Paton, D. (1999). Volcanic hazard perceptions: comparative shifts in knowledge and risk. Disaster Prevention and Management: An International Journal, 8(2), 118-126.

Kaminski, E., Jaupart, C. (1997). Expansion and quenching of vesicular magma fragments in Plinian eruptions. Journal of Geophysical Research: Solid Earth, 102 (B6), 12,187-12,203.

Katsui, Y., Katz, H.R. (1967). Lateral fissure eruptions in the southern Andes of Chile: Journal of the Faculty of Science, Hokkaido University Geology and Mineralogy, v. 13, p. 433–448.

Kueppers, U., Scheu, B., Spieler, O., Dingwell, D. B. (2006). Fragmentation efficiency of explosive volcanic eruptions: a study of experimentally generated pyroclasts. Journal of Volcanology and Geothermal Research, 153(1-2), 125-135

LADA (2010). Proyecto de Evaluación de Degradación de Tierras en Zonas Áridas (LADA) – Argentina. Sitio Piloto Ing. Jacobacci, Provincia de Rio Negro. Resultado de la evaluación del sitio Patagonia Norte. Noviembre. INTA Bariloche. Available in:

http://www.desertificacion.gob.ar/wp-content/uploads/2013/06/Informe-Final-SP-Jacobacci.pdf

Lara, L.E., Moreno-Roa, H., Naranjo, J.A. (2004). Rhyodacitic fissure eruption in Southern Andes (Cordón Caulle; 40.5°S) after the 1960 (Mw:9.5) Chilean earth- quake: A structural interpretation: Journal of Volcanology and Geothermal Research, v. 138, p. 127–138, doi: 10.1016/j.jvolgeores.2004.06.009.

Lara, L.E., Moreno, H. (2006). Geología del complejo volcánico Puyehue-Cordón Caulle, región de Los Lagos: Santiago, Servicio Nacional de Geología y Minería, Carta Geológica de Chile, Serie Geología Básica, no. 99, 26 p., 1 mapa escala 1:50,000.

Lara, L.E. (2009). The 2008 eruption of the Chaitén Volcano, Chile: a preliminary report. Andean geology, 36(1), 125-130.

Lara, L.E., Amigo, A., Silva, C., Orozco, G., Bertin, D. (2012). La erupción 2011-2012 del Cordón Caulle: antecedentes generales y rasgos notables de una erupción en curso. In Actas 13 Congreso Geológico Chileno, Antofagasta, Chile, 05–09 August 2012 (pp. 531-533).

Lara, L.E., Moreno, R., Amigo, Á., Hoblitt, R.P., Pierson, T.C. (2013). Late Holocene history of Chaitén Volcano: New evidence for a 17th century eruption. Andean Geology, 40(2).

Lavallée, Y., Dingwell, D.B., Johnson, J.B., Cimarelli, C., Hornby, A.J., Kendrick, J.E., Rhodes, E. (2015). Thermal vesiculation during volcanic eruptions. Nature, 528(7583), 544-547.

Lavenu, A., Cembrano, J. (1999). Compressional-and transpressional-stress pattern for Pliocene and Quaternary brittle deformation in fore arc and intra-arc zones (Andes of Central and Southern Chile). Journal of Structural Geology, 21(12), 1669-1691.

Leadbetter, S.J., Hort, M.C., Löwis, S., Weber, K., Witham, C.S. (2012). Modeling the resuspension of ash deposited during the eruption of Eyjafjallajökull in spring 2010. Journal of Geophysical Research: Atmospheres,117(D20).

Le Bas, M. J., Le Maitre, R. W., Streckeisen, A., Zanettin, B., IUGS Subcommission on the Systematics of Igneous Rocks. (1986). A chemical classification of volcanic rocks based on the total alkali-silica diagram. Journal of petrology, 27(3), 745-750.

Lensky, N.G., Navon, O., Lyakhovsky, V. (2004). Bubble growth during decompression of magma: experimental and theoretical investigation. Journal of Volcanology and Geothermal Research, 129(1-3), 7-22.

Leschik, M., Heide, G., Frischat, G. H., Behrens, H., Wiedenbeck, M., Wagner, N., Reinholz, U. (2004). Determination of H2O and D2O contents in rhyolitic glasses. Physics and Chemistry of Glasses, 45(4), 238-251.

Liu, E.J., Cashman, K.V., Beckett, F.M., Witham, C.S., Leadbetter, S.J., Hort, M.C., Guðmundsson, S. (2014). Ash mists and brown snow: Remobilization of volcanic ash from recent Icelandic eruptions. Journal of Geophysical Research: Atmospheres, 119(15), 9463-9480.

Liu, Y., Zhang, Y. (2000). Bubble growth in rhyolitic melt. Earth and Planetary Science Letters, 181(1-2), 251-264.

Liu, Y., Zhang, Y., Behrens, H. (2005). Solubility of H2O in rhyolitic melts at low pressures and a new empirical model for mixed H2O–CO2 solubility in rhyolitic melts. Journal of Volcanology and Geothermal Research, 143(1-3), 219-235.

Lopez-Escobar, L., Kilian, R., Kempton, P.D., Tagiri, M. (1993). Petrography and geochemistry of Quaternary rocks from the Southern Volcanic Zone of the Andes between 41 30’and 46 00’S, Chile. Andean Geology, 20(1), 33-55.

López-Escobar, L., Cembrano, J., Moreno, H. (1995). Geochemistry and tectonics of the Chilean Southern Andes basaltic Quaternary volcanism (37-46 S). Andean Geology, 22(2), 219-234.

Lowenstern, J.B., Bleick, H., Vazquez, J.A., Castro, J.M., Larson, P.B. (2012). Degassing of Cl, F, Li, and Be during extrusion and crystallization of the rhyolite dome at Volcán Chaitén, Chile during 2008 and 2009. Bulletin of Volcanology, 74(10), 2303-2319.

Lyakhovsky, V., Hurwitz, S., Navon, O. (1996). Bubble growth in rhyolitic melts: experimental and numerical investigation. Bulletin of volcanology, 58(1), 19-32

Mangan, M., Sisson, T. (2000). Delayed, disequilibrium degassing in rhyolite magma: decompression experiments and implications for explosive volcanism. Earth and Planetary Science Letters, 183(3-4), 441-455.

Martel, C., Dingwell, D.B., Spieler, O., Pichavant, M., Wilke, M. (2000). Fragmentation of foamed silicic melts: an experimental study. Earth and Planetary Science Letters, 178(1-2), 47-58.

Martel, C., Dingwell, D.B., Spieler, O., Pichavant, M., Wilke, M. (2001) Experimental fragmentation of crystal- and vesicle-bearing silicic melts. Bulletin of Volcanology, 63, 398-405.

Martin, R.S., Watt, S.F.L., Pyle, D.M., Mather, T.A., Matthews, N.E., Georg, R.B., Quayle, B.M. (2009). Environmental effects of ashfall in Argentina from the 2008 Chaitén volcanic eruption. Journal of Volcanology and Geothermal Research, 184(3), 462-472.

Mastin, L. G. (2001), A simple calculator of ballistic trajectories for blocks ejected during volcanic eruptions, U.S. Geol. Surv. Open File Rep., 01-45

Miller, E.R. (1934). Meteorology of the dustfall of November 12–13, 1933, J. Sediment. Petrol., 4, 78–81.

Mingari, L.A., Collini, E.A., Folch, A., Báez, W., Bustos, E., Osores, M. S., Viramonte, J. G. (2017). Numerical simulations of windblown dust over complex terrain: the Fiambalá Basin episode in June 2015. Atmospheric Chemistry and Physics, 17(11), 6759.

Mitchell, S. J., McIntosh, I. M., Houghton, B. F., Carey, R. J., Shea, T. (2018). Dynamics of a powerful deep submarine eruption recorded in H 2 O contents and speciation in rhyolitic glass: The 2012 Havre eruption. Earth and Planetary Science Letters, 494, 135-147.

Moreno, P.I., Alloway, B.V., Villarosa, G., Outes, V., Henríquez, W.I., De Pol-Holz, R., Pearce, N.J.G. (2015). A past-millennium maximum in postglacial activity from Volcán Chaitén, southern Chile. Geology, 43(1), 47-50.

Mourtada-Bonnefoi, C.C., Laporte, D. (1999). Experimental study of homogeneous bubble nucleation in rhyolitic magmas. Geophysical Research Letters, 26(23), 3505-3508.

Murase, T., McBirney A.R. (1973). Properties of some common igneous rocks and their melts at high temperatures. Geological Society of America Bulletin, 84(11), 3563-3592.

Murgida, A.M., Gentile E.E. (2015). Aceptabilidad y amplificación del riesgo en la estepa nor-patagónica. In: Viand, J. and Briones, F. (eds.) Riesgos al Sur. Diversidad de riesgos de desastres en Argentina. Red de Estudios Sociales en Prevención de Desastres en América Latina, pp. 195-214.

Murgida, A.M., Laham, F.M., Chiappe, C.J.P., Kazimierski, M.A. (2015). Desarrollo Territorial bajo Sequía y Cenizas. ILUMINURAS, 17(41).

Naranjo, J.A., Stern, C.R. (2004). Holocene tephrochronology of the southernmost part (42 30'-45 S) of the Andean Southern Volcanic Zone. Revista geológica de Chile, 31(2), 224-240.

Navon, O., Lyakhovsky, V. (1998). Vesiculation processes in silicic magmas. Geological Society, London, Special Publications, 145(1), 27-50.

Newman, S., Epstein, S., Stolper, E. (1988). Water, carbon dioxide, and hydrogen isotopes in glasses from the ca. 1340 AD eruption of the Mono Craters, California: constraints on degassing phenomena and initial volatile content. Journal of Volcanology and Geothermal Research, 35(1), 75-96.

Newman, S., Lowenstern, J.B. (2002). VolatileCalc: a silicate melt–H2O–CO2 solution model written in Visual Basic for excel. Computers & Geosciences, 28(5), 597-604.

Ni, H., Zhang, Y. (2008). H 2 O diffusion models in rhyolitic melt with new high pressure data. Chemical Geology, 250(1), 68-78.

Nowak, M., Behrens, H. (2001). Water in rhyolitic magmas: getting a grip on a slippery problem. Earth and Planetary Science Letters, 184(2), 515-522.

Ochs, F. A., Lange, R. A. (1999). The density of hydrous magmatic liquids. Science, 283(5406), 1314-1317.

Pallister, J.S., Diefenbach, A., Burton, W., Muñoz, J., Griswold, J., Lara, L., Valenzuela, C.E. (2013). The Chaitén rhyolite lava dome: Eruption sequence, lava dome volumes, rapid effusion rates and source of the rhyolite magma. Andean Geology, 40(2), 277-294.

Panebianco, J.E., Mendez, M.J., Buschiazzo, D.E., Bran, D., Gaitán, J.J. (2017). Dynamics of volcanic ash remobilisation by wind through the Patagonian steppe after the eruption of Cordón Caulle, 2011. Scientific Reports, 7.

Papale, P. (1999). Strain-induced magma fragmentation in explosive eruptions. Nature, 397(6718), 425.

Paton, D., Millar, M., Johnston, D. (2001). Community resilience to volcanic hazard consequences. Natural hazards, 24(2), 157-169.

Peterson, T. D. (1996). A refined technique for measuring crystal size distributions in thin section. Contributions to Mineralogy and Petrology, 124(3-4), 395-405.

Pierson, T. C., Major, J. J., Amigo, Á., Moreno, H. (2013). Acute sedimentation response to rainfall following the explosive phase of the 2008–2009 eruption of Chaitén volcano, Chile. Bulletin of Volcanology, 75(5), 723.

Pistolesi, M., Cioni, R., Bonadonna, C., Elissondo, M., Baumann, V., Bertagnini, A., Francalanci, L. (2015). Complex dynamics of small-moderate volcanic events: the example of the 2011 rhyolitic Cordón Caulle eruption, Chile. Bulletin of Volcanology, 77(1), 1-24.

Potuzak, M., Mangiacapra, A., Kueppers, U., Richard, D., Dingwell, D.B., Orsi, G., di Vito, M.A. (2006). The Da'ure' eruption at the Boyna Volcanic Complex during the September 2005 Afar Extension Episode: Petrophysical Characterisation and Eruptive Implications. In AGU Fall Meeting Abstracts.

Proussevitch, A.A., Sahagian, D.L. (1996). Dynamics of coupled diffusive and decompressive bubble growth in magmatic systems. Journal of Geophysical Research: Solid Earth, 101(B8), 17447-17455.

Quality of Urban Air Review Group. (1996). Airborne particulate matter in the United Kingdom. Department of the Environment, Belfast, 3, pp 30.

Reckziegel, F., Bustos, E., Mingari, L., Báez, W., Villarosa, G., Folch, A., Osores, S. (2016). Forecasting volcanic ash dispersal and coeval resuspension during the April–May 2015 Calbuco eruption. Journal of Volcanology and Geothermal Research, 321, 44-57.

Romero, J.E., Morgavi, D., Arzilli, F., Daga, R., Caselli, A., Reckziegel, F., Perugini, D. (2016). Eruption dynamics of the 22–23 April 2015 calbuco volcano (Southern Chile): Analyses of tephra fall deposits. Journal of Volcanology and Geothermal Research, 317, 15-29.

Rust, A.C., Cashman, K.V. (2007). Multiple origins of obsidian pyroclasts and implications for changes in the dynamics of the 1300 BP eruption of Newberry Volcano, USA. Bulletin of Volcanology, 69(8), 825-845.

Rust, A.C., Cashman, K.V., Wallace, P.J. (2004). Magma degassing buffered by vapor flow through brecciated conduit margins. Geology, 32(4), 349-352.

Ryan, A.G., Russell, J.K., Nichols, A.R., Hess, K.U., Porritt, L.A. (2015). Experiments and models on H2O retrograde solubility in volcanic systems.American Mineralogist, 100(4), 774-786.

Sato, H., Fujii, T., Nakada, S. (1992). Crumbling of dacite dome lava and generation of pyroclastic flows at Unzen volcano. Nature, 360, 664-666.

Scasso, R.A., Corbella, H., Tiberi, P. (1994). Sedimentological analysis of the tephra from the 12–15 August 1991 eruption of Hudson volcano. Bulletin of Volcanology, 56(2), 121-132.

Schipper, C.I., Castro, J.M., Tuffen, H., James, M.R., How, P. (2013). Shallow vent architecture during hybrid explosive–effusive activity at Cordón Caulle (Chile, 2011–12): evidence from direct observations and pyroclast textures. Journal of Volcanology and Geothermal Research, 262, 25-37.

SERNAGEOMIN (2015a). Reporte de la Actividad Volcánica (RAV) Región de Los Lagos Año 2015 Abril Volumen 4. Available in: < http://www.sernageomin.cl/reportesVolcanes/2015042307582239RAV_Los_Lagos_2015_abril_vol_4.pdf>

SERNAGEOMIN (2015b). Reporte de Actividad Volcánica (RAV) Región de Los Lagos Año 2015 Mayo Volumen 31. Available in: < http://www.sernageomin.cl/reportesVolcanes/20150519124146145RAV_Los_Lagos_2015_05_19_vol_31.pdf>#

Silver, L.A. (1988). Water in silicate glasses. Ph. D. Thesis, Cal. Tech., 238 pp.

Silver, L.A., Ihinger, P.D., Stolper, E. (1990). The influence of bulk composition on the speciation of water in silicate glasses. Contributions to Mineralogy and Petrology, 104(2), 142-162.

Silva Parejas, C., Lara, L.E., Bertin, D., Amigo, A., Orozco, G. (2012). The 2011-2012 eruption of Cordón Caulle volcano (Southern Andes): Evolution, crisis management and current hazards. In EGU General Assembly Conference Abstracts (Vol. 14, p. 9382).

Singer, B.S., Jicha, B.R., Harper, M.A., Naranjo, J.A., Lara, L.E., Moreno-Roa, H. (2008). Eruptive history, geochronology, and magmatic evolution of the Puyehue-Cordón Caulle volcanic complex, Chile. Geological Society of America Bulletin, 120(5-6), 599-618.

Sivakumar, M.V. (2005). Impacts of sand storms/dust storms on agriculture. In Natural disasters and extreme events in agriculture (pp. 159-177). Springer Berlin Heidelberg.

Shao, Y., Raupach, M.R., Findlater, P.A. (1993). Effect of saltation bombardment on the entrainment of dust by wind. Journal of Geophysical Research: Atmospheres, 98(D7), 12719-12726.

Shaw, H. R. (1972). Viscosities of magmatic silicate liquids; an empirical method of prediction. American Journal of Science, 272(9), 870-893.

Sparks, R.S.J. (1978). The dynamics of bubble formation and growth in magmas: a review and analysis. Journal of Volcanology and Geothermal Research, 3(1-2), 1-37.

Sparks, R.S.J., Barclay, J., Jaupart, C., Mader, H.M., Phillips. (1994). Physical aspects of Magmatic Degassing I. Experimental and Theoretical Constraints on Vesiculation. Reviews in Mineralogy, 30, 413-445.

Spieler, O., Kennedy, B., Kueppers, U., Dingwell, D.B., Scheu, B., Taddeucci, J. (2004). The fragmentation threshold of pyroclastic rocks. Earth and Planetary Science Letters, 226, 139-148.

Stern, C.R. (2004). Active Andean volcanism: its geologic and tectonic setting. Revista geológica de Chile, 31(2), 161-206.

Stevenson, R.J., Bagdassarov, N.S., Romano, C. (1997). Vesiculation processes in a water-rich calc-alkaline obsidian. Earth and planetary science letters, 146(3), 555-571.

Stolper, E. (1982a). The speciation of water in silicate melts. Geochimica et Cosmochimica Acta, 46(12), 2609-2620.

Stolper, E. (1982b). Water in silicate glasses: an infrared spectroscopic study. Contributions to Mineralogy and Petrology, 81(1), 1-17.

Stone, J.B. (1935). The volcanoes of southern Chile: Zeit Vulkanologie, v. 16, p. 81–97

Taddeucci, J., Spieler, O., Kennedy, B., Pompilio, M., Dingwell, D. B., Scarlato, P. (2004), Experimental and analytical modelling of basaltic ash explosions at Mount Etna, Italy, 2001. Journal of Geophysical Research: Solid Earth, 109(B8).

Tait, S., Jaupart, C., Vergniolle, S. (1989). Pressure, gas content and eruption periodicity of a shallow, crystallising magma chamber. Earth and Planetary Science Letters, 92(1), 107-123.

Tamic, N., Behrens, H., Holtz, F. (2001). The solubility of H2O and CO2 in rhyolitic melts in equilibrium with a mixed CO2–H2O fluid phase. Chemical geology, 174(1-3), 333-347.

Tatur, A., del Valle, R., Bianchi, M.M., Outes, V., Villarosa, G., Niegodzisz, J., Debaene, G. (2002). Late Pleistocene palaeolakes in the Andean and Extra-Andean Patagonia at mid-latitudes of South America. Quaternary International,89(1), 135-150

Taylor, B.E. (1991). Degassing of obsidian dome rhyolite, Inyo volcanic chain, California. Geochemical Society Special Publication, 3, 339-353.

Taylor, H. P. (1983). Oxygen and hydrogen isotope studies of hydrothermal interactions at submarine and subaerial spreading centers. In Hydrothermal Processes at Seafloor Spreading Centers (pp. 83-139). Springer, Boston, MA.

Thorarinsson, S. (1944). Tefrokronologiska studier på Island: Þjórsárdalur och dess förödelse. Geografiska annaler, 26(1-2), 1-217.

Toramaru, A. (1989). Vesiculation process and bubble size distributions in ascending magmas with constant velocities. Journal of Geophysical Research: Solid Earth, 94(B12), 17523-17542.

Toramaru, A. (1995). Numerical study of nucleation and growth of bubbles in viscous magmas. Journal of Geophysical Research: Solid Earth, 100(B2), 1913-1931

Toramaru, A. (2006). BND (bubble number density) decompression rate meter for explosive volcanic eruptions. Journal of Volcanology and Geothermal Research, 154(3-4), 303-316.

Toschev S (1973) Homogeneous nucleation. In: Hartman P (ed) Crystal growth: an introduction. Elsevier, New York, pp 1– 49

Turcotte, D. L., H. Ockendon, J. R. Ockendon, and S. J. Cowley (1990). A mathematical model for Vulcanian eruptions, Geophys. J. Int., 103,211– 217.

Tuffen, H., Dingwell, D.B., Pinkerton, H. (2003). Repeated fracture and healing of silicic magma generate flow banding and earthquakes?. Geology,31(12), 1089-1092.

Tuffen, H., Castro, J. M. (2009). The emplacement of an obsidian dyke through thin ice: Hrafntinnuhryggur, Krafla Iceland. Journal of Volcanology and Geothermal Research, 185(4), 352-366.

Tuffen, H., Owen, J., Denton, J. (2010). Magma degassing during subglacial eruptions and its use to reconstruct palaeo-ice thicknesses. Earth-Science Reviews, 99(1-2), 1-18

Tuffen, H., James, M.R., Castro, J.M., Schipper, C.I. (2013). Exceptional mobility of an advancing rhyolitic obsidian flow at Cordón Caulle volcano in Chile. Nature communications, 4.

Tuttle, O. F., Bowen, N. L. (1958). Origin of granite in the light of experimental studies in the system: NaAlSi3O8 (Vol. 74). Geological Society of America.

Ulke, A.G., Brizuela, M.M.T., Raga, G.B., Baumgardner, D. (2016). Aerosol properties and meteorological conditions in the city of Buenos Aires, Argentina, during the resuspension of volcanic ash from the Puyehue-Cordón Caulle eruption. Natural Hazards and Earth System Sciences, 16(9), 2159.

UNEP. (1992). World Atlas of Desertification. London: Edward Arnold. ix+ 69pp

Van Eaton, A.R., Amigo, Á., Bertin, D., Mastin, L.G., Giacosa, R.E., González, J., Behnke, S. A. (2016). Volcanic lightning and plume behavior reveal evolving hazards during the April 2015 eruption of Calbuco volcano, Chile. Geophysical Research Letters, 43(7), 3563-3571.

von Aulock, F. W., Kennedy, B. M., Schipper, C. I., Castro, J. M., Martin, D. E., Oze, C., Nichols, A. R. (2014). Advances in Fourier transform infrared spectroscopy of natural glasses: From sample preparation to data analysis. Lithos, 206, 52-64.

von Aulock, F.W., Kennedy, B.M., Maksimenko, A., Wadsworth, F.B., Lavallée, Y. (2017). Outgassing from Open and Closed Magma Foams. Frontiers in Earth Science, 5, 46.

Wadsworth, F. B., Witcher, T., Vossen, C. E., Hess, K. U., Unwin, H. E., Scheu, B., Castro, J.M., Dingwell, D. B. (2018). Combined effusive-explosive silicic volcanism straddles the multiphase viscous-to-brittle transition. Nature communications, 9(1), 4696.

Wallace, K., Hansen, H., Schneider, D. Scwaiger, H. (2015). Resuspended Volcanic Ash from the Katmai Region to Kodiak Island. In World Meteorological Organization 7th International Workshop on Volcanic Ash, Anchorage, Alaska, 19-23 October, 2015.

Wallace, P.J. (2005). Volatiles in subduction zone magmas: concentrations and fluxes based on melt inclusion and volcanic gas data. Journal of Volcanology and Geothermal Research, 140(1-3), 217-240.

Wallace, P.J., Plank, T., Edmonds, M., Hauri, E.H. (2015). Volatiles in magmas. In The Encyclopedia of Volcanoes (Second Edition), 163-183.

Wasserburg, G. J. (1957). The Effects of in Silicate Systems. The Journal of Geology, 65(1), 15-23.

Watkins, J. M., Manga, M., De Paolo, D. J. (2012). Bubble geobarometry: A record of pressure changes, degassing, and regassing at Mono Craters, California. Geology, 40(8), 699-702.

Watt, S.F., Pyle, D.M., Mather, T.A., Martin, R.S., Matthews, N.E. (2009). Fallout and distribution of volcanic ash over Argentina following the May 2008 explosive eruption of Chaitén, Chile. Journal of Geophysical Research: Solid Earth, 114(B4).

Watt, S.F., Pyle, D.M., Mather, T.A. (2013). Evidence of mid-to late-Holocene explosive rhyolitic eruptions from Chaitén Volcano, Chile. Andean Geology, 40(2).

Webb, S. L., Dingwell, D. B. (1990). The onset of non-Newtonian rheology of silicate melts. Physics and Chemistry of Minerals, 17(2), 125-132.

Wicks, C., de La Llera, J.C., Lara, L.E., Lowenstern, J. (2011). The role of dyking and fault control in the rapid onset of eruption at Chaitén volcano, Chile. Nature, 478(7369), 374.

Wilson, L. (1980). Relationships between pressure, volatile content and ejecta velocity in three types of volcanic explosions, J. Volcanol. Geotherm. Res., 8, 297–313

Wilson, T.M., Cole, J.W., Stewart, C., Cronin, S.J., Johnston, D.M. (2011). Ash storms: impacts of wind-remobilised volcanic ash on rural communities and agriculture following the 1991 Hudson eruption, southern Patagonia, Chile. Bulletin of Volcanology, 73(3), 223-239.

Wilson, T.M., Stewart, C., Sword-Daniels, V., Leonard, G.S., Johnston, D.M., Cole, J.W. Barnard, S. T. (2012). Volcanic ash impacts on critical infrastructure. Physics and Chemistry of the Earth, Parts A/B/C, 45, 5-23.

Wilson, T., Stewart, C., Bickerton, H., Baxter, P., Outes, V., Villarosa, G., Rovere, E. (2013). Impacts of the June 2011 Puyehue–Cordón Caulle volcanic complex eruption on urban infrastructure, agriculture and public health. GNS Science Report, 20.

Withers, A. C., Behrens, H. (1999). Temperature-induced changes in the NIR spectra of hydrous albitic and rhyolitic glasses between 300 and 100 K. Physics and Chemistry of Minerals, 27(2), 119-132.

Woods, A.W., Koyaguchi, T. (1994). Transitions between explosive and effusive eruptions of silicic magmas. Nature, 370(6491), 641-644.

Woods, A. W. (1995). A model for Vulcanian explosions, Nucl. Eng. Design, 155, 345–357.

Wright, T.J., Ebinger, C., Biggs, J., Ayele, A., Yirgu, G., Keir, D., Stork, A. (2006). Magma-maintained rift segmentation at continental rupture in the 2005 Afar dyking episode. Nature, 442(7100), 291.

Yoshimura, S., Nakamura, M. (2008). Diffusive dehydration and bubble resorption during open-system degassing of rhyolitic melts. Journal of Volcanology and Geothermal Research, 178(1), 72-80.

Zhang, Y., Stolper, E. M. (1991). Water diffusion in a basaltic melt. Nature, 351(6324), 306.

Zhang, Y., Stolper, E. M., Wasserburg, G. J. (1991). Diffusion of water in rhyolitic glasses. Geochimica et Cosmochimica Acta, 55(2), 441-456.

Zhang, Y. (1999a). A criterion for the fragmentation of bubbly magma based on brittle failure theory. Nature, 402(6762), 648.

Zhang, Y. (1999b). H2O in rhyolitic glasses and melts: measurement, speciation, solubility, and diffusion. Reviews of Geophysics, 37(4), 493-516.

Zhang, Y., Behrens, H. (2000). H_2O diffusion in rhyolitic melts and glasses. Chemical Geology, 169(1), 243-262.

Zhang, Y., Xu, Z., & Behrens, H. (2000). Hydrous species geospeedometer in rhyolite: improved calibration and application. Geochimica et Cosmochimica Acta, 64(19), 3347-3355.

Zhang, Y., Xu, Z., Zhu, M., Wang, H. (2007). Silicate melt properties and volcanic eruptions. Reviews of Geophysics, 45(4).

Zhang, Y., & Ni, H. (2010). Diffusion of H, C, and O components in silicate melts. Reviews in Mineralogy and Geochemistry, 72(1), 171-225.

Appendices

A. FTIR measurements

Explosive phase - Tephra fallout deposit sampled in 2008 (CH_Exp)

Sample		OH^- wt.% (4500)	sd	H_2O_m wt.% (5200)	sd	H2Ot* wt.%	sd	n
CH_Exp_1	1_1	0.83	0.01	0.22	0.01	1.06	0.02	2
	1_2	0.64	0.03	0.11	0.01	0.75	0.04	2
	1_3	0.75	0.01	0.18	0.00	0.93	0.02	2
	1_4	0.67	0.06	0.14	0.01	0.80	0.07	2
	1_5	0.72	0.03	0.13	0.01	0.85	0.03	3
	1_6	0.58	0.00	0.12	0.01	0.70	0.01	2
	1_7	0.68	0.06	0.14	0.01	0.81	0.07	2
	1_8	0.69	0.06	0.14	0.01	0.83	0.07	2
	1_9	0.74	0.00	0.14	0.02	0.88	0.02	2
	1_10	0.51	0.02	0.13	0.02	0.64	0.04	2
	1_11	0.67	0.01	0.17	0.03	0.84	0.05	2
	1_12	0.90	0.01	0.24	0.00	1.14	0.01	2
	1_13	0.89	0.00	0.26	0.02	1.15	0.02	2
	1_14	0.56	0.02	0.07	0.00	0.63	0.02	2
CH_Exp_2	2_1	1.23	0.06	0.38	0.06	1.61	0.12	2
	2_2	0.75	0.07	0.18	0.01	0.92	0.08	2
	2_3	0.84	0.00	0.18	0.01	1.02	0.01	2
	2_4	0.90	0.02	0.21	0.01	1.11	0.03	2
	2_5	0.88	0.00	0.18	0.00	1.06	0.00	2
	2_6	0.75	0.00	0.14	0.00	0.89	0.00	3
	2_7	0.92	0.02	0.25	0.01	1.17	0.03	2
	2_8	0.99	0.04	0.34	0.01	1.34	0.05	2
	2_9	0.74	0.01	0.16	0.01	0.90	0.02	2
	2_10	0.71	0.00	0.14	0.00	0.85	0.00	2
CH_Exp_3	3_1	0.94	0.00	0.26	0.01	1.21	0.01	2
	3_2	1.00	0.00	0.33	0.00	1.33	0.01	2
	3_3	0.78	0.02	0.17	0.00	0.95	0.02	2
	3_4	0.99	0.02	0.37	0.00	1.36	0.03	2
	3_5	0.83	0.04	0.24	0.01	1.07	0.05	2
	3_6	0.80	0.01	0.19	0.00	0.99	0.01	2
	3_7	0.97	0.00	0.29	0.02	1.25	0.02	2
	3_8	0.90	0.03	0.28	0.01	1.18	0.04	2
	3_9	1.11	0.01	0.45	0.00	1.56	0.02	2
	3_10	0.94	0.00	0.32	0.01	1.25	0.01	2

CH_Exp_4	4_1	1.44	0.02	1.16	0.08	2.61	0.10	2
	4_2	0.97	0.05	0.37	0.02	1.34	0.07	2
	4_3	0.75	0.05	0.16	0.00	0.90	0.05	2
	4_4	1.27	0.01	0.80	0.01	2.08	0.02	2
	4_5	1.16	0.03	0.59	0.01	1.74	0.03	2
	4_6	0.81	0.05	0.22	0.00	1.03	0.05	2
	4_7	0.93	0.02	0.27	0.02	1.21	0.04	2
	4_8	1.08	0.00	0.37	0.02	1.45	0.02	2
	4_9	-	-	-	-	0.16	0.01	2
	4_10	1.13	0.01	0.47	0.01	1.60	0.02	2
CH_Exp_5	5_1	-	-	-	-	0.24	0.00	2
	5_2	0.71	0.09	0.62	0.09	1.34	0.18	2
	5_3	0.77	0.11	0.23	0.03	1.00	0.14	2
	5_4	-	-	-	-	0.20	0.00	2
	5_5	0.67	0.02	0.18	0.01	0.85	0.03	2
	5_6	-	-	-	-	0.19	0.01	2
	5_7	0.67	0.03	0.13	0.01	0.81	0.04	2
	5_8	-	-	-	-	0.22	0.01	2
	5_9	1.43	0.06	1.05	0.02	2.47	0.08	2
	5_10	-	-	-	-	0.50	0.01	2
	5_11	0.92	0.03	0.32	0.00	1.24	0.03	2
	5_12	-	-	-	-	0.14	0.00	2
	5_13	1.21	0.19	0.84	0.13	2.04	0.32	4
	5_14	-	-	-	-	0.12	0.00	2

Explosive phase - Tephra fallout deposit sampled in 2016 (Rio_AM)

Sample		OH^- wt.% (4500)	sd	H_2O_mwt.% (5200)	sd	H_2O_t* wt.%	sd	n
Rio AM_0	0_1	-	-	-	-	0.20	0.02	2
	0_2	0.67	0.04	0.14	0.00	0.81	0.04	2
	0_3	-	-	-	-	0.21	0.00	2
	0_4	1.19	0.02	0.41	0.03	1.60	0.05	2
	0_5	0.67	0.03	0.14	0.01	0.81	0.04	2
	0_6	0.61	0.01	0.13	0.04	0.74	0.05	2
	0_7	0.63	0.02	0.15	0.01	0.78	0.03	2
	0_8	0.94	0.01	0.24	0.01	1.18	0.02	2
	0_9	0.56	0.01	0.13	0.00	0.69	0.02	2
	0_10	0.67	0.01	0.10	0.00	0.76	0.01	2
	0_11	-	-	-	-	0.24	0.00	2
Rio_AM_1	1_1	0.89	0.04	0.35	0.00	1.24	0.05	2
	1_2	0.97	0.01	0.29	0.01	1.25	0.02	2
	1_3	1.00	0.01	0.35	0.00	1.35	0.01	2

	1_4	0.67	0.01	0.20	0.01	0.88	0.02	2
	1_5	1.53	0.00	0.75	0.02	2.28	0.02	2
	1_6	1.02	0.00	0.41	0.02	1.43	0.03	2
	1_7	0.95	0.02	0.30	0.00	1.24	0.02	2
	1_8	1.18	0.02	0.56	0.03	1.74	0.06	2
	1_9	0.95	0.05	0.34	0.01	1.29	0.06	2
	1_10	0.95	0.02	0.35	0.02	1.30	0.04	2
	1_11	1.22	0.03	0.66	0.01	1.88	0.04	2
Rio _AM_2	2_1	0.87	0.02	0.27	0.00	1.13	0.02	2
	2_2	0.97	0.04	0.21	0.01	1.18	0.05	2
	2_3	0.76	0.01	0.29	0.17	1.05	0.18	2
	2_4	1.07	0.58	0.21	0.00	1.28	0.58	2
	2_5	0.79	0.00	0.25	0.02	1.05	0.02	2
	2_6	1.02	0.02	0.43	0.01	1.46	0.03	2
Rio_AM_3	3_1	0.58	0.01	0.15	0.03	0.73	0.04	2
	3_2	0.82	0.04	0.28	0.04	1.11	0.08	2
	3_3	0.89	0.01	0.24	0.01	1.13	0.02	2
	3_4	0.72	0.00	0.17	0.01	0.89	0.02	2
	3_5	0.84	0.07	0.25	0.00	1.09	0.08	2
	3_6	0.60	0.05	0.11	0.00	0.70	0.05	2
	3_7	0.79	0.01	0.20	0.03	0.99	0.04	2
	3_8	0.89	0.03	0.31	0.00	1.21	0.03	2
	3_9	0.83	0.01	0.21	0.02	1.04	0.03	2
Rio_AM_4	4_1	0.81	0.01	0.27	0.00	1.08	0.01	2
	4_2	0.73	0.01	0.21	0.01	0.94	0.02	2
	4_3	0.68	0.11	0.29	0.17	0.97	0.28	2
	4_4	0.76	0.01	0.21	0.00	0.96	0.01	2
	4_5	0.79	0.00	0.25	0.02	1.05	0.02	2
	4_6	1.02	0.02	0.43	0.01	1.46	0.03	2
	4_7	0.86	0.03	0.27	0.02	1.14	0.06	2
	4_8	0.71	0.01	0.18	0.01	0.89	0.01	2
	4_9	0.76	0.00	0.20	0.00	0.96	0.01	2
	4_10	0.53	0.01	0.20	0.01	0.73	0.02	2
	4_11	0.78	0.02	0.42	0.01	1.21	0.03	2
Rio_AM_5	5_1	-	-	-	-	0.14	0.00	2
	5_2	-	-	-	-	0.25	0.00	2
	5_3	-	-	-	-	0.17	0.00	2
	5_4	0.79	0.00	0.25	0.02	1.05	0.02	2
	5_5	1.02	0.02	0.43	0.01	1.46	0.03	2
	5_6	0.86	0.03	0.27	0.02	1.14	0.06	2
	5_7	0.71	0.01	0.18	0.01	0.89	0.01	2

	5_8	0.76	0.00	0.20	0.00	0.96	0.01	2
	5_9	0.53	0.01	0.20	0.01	0.73	0.02	2
Rio_AM_6	6_1	0.92	0.00	0.26	0.01	1.18	0.01	2
	6_2	0.90	0.00	0.26	0.00	1.16	0.01	2
	6_3	0.87	0.01	0.24	0.02	1.12	0.04	2
	6_4	0.93	0.00	0.27	0.00	1.21	0.00	2
	6_5	0.99	0.10	0.36	0.02	1.34	0.11	2
	6_6	-	-	-	-	0.25	0.00	3
	6_7	1.01	0.02	0.33	0.00	1.34	0.02	2
	6_8	0.86	0.01	0.31	0.03	1.17	0.03	2
	6_9	-	-	-	-	0.65	0.07	2
	6_10	1.09	0.13	0.53	0.10	1.62	0.23	2
Rio_AM_7	7_1	-	-	-	-	0.34	0.01	2
	7_2	-	-	-	-	0.36	0.03	2
	7_3	-	-	-	-	0.64	0.03	2
	7_4	-	-	-	-	0.34	0.02	2
	7_5	-	-	-	-	0.62	0.01	2
	7_6	-	-	-	-	0.64	0.00	2
	7_7	-	-	-	-	0.37	0.03	3
	7_8	0.64	0.03	0.19	0.01	0.82	0.04	2
	7_9	0.74	0.00	0.18	0.00	0.92	0.00	2
	7_10	-	-	-	-	0.41	0.02	2
Rio_AM_8	8_1	0.85	0.02	0.22	0.01	1.07	0.02	2
	8_2	1.10	0.06	0.51	0.04	1.61	0.09	2
	8_3	1.18	0.07	0.38	0.00	1.56	0.07	2
	8_4	1.02	0.01	0.34	0.01	1.36	0.01	2
	8_5	1.26	0.02	0.48	0.02	1.74	0.04	2
Río_AM_9	9_1	-	-	-	-	0.29	0.03	2
	9_2	1.44	0.01	0.69	0.00	2.13	0.01	2
	9_3	1.69	0.17	0.99	0.29	2.68	0.45	2
	9_4	2.01	0.15	1.43	0.18	3.44	0.33	2
	9_5	0.46	0.07	0.43	0.08	0.89	0.15	2
	9_6	1.63	0.04	1.22	0.04	2.85	0.08	2
	9_7	-	-	-	-	0.17	0.00	2
	9_8	1.66	0.13	1.74	0.10	3.40	0.23	2
	9_9	1.61	0.02	1.17	0.02	2.77	0.04	2

Explosive phase – Bomb field

Sample	OH- wt.% (4500)	sd	H_2O_mwt.% (5200)	sd	H2Ot* wt.%	sd	n
CH_2015_02	0.61	0.05	0.12	0.02	0.73	0.06	18
CH_2015_04	0.59	0.03	0.15	0.02	0.74	0.04	21

CH_2015_05	0.69	0.15	0.34	0.06	1.03	0.21	26
CH_2015_06	0.67	0.03	0.18	0.02	0.85	0.05	15
CH_2011_05	0.93	0.08	0.53	0.03	1.46	0.11	38
CH_2011_06	0.97	0.03	0.50	0.04	1.47	0.08	18
CH_Bomb Cald_14	0.60	0.05	0.14	0.04	0.74	0.08	17
CH_Castro	0.68	0.02	0.19	0.02	0.87	0.03	20
CH_2016_01	0.49	0.01	0.10	0.00	0.58	0.02	9
CH_2016_02	0.46	0.02	0.10	0.04	0.57	0.06	5
CH_2016_03	0.63	0.06	0.17	0.05	0.80	0.11	5
CH_2016_04	1.08	0.02	0.64	0.04	1.72	0.06	8
CH_2016_05	0.57	0.01	0.13	0.01	0.70	0.02	5
CH_2016_5B	0.56	0.03	0.08	0.01	0.64	0.04	14
CH_2016_06	0.74	0.02	0.19	0.01	0.93	0.03	5
CH_2016_07	0.74	0.00	0.26	0.01	1.00	0.01	4
CH_2016_08	1.01	0.04	0.42	0.03	1.43	0.07	11
CH_2016_10	1.05	0.00	0.56	0.05	1.61	0.05	14
CH_2016_11	0.71	0.02	0.24	0.00	0.95	0.02	5
CH_2016_12	0.72	0.02	0.22	0.01	0.94	0.03	5
CH_2016_14	0.75	0.01	0.27	0.02	1.02	0.03	7
CH_2016_15	0.67	0.05	0.18	0.01	0.85	0.06	11
CH_2016_16	0.63	0.01	0.15	0.01	0.77	0.02	11
CH_2016_17	0.60	0.02	0.14	0.02	0.73	0.04	5
CH_2016_18	0.85	0.01	0.26	0.01	1.11	0.01	5
CH_2016_19	0.65	0.01	0.17	0.02	0.82	0.03	5
CH_2016_20	0.69	0.04	0.26	0.02	0.95	0.06	5
CH_2016_21	0.58	0.01	0.14	0.01	0.72	0.02	6
CH_2016_22	0.56	0.01	0.09	0.00	0.65	0.01	4
CH_2016_23	0.53	0.03	0.13	0.03	0.65	0.06	6
CH_2016_24	0.69	0.02	0.19	0.46	0.88	0.48	5
CH_2016_26	0.89	0.01	0.46	0.01	1.35	0.03	6
CH_2016_27	0.52	0.12	0.11	0.06	0.63	0.18	6
CH_2016_28	0.79	0.02	0.30	0.01	1.08	0.03	5
CH_2016_29	0.53	0.02	0.11	0.01	0.64	0.03	5
CH_2016_30	0.60	0.00	0.14	0.01	0.75	0.01	5
CH_2016_31	0.57	0.02	0.10	0.01	0.67	0.03	6
CH_2016_32	0.61	0.01	0.13	0.01	0.73	0.02	5
CH_2016_33	0.71	0.00	0.22	0.01	0.93	0.01	5
CH_2016_34	0.69	0.01	0.15	0.02	0.84	0.02	5
CH_2016_35	0.57	0.02	0.19	0.01	0.76	0.03	5
CH_2016_36	0.64	0.04	0.18	0.01	0.83	0.05	5
CH_2016_37	0.76	0.01	0.27	0.01	1.04	0.02	5

CH_2016_38	0.51	0.01	0.10	0.01	0.61	0.02	5
CH_2016_39	0.86	0.02	0.37	0.02	1.23	0.04	5
CH_2016_40	0.54	0.02	0.11	0.01	0.65	0.03	5
CH_2016_41	0.82	0.03	0.39	0.06	1.21	0.09	5
CH_2016_42	0.72	0.01	0.17	0.01	0.89	0.02	5
CH_2016_47	0.62	0.04	0.16	0.02	0.78	0.06	5
CH_2016_48	0.63	0.03	0.18	0.02	0.80	0.04	5
CH_2016_49	0.51	0.01	0.11	0.00	0.62	0.01	5
CH_2016_54	0.50	0.03	0.10	0.01	0.60	0.04	5
CH_2016_55	0.90	0.02	0.57	0.05	1.47	0.07	5
CH_2016_56	1.11	0.05	0.66	0.03	1.77	0.08	5
CH_2016_57	0.51	0.01	0.10	0.01	0.61	0.02	5
CH_2016_01_f	0.72	0.02	0.21	0.02	0.93	0.04	5
CH_2016_02_f	0.52	0.00	0.09	0.01	0.61	0.01	5
CH_2016_03_f	0.94	0.05	0.52	0.04	1.46	0.09	9
CH_2016_04_f	0.74	0.02	0.25	0.00	0.99	0.03	5
CH_2016_05_f	0.58	0.01	0.11	0.01	0.68	0.02	5
CH_2016_06_f	0.90	0.05	0.52	0.06	1.41	0.11	8
CH_2016_07_f	0.64	0.03	0.19	0.02	0.83	0.05	5
CH_2016_08_f	0.78	0.02	0.25	0.01	1.02	0.03	5
CH_2016_09_f	0.49	0.01	0.09	0.01	0.59	0.02	5
CH_2016_10_f	0.72	0.04	0.22	0.01	0.94	0.05	5
CH_2016_11_f	0.71	0.01	0.22	0.01	0.93	0.02	5
CH_2016_12_f	0.51	0.03	0.09	0.01	0.60	0.04	5
CH_2016_13_f	0.78	0.01	0.37	0.03	1.14	0.05	5
CH_2016_14_f	0.68	0.06	0.27	0.01	0.95	0.07	5

Transitional phase

Sample		OH^- wt.% (4500)	sd	H_2O_mwt.% (5200)	Sd	$H2O_t$* wt.%	sd	n
A1	A1_1	-	-	-	-	0.15	0.004	2
	A1_2	-	-	-	-	0.23	0.005	2
	A1_3	0.99	0.10	0.80	0.15	1.79	0.25	2
	A1_4	1.09	0.02	0.49	0.02	1.58	0.04	2
	A1_5	0.84	0.01	0.30	0.001	1.14	0.01	2
	A1_6	1.00	0.01	0.31	0.01	1.32	0.02	2
	A1_7	1.13	0.01	0.86	0.01	1.98	0.02	2
	A1_8	1.03	0.01	0.55	0.01	1.58	0.02	2
	A1_1_a	1.19	0.03	0.79	0.02	1.98	0.05	2
	A1_2_a	1.08	0.01	0.82	0.00	1.90	0.01	2
	A1_3_a	0.97	0.01	0.29	0.02	1.27	0.03	2

	A1_4_a	0.82	0.001	0.26	0.001	1.08	0.002	2
	A1_5_a	1.04	0.04	0.50	0.03	1.54	0.07	2
	A1_6_a	0.93	0.06	0.72	0.01	1.65	0.06	2
	A1_7_a	0.91	0.03	0.74	0.07	1.65	0.10	2
	A1_8_a	1.28	0.05	1.07	0.01	2.35	0.06	2
	A1_9_a	1.20	0.01	1.37	0.08	2.56	0.09	2
	A1_10_a	1.21	0.02	0.97	0.05	2.18	0.06	2
	A1_11_a	1.08	0.08	0.42	0.05	1.50	0.13	2
	A1_12_a	-	-	-	-	0.15	0.004	2
	A1_13_a	-	-	-	-	0.05	0.07	2
	A1_14_a	1.25	0.04	1.01	0.04	2.26	0.08	
A2	A2_1	-	-	-	-	0.29	0.03	2
	A2_2	-	-	-	-	0.15	0.03	2
	A2_3	-	-	-	-	0.19	0.01	2
	A2_4	-	-	-	-	0.09	0.001	2
	A2_5	-	-	-	-	0.34	0.01	2
	A2_1_a	1.31	0.00	0.98	0.07	2.29	0.07	2
	A2_2_a	1.23	0.02	0.76	0.02	1.99	0.04	2
	A2_3_a	1.01	0.00	0.81	0.01	1.81	0.01	2
	A2_4_a	-	-	-	-	0.13	0.01	2
	A2_5_a	-	-	-	-	0.11	0.02	2
	A2_6_a	-	-	-	-	0.10	0.02	2
	A2_7_a	-	-	-	-	0.16	0.03	2
	A2_8_a	0.50	0.01	0.21	0.01	0.71	0.01	2
	A2_9_a	1.24	0.02	0.68	0.01	1.93	0.02	2
	A2_10_a	-	-	-	-	0.09	0.00	2
A3	A3_1	-	-	-	-	0.16	0.00	2
	A3_2	1.01	0.10	0.39	0.06	1.39	0.16	2
	A3_3	0.95	0.003	0.28	0.00	1.23	0.003	2
	A3_1_a	1.06	0.03	0.97	0.07	2.03	0.10	2
	A3_2_a	1.06	0.001	0.40	0.01	1.46	0.01	2
	A3_3_a	0.80	0.01	0.16	0.02	0.97	0.02	2
	A3_4_a	1.02	0.03	0.54	0.09	1.56	0.12	2
	A3_5_a	0.23	0.02	0.06	0.03	0.29	0.05	2
	A3_6_a	0.57	0.01	0.18	0.01	0.75	0.01	2
	A3_7_a	0.59	0.01	0.61	0.02	1.19	0.03	2
	A3_8_a	1.25	0.01	0.74	0.03	1.99	0.05	2
	A3_9_a	0.91	0.09	0.44	0.04	1.35	0.12	2
	A3_10_a	1.06	0.01	0.55	0.02	1.61	0.03	2
	A3_11_a	1.09	0.02	0.50	0.03	1.59	0.04	2
	A3_12_a	-	-	-	-	0.18	0.01	2

	A3_13_a		-	-	-	0.15	0.01	2
	A3_14_a	1.10	0.09	1.05	0.28	2.15	0.38	2
	A3_15_a	1.01	0.04	0.37	0.00	1.38	0.04	2
	A3_16_a	0.22	0.01	0.10	0.02	0.33	0.03	2
B1	B1_1	1.04	0.003	0.30	0.05	1.34	0.05	2
	B1_2	-	-	-	-	0.25	0.01	2
	B1_3	0.97	0.00	0.31	0.02	1.28	0.02	2
	B1_4	0.91	0.01	0.27	0.00	1.18	0.02	2
	B1_5	-	-	-	-	0.20	0.03	2
	B1_6	1.00	0.05	0.22	0.03	1.22	0.08	2
	B1_1_a	0.88	0.01	0.25	0.02	1.13	0.04	2
	B1_2_a	0.92	0.00	0.26	0.001	1.18	0.00	2
	B1_3_a	0.72	0.007	0.15	0.002	0.87	0.01	2
	B1_4_a	0.84	0.004	0.36	0.01	1.21	0.01	2
	B1_5_a	-	-	-	-	0.12	0.00	2
	B1_6_a	0.90	0.03	1.28	0.03	2.18	0.06	2
	B1_7_a	0.86	0.07	1.14	0.09	2.00	0.17	2
	B1_8_a	0.57	0.02	0.73	0.01	1.30	0.02	2
	B1_9_a	0.99	0.03	1.47	0.05	2.46	0.09	2
	B1_10_a	0.92	0.00	1.24	0.00	2.16	0.00	2
	B1_11_a	0.93	0.02	1.20	0.03	2.13	0.04	2
	B1_12_a	0.68	0.01	0.79	0.01	1.47	0.02	2
	B1_13_a	0.90	0.01	1.24	0.04	2.14	0.05	2
	B1_15_a	1.01	0.00	1.55	0.02	2.56	0.02	2
	B1_16_a	0.67	0.01	0.79	0.01	1.46	0.01	2
B2	B2_1	-	-	-	-	0.19	0.01	3
	B2_2	0.86	0.00	0.30	0.01	1.16	0.01	2
	B2_3	0.84	0.02	0.31	0.00	1.15	0.02	2
	B2_4	-	-	-	--	0.11	0.01	2
	B2_5	0.92	0.01	0.29	0.00	1.21	0.01	2
	B2_6	0.79	0.03	0.22	0.01	1.01	0.04	2
	B2_7	0.81	0.02	0.22	0.01	1.03	0.02	2
	B2_8	1.06	0.01	0.48	0.02	1.53	0.03	2
	B2_9	0.84	0.00	0.33	0.03	1.17	0.03	2
B3	B3_1	0.58	0.02	0.19	0.02	0.76	0.04	2
	B3_2	0.81	0.05	0.25	0.02	1.06	0.06	2
	B3_3	0.88	0.08	0.33	0.02	1.21	0.10	2
	B3_4	0.70	0.04	0.21	0.01	0.91	0.05	2
	B3_5	0.87	0.02	0.32	0.02	1.19	0.04	2
	B3_6	-	-	-	-	0.28	0.01	2
	B3_7	-	-	-	-	0.18	0.00	2

	B3_8	-	-	-	-	0.17	0.01	2
	B3_1_a	0.83	0.00	0.21	0.00	1.05	0.00	2
	B3_2_a	1.05	0.05	0.41	0.06	1.46	0.10	2
	B3_3_a	0.79	0.00	0.19	0.00	0.99	0.01	2
	B3_4_a	0.78	0.01	0.21	0.00	0.99	0.01	2
	B3_5_a	1.09	0.02	0.70	0.04	1.79	0.06	2
	B3_6_a	-	-	-	-	0.21	0.01	2
B4	B4_1	-	-	-	-	0.18	0.02	2
	B4_2	-	-	-	-	0.22	0.04	2
	B4_3	1.14	0.02	0.94	0.09	2.08	0.10	2
	B4_4	-	-	-	-	0.15	0.00	2
	B4_5	1.10	0.04	0.47	0.004	1.57	0.05	2
	B4_6	0.97	0.03	0.38	0.02	1.35	0.05	2
	B4_1_a	1.13	0.03	0.48	0.03	1.61	0.06	2
	B4_2_a	1.08	0.01	0.56	0.01	1.65	0.03	2
	B4_3_a	1.11	0.01	0.51	0.03	1.62	0.04	2
	B4_4_a	1.15	0.01	0.61	0.02	1.76	0.03	2
	B4_5_a	1.20	0.002	0.62	0.01	1.81	0.01	2
	B4_6_a	1.19	0.01	0.74	0.08	1.93	0.09	2
B5	B5_1	-	-	-	-	0.11	0.01	2
	B5_2	-	-	-	-	0.16	0.02	2
	B5_3	0.95	0.03	0.50	0.01	1.45	0.03	2
	B5_4	1.00	0.02	0.40	0.003	1.40	0.02	2
	B5_5	-	-	-	-	0.15	0.01	2
	B5_6	1.01	0.02	0.49	0.02	1.50	0.04	2
	B5_7	1.10	0.04	0.84	0.00	1.95	0.04	2
	B5_8	-	-	-	-	0.14	0.002	2
	B5_9	0.84	0.05	0.37	0.03	1.21	0.08	2
	B5_10	1.31	0.10	1.38	0.02	2.70	0.12	2
B6	B6_1_a	1.16	0.02	0.52	0.05	1.68	0.07	2
	B6_2_a	1.13	0.02	0.65	0.03	1.79	0.05	2
	B6_3_a	1.13	0.02	0.72	0.10	1.85	0.12	2
	B6_4_a	1.05	0.01	0.56	0.02	1.61	0.02	2
	B6_5_a	0.95	0.004	0.36	0.01	1.31	0.02	2
	B6_6_a	0.96	0.01	0.34	0.01	1.30	0.02	2
	B6_7_a	0.95	0.06	0.31	0.03	1.26	0.09	2
C1	C1_1	1.11	0.05	0.56	0.05	1.68	0.09	2
	C1_2	0.97	0.01	0.63	0.02	1.60	0.03	2
	C1_3	0.75	0.05	0.24	0.005	0.99	0.05	2
	C1_1_a	1.16	0.02	0.60	0.02	1.75	0.04	2
	C1_2_a	1.23	0.02	0.92	0.08	2.15	0.10	2

	C1_3_a	0.94	0.01	0.32	0.02	1.26	0.03	2
	C1_4_a	1.13	0.00	0.66	0.004	1.80	0.01	2
	C1_5_a	0.73	0.02	0.15	0.01	0.89	0.03	2
	C1_6_a	0.89	0.02	0.26	0.01	1.15	0.03	2
	C1_7_a	0.97	0.002	0.38	0.001	1.35	0.003	2
	C1_8_a	0.99	0.002	0.56	0.00	1.55	0.002	2
	C1_9_a	1.08	0.00	0.56	0.03	1.64	0.03	2
C2	C2_1	-	-	-	-	0.15	0.01	2
	C2_2	0.76	0.00	0.13	0.01	0.90	0.01	2
	C2_3	-	-	-	-	0.18	0.01	2
	C2_4	1.16	0.01	0.78	0.01	1.94	0.02	2
	C2_5	0.93	0.01	0.41	0.01	1.33	0.02	2
	C2_6	1.02	0.01	0.36	0.00	1.38	0.02	2
	C2_7	0.75	0.04	0.16	0.02	0.91	0.06	2
	C2_8	0.39	0.01	0.07	0.01	0.46	0.02	2
	C2_1_a	0.83	0.00	0.21	0.00	1.05	0.004	2
	C2_2_a	1.05	0.05	0.41	0.06	1.46	0.10	2
	C2_3_a	0.79	0.00	0.19	0.00	0.99	0.01	2
	C2_4_a	0.78	0.01	0.21	0.004	0.99	0.01	2
	C2_5_a	1.09	0.02	0.70	0.04	1.79	0.06	2
	C2_6_a	-	-	-	-	0.21	0.01	2
	C2_7_a	-	-	-	-	0.35	0.001	2
	C2_8_a	1.08	0.03	0.54	0.02	1.62	0.05	2
	C2_9_a	-	-	-	-	0.21	0.02	2
	C2_10_a	0.76	0.01	0.17	0.02	0.93	0.03	2
	C2_11_a	1.17	0.02	0.72	0.003	1.89	0.02	2
	C2_12_a	0.78	0.06	0.24	0.07	1.02	0.13	2
	C2_13_a	1.08	0.09	0.49	0.01	1.57	0.10	2
	C2_14_a	0.74	0.01	0.90	1.00	1.63	1.01	2
	C2_15_a	1.35	0.07	0.69	0.06	2.04	0.12	2
	C2_16_a	1.17	0.00	0.89	0.12	2.07	0.12	2
	C2_17_a	0.83	0.07	0.22	0.05	1.05	0.12	2
C3	C3_1_a	1.05	0.02	0.47	0.01	1.52	0.04	2
	C3_2_a	0.59	0.002	0.11	0.01	0.70	0.01	2
	C3_3_a	1.28	0.02	0.63	0.04	1.91	0.06	2
	C3_4_a	1.33	0.02	1.31	0.01	2.64	0.02	2
	C3_5_a	1.31	0.06	0.67	0.04	1.98	0.10	2
	C3_6_a	1.18	0.01	0.55	0.01	1.72	0.01	2
	C3_7_a	1.13	0.00	0.64	0.04	1.77	0.04	2
	C3_8_a	1.05	0.02	0.43	0.01	1.48	0.03	2
	C3_9_a	1.11	0.00	0.51	0.02	1.62	0.02	2

	C3_10_a	0.79	0.002	0.16	0.01	0.95	0.01	2
C4	C4_1	0.90	0.00	1.13	0.003	2.03	0.003	2
	C4_2	0.76	0.06	0.91	0.09	1.67	0.15	2
	C4_3	0.86	0.02	1.11	0.04	1.97	0.06	2
	C4_4	0.98	0.01	0.31	0.002	1.29	0.01	2
	C4_5	0.86	0.02	1.08	0.02	1.94	0.04	2
	C4_1_a	0.61	0.08	0.09	0.001	0.70	0.08	2
	C4_2_a	0.66	0.001	0.11	0.005	0.77	0.01	2
	C4_3_a	0.68	0.04	0.13	0.04	0.81	0.08	3
	C4_4_a	0.86	0.01	0.29	0.003	1.15	0.01	2
	C4_5_a	1.02	0.01	0.35	0.02	1.37	0.03	2
	C4_6_a	0.71	0.01	0.14	0.01	0.85	0.02	2
	C4_7_a	0.66	0.005	0.11	0.01	0.78	0.01	2
	C4_8_a	0.61	0.01	0.13	0.01	0.74	0.02	2
	C4_9_a	0.69	0.01	0.12	0.03	0.81	0.04	2
	C4_10_a	0.76	0.02	0.15	0.001	0.91	0.02	2
	C4_11_a	0.68	0.001	0.10	0.002	0.78	0.003	2
	C4_12_a	0.86	0.02	0.19	0.01	1.05	0.03	2
	C4_13_a	0.82	0.01	0.20	0.01	1.02	0.01	2
	C4_14_a	0.76	0.01	0.18	0.03	0.94	0.05	2
	C4_15_a	0.83	0.06	0.17	0.03	1.01	0.09	2
	C4_16_a	0.85	0.01	0.20	0.001	1.06	0.01	2
C5	C5_1	0.48	0.03	0.07	0.01	0.55	0.03	3
	C5_2	0.70	0.02	0.20	0.01	0.90	0.03	2
	C5_3	1.02	0.07	0.49	0.10	1.51	0.17	2
	C5_4	0.96	0.19	0.28	0.04	1.24	0.24	2
	C5_5	0.83	0.02	0.26	0.00	1.08	0.02	2
	C5_6	0.85	0.04	0.36	0.05	1.21	0.09	2
C6	C6_1	0.83	0.00	0.26	0.00	1.09	0.00	2
	C6_2	0.83	0.04	0.29	0.08	1.12	0.12	2
	C6_3	0.89	0.02	0.28	0.01	1.17	0.02	2
	C6_4	0.91	0.01	0.43	0.00	1.34	0.01	2
	C6_5	0.77	0.07	0.20	0.05	0.96	0.12	2
D1	D1_1	0.90	0.00	0.22	0.00	1.12	0.00	2
	D1_2	0.56	0.01	0.08	0.01	0.63	0.02	2
	D1_3	0.73	0.02	0.14	0.02	0.87	0.04	2
	D1_4	0.66	0.04	0.11	0.01	0.78	0.05	2
	D1_5	0.59	0.00	0.10	0.00	0.68	0.00	2
	D1_6	0.54	0.02	0.11	0.02	0.64	0.04	2
	D1_7	0.53	0.04	0.43	0.46	0.96	0.51	2
	D1_1_a	0.74	0.00	0.17	0.00	0.91	0.00	2

	D1_2_a	0.89	0.02	0.26	0.02	1.15	0.03	2
	D1_3_a	0.68	0.00	0.15	0.01	0.83	0.01	2
	D1_4_a	0.66	0.01	0.13	0.00	0.80	0.02	2
	D1_5_a	0.80	0.02	0.24	0.01	1.04	0.03	2
	D1_6_a	1.08	0.01	1.11	0.02	2.18	0.02	2
	D1_7_a	0.76	0.02	0.14	0.01	0.89	0.03	2
	D1_8_a	0.77	0.00	0.23	0.01	1.00	0.01	2
	D1_9_a	0.65	0.00	0.15	0.00	0.81	0.01	2
	D1_10_a	0.92	0.03	0.31	0.03	1.22	0.06	2
	D1_11_a	0.71	0.02	0.16	0.04	0.86	0.06	2
	D1_12_a	0.92	0.02	0.27	0.02	1.20	0.04	2
	D1_13_a	0.95	0.01	0.51	0.00	1.46	0.01	2
	D1_14_a	0.82	0.05	0.18	0.01	1.00	0.06	2
	D1_15_a	0.91	0.03	0.24	0.00	1.15	0.03	2
	D1_16_a	1.00	0.02	0.57	0.01	1.57	0.03	2
D2	D2_1	0.88	0.08	0.38	0.11	1.26	0.19	2
	D2_2	0.56	0.03	0.28	0.01	0.84	0.04	2
	D2_3	0.76	0.01	0.22	0.00	0.98	0.01	2
	D2_4	0.86	0.02	0.39	0.01	1.25	0.03	2
D3	D3_1_a	0.83	0.04	0.16	0.03	0.98	0.06	2
	D3_2_a	0.88	0.04	0.27	0.13	1.16	0.17	2
	D3_3_a	0.99	0.01	0.40	0.01	1.39	0.02	2
	D3_4_a	0.63	0.04	0.11	0.03	0.74	0.07	2
	D3_5_a	0.75	0.01	0.19	0.01	0.94	0.02	2
	D3_6_a	1.02	0.01	0.48	0.01	1.49	0.03	2
	D3_7_a	0.95	0.02	0.24	0.00	1.18	0.02	2
	D3_8_a	0.89	0.01	0.34	0.00	1.23	0.01	2
	D3_9_a	1.15	0.00	0.29	0.00	1.44	0.01	2
	D3_10_a	0.96	0.03	0.27	0.01	1.22	0.04	2
	D3_11_a	0.96	0.01	0.37	0.00	1.32	0.02	2
	D3_12_a	0.92	0.01	0.39	0.11	1.31	0.12	2
D4	D4_1	0.55	0.00	0.05	0.01	0.60	0.01	2
	D4_2	0.76	0.00	0.23	0.01	1.00	0.01	2
	D4_3	0.62	0.03	0.11	0.02	0.73	0.04	2
	D4_4	0.62	0.02	0.08	0.00	0.70	0.03	2
	D4_5	0.71	0.04	0.20	0.03	0.91	0.08	2
	D4_6	0.98	0.02	0.29	0.04	1.28	0.06	2
D5	D5_1	0.63	0.01	0.12	0.00	0.75	0.02	2
	D5_2	0.67	0.04	0.12	0.02	0.79	0.06	2
	D5_3	0.51	0.00	0.06	0.01	0.57	0.01	2
	D5_4	0.57	0.01	0.05	0.00	0.62	0.01	2

D5_5	0.74	0.05	0.13	0.03	0.88	0.08	2
D5_6	0.74	0.07	0.14	0.00	0.88	0.07	2
D5_7	0.69	0.06	0.14	0.01	0.84	0.07	2
D5_8	0.72	0.03	0.13	0.01	0.85	0.04	2
D5_9	0.61	0.00	0.08	0.00	0.68	0.00	2
D5_1_a	0.53	0.01	0.09	0.01	0.62	0.02	2
D5_2_a	0.52	0.01	0.10	0.01	0.62	0.02	2
D5_3_a	0.65	0.03	0.12	0.01	0.77	0.04	2
D5_4_a	0.37	0.00	0.03	0.00	0.40	0.01	2
D5_5_a	0.71	0.01	0.14	0.00	0.84	0.01	2
D5_6_a	0.68	0.00	0.12	0.01	0.80	0.02	2
D5_7_a	0.85	0.00	0.28	0.01	1.13	0.01	2
D5_8_a	0.69	0.01	0.10	0.00	0.79	0.01	2
D5_9_a	0.53	0.03	0.05	0.00	0.59	0.03	2
D5_10_a	0.68	0.03	0.13	0.01	0.81	0.03	2
D5_11_a	0.75	0.03	0.14	0.01	0.89	0.04	2
D5_12_a	0.61	0.00	0.10	0.00	0.71	0.00	2

Effusive phase

Sample	OH^- wt.% (4500)	sd	H_2O_mwt.% (5200)	Sd	H2O$_t$* wt.%	sd	n
CH_2015_01	-	-	-	-	0.13	0.002	5
Pre-CH_Cone	-	-	-	-	0.29	0.01	5

B. Electron Microprobe Analysis (EMPA)

		Na_2O	SiO_2	CaO	FeO	P_2O_5	F	MgO	K_2O	MnO	Cl	Al_2O_3	SO_3	TiO_2	Total
Effusive	CH_2015_01	3	75.54	1.3008	1.113	-	-	0.2143	3.01	0.0687	-	13.86	-	0.1237	98.2732
		2.93	75.47	1.2671	1.2237	-	-	0.2135	3.02	0.0544	-	13.79	-	0.1553	98.1345
		3.06	75.37	1.2871	1.1957	-	-	0.2168	3.04	0.028	-	13.84	-	0.1673	98.205
		2.98	75.87	1.3175	1.1156	-	-	0.1886	3.19	0.0534	-	13.71	-	0.0976	98.5247
		2.83	75.64	1.3105	1.1581	-	-	0.1658	3.11	0.0689	-	13.73	-	0.1535	98.1669
		2.94	75.86	1.2457	1.1372	-	-	0.202	3.09	0.0455	-	13.79	-	0.1295	98.4752
	Pre-CH_cone	4.14	75.05	1.41	1.15	0.052	0	0.19	3.05	0.073	0.079	13.876	0	0.132	99.178
		4.01	75.13	1.36	1.18	0.061	0.112	0.191	3.03	0.007	0.079	13.99	0.023	0.131	99.234
		4.01	74.64	1.34	1.22	0.074	0.141	0.203	3.06	0.064	0.072	13.895	0	0.13	98.771
		4.11	75.24	1.38	1.22	0.036	0	0.196	3.08	0.074	0.082	13.905	0.02	0.113	99.426
		3.97	74.96	1.32	1.08	0.057	0.029	0.198	3.04	0.002	0.071	13.681	0.002	0.116	98.491
Explosive	CH_2016_04	4.03	73.67	1.38	1.32	0.064	0	0.22	2.99	0.067	0.08	13.682	0.005	0.15	97.632
		3.98	73.80	1.40	1.34	0.059	0	0.226	3.01	0.068	0.086	13.723	0	0.142	97.807
		3.92	74.64	1.34	1.22	0.06	0	0.259	2.97	0.037	0.082	13.757	0.003	0.116	98.376
		3.93	74.26	1.38	1.35	0.058	0.17	0.279	3.04	0.08	0.084	13.848	0.026	0.152	98.565
		3.91	74.68	1.43	1.22	0.068	0	0.259	3.06	0.058	0.073	13.814	0.012	0.147	98.713
Transitional	D5_1	4.06	75.86	1.42	1.29	0.044	0	0.243	3.12	0.045	0.084	13.854	0	0.154	100.149
		4.01	75.99	1.36	1.37	0.027	0.038	0.23	3.09	0.051	0.085	13.769	0	0.17	100.151
		4.08	75.83	1.37	1.30	0.02	0.002	0.233	2.96	0.051	0.089	13.779	0	0.147	99.839
	D5_3	4.13	75.90	1.35	1.30	0.064	0.119	0.241	3.02	0.054	0.097	13.883	0	0.134	100.216
		4.12	76.25	1.34	1.38	0.083	0.201	0.251	3.12	0.075	0.093	13.861	0.011	0.121	100.792
		4.05	76.16	1.33	1.31	0.029	0	0.241	3.00	0.074	0.085	13.877	0.011	0.143	100.294
	D5_5	4.16	75.95	1.43	1.37	0.072	0	0.253	2.98	0.014	0.077	13.896	0	0.149	100.32
		4.03	75.62	1.39	1.30	0.073	0.107	0.256	3.03	0.087	0.065	13.92	0	0.166	99.979
		3.94	75.85	1.38	1.34	0.058	0	0.267	2.99	0.089	0.087	13.898	0.01	0.16	100.047
	D5_7	4.00	75.85	1.36	1.36	0.036	0.084	0.259	2.99	0.068	0.086	13.86	0	0.153	100.044
		4.10	75.45	1.38	1.38	0.041	0.072	0.247	3.03	0.04	0.084	13.851	0	0.165	99.789
		4.09	75.71	1.44	1.28	0.073	0	0.283	3.08	0.067	0.085	13.763	0	0.152	99.996

D5_9	3.93	75.49	1.41	1.32	0.066	0	0.238	3.02	0.02	0.09	13.826	0	0.168	99.546
	4.14	75.20	1.43	1.39	0.049	0	0.27	3.14	0.065	0.092	13.861	0.025	0.149	99.78
	4.07	75.98	1.47	1.34	0.074	0	0.259	3.06	0.056	0.076	14.033	0	0.145	100.541
C4_2	3.89	74.47	1.33	1.99	0.053	0.048	0.52	3.01	0.04	0.091	13.71	0.003	0.164	99.282
	3.90	75.71	1.33	1.20	0.06	0.111	0.199	3.10	0.035	0.092	13.786	0	0.145	99.601
	3.85	74.98	1.33	1.13	0.047	0	0.217	3.15	0.058	0.085	13.694	0	0.141	98.672
	3.79	75.65	1.35	1.27	0.042	0.054	0.262	3.14	0.075	0.078	13.831	0	0.146	99.641
C4_3	4.05	75.27	1.40	1.34	0.06	0.121	0.251	3.02	0.044	0.077	13.714	0.005	0.163	99.449
	4.01	75.81	1.39	1.31	0.068	0	0.278	3.14	0.049	0.072	13.792	0.018	0.168	100.087
	3.96	75.28	1.39	1.28	0.08	0	0.245	3.11	0.028	0.091	13.772	0.008	0.123	99.346
C4_4	3.99	74.90	1.35	1.39	0.063	0.002	0.241	3.03	0.069	0.082	13.875	0	0.164	99.141
	4.05	74.53	1.39	1.32	0.051	0.069	0.267	3.08	0.046	0.086	13.769	0	0.129	98.735
	3.91	74.88	1.42	1.30	0.079	0	0.252	3.02	0.05	0.087	13.787	0	0.13	98.895
C4_6	4.05	74.89	1.47	1.34	0.067	0	0.284	3.08	0.035	0.073	13.788	0.007	0.159	99.222
	4.10	74.43	1.39	1.34	0.02	0.154	0.279	2.99	0.039	0.079	13.809	0.019	0.142	98.701
	3.96	74.96	1.40	1.38	0.017	0	0.238	3.03	0.059	0.08	13.857	0.007	0.119	99.094
	4.05	74.57	1.45	1.35	0.063	0.054	0.261	3.03	0.08	0.083	13.874	0	0.14	98.959

C. Table of experimental conditions (High T – 0.1 MPa experiments)

	Experiment	H_2O_t (wt.%)	T (°C)	Duration (s)	Time lag (s)	Time eq (s)	mass (gr)	A_f/A_0	Φ (%)
CH_2015_01	CH_2015_01_01	0.13	766	1683	-	Not eq.	0.695	1.00	-
	CH_2015_01_02		842	1667	-	Not eq.	0.660	1.00	-
	CH_2015_01_03		900	1629	-	Not eq.	0.685	1.00	2
	CH_2015_01_04		900	9782	-	Not eq.	0.779	1.01	1
	CH_2015_01_05		899	35755	-	Not eq.	0.746	1.00	25
	CH_2015_01_06		1032	9148	-	Not eq.	0.594	1.88	57
	CH_2015_01_07		1000	11033	-	Not eq.	0.758	1.93	65
	CH_2015_01_08		955	46996	-	Not eq.	0.702	1.86	62
	CH_2015_01_09		988	16367	-	Not eq.	0.639	1.59	47
	CH_2015_01_10		935	39128	-	Not eq.	0.598	1.07	24
	CH_2015_01_11		998	25320	-	19980	-	-	-
	CH_2015_01_12		950	71100	-	68340	0.703	1.80	-
CH_2015_02	CH_2015_02_01	0.75	728	1620	-	No eq.	0.634	1.00	1
	CH_2015_02_02*		746	1620	-	No eq.	0.704	1.04	29
	CH_2015_02_03*		767	1620	1180	No eq.	0.696	1.09	31
	CH_2015_02_04*		785	1620	946	No eq.	0.552	1.49	35
	CH_2015_02_05*		804	1620	448	No eq.	0.729	4.94	89
	CH_2015_02_06*		824	1620	352	No eq.	0.732	6.22	91
	CH_2015_02_07*		844	1620	211	1260	0.632	6.28	92
	CH_2015_02_08*		864	1600	173	780	0.703	6.98	93
	CH_2015_02_09*		884	1620	133	540	0.690	7.22	93
	CH_2015_02_10*		902	1620	95	330	0.708	7.63	94
	CH_2015_02_11*		923	1620	68	210	0.768	7.53	94
	CH_2015_02_12*		942	1620	64	158	0.627	7.70	94
	CH_2015_02_13		963	720	62	120	0.722	6.26	94
	CH_2015_02_14*		982	1606	43	100	0.705	6.31	93
	CH_2015_02_15*		1001	1612	49	90	0.779	4.68	90
	CH_2015_02_16		790	5767	752	4166	0.663	5.24	-
	CH_2015_02_17		815	5568	241	1466	0.430	4.83	-
	CH_2015_02_18		805	3207	543	2833	0.575	4.60	-
	CH_2015_02_19		824	3985	359	1900	0.515	5.90	-
	CH_2015_02_20		780	14932	1316	-	0.479	5.13	-
	CH_2015_02_21		780	5448	845	4666	0.525	4.36	-
	CH_2015_02_22		821	3134	444	2333	-	5.74	-
CH_2015_05	CH_2015_05_01*	0.97	776	1620	218	No eq.	0.691	5.27	89
	CH_2015_05_02*		790	1620	85	No eq.	0.566	5.03	89
	CH_2015_05_03*		810	1620	97	1020	0.674	6.41	92
	CH_2015_05_04*		829	1620	68	1320	0.633	7.84	93
	CH_2015_05_05*		849	1620	63	900	0.695	7.91	94
	CH_2015_05_06*		868	1620	64	480	0.844	7.55	94
	CH_2015_05_07		887	270	65	-	0.566	7.91	95
	CH_2015_05_08*		907	1620	33	150	0.690	6.25	93
	CH_2015_05_09*		926	1620	31	166	0.652	8.57	95
	CH_2015_05_10*		945	1620	45	120	0.790	8.44	96
	CH_2015_05_11*		964	1620	36	120	0.749	10.29	96

	CH_2015_05_12		982	900	30	75	0.671	8.07	93
	CH_2015_05_13*		1004	1633	28	67	0.701	4.34	-
	CH_2015_05_14		1024	750	29	58	0.691	5.08	-
	CH_2015_05_15		1024	402	24	48	0.632	5.86	-
	CH_2015_05_16*		986	1648	37	67	0.604	6.39	-
	CH_2015_05_17		990	598	31	65	0.661	6.56	-
	CH_2015_05_18		974	1543	27	75	0.618	6.67	-
	CH_2015_05_19		965	183	30	77	0.609	7.82	-
	CH_2015_05_20		958	210	34	72	0.575	7.44	-
	CH_2015_05_21		983	120	25	-	0.417	1.83	-
	CH_2015_05_22		907	83	50	No eq.	0.685	4.15	-
	CH_2015_05_23		908	323	61	200	0.631	7.97	-
	CH_2015_05_24		896	277	52	208	0.683	12.03	-
	CH_2015_05_25		915	417	50	142	0.605	9.11	-
	CH_2015_05_26		840	345	91	-	0.458	7.00	-
	CH_2015_05_27		771	603	175	No eq.	0.551	2.02	-
	CH_2015_05_28		755	667	283	No eq.	0.507	1.77	-
	CH_2015_05_29*		887	1613	58	260	0.611	7.36	-
	CH_2015_05_30		854	1620	77	500	0.535	6.46	-
	CH_2015_05_31		832	1631	97	1167	0.609	6.11	-
	CH_2015_05_32*		746	6728	362	4333	0.576	5.02	-
	CH_2015_05_33		760	2185	208	-	0.548	4.59	-
	CH_2015_05_34		773	2574	219	-	0.559	6.42	-
	CH_2015_05_35		781	4194	209	2617	0.556	5.63	-
	CH_2015_05_36		775	4637	198	2433	0.359	4.87	-
	CH_2015_05_37		791	5961	171	1167	0.547	5.30	-
	CH_2015_05_38		801	3004	234	1167	0.549	6.07	-
	CH_2015_05_39*		762	6827	356	5167	0.399	5.92	-
CH_2011_05	CH_2011_05_01*	1.4	741	1620	129	1200	0.341	5.24	88
	CH_2011_05_02*		767	1620	96	780	0.640	6.00	91
	CH_2011_05_03*		786	1620	80	540	0.421	6.03	90
	CH_2011_05_04*		805	1620	62	480	0.773	8.61	92
	CH_2011_05_05*		821	1620	63	360	0.908	8.04	94
	CH_2011_05_06*		845	1620	54	300	0.577	7.62	94
	CH_2011_05_07*		855	1620	55	180	0.979	7.39	94
	CH_2011_05_08*		861	1620	58	210	0.744	7.35	93
	CH_2011_05_09*		876	70	39	blew up	0.552	5.90	-
	CH_2011_05_10*		885	73	41	blew up	0.695	7.18	-
	CH_2011_05_11		790	1683	87	-	-	-	-
	CH_2011_05_12*		879	1620	45	135	0.543	8.31	-
	CH_2011_05_13*		887	73	44	blew up	0.656	6.88	-
	CH_2011_05_14*		892	161	43	100	0.649	8.22	-
	CH_2011_05_15*		901	58	33	blew up	0.591	5.88	-
	CH_2011_05_16*		900	63	36	blew up	0.493	8.24	-
	CH_2011_05_17*		897	1620	25	80	0.537	9.31	-
	CH_2011_05_18*		874	63	23	blew up	0.982	7.64	-

*Experiment plot in Fig. 3A-D

D. Newspaper analysis

		Reported event				Reported impacts					
	Event Code	news date	Start	End	Wind velocity (km/h)	Transportation Accessibility	Electricty supply	Telecommunications	School activities	Visibility	
2011	1	07/06/2011	06/06/2011	07/06/2011	> 100	x	x	x	x	x	
		08/06/2011	06/06/2011	07/06/2011	> 80	x	x		x	x	10 meters
	2	12/06/2011	12/06/2011								
		13/06/2011	12/06/2011	12/06/2011						x	almost 0
	3	18/06/2011	17/06/2011			x				x	almost 0
	4	24/06/2011	23/06/2011	23/06/2011					x		
	5	28/06/2011	27/06/2011							x	
		29/06/2011	28/06/2011							x	
		30/06/2011	28/06/2011	29/06/2011		x			x		
		30/06/2011	27/06/2011	30/06/2011		x			x		
		01/07/2011	27/06/2011	30/06/2011		x				x	few meters
	6	21/07/2011	20/07/2011	21/07/2011		x				x	
		22/07/2011	20/07/2011	21/07/2011	> 80	x			x	x	10 meters
	7	26/07/2011	25/07/2011	25/07/2011	70				x	x	few meters
	8	28/07/2011	27/07/2011	27/07/2011					x	x	50 meters
	9	06/08/2011	05/08/2011	05/08/2011		x			x	x	few meters
	10	30/08/2011	29/08/2011	29/08/2011		x			x	x	
	11	06/09/2011	01/09/2011	05/09/2011	< 50				x		
	12	10/09/2011	09/09/2011	10/09/2011	>90	x			x	x	10 meters
	13	26/09/2011	25/09/2011		30						
	14	15/10/2011	14/10/2011		> 70						
		16/10/2011	14/10/2011	15/10/2011	70	x				x	almost 0
	15	28/10/2011	26/10/2011	28/10/2011		x				x	
	16	09/11/2011	09/11/2011	09/11/2011		x				x	
		10/11/2011	09/11/2011	10/11/2011		x				x	
	17	24/11/2011	21/11/2011	21/11/2011					x		
			23/11/2011	23/11/2011	>70	x			x	x	
		27/11/2011	16/11/2011	26/11/2011							
20	18	08/02/	07/02/	07/02/	60	x				x	

12		2012	2012	2012								
	19	22/06/2012	21/06/2012		>90	x	x			x	x	few meters
	20	10/08/2012	09/08/2012							x	x	
	21	05/10/2012	04/10/2012	04/10/2012	> 70	x				x	x	few meters
	22	31/10/2012	31/10/2012		> 90	x				x	x	
		01/11/2012	31/10/2012		> 90	x				x	x	> 100 m
	23	12/12/2012	11/12/2012	11/12/2012	> 70							
	24	15/12/2012	14/12/2012			x					x	
	25	19/12/2012	18/12/2012		> 70						x	
2013	26	30/05/2013	29/05/2013	30/05/2013	> 120	x	x			x	x	
	27	21/08/2013	21/08/2013	21/08/2013								
		22/08/2013	21/08/2013	21/08/2013	100						x	few meters
	28	10/09/2013	09/09/2013	09/09/2013	> 100	x	x			x		
	29	11/11/2013	11/11/2013	11/11/2013						x		
		12/11/2013	11/11/2013	11/11/2013						x		